ABSTRACT

Title of dissertation: ROTATING, HYDROMAGNETIC
                           LABORATORY EXPERIMENT
                           MODELLING PLANETARY CORES

                           Douglas H. Kelley, Doctor of Philosophy, 2009

Dissertation directed by: Professor Daniel P. Lathrop
                            Department of Physics

This dissertation describes a series of laboratory experiments motivated by planetary cores and the dynamo effect, the mechanism by which the flow of an electrically conductive fluid can give rise to a spontaneous magnetic field. Our experimental apparatus, meant to be a laboratory model of Earth's core, contains liquid sodium between an inner, solid sphere and an outer, spherical shell. The fluid is driven by the differential rotation of these two boundaries, each of which is connected to a motor. Applying an axial, DC magnetic field, we use a collection of Hall probes to measure the magnetic induction that results from interactions between the applied field and the flowing, conductive fluid. We have observed and identified inertial modes, which are bulk oscillations of the fluid restored by the Coriolis force. Over-reflection at a shear layer is one mechanism capable of exciting such modes, and we have developed predictions of both onset boundaries and mode selection from over-reflection theory which are consistent with our observations. Also, motivated by previous experimental devices that used ferromagnetic boundaries to

achieve dynamo action, we have studied the effects of a soft iron (ferromagnetic) inner sphere on our apparatus, again finding inertial waves. We also find that all behaviors are more broadband and generally more nonlinear in the presence of a ferromagnetic boundary. Our results with a soft iron inner sphere have implications for other hydromagnetic experiments with ferromagnetic boundaries, and are appropriate for comparison to numerical simulations as well. From our observations we conclude that inertial modes almost certainly occur in planetary cores and will occur in future rotating experiments. In fact, the predominance of inertial modes in our experiments and in other recent work leads to a new paradigm for rotating turbulence, starkly different from turbulence theories based on assumptions of isotropy and homogeneity, starting instead with inertial modes, which are the linear eigenmodes of any rapidly rotating fluid.

ROTATING, HYDROMAGNETIC LABORATORY EXPERIMENT MODELLING PLANETARY CORES

by

Douglas H. Kelley

Dissertation submitted to the Faculty of the Graduate School of the
University of Maryland, College Park in partial fulfillment
of the requirements for the degree of
Doctor of Philosophy
2009

Advisory Committee:
     Professor Daniel P. Lathrop, Chair/Advisor
     Professor James F. Drake
     Professor Saswata Hier-Majumder
     Professor Edward Ott
     Professor James M. Wallace

Preface

From the time I was six, I was in the habit of sketching things I saw around me, and around the age of fifty, I began to work in earnest, producing numerous designs. It was not until after my seventieth year, however, that I produced anything of significance. At the age of seventy-three, I began to grasp the underlying structure of birds and animals, insects and fish, and the way trees and plants grow. Thus, if I keep up my efforts, I will have even a better understanding when I am eighty, and by ninety will have penetrated to the heart of things. At one hundred, I may reach a level of divine understanding, and if I live a decade beyond that, everything I paint — every dot and line — will be alive. I ask the god of longevity to grant me a life long enough to prove this true.

— Katsushika Hokusai, postscript to *One Hundred Views of Mount Fuji*

Dedication

To my wife and daughters,

who are both the fundamental motivation for all my work

and the daily joy that makes it possible.

Acknowledgments

The laws of Providence that mold our lives are published in no scientific journal and foreseen by no human being. It has been a blessing, a privilege, and often a surprise to walk the particular path I have thus far travelled.

First and foremost I must acknowledge Dan Lathrop and the shifting group of bricolage-cowboy-scientists he has assembled, including Dan "Axl" Zimmerman, Santiago Andrés Triana, Matt Paoletti, Greg Bewley, Matthew Adams, Kristy Gaff, Kaveri Joshi, Chirag Kalelkar, Barbara Brawn-Cinani, and Dan Lanterman. I have never encountered another group so evidently brilliant. In particular, I would not have solved half the elctronics/plumbing/code/theory problems I did without constant back-and-forth with Axl and Santiago (not to mention that they were directly involved in all the early data recording). And though the Graduate School may not acknowledge it, I've had two academic advisors, not one. Our Übertechnician Don Martin was always in the trenches, not just teaching me how to drill titanium or run a lathe, but uniformly offering the best solutions for designing, building, and fixing all manner of things.[1] Dan Lathrop himself, through his endless streams of scientific ideas, insights, guidance, funding, and support, gives us every opportunity to succeed, and we are all thankful.

Deep gratitude goes as well to my wife and daughters, who have endured my long semi-absence by offering constant encouragement. When the workload overwhelmed Neely and me, our family and friends kept the kids, made dinner, took

---

[1]Not least of all, my wife's car.

us out, and in general made our lives possible and (relatively) sane. We owe them bigtime.

John Rodgers has gotten me out of more than a couple of scrapes. Neither while studying engineering nor while working in that field did I ever meet a more capable electrical engineer. Dan O'Halloran has dramatically encouraged my career twice, first by getting it all started in a high school physics class, then by putting me in graduate school when nobody (least of all me) expected. Woody Shew, my predecessor and academic big brother, has always been enthusiastic to give me good advice and career help. J. Pyle is a man among men. Finally, I am grateful to the National Science Foundation for supporting our group financially.

Table of Contents

List of Tables

List of Figures

List of Symbols

a	radius of inner spherical boundary
b	spherical harmonic normalization radius, radius of outer spherical boundary
B_0	applied, external magnetic field
$\mathbf{B}$	magnetic field
c	speed of light
c_A	Alfvén speed
c_g	group velocity
c_p	phase velocity
c_s	speed of sound
E	Ekman number[1]
$\mathcal{E}$	spectral energy or energy per unit volume
$\mathbf{E}$	electric field
$\mathbf{F}$	fluid forcing (general)
g_l^{mc}, g_l^{ms}	Gauss coefficients
$\mathbf{J}$	current density
$\mathbf{k}$	wave vector
$\mathbf{K}_f$	free surface current
l	spherical harmonic degree
L	characteristic length scale
m	spherical harmonic order; equivalently, azimuthal wavenumber
M	normalized shear speed
$\hat{\mathbf{n}}$	unit normal vector
p	pressure
P	reduced pressure (includes centrifugal force)
$\mathcal{P}$	characteristic power scale
$P_l^m(\cos\theta)$	Schmidt semi-normalized Legendre functions
Pm	magnetic Prandtl number[1]
r	radial spherical coordinate; see θ and ϕ
R	coefficient of reflection
$\mathbf{r}$	coordinate vector
Re	Reynolds number[1]
Rm	magnetic Reynolds number[1]
Ro	Rossby number[1]
s	radial cylindrical coordinate; see ϕ and z
$\hat{\mathbf{s}}$	unit vector along s
S	Lundquist number[1]
$\mathbf{S}_l^{mc}, \mathbf{S}_l^{ms}$	poloidal vector spherical harmonics

.

---

[1]For definitions of dimensionless quantities, see table 3.1

$\mathbf{S}_\alpha$, $\mathbf{T}_\alpha$	vector spherical harmonic components of the velocity field
$\mathbf{S}_\beta$, $\mathbf{T}_\beta$	vector spherical harmonic components of the initial magnetic field
$\mathbf{S}_\gamma$, $\mathbf{T}_\gamma$	vector spherical harmonic components of the induced magnetic field
t	time
$\mathbf{T}_l^{mc}$, $\mathbf{T}_l^{ms}$	toroidal vector spherical harmonics
$\mathbf{u}$	velocity field
U	characteristic velocity scale
V_{B_0}	magnetic offset voltage
V_e	electronic offset voltage
V_s	desired signal voltage
V_t	total probe voltage
$Y_l^{mc}(\theta, \phi)$, $Y_l^{ms}(\theta, \phi)$	scalar spherical harmonics
z	axial cylindrical coordinate; see s and ϕ
Z	acoustic impedance
$\hat{\mathbf{z}}$	unit vector along z
α	angle of incidence
ϵ	energy dissipation rate
ζ	radius ratio[1]
η	magnetic diffusivity
θ	colatitude (polar spherical coordinate); see r and ϕ
θ_c	characteristic angle (colatitude) of an inertial mode
μ	magnetic permeability
ν	kinematic viscosity
ρ	density
σ	electrical conductivity
τ	Ekman spin-up time
ϕ	azimuthal angle in spherical or cylindrical coordinates; see r, θ, s, and z
Φ	scalar magnetic potential
χ	rotation rate ratio[1]
ω	wave frequency in the rotating frame
ω_{lab}	wave frequency in the laboratory frame
Ω_i	rotation rate of inner sphere
Ω_o	rotation rate of outer sphere
$\mathbf{\Omega}$	fluid rotation vector

.

---

[1]For definitions of dimensionless quantities, see table 3.1

Chapter 1

Introduction and review

Flowing, electrically conductive fluids have an amazing aptitude for organizing themselves to generate magnetic fields *ex nihilo*. Known as the dynamo effect, the process is so common in astrophysical objects that we are surprised only when we do not find dynamos. Closest to home is the geodynamo, by which the swirling molten iron in the outer core of our own planet produces Earth's magnetic field. Birds, fish, and other animals use it to navigate, as does humankind, whether by holding a compass or by consulting a global positioning system (GPS) satellite which is protected from solar charged particle radiation because of the presence of the field. In fact, the ubiquity of high-energy solar radiation means that an otherwise Earth-like planet without a magnetic field is inhospitable to life as we know it.

Joseph Larmor suggested in 1919 that the Earth's magnetic field might arise from the fluid motions of our planet's outer core [1]. Testing his hypothesis and understanding the associated mechanism has been a key question in geophysics (and soon thereafter, astrophysics) ever since, but even as we approach the hundredth anniversary of Larmor's idea, we cannot claim to understand dynamo action completely. The difficulties begin with turbulence (since the Earth's outer core is vigorously turbulent) and get worse as we include rotation and feedback (since the generated magnetic fields apply forces to the flow itself). Rotating turbulence is

poorly understood even without magnetic fields, which compound our problems.

Nonetheless, great progress has been made in the field. A collection of mathematically rigorous anti-dynamo theorems puts constraints on the class of flows that can generate magnetic fields. A complementary collection of known analytic models shows that dynamo action is possible, even in simple flows. Since the advent of numerical experiments in science, a great many dynamo simulations have been undertaken, becoming more and more like the corresponding geophysical and astrophysical systems as processing power increases. Since the mid-1990s, simulations with Earth-like geometry have shown the onset of dynamo action [2, 3]. Meanwhile experimental realizations of analytic models have yielded dynamo action [4–7], and recently an apparatus with a simpler vessel geometry has shown not only dynamo action [8] but also reversals of the induced dipole [9] which are reminiscent of the reversals in Earth's field over geologic history.

Still, much work remains to improve our understanding. Direct numerical simulation of turbulent flows on a planetary scale requires supercomputers many orders of magnitude more powerful than those currently available. To cope with this problem, existing dynamo simulations must model a fluid whose properties differ from the actual fluids of interest (having abnormally large viscosities). Meanwhile, relatively little experimental data is available because of the scarcity of liquid metal experiments, not to mention experiments that have actually produced dynamo action. In particular, no apparatus shaped like a planet has ever yielded a dynamo.

This dissertation describes our efforts to improve the common understanding of dynamo action and hydromagnetics through a series of laboratory experiments.

Our experimental vessel has a geometry to match the core of the Earth and is filled with sodium, a better electrical conductor than any other liquid at temperatures accessible in the laboratory. Its outer and inner spheres can rotate independently and are driven by motors. Applying an external, DC, axial magnetic field, we use Hall probes to measure the magnetic induction produced by the flowing fluid. This dissertation describes two sets of experiments: one with a copper inner sphere, to match the electrically conductive inner sphere of the Earth, and one with a soft iron inner sphere, motivated by past experimental devices whose dynamo action depended on the use of ferromagnetic materials.

1.1 Motivation

Before pressing onward to describe our own scientific contributions, it seems worthwhile to spend some moments considering the motivation for studying rotating, conductive flows. In short, dynamos are overwhelmingly common in large hydromagnetic systems — that is, large systems of flowing, electrically conductive fluid.[1] Dynamos play fundamental roles in both geophysics and astrophysics.

1.1.1 Geophysics

It was the year 1600 when William Gilbert suggested that a compass points north not because of an attraction to Polaris, but rather because the Earth itself is a magnet [10]. By the time of Edmund Halley, Earth's magnetic field was known to

---

[1]We prefer "hydromagnetic" to the more common but more cumbersome "magnetohydrodynamic" or the more opaque "MHD."

change over time, and in 1692 he proposed that the planet was hollow, accounting for field dynamics by postulating either one or three concentric shells and an inner core, each magnetized and rotating independently [11]. Like the epicycles of Ptolemaic astronomy, Halley's model possessed a pleasing spherical symmetry but would soon be superseded. Though sailors and others interested in navigation had been logging the local inclination (angle to vertical) and declination (angle to geographic north) of Earth's magnetic field for many years, measuring the amplitude of the field proved more difficult. The problem was first solved by Wilhelm Weber and Johann Carl Friedrich Gauss, who first published measurements of the amplitude of Earth's field in 1839 [12]. Gauss illustrated the global structure of the field using only local measurements by fitting to the vector spherical harmonics, having invented the least-square fitting technique himself. The results of this sort of calculation are known as Gauss coefficients (see Chapter 2), and are even now the most common way for geophysicists to represent Earth's magnetic field.

As human knowledge of the structure of Earth's magnetic field developed, so did human knowledge of the structure of Earth's interior. The approximate density and pressure of our planet, varying radially, are shown in Fig. 1.1. Earth is roughly spherical, with its thin crust extending only a few tens of kilometers below the surface. Under the crust lies the thick and gummy mantle, accounting for the majority of the mass of our planet. Below the mantle lies an outer core thought to be composed mostly of liquid iron, mixed with lighter elements at concentrations of perhaps 15%. Though the temperature increases with depth, the pressure increases as well, so that the center of our planet is in fact a solid, inner core, likely com-

posed of crystalline iron. One commonly-cited model puts the radii of the surface, core-mantle boundary (CMB), and inner core at 6371 km, 3480 km, and 1221 km, respectively [13]. Essentially all information about Earth's interior has come from seismology, with careful study of the shear and compression waves that propagate through the planet after earthquakes, underground nuclear tests, and other seismological events. Though the details of the material properties of the various layers remain topics of active scientific debate, the presence and size of those layers are widely agreed upon. Because the mantle is substantially an electrical insulator, and because the inner core is solid, the observed geodynamo must originate in the outer core. This is the region of interest for geodynamo modelers, either numerical or experimental. The energy source for Earth's dynamo is thought to be convection: thermal convection as the planet cools from the outside, as well as material convection as the liquid iron of the outer core crystallizes to become the inner core, leaving lighter impurities to float upward toward the mantle. Radioactive decay of potassium may also contribute to the heat driving thermal convection.

So Earth's magnetic field is produced in its outer core while being carefully monitored at its surface, at least for the last century and a half, by geoscientists. (For an interesting overview, see [14].) Meanwhile others are reconstructing the field in previous epochs (the "archeaomagnetic" and "paloemagnetic" fields) by studying magnetization of lavas, cores from ocean floors, man-made ceramics, and so forth, and combining their results to make models (e.g., [15, 16]). From the growing database of observational data, we know much about the geodynamo. It is dominated by a dipole which is nearly aligned with the axis of rotation and which
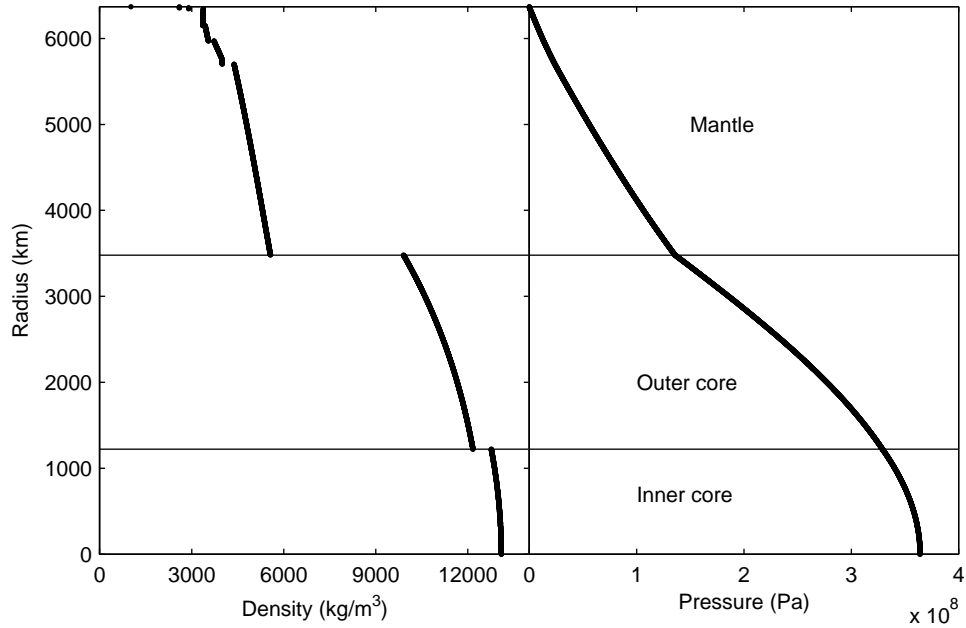
Figure 1.1: One-dimensional density and pressure profiles of the interior of the Earth, according to the Preliminary Reference Earth Model (PREM) [13].

currently has its magnetic south pole near the geographic north pole. That has not always been the case, however — the field has reversed its polarity many times through the course of geologic history [17]. (Incidentally, these reversals preclude any naïve ideas that might attribute Earth's magnetic field to a permanent magnet in the planetary interior. More sophisticated arrangements of permanent magnets, like the one proposed by Halley, are ruled out because the core of the Earth is hotter than the surface of the sun and far exceeds the Curie temperature of all known materials. Hence Larmor's suggestion and the current belief that the field arises via fluid motions.) Since the time of Gauss, the field has weakened by about 10%, suggesting an imminent reversal. The mean time between reversals as measured from the geologic record would also suggest that we are overdue for a reversal.

A key question for geoscientists, then, is how a dynamo reversal will affect our planet. We know that the reversal process is very fast in geologic terms, lasting less than 1000 years or so. Consequently very little observational data can be gleaned from any past reversal. If the geodynamo were to turn off altogether, Earth would lose all magnetic shielding from solar radiation and the atmosphere would begin to ablate as it absorbed charged particles, eventually posing real danger for most of the planet's organisms. Since the number of past reversals is much larger than the number of mass extinctions,[2] this is not usually the case; even as the dipole reverses, it seems that the higher-order components of the field (quadrupole, octupole, etc.) persist. Does the dipole reverse by moving from pole to pole along the surface or by decaying and restarting? Without its dipole component, Earth's field would be dominated by its quadrupole, yielding a very different magnetosphere with a much smaller effective radius. Space weather would affect the surface much more directly, and many of the higher man-made satellites, including all geosynchronous satellites, would find themselves unshielded from solar radiation.

Mankind can and should increase its understanding of the geodynamo through continued observation. Visiting the core to make direct measurements, however, would be prohibitively difficult, more so than visiting the sun or any of the other

---

[2]Geomagnetic reversals may not be altogether irrelevant to mass extinctions, however. At least one study [18] has found correlations in time between mass extinctions, violent volcanic activity, and conclusions of "superchrons," which are times of long delay between reversals. Its authors hypothesize that when the dynamo reverses at the end of a superchron, a very large, hot plume of material convects up from the core to the surface, causing widespread volcanism which alters the global climate and causes extinctions.

planets (though at least one proposal [19] has been presented, perhaps tongue-in-cheek). A more debilitating problem is the one of timescale — it takes millenia for reversals to occur. One way to learn about the geodynamo more quickly is with numerical experiments, and a great many groups have now succeeded in producing numerical dynamos by imposing planet-like boundary conditions (see Fig. 1.1), allowing convection, and letting the simulation run for a few thousand years (early examples include [2, 3]). Researchers often see dipole-dominated fields that reverse, precess, and in other ways give qualitative agreement with the behavior of the Earth's core. Making predictions about Earth from today's numerical dynamo models seems reasonable. But numericists are plagued by the lingering question of resolution. Direct numerical simulation (DNS) of a turbulent system the size of a planet requires orders of magnitude more processing power than the largest supercomputers can currently deliver. Large-scale simulations compensate by simulating a fluid that is orders of magnitude more viscous, more electrically conductive, and/or more thermally conductive than the molten iron that actually comprises Earth's outer core. The effect is to damp small-scale variations in velocity, magnetic field, and temperature, allowing for simulations with larger grid spacing. Given this artificial viscosity, numerical experiments may be getting the right answers for the wrong reasons, and have unknown predictive capability.

If a laboratory experiment with planetary geometry were to show dynamo action, it might prove a better predictor of the behavior of the Earth. Nature does not exclude the small scales — or, to put it differently, some of the relevant dimensionless parameters (see Chapter 2) can be matched more closely with an

experiment than with a simulation. Reversals and other dynamics would proceed on the timescales of the experiment, rotating perhaps once per second instead of once per day, faster than Earth by about five orders of magnitude, allowing for correspondingly quicker observations. Our group and others have pursued the goal of a laboratory dynamo model for a number of years, as will be detailed below.

1.1.2 Astrophysics

Looking beyond our own tiny planet, we find that dynamo action is the norm in astrophysical objects. Nearly all stars are believed to show dynamo action, including of course our sun, whose 11-year magnetic sunspot cycle affects our everyday radio communication and whose magnetic heliopause defines the edges of our solar system. Within that solar system, all planets show clear signs of dynamo action, either past or present, except Venus (see Table 1.1). Jupiter's moon Ganymede shows it as well. Stepping upward through the astronomical scales, we know that evidence from Zeeman splitting, Faraday rotation, and other clever ways of detecting faraway magnetic fields suggests that dynamo action occurs in black holes, galaxies, accretion discs, and galaxy clusters as well [20].

Little is known about these distant dynamos (except perhaps the solar dynamo), but their importance for astrophysics is clear. For example, a paradox arose when researchers [22] realized that fluid viscosity could not account for the observed rate of outflow of angular momentum in astrophysical accretion discs. Accretion discs collapse to form stars and drive emission from compact objects much faster

Object	Dynamo?	Notes
Mercury	Yes	Weak external field (230 to 290 nT R_M^3) is consistent with a large-scale dipole as confirmed by January 2008 MESSENGER observations [21].
Venus	No	Perhaps lacks convection because it lacks an inner core or is heating, not cooling.
Earth	Yes	Earth's dynamo is 3.5 Gy old, perplexing because the energy budget is marginal at best. Rotational precession may provide an alternate energy source.
Mars	No	Strong, small-scale magnetic field frozen into the planetary crust implies a past planetary dynamo which has since ceased.
Jupiter	Yes	Very Earth-like in its shape, the strongest external field of any planet by far.
Saturn	Yes	Surprisingly axisymmetric, perhaps due to super-rotation via zonal winds.
Uranus	Yes	Not dominated by a dipole and tilted far from the axis of rotation.
Neptune	Yes	Not dominated by a dipole and tilted far from the axis of rotation.
Sun	Yes	Intimately related to solar dynamics, solar wind, sunspots, etc.
Moon	No	Has a liquid core; may have had a dynamo for the first 1 Gy of its existence.
Ganymede	Yes	Larger diameter than Mercury. If Ganymede has a dynamo, why not Titan, Europa, Callisto?

Table 1.1: Dynamos in our solar system

than viscous dissipation would allow. The problem was solved some years later with the re-discovery of the magnetorotational insability (MRI) [23], which had been earlier demonstrated by fluid researchers [24, 25] and might be more aptly titled the Velikhov-Chandrasekhar instability. In brief, if a magnetic field of appropriate strength is present, a rotating, conductive fluid can expel angular momentum much more quickly, allowing for astrophysical accretion to proceed at the observed rates. (It is worth mentioning that the first experimental observation of the Velikhov-Chandrasekhar instability has been reported by our own group [26].) Whereas the Velikhov-Chandrasekhar instability requires finite-sized magnetic fields, dynamo action by definition amplifies arbitrarily small seed fields to produce appreciable ones. So then in nature, the Velikhov-Chandrasekhar instability is driven by dynamo action.

To be clear, our apparatus is not a particularly good model for dynamos in large astrophysical objects like stars and accretion discs. Such objects are composed of plasmas which have material properties quite different than the liquid sodium used in our apparatus. Moreover such objects typically produce small-scale dynamos, in which the features of the magnetic field are typically much smaller than the extent of the fluid. Our apparatus was designed to model Earth, with a solid inner core and with instrumentation optimized for detecting large-scale magnetic induction. However, from these experiments we hope to glean insights about generic features of rotating, turbulent, hydromagnetic systems that might prove broadly useful in fluid dynamics, geophysics, and astrophysics.

1.2   Past work

1.2.1   Theory

Dynamo theory has received vigorous attention since its inception with Larmor. An early and influential theoretical advance was Cowling's anti-dynamo theorem [27], a mathematical proof that an axisymmetric magnetic field vanishing at infinity cannot be maintained by dynamo action in an axisymmetric flow. A subsequent generalization proved that no two-dimensional magnetic field of any sort that vanishes at infinity can be maintained by dynamo action [28]. It has also been proved that no dynamo can be maintained by a planar flow (whether two-dimensional or not) [29] and that a purely toroidal flow (see Chapter 2) cannot maintain a dynamo. After some concern that fluid dynamos might not be possible at all, researchers were able to devise a collection of working, kinematic dynamo models. These are simple, prescribed flow patterns that meet the usual definition of a dynamo: seeded by an arbitrarily small magnetic field, the flows cause exponential magnetic amplification. A few such models include the Ponomarenko dynamo [30], the G. O. Roberts dynamo [31], the Kumar-Roberts dynamo [32], and three dynamos found numerically by Dudley and James [33].

Being kinematic, all of the above models are prescribed fluid flows which are not affected by the presence or absence of a magnetic field — a somewhat artificial situation. A much harder problem is to find a *dynamical* system exhibiting dynamo action, that is, one whose fluid is governed by the Navier-Stokes (momentum) equation (see Chapter 2) and whose behavior is affected by magnetic fields

via the Lorentz force. Given that the Navier-Stokes equation is a three-dimensional nonlinear partial differential equation, few analytic solutions of any kind are known, and none of those are dynamos. In the last two decades, however, computers have become capable of fluid simulations sufficiently large to produce self-consistent dynamos. Perhaps the best known numerical dynamos are those driven by convection and devised with boundary conditions similar to those of a planetary core (for example, [2, 3]). A zoo of other numerical dynamos have come to be studied as well, some focusing on the solar dynamo [34], others on other astronomical objects or other geometries altogether. The ability of numerical simulations to match the dimensionless parameters (see Chapter 2) of real-world systems improves steadily with technology, but some parameters still differ by many orders of magnitude.

1.2.2   Experiments

Laboratory experiments have demonstrated the viability of the dynamo effect as well. First came the pioneering work of Lowes and Wilkinson [4, 5], who demonstrated exponential growth of magnetic fields in two different systems, each composed mostly of rotating iron alloy cylinders, with with a thin but important layer of liquid mercury between, as conceived by Herzenberg [35]. The race to produce a homogeneous laboratory dynamo ended in 2000 in a near tie between a group in Riga, Latvia [6], and a group in Karlsruhe, Germany [7]. The Riga group constructed an apparatus meant to approximate the Ponamarenko model, while the Karlsruhe group constructed an apparatus meant to approximate the G. O.

Roberts model. Both did produce exponential amplification of magnetic fields, followed by saturation due to feedback from the Lorentz force. Neither was shaped like any astrophysical or planetary object, however — the apparatuses pumped liquid sodium through closed loops of spirals with concentric return paths. In 2006 came another experimental dynamo, called Von Kármán Sodium 2 (VKS2) and constructed in Cadarache, France [8]. As its name would imply, VKS2 is built with the geometry suggested by Von Kármán, a cylinder of liquid sodium driven by two counter-rotating discs, one at each end.[3] When its discs rotate at equal and opposite speed, VKS2 produces turbulent, statistically steady, dipole-dominated dynamo action giving magnetic fields on the order of 40 G.[4] When its discs counter-rotate at unequal speeds, a net rotation is imposed upon the flow and VKS2 produces a dynamo with a dynamo that reverses chaotically similar to that of the Earth [9]. Its reversals and its relatively unconstrained geometry make VKS2 a very interesting apparatus, more similar to astrophysical and planetary objects than previous dynamos. In order to achieve dynamo action, VKS2 was highly optimized with the use of numerical simulations and laboratory results. The final step necessary was to replace the stainless steel propulsion discs (impellers, actually) with identical ones made of ferromagnetic soft iron. Numerical simulations by the VKS2 team had suggested that eliminating the regions of stagnant sodium behind the impellers would encourage dynamo action. For engineering reasons it was not possible to remove the fluid directly, so researchers reasoned that the ferromagnetic impellers would

---

[3]This geometry is affectionately known as the "French washing machine."

[4]1 G = 10^{-4} T is a convenient unit of magnetic flux for the purposes of this dissertation.

serve as a sort of magnetic shielding. But since ferromagnetic materials concentrate magnetic fields and change the magnetic boundary condition (see Chapter 5), the impellers may be playing a much more direct role in the generation of large-scale fields. Similarly, the laboratory dynamos of Lowes and Wilkinson also made use of ferromagnetic materials (first "Perminvar" [4], then annealed mild steel [5]) which raises the same set of questions. An interest in better understanding the effects of ferromagnetic boundaries motivated our experiments with a soft iron sphere (see Chapter 5).

As VKS2 demonstrates, whether or not dynamo action will arise in an unconstrained flow is difficult to predict (this is a matter of accurately calculating the critical magnetic Reynolds number for the apparatus; see Chapter 2). Accordingly a number of groups have attempted laboratory dynamos without achieving them, though the results are often quite valuable to science and to an improved understanding of hydromagnetics. One such experiment is our own, the 60 cm spherical Couette cell detailed in this dissertation. It has not shown dynamo action though by many measures its parameters would suggest it might. Past efforts in our own group have included a 30 cm spherical cell with propellers [36] or with an inner sphere. (Studies with the inner sphere led not to dynamo action but to the Velikhov-Chandrasekhar instability [26]; see above). The 60 cm apparatus was originally configured as a rotating convection experiment during the dissertation work of W. L. Shew [37, 38] before being configured for mechanical forcing as part of the present work. Sibling to the current 60 cm apparatus is a 3 m spherical Couette apparatus, identical in geometry and also capable of dual rotation, which is currently filled with water

and in use for hydrodynamic (not hydromagnetic) experiments. The 3 m apparatus is by far the largest of its kind in the world (our 60 cm apparatus is the second-largest) and therefore has the best possibility to yield dynamo action in a planetary geometry. Its results will be published soon in the scientific literature and in the dissertations of D. S. Zimmerman and S. A. Triana.

Other groups have attempted laboratory dynamos as well, of course. The Derviche Tourneur Sodium (DTS) apparatus in Grenoble, France, is a liquid sodium experiment with a dually-rotating, spherical Couette boundary [39] and is thus more similar to our experiment than any other. DTS differs in that it is slightly smaller (40 cm in diameter) and in that its inner sphere is a strong, permanent magnet. Observations of DTS document axisymmetric flows [40] and wave modes [41] similar to those we observe (see Chapter 4). The Madison Dynamo Experiment (MDX) in Madison, Wisconsin, is a 1 m diameter sphere containing liquid sodium. It does not rotate but instead drives the fluid with a pair of counter rotating propellers, similar to VKS2 and to the 30 cm experiment previously constructed in our group. Applying external magnetic fields, the Madison group has observed large-scale magnetic fields [42] which have intermittent temporal dynamics of the sort common in turbulent flows [43]. A great many more hydromagnetic laboratory experiments have been undertaken over the years, including many using gallium instead of sodium as a test fluid (e.g., [44, 45]).

1.3 Outline of this dissertation and contribution of the author

Below, a more detailed and quantitative description of the physics governing fluid dynamos and our experiment is presented in Chapter 2, and the apparatus is described in Chapter 3. Chapter 4 presents results gathered with a copper inner sphere, focusing on the presence, pumping, and selection of inertial modes in the flow. Chapter 5 presents results gathered with a soft iron inner sphere, again identifying inertial modes and also making some preliminary observations of parameter dependence. In Chapter 6, we present a broad description of the nature of rotating turbulence suggested by our experimental results. We conclude with a summary, some discussion about the geophysical implications of our findings, and a collection of ideas for future work in Chapter 7.

The author took the lead in experiments detailed in this dissertation, both in choosing what parameters to explore and in repairing and maintaining the apparatus. The author re-designed the inner shaft and re-designed and machined the top inner bearing seat, spacers, and other mechanical parts. The inner shaft and sphere were originally designed by D. L. Ellingston and D. H. Martin, while the outer vessel was designed by W. L. Shew and D. P. Lathrop. The author designed and led construction (with B. E. Brawn, J. Maher, and M. Martin) of the magnets, their support frame, and the cooling manifolds and plumbing used to distribute kerosene. The author designed and constructed the opto-isolated D/A, the digital counter, the surge suppressors, and other electronics described in Chapter 3. He designed and led construction of one motor mount; the other was designed by D. L.

Ellingston. The author designed and constructed the heater array and the equatorial Hall probe array. The Gauss array we use essentially follows the design of D. R. Sisan, but was constructed by the author. The author modified the LabView codes used for control and acquisition, which were originally written by S. A. Triana and N. Mujica. The author substantially modified the C code used for calculating Gauss coefficients, which was originally written by D. R. Sisan and D. P. Lathrop. The author has taken a lead role in the calculations, analysis, and conclusions presented in subsequent chapters.

In particular, we have discovered and identified inertial modes in spherical Couette flow, also constructing a theory to explain their amplification and mode selection, which is consistent with our experimental results. We have experimentally studied the effects of ferromagnetic boundaries on a hydromagnetic flow, finding increased nonlinearity and magnetic induction with a broader bandwidth. Drawing on our experimental observations, we have gone on to offer some broad conclusions and predictions about the nature of rotating turbulence in nature and in experiments.

Chapter 2

Theoretical background

In this chapter we build up some theoretical background that will become useful in understanding the motivations for and results of our work. First comes a discussion of rotating fluids. The equations that govern their motion are easy to write but remarkably difficult to solve, so we spend some time with two special cases that are analytically tractable: the Taylor-Proudman theorem and inertial waves. Next comes a parallel discussion of conductive fluids, discussing Alfvén waves as a special case. Then we dedicate a few pages to the mathematical theory of spherical harmonics, in both scalar and vector form, and their usefulness as a basis set. When we express both velocity fields and magnetic fields in terms of the vector spherical harmonics, the magnetic induction is governed by a collection of selection rules, which we repeat from [46]. In the closing section, we non-dimensionalize the equations of motion given in earlier sections to cast our work in terms of dimensionless parameters for easy comparison to other studies.

2.1 Rotating fluids

2.1.1 Equations of motion

As has been known for more than 150 years, the momentum of incompressible, Newtonian, viscous fluids is governed by the Navier-Stokes equation,

$$\frac{\partial \mathbf{u}}{\partial t} + (\mathbf{u} \cdot \nabla)\,\mathbf{u} = -\frac{1}{\rho}\nabla p + \nu \nabla^2 \mathbf{u} + \mathbf{F}, \tag{2.1}$$

where $\mathbf{u}$ is the velocity of the fluid, t is time, ρ is the density of the fluid, p is the pressure, ν is the kinematic viscosity of the fluid, and $\mathbf{F}$ is the forcing. The Navier-Stokes equation cannot be derived from more fundamental principles but has been validated by a vast array of empirical observations. Landau [47] shows that it can be constructed from a small number of reasonable assumptions. Essentially, it is a statement of Newton's second law for an infinitesimal parcel of fluid: the net acceleration must equal the sum of the forces (per unit mass) on the parcel. The first term on the left-hand side quantifies the acceleration of our test parcel as it changes over time. The second term on the left-hand side is called the "convective derivative," and quantifies accelerations of the parcel due to its motion in space. The convective derivative does not appear when the equation is written in the frame of reference of our parcel (known as the Lagrangian frame), but since the parcel accelerates, that frame is non-inertial. Hence when we transform to the frame of the fluid container (known as the Eulerian frame, used throughout this dissertation), this additional term arises. Incidentally, it is also the term where nonlinearity is always present. Together, the two terms on the left-hand side give the net acceleration of

the fluid parcel. The first term on the right-hand side quantifies the acceleration applied to the parcel by pressure. The second term on the right-hand side quantifies the acceleration applied by viscous forces. It accounts for diffusion of fluid parcels and tends to smooth flows. Finally, $\mathbf{F}$ is included as a general term, to encompass whatever specific forcing is present in the fluid system of interest.

Our work focuses on rotating fluids. If we consider the flow of a fluid in a frame with rotation vector $\boldsymbol{\Omega}$, its flow is governed by

$$\frac{\partial \mathbf{u}}{\partial t} + (\mathbf{u} \cdot \nabla) \mathbf{u} = -\frac{1}{\rho} \nabla P + \nu \nabla^2 \mathbf{u} - 2 (\boldsymbol{\Omega} \times \mathbf{u}). \tag{2.2}$$

Since a rotating frame of reference is non-inertial, new terms have appeared in the equation. The centrifugal acceleration is combined with p to give the reduced pressure, $P = p - \boldsymbol{\Omega} \times (\boldsymbol{\Omega} \times \mathbf{r})$, and the Coriolis acceleration is included as the final term. To complete the description of fluid motions, we assert that the fluid is incompressible,

$$\nabla \cdot \mathbf{u} = 0, \tag{2.3}$$

a simplification which holds as long as $u = |\mathbf{u}| \ll c_s$, where c_s is the speed of sound in the fluid — true for all cases described in this dissertation. With Eqn. 2.2, Eqn. 2.3, and the proper boundary conditions, a hydrodynamic problem is properly posed. Common boundary conditions are either the no-slip case, in which $\mathbf{u}|_{boundary} = 0$, or the free-slip (also called "no penetration" or "zero shear") case, in which $(\mathbf{u} \cdot \hat{\mathbf{n}})|_{boundary} = 0$. Strictly speaking, any physical system with a rigid boundary is governed by no-slip boundary conditions. Analysis is often far simpler with free-slip boundary conditions, however, and many physical systems approximate free-slip

behavior closely in all regions except a thin boundary layer at the wall [47], known in rotating systems as the Ekman layer.

2.1.2 Limiting cases

Since Eqn. 2.2 is a three-dimensional, nonlinear, partial differential equation, few analytic solutions of any kind are known. Behaviors of rotating fluids are tractable in limiting cases. For large rotation rates, for instance, the viscous term can often be neglected. Varying the rotation rate does not affect the relative strengths of the remaining terms,[1] but if we assert that fluid motions are small enough to ignore the $(\mathbf{u} \cdot \nabla)\mathbf{u}$ (nonlinear) term and that their time variation is slow enough to ignore the time derivative term, Eqn. 2.2 reduces to

$$2\left(\boldsymbol{\Omega} \times \mathbf{u}\right) = -\frac{1}{\rho}\nabla P. \tag{2.4}$$

Taking a curl of both sides eliminates the pressure thanks to vector identity A.1. Using vector identity A.2, using Eqn. 2.3, and choosing our coordinates such that the axis of rotation aligns with the z axis ($\boldsymbol{\Omega} = \Omega\hat{\mathbf{z}}$), we find

$$\frac{\partial\mathbf{u}}{\partial z} = 0. \tag{2.5}$$

Hence we conclude that steady, small-amplitude flows at large rotation rate are strictly two-dimensional, a result known as the Taylor-Proudman theorem.

Choosing a slightly less restrictive special case, we again consider fast rotation and small fluid motions but allow the flow to have time dependence. The viscous

---

[1]For a mathematical demonstration of this fact, see Eqn. 2.40

22

and nonlinear terms disappear as before, but the time derivative remains. Again taking a curl of both sides and invoking the same vector identity A.2, we find

$$\frac{\partial}{\partial t} \nabla \times \mathbf{u} = 2 \left(\mathbf{\Omega} \cdot \nabla \right) \mathbf{u}, \tag{2.6}$$

which admits wave solutions of the form $\mathbf{u} = \tilde{\mathbf{u}} \exp i(\mathbf{k} \cdot \mathbf{r} + \omega t)$, provided that the waves are transverse and that they obey the peculiar dispersion relation

$$\omega = 2\hat{\mathbf{k}} \cdot \mathbf{\Omega}. \tag{2.7}$$

In these expressions $\tilde{\mathbf{u}}$ is a vector constant, $\hat{\mathbf{k}} = \mathbf{k}/|\mathbf{k}|$ is the unit wave vector, $\mathbf{r}$ is the position vector, and ω is the wave frequency in the rotating frame.

Waves of this type are known as inertial waves and have been studied at least since the time of Kelvin [48]. They are bulk waves that can exist in any rotating fluid and are restored by the Coriolis force. Their dispersion relation implies that no inertial waves have a frequency greater than twice the rotation rate of the container, whatever the geometry. Moreover, when inertial waves reflect from a boundary, they reflect in such a way as to conserve the angle with respect to the rotation axis, not the angle with respect to the boundary. Their phase velocity and group velocity are

$$\mathbf{c}_p = \pm \frac{2\hat{\mathbf{k}} \cdot \hat{\mathbf{\Omega}}}{|\mathbf{k}|} \hat{\mathbf{k}}, \tag{2.8}$$

$$\mathbf{c}_g = \pm \frac{2\hat{\mathbf{k}} \times \left(\hat{\mathbf{\Omega}} \times \hat{\mathbf{k}} \right)}{|\mathbf{k}|}, \tag{2.9}$$

respectively, where $\hat{\mathbf{\Omega}} = \mathbf{\Omega}/|\mathbf{\Omega}|$ is the unit rotation vector. Thus the phase velocity of an inertial wave is orthogonal to its group velocity [49]. Rossby waves [50] (also known as planetary waves), a common topic of study in meteorology, are derived

with different mathematics[2] but are in fact a subset of the inertial waves. Likewise the Proudman-Taylor theorem represents the special case of inertial waves with frequency zero. Mathematically, the inertial waves are the linear eigenmodes of a rotating, inviscid ($\nu = 0$) fluid — all solutions of Eqn. 2.6 are inertial waves or their superpositions. Thus any motions for which viscosity and nonlinear interactions can be neglected must be composed of inertial waves. For this reason, though the inertial waves are not a complete set in the mathematical sense, they are often a reasonable basis. For a thorough theoretical treatment of inertial waves (as well as a wide variety viscous and nonlinear phenomena that arise in rotating fluids), see the monograph by Greenspan [52]. Our group has identified inertial waves in a variety of experiments, including the one detailed in this dissertation. In Chapter 4 we describe our discovery of inertial waves in a spherical shear flow [53]; previous work has focused on square and cylindrical channels [54, 55]. We refer to these findings again in Chapter 6.

In an infinite body of rotating fluid, inertial waves exist at all frequencies as plane waves in space. In a spherical container with free-slip boundaries, the inertial waves (or better, "inertial modes") form a countably infinite set, discrete and dense in frequency. The inertial modes are known analytically [56–58], and each mode can be identified by three quantities. We typically identify modes by their degree, or-

---

[2]Rossby waves are commonly derived by approximating the atmosphere as a thin fluid layer and using β-plane coordinates, which are beyond the scope of this dissertation. For an overview, see [51].

der, and normalized frequency, which we write as $(l, m, \omega/\Omega)$, respectively.[3] Here the degree m and order l have the same meaning as they do in spherical harmonic notation (see below). Though the inertial modes in a sphere are *not* spherical harmonics, they have the common boundary requirements. Namely, both are waveforms, and therefore must be 2π periodic around the equator (in the azimuthal coordinate) and around a meridian (in the polar coordinate). Thus they can be characterized with an order m, which describes the azimuthal symmetry, and a degree l, which (along with m) describes the polar symmetry.

A similar classification was devised by Greenspan [52], who used spherical harmonic degree, an ordinal that corresponds one-to-one to frequency, and spherical harmonic order, which he writes as (n, m, k), respectively. A third classification scheme is employed by Zhang [58]; we note for reference that the degree l and order m relate to his ordinal N according to $N = \text{floor}((l - m)/2)$. A few full-sphere, free-slip inertial wave modes are illustrated in Fig. 2.1.

The presence of a rigid boundary, such as Earth's mantle and inner core or the walls of an experimental apparatus, imposes non-slip boundary conditions, not the free-slip conditions used in solving for the inertial modes. This discrepancy might seem to make the known free-slip modes irrelevant. As mentioned above, however, empirical studies document that fluids contained by non-slip boundaries often display something very much like free-slip behavior through their bulk, differing appreciably from the free-slip solution only in a narrow boundary layer near the wall [47]. Hence the free-slip inertial modes remain relevant, and we have only to

---

[3]Note $\Omega = |\boldsymbol{\Omega}|$.

(2,1,1) (4,1,0.612) (6,1,0.44) (3,2,0.667)

(5,2,0.467) (4,3,0.5) (6,3,0.378) (5,4,0.4)
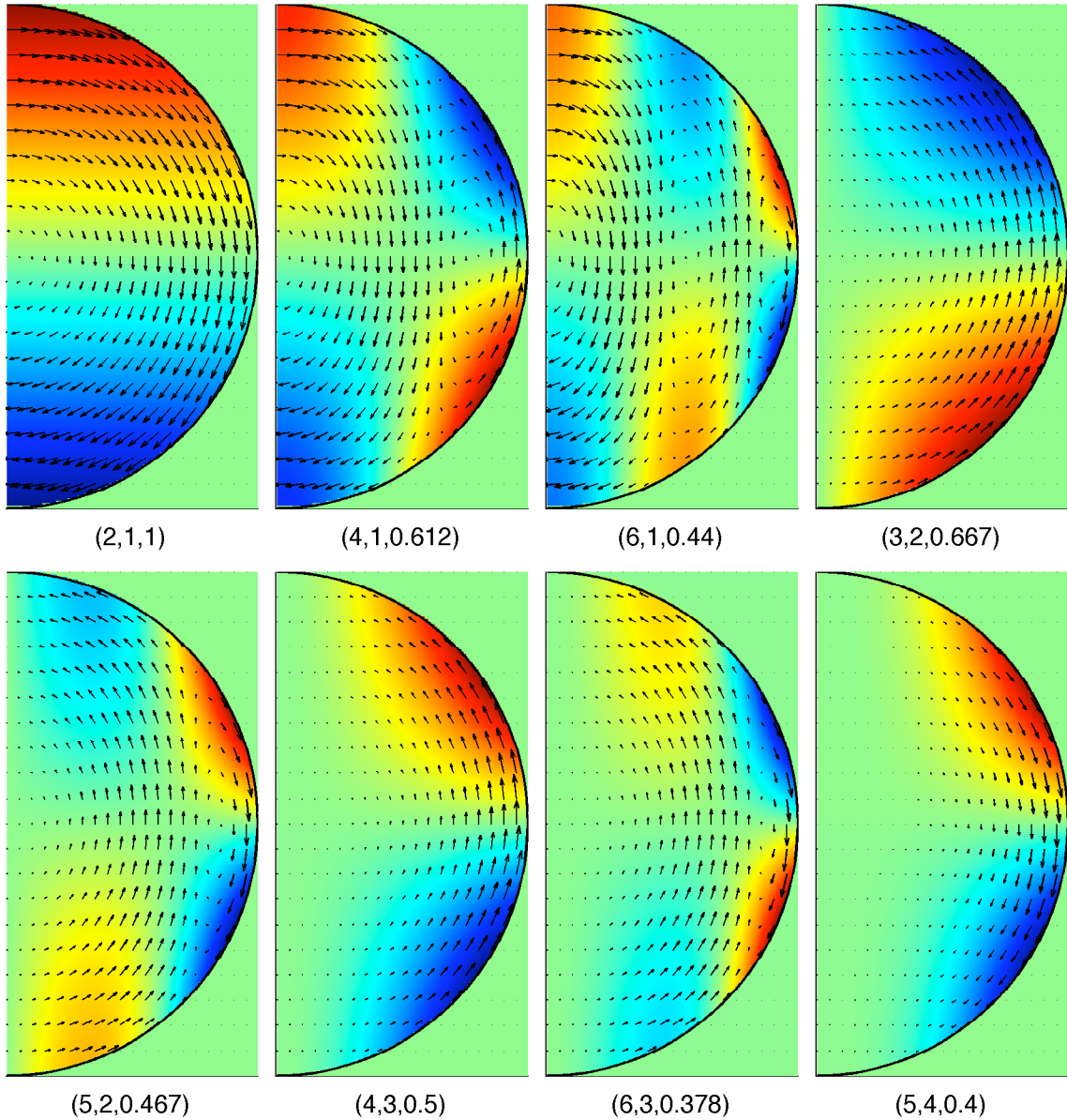
Figure 2.1: Examples of inertial modes in a full sphere. Each image shows a meridional cross-section of the sphere, with the axis of rotation at left. The polar and radial components of the velocity are indicated with arrows, while the azimuthal component is indicated with color (red indicates flow out of the page; blue, into the page). The amplitudes are arbitrary. The corresponding degree l, order m, and normalized frequency ω/Ω are listed below each image. A version of this figure better adapted for grayscale printing is included as Fig. D.1.

discern the form of the boundary layers that arise when they are present.

In analytical studies of those layers, past researchers were surprised to find that at a particular colatitude (polar angle) θ_c, each boundary layer detaches (or "erupts," to use the verb common in the literature) from the wall and forms a conical surface in the bulk of the fluid which makes angle $\pi - \theta_c$ with the axis of rotation [49, 52, 59]. This particular colatitude θ_c varies from mode to mode and is known as the characteristic angle of the mode. Its value is given by

$$\cos\theta_c = \frac{\omega}{2\Omega_o}. \tag{2.10}$$

Characteristic angles will become important when we consider mode selection in Chapter 4.

2.2   Conductive fluids

Many fluids are electrically conductive, and though most day-to-day fluids (e.g., water) do not conduct well enough to affect their dynamics, hydromagnetic behaviors are the norm in geophysics and astrophysics. Planetary cores are typically composed of liquid metals, while stars, accretion discs, and larger astrophysical objects are composed of plasma. Liquid metals and plasmas have vastly different parameters, but both can often be modelled by the same physics: the induction equation.

2.2.1 Equations of motion

The electromagnetic behaviors of conductive fluid, like all electromagnetic phenomena, are governed by Maxwell's equations, three of which will be required for our purposes:

$$\nabla \times \mathbf{E} = -\frac{\partial \mathbf{B}}{\partial t}, \tag{2.11}$$

$$\nabla \cdot \mathbf{B} = 0, \tag{2.12}$$

$$\nabla \times \mathbf{B} = \mu_0 \mathbf{J}. \tag{2.13}$$

Here $\mathbf{E}$ is the electric field, $\mathbf{B}$ is the magnetic field, $\mathbf{J}$ is the current density, and μ_0 is the permeability of free space. Note that the displacement current is absent — we can neglect it as long as the fluid velocity remains small with respect to the speed of light ($u = |\mathbf{u}| \ll c$), which holds true in known planetary cores but breaks down in some astrophysical plasmas, in which more general theories are required instead; they are outside the scope of this dissertation. The systems of our interest flow much slower than c and are also well-modelled by Ohm's law,

$$\mathbf{J} = \sigma(\mathbf{E} + \mathbf{u} \times \mathbf{B}), \tag{2.14}$$

where σ is the conductivity of the material. We obtain another expression for $\mathbf{J}$ by rearranging Eqn. 2.13, then use the result in the left-hand side of Eqn. 2.14. Taking a curl of both sides of the result, then making use of Eqns. 2.11 and 2.12 as well as vector identity A.3, we eventually find

$$\frac{\partial \mathbf{B}}{\partial t} = \eta \nabla^2 \mathbf{B} + \nabla \times (\mathbf{u} \times \mathbf{B}). \tag{2.15}$$

Here we introduce the magnetic diffusivity, $\eta = (\mu_0 \sigma)^{-1}$, a material property which plays a role in the dynamics of $\mathbf{B}$ entirely analogous to the role played by the kinematic viscosity ν in the dynamics of $\mathbf{u}$. Expression 2.15 is known as the induction equation, and governs the production and decay of magnetic fields by a moving, conductive fluid. In fact, using vector identity A.2, we can write

$$\frac{\partial \mathbf{B}}{\partial t} + (\mathbf{u} \cdot \nabla) \, \mathbf{B} = \eta \nabla^2 \mathbf{B} + (\mathbf{B} \cdot \nabla) \, \mathbf{u}, \qquad (2.16)$$

a form in which the analogy is even more apparent (compare to Eqn. 2.2). Magnetic fields are smoothed and attenuated by the diffusion term (first of the right-hand side) but can be generated or amplified over time by the second term on each side of the expression. Here, perhaps, Larmor's suggestion of dynamo action [1] becomes a bit more concrete.

Given Eqns. 2.2 and 2.15, we can (in some vague way) understand hydrodynamic motions and also understand their production of magnetic fields. We have not yet instituted a mechanism, however, to allow hydromagnetics, because Eqn. 2.2 does not account for the induced magnetic field feeding back to affect the flow. That feedback occurs via the Lorentz force — a conductive fluid in a magnetic field experiences an acceleration $a_L = \mathbf{J} \times \mathbf{B} / \rho$. Using Eqn. 2.13 to re-write $\mathbf{J}$ and inserting the result into Eqn. 2.2, we have the hydromagnetic Navier-Stokes equation for rotating fluids,

$$\frac{\partial \mathbf{u}}{\partial t} + (\mathbf{u} \cdot \nabla) \, \mathbf{u} = -\frac{1}{\rho} \nabla P + \nu \nabla^2 \mathbf{u} + \frac{1}{\rho \mu_0} \left(\nabla \times \mathbf{B} \right) \times \mathbf{B} - 2 \left(\mathbf{\Omega} \times \mathbf{u} \right). \qquad (2.17)$$

We will make frequent use of this expression below.

2.2.2 Alfvén waves

Above we showed how rotating fluid systems can support waves restored by the Coriolis force, which are known as inertial waves. Wielding the hydromagnetic Navier-Stokes equation, we find many more sorts of waves than were possible in pure hydrodynamics, the simplest of which were first explicated in 1942 by H. Alfvén [60]. Being interested in small-amplitude, inviscid ($\nu = 0$) perturbations in a non-rotating ($\Omega = 0$), perfectly conductive ($\eta = 0$) fluid, we drop the convective derivative term, the viscous term, and the Coriolis term from Eqn. 2.17. Using vector identity A.4 and grouping gradient terms, we find

$$\frac{\partial \mathbf{u}}{\partial t} = -\nabla \left(\frac{1}{\rho} P + \frac{\mathbf{B}^2}{2\rho\mu_0} \right) + \frac{1}{\rho\mu_o} \left(\mathbf{B} \cdot \nabla \right) \mathbf{B}. \tag{2.18}$$

Taking a curl eliminates the first term on the right-hand side according to vector identity A.1, giving

$$\frac{\partial}{\partial t} \nabla \times \mathbf{u} = \nabla \times \left(\left(\mathbf{B} \cdot \nabla \right) \mathbf{B} \right). \tag{2.19}$$

Next we quantify our assertion about the velocity perturbations being small, and make a similar assertion about the magnetic field, that is,

$$\mathbf{B} = \mathbf{B}_0 + \mathbf{B}_1, \quad \mathbf{u} = \mathbf{u}_1, \tag{2.20}$$

where $|\mathbf{B}_1| \ll |\mathbf{B}_0|$ and $|\mathbf{u}_1|$ is also small. Further, we consider the case of a constant and uniform background field $\mathbf{B}_0$. Inserting Eqn. 2.20 into Eqn. 2.19 and dropping all terms that are second-order small (any terms having more than one factor with subscript 1), we find

$$\frac{\partial}{\partial t} \nabla \times \mathbf{u_1} = \nabla \times \left(\left(\mathbf{B_0} \cdot \nabla \right) \mathbf{B_1} \right). \tag{2.21}$$

Now we seek wave motion along the direction of $\mathbf{B}_0$, writing the flow field and magnetic field as $\mathbf{u}_1 = \tilde{\mathbf{u}}_1 \exp i\mathbf{k} \cdot \mathbf{r} - \omega t$ and $\mathbf{B}_1 = \tilde{\mathbf{B}}_1 \exp i\mathbf{k} \cdot \mathbf{r} - \omega t$, respectively, with $\mathbf{k} \parallel \mathbf{B}_0$. Inserting these expressions into Eqn. 2.21, we find

$$\omega \mathbf{k} \times \mathbf{u}_1 = -\frac{B_0 k}{\rho \mu_o} \mathbf{k} \times \mathbf{B}_1. \tag{2.22}$$

Turning to the induction equation (Eqn. 2.15), we drop its magnetic diffusion term since $\eta = 0$ in the case of our interest, and use our assertion that both velocity and magnetic perturbations are small. Hence

$$\frac{\partial \mathbf{B}_1}{\partial t} = \nabla \times (\mathbf{u}_1 \times \mathbf{B}_0). \tag{2.23}$$

Taking the curl of both sides and again seeking wave motion, we find

$$\mathbf{k} \times \mathbf{B}_1 = \frac{B_0 k}{\omega} \mathbf{k} \times \mathbf{u}_1. \tag{2.24}$$

Combining Eqns. 2.22 and 2.24 yields the dispersion relation for Alfvén waves:

$$\omega = c_A k, \tag{2.25}$$

where

$$c_A = \frac{|\mathbf{B}_0|}{\sqrt{\rho \mu_0}} \tag{2.26}$$

is their speed, known as the Alfvén velocity. Alfvén waves are transverse, non-dispersive perturbations in the magnetic field that travel along the lines of $\mathbf{B}_0$. They exist as well, in generalized form, in fluids that are imperfect conductors ($\eta > 0$) with finite viscosity ($\nu > 0$), and at arbitrary speeds. The generalized form allows longitudinal wave modes and introduces attenuation [61].

31

Another class of waves occurs when rotation and conductivity are both present. They are the magnetocoriolis (MC) waves, beyond the scope of this dissertation but explicated thoroughly in [62].

2.3   The spherical harmonic basis

Since mathematics is the language of physics, time spent focusing upon the vocabulary of that language is time well-spent. Here we consider the spherical harmonic basis before using it extensively in making predictions, representing our data, and drawing conclusions.

2.3.1   Scalar spherical harmonics

In regions where no appreciable currents are present (such as outside our experiment or on the surface of the Earth), $\mathbf{J} = 0$ and Eqn. 2.13 becomes $\nabla \times \mathbf{B} = 0$. Since any curl-free vector can be represented as the gradient of a scalar field, we write

$$\mathbf{B} = -\nabla \Phi, \tag{2.27}$$

where Φ is the magnetic scalar potential. Taking a curl of both sides and using Eqn. 2.12, we come to Laplace's equation,

$$\nabla^2 \Phi = 0. \tag{2.28}$$

In spherical coordinates (r, θ, ϕ), it is expressed as

$$\frac{1}{r}\frac{\partial^2}{\partial r^2} r\Phi + \frac{1}{r^2 \sin\theta}\frac{\partial}{\partial \theta}\left(\sin\theta \frac{\partial \Phi}{\partial \theta}\right) + \frac{1}{r^2 \sin^2\theta}\frac{\partial^2 \Phi}{\partial \phi^2} = 0, \tag{2.29}$$

the solution of which is well-known and commonly used in quantum mechanics. Separation of variables leads to the specific solution

$$\Phi(\mathbf{r}) = \left(A_l r^l + B_l r^{-(l+1)}\right)\left(a_m \cos m\phi + b_m \sin m\phi\right) P_l^m(\cos\theta), \qquad (2.30)$$

where A_l, B_l, a_m and b_m are coefficients, $P_l^m(\cos\theta)$ are the generalized, Schmidt semi-normalized Legendre functions (see Table 2.1), and l and m are integers satisfying $l \geq 0$ and $-l \leq m \leq l$. The functions $Y_l^{mc} = \cos m\phi\, P_l^m(\cos\theta)$ and $Y_l^{ms} = \sin m\phi\, P_l^m(\cos\theta)$ are collectively known as the spherical harmonics of degree l and order m. To describe Φ (and therefore $\mathbf{B}$) in a region that includes $r = \infty$, with the assertion that the field does not diverge, we must set $A_l = 0$. Keeping only the $r^{-(l+1)}$ term, of course, we cannot describe fields at the origin. But neither our experiment nor the Earth's core allows for a probe at its center! In fact, our choice means that we can describe only the contributions from internal sources (nearer the origin than our measurement locations), which specifically excludes magnetic fields produced in the ionosphere (for the case of the Earth) or in external magnets (in the case of our experiment). This point will arise again in Chapter 3.

The general solution for all external fields is a superposition of specific solutions,

$$\Phi(\mathbf{r}) = b \sum_{l=1}^{\infty} \sum_{m=-l}^{l} \left(g_l^{mc} \cos m\phi + g_l^{ms} \sin m\phi\right) \left(\frac{r}{b}\right)^{-(l+1)} P_l^m(\cos\theta), \qquad (2.31)$$

where b is a normalization radius (taken either as the radius of the Earth's core or of the experimental vessel) and g_l^{mc} and g_l^{ms} are the Gauss coefficients, which have units of magnetic field. The $l = 0$ term is neglected because it represents the aphysical magnetic monopole. Each remaining term in the sum yields a magnetic

33

l	m	$P_l^m(\cos\theta)$
0	0	1
1	0	$\cos\theta$
1	1	$\sin\theta$
2	0	$\frac{3}{2}\cos^2\theta - \frac{1}{2}$
2	1	$\sqrt{3}\cos\theta\sin\theta$
2	2	$\frac{\sqrt{3}}{2}\sin^2\theta$
3	0	$\frac{5}{2}\cos^3\theta - \frac{3}{2}\cos\theta$
3	1	$\frac{1}{2}\sqrt{\frac{3}{2}}\sin\theta\,(5\cos^2\theta - 1)$
3	2	$\frac{\sqrt{15}}{2}\sin^2\theta\cos\theta$
3	3	$\frac{1}{2}\sqrt{\frac{5}{2}}\sin^3\theta$
4	0	$\frac{35}{8}\cos^4\theta - \frac{15}{4}\cos^2\theta + 3$
4	1	$\frac{1}{2}\sqrt{\frac{5}{2}}\sin\theta\,(7\cos^3\theta - 3\cos\theta)$
4	2	$\frac{\sqrt{5}}{4}\sin^2\theta\,(7\cos^2\theta - 1)$
4	3	$\frac{1}{2}\sqrt{\frac{35}{2}}\sin^3\theta\cos\theta$
4	4	$\frac{\sqrt{35}}{8}\sin^4\theta$

Table 2.1: The generalized, Schmidt semi-normalized Legendre functions through $l = 4$. Adapted from [63].

field that satisfies Eqn. 2.12 automatically, and together the terms form a complete and orthogonal set which can therefore represent *any* divergence-free scalar $\Phi(\mathbf{r})$ in spherical coordinates.

Powerful as it is, this representation has one serious limit: being valid only for regions where $\mathbf{J} = 0$ means it can tell us nothing about Φ, $\mathbf{B}$, or $\mathbf{u}$ in the interior of the Earth or our experiment. For that, a more general representation is necessary.

2.3.2 Vector spherical harmonics

Above we represented an arbitrary scalar field in terms of the natural scalar basis in spherical coordinates, the spherical harmonics. Now we shall represent an arbitrary *vector* field in terms of the natural vector basis in spherical coordinates, the vector spherical harmonics, following [46]. The vector spherical harmonics are a complete and orthogonal set, defined in spherical coordinates as

$$\mathbf{T}_l^{mc} = \nabla \times T(r)Y_l^{mc}(\theta, \phi)\hat{\mathbf{r}},$$

$$\mathbf{T}_l^{ms} = \nabla \times T(r)Y_l^{ms}(\theta, \phi)\hat{\mathbf{r}},$$

$$\mathbf{S}_l^{mc} = \nabla \times \nabla \times S(r)Y_l^{mc}(\theta, \phi)\hat{\mathbf{r}},$$

$$\mathbf{S}_l^{ms} = \nabla \times \nabla \times S(r)Y_l^{ms}(\theta, \phi)\hat{\mathbf{r}},$$

(2.32)

where $\mathbf{T}_l^{mc}$ are called the toroidal vector spherical harmonics, $\mathbf{S}_l^{mc}$ are called the poloidal vector spherical harmonics, $T(r)$ and $S(r)$ are (not yet specified) complete and orthogonal scalar functions, $\hat{\mathbf{r}}$ is the radial unit vector, and $Y_l^{mc}(\theta, \phi)$ and $Y_l^{ms}(\theta, \phi)$ are the scalar spherical harmonics described above. Any differentiable, divergence-free, three-dimensional vector field can be expressed in terms of the vector spherical harmonics with $l > 0$. For an enlightening illustration of the first few, see Fig. 2 in [46].

2.3.3 Selection rules

Mathematics in hand, we return now to physics. Consider the problem of a conductive fluid in the presence of some initial magnetic field. Representing the two fields in terms of vector spherical harmonics, we write

$$\mathbf{u} = \sum_\alpha \left(\mathbf{S}_\alpha + \mathbf{T}_\alpha \right),$$

$$\mathbf{B} = \sum_\beta \left(\mathbf{S}_\beta + \mathbf{T}_\beta \right),$$

(2.33)

where α and β are shorthand ways of representing the labels of each function (l, m, and c or s), α always being used for velocities and β always being used for magnetic fields. What magnetic induction results? To address the question, we can represent the induced field in terms of vector spherical harmonics as well, labelling it γ. Inserting Eqn. 2.33 into Eqn. 2.15 and continuing through considerable mathematical manipulation, Bullard and Gellman [46] find expressions for the growth rates of the γ terms, which obey the selection rules listed in Table 2.2. No assumptions are made about the relative strengths of the initial and induced magnetic fields, so that even with a fixed velocity field, a bewildering variety of feedback mechanisms are possible. Each newly-induced magnetic field component can in turn induce more components. In the fully nonlinear problem, where the velocity field varies in time with Lorentz forcing playing a role, the complexity increases further.

Interactions	Conditions for nonzero result
$< \mathbf{S}_\gamma \vert \mathbf{S}_\beta \vert \mathbf{S}_\alpha >$ $< \mathbf{T}_\gamma \vert \mathbf{T}_\beta \vert \mathbf{S}_\alpha >$ $< \mathbf{T}_\gamma \vert \mathbf{S}_\beta \vert \mathbf{T}_\alpha >$	$\alpha + \beta + \gamma$ is even; α, β, and γ can form the sides of a triangle; $m_\alpha \pm m_\beta \pm m_\gamma = 0$; Three of the harmonics have $\cos m\phi$ or one has, with $m = 0$ counting as a cosine.
$< \mathbf{S}_\gamma \vert \mathbf{T}_\beta \vert \mathbf{S}_\alpha >$ $< \mathbf{T}_\gamma \vert \mathbf{S}_\beta \vert \mathbf{S}_\alpha >$ $< \mathbf{S}_\gamma \vert \mathbf{S}_\beta \vert \mathbf{T}_\alpha >$ $< \mathbf{T}_\gamma \vert \mathbf{T}_\beta \vert \mathbf{T}_\alpha >$	$\alpha + \beta + \gamma$ is odd; α, β, and γ can form the sides of a triangle; $m_\alpha \pm m_\beta \pm m_\gamma = 0$; Two of the harmonics have $\cos m\phi$ or none has, with $m = 0$ counting as a cosine; No two harmonics are identical.
$< \mathbf{S}_\gamma \vert \mathbf{T}_\beta \vert \mathbf{T}_\alpha >$	Always zero.

Table 2.2: Selection rules for toroidal ($\mathbf{T}_\gamma$) and poloidal ($\mathbf{S}_\gamma$) components of the induced magnetic field as a function of the toroidal and poloidal components of the velocity field (subscript α) and initial magnetic field (subscript β). The notation $< \mathbf{C}_\gamma \vert \mathbf{B}_\beta \vert \mathbf{A}_\alpha >$ signifies an initial magnetic field $\mathbf{B}_\beta$ acted upon by a flow field $\mathbf{A}_\alpha$ to produce an induced magnetic field $\mathbf{C}_\gamma$, all described in terms of vector spherical harmonics. Taken from [46]. For the specific case appropriate to our experimental observations, see Table 3.6.

2.4   Dimensionless parameters

For comparing the experimental, numerical, and analytical work of various researchers using various parameters, the governing equations and results are often cast in dimensionless form. The Buckingham Π theorem [64] states that any dimensionless result of a problem with p dimensional parameters using q fundamental units is a function of $p - q$ dimensionless quantities. Our apparatus has $p = 9$ dimensional parameters, four of which are material properties of the fluid (ρ, η, ν, and $\mu = \mu_0$), two of which are geometric characteristics of our apparatus (a, the inner sphere radius; and b, the outer sphere radius), and three of which are parameters

we control during an experiment (Ω_i, the inner sphere rotation rate; Ω_o, the outer sphere rotation rate; and B_0, the applied magnetic field). There are $q = 4$ fundamental units involved (m, kg, s, and A), so we anticipate that all results will depend upon a set of five dimensionless parameters. To write the dimensionless governing equations, we construct the dimensionless quantities

$$\mathbf{u}' = \frac{\mathbf{u}}{a\Omega_i}, \quad P' = \frac{P}{\rho b^2 \Omega_o^2}, \quad \mathbf{\Omega}' = \frac{\mathbf{\Omega}}{\Omega_o}, \quad \mathbf{B}' = \frac{\mathbf{B}}{B_0}, \quad t' = \Omega_o t, \quad \nabla' = b\nabla. \tag{2.34}$$

Inserting these into Eqn. 2.15 and rearranging gives the *dimensionless* induction equation,

$$\frac{\partial \mathbf{B}'}{\partial t'} = \frac{E}{Pm}\nabla'^2\mathbf{B}' + \chi\zeta\nabla' \times (\mathbf{u}' \times \mathbf{B}'), \tag{2.35}$$

where

$$E = \frac{\nu}{\Omega_o b^2}, \tag{2.36}$$

$$Pm = \frac{\nu}{\eta}, \tag{2.37}$$

$$\chi = \frac{\Omega_i}{\Omega_o}, \tag{2.38}$$

$$\zeta = \frac{a}{b}, \tag{2.39}$$

are four of the five dimensionless parameters we expected to find. E is the Ekman number, giving the ratio of viscous forces to rotational forces. Pm is the magnetic Prandtl number, giving the ratio of viscous diffusion to magnetic diffusion. Similarly χ is the rotation rate ratio and ζ is the radius ratio of the apparatus. We should also mention the Rossby number, $Ro = \chi - 1$, a dimensionless parameter interchangeable with χ and more common in the literature.

Likewise inserting our dimensionless quantities (Eqn. 2.34) into Eqn. 2.17 and

rearranging, we find the *dimensionless* Navier-Stokes equation,

$$\frac{\partial \mathbf{u}'}{\partial t'} + \chi\zeta\left(\mathbf{u}'\cdot\nabla'\right)\mathbf{u}' = -\frac{1}{\chi\zeta}\nabla'P' + E\nabla'^2\mathbf{u}' + \frac{E^2S^2}{\chi\zeta Pm^2}\left(\nabla'\times\mathbf{B}'\right)\times\mathbf{B}' - 2\left(\mathbf{\Omega}\times\mathbf{u}\right).$$

(2.40)

The remaining dimensionless parameter,

$$S = \frac{B_0 b}{\eta\sqrt{\rho\mu}},$$

(2.41)

is the Lundquist number, giving the ratio of magnetic excitation to magnetic damping.

Though the Buckingham Π theorem predicts the number of necessary dimensionless parameters, it does not specify how they must be constructed, and in fact their particular construction is highly non-unique. One alternate construction bears mention here because its members are common in related literature and because we shall refer to it in Chapter 6. Equations 2.35 and 2.40 could be written as

$$\frac{\partial \mathbf{B}'}{\partial t'} = \frac{ERe}{Rm}\nabla'^2\mathbf{B}' + ERe\nabla'\times\left(\mathbf{u}'\times\mathbf{B}'\right),$$

(2.42)

$$\frac{\partial \mathbf{u}'}{\partial t'} + ERe\left(\mathbf{u}'\cdot\nabla'\right)\mathbf{u}' = -\frac{1}{ERe}\nabla'P' + E\nabla'^2\mathbf{u}' + \frac{S^2ERe}{\zeta Re}\left(\nabla'\times\mathbf{B}'\right)\times\mathbf{B}' - 2\left(\mathbf{\Omega}\times\mathbf{u}\right),$$

(2.43)

where Rm and Re together replace Pm and χ in our set of dimensionless parameters. They are defined as

$$Re = \frac{\Omega_i ab}{\nu},$$

(2.44)

$$Rm = \frac{\Omega_i ab}{\eta}.$$

(2.45)

Re is the Reynolds number, giving the ratio of flow stretching to viscous smoothing. It is named for O. Reynolds, who concluded in 1883 that turbulence occurred in

39

pipe flow experiments above a critical value of this particular dimensionless group $(Re > Re_c \approx 2000)$ [65]. Though subsequent work has determined that pipe flow is linearly stable and technically has no Re_c, Re remains a good predictor for turbulence in many fluid flows. Rm is the magnetic Reynolds number, giving the ratio of of magnetic field stretching to magnetic dissipation. It is used in analytical predictions of the onset of dynamo action — above some critical value $(Rm > Rm_c)$, an appropriate flow of conductive fluid generates its own magnetic field. The difficulty, of course, comes in determining Rm_c for each particular flow.

The values of these dimensionless parameters, both in our experiment and in relevant natural systems, are listed in Table 3.1.

Chapter 3

Experimental apparatus

In this chapter we describe our experimental apparatus in detail, both to lay groundwork for the scientific results that we report in Chapters 4 and 5 and to document our designs and procedures for future experimentalists. First comes an overview of the apparatus, its capabilities, and its relation to Earth's core. We spend the remainder of the chapter describing each subsystem in detail: the test fluid (sodium), the vessel (outer sphere, inner sphere, gas management, and boundary material), the mechanical drive system, the magnets, the thermal control system, and the magnetic field probes (especially the construction and properties of our Gauss array).

3.1   Our apparatus: the big picture

Our experimental apparatus, shown in Figs. 3.1 and 3.2, is designed to match as many of the dimensionless parameters of Earth's core as possible. A so-called spherical Couette cell, the apparatus is composed of an outer, spherical shell (which is analogous to the Earth's core-mantle boundary) and a solid, concentric, inner sphere (which is analogous to the inner core of the Earth) with about 110 L of liquid sodium filling the gap between the spheres. Both spheres can rotate independently, as driven by AC induction motors. The outer sphere rotates up to ± 35 Hz

to impose bulk rotation on the fluid, providing the centrifugal and Coriolis forces which are also present in Earth's core. The inner sphere rotates up to ± 45 Hz to provide mechanical forcing of fluid flows. Because the apparatus does not exhibit dynamo action (i.e., does not generate its own magnetic field), and because other hydromagnetic behaviors are interesting as well, we apply a DC, axial magnetic field and observe the magnetic fields induced through interactions between the applied field and the fluid flow. Thus we vary three dimensional parameters during experiments: the outer rotation rate Ω_o, the inner rotation rate Ω_i, and the applied magnetic field $\mathbf{B}_o$. Equivalently, we vary the Ekman number E, the rotation rate ratio χ, and the Lundquist number S, three dimensionless parameters defined in Eqns. 2.36 and 2.41. The two remaining dimensionless parameters, Pm and ζ, do not change during our experiments because they depend on fluid properties and vessel geometry. Table 3.1 gives a comparison of the dimensionless parameters of the apparatus to those of the Earth.

The driven rotation of our inner sphere is perhaps the least "Earth-like" aspect of the apparatus. Whether or not Earth's inner core rotates differentially with respect to the mantle is a topic of lively debate in the geophysics community. Some measurements do show that the inner core super-rotates, but the upper bound for that rotation rate is about 0.5°/year [67, 68]. Our inner sphere rotates much more vigorously. By imposing vigorous differential rotation, we gain access to dynamical regimes which are interesting in their own right and which may hold predictive power for the behavior of Earth's core, even if the boundary conditions differ appreciably.
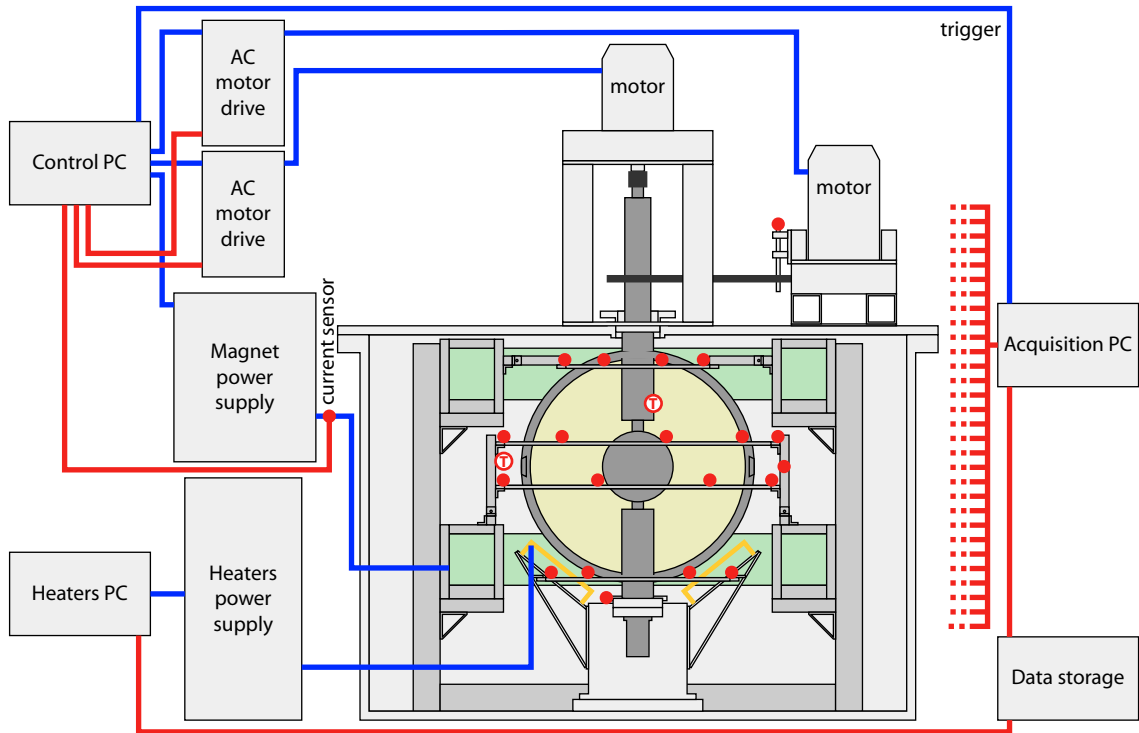
Figure 3.1: Cut-away sketch of the experimental apparatus. The spherical test vessel is at center. Our magnet coils are shown in green, and heaters are shown in gold. Red dots illustrate approximate Hall probe locations (see also Fig. 3.4), and each red "T" indicates a thermocouple. Control connections are shown in blue; data connections are shown in red. The outer sphere is driven by a belt, shown in black, to which a rotation rate sensor also interfaces. The inner sphere is driven by an on-axis motor through a flexible shaft coupler. One PC controls and records data from the motors and magnets, as well as producing a trigger used for synchronization. Another PC, controlled by that trigger, acquires the bulk of our data (signal connections not shown) and records it on a server. A third PC retrieves temperature readings from the server and controls the heaters.
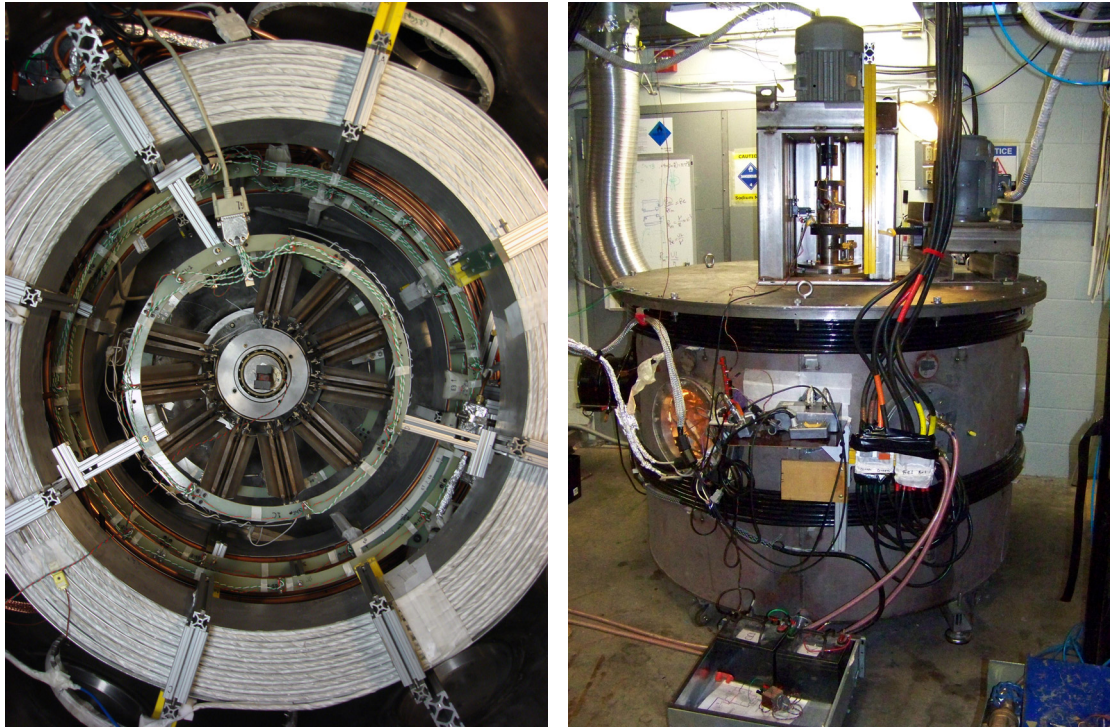
Figure 3.2: Photographs of the experimental apparatus. Left: the interior of the containment vessel, with the fluid vessel removed, viewed from above. The upper magnet is visible in white. The copper cooling tubes that cover the lower magnet are visible below, as are other copper tubes that serve to cool the magnets and Ohio Semitronics HR72 Hall probes. Concentric with the magnets are four fiberglass rings in light green, which support the Hall probes that comprise our Gauss array. Other Hall probes are visible between the magnets, either supported by light green fiberglass or covered in white tape. Our infrared thermocouple is covered in aluminum foil and mounted between the magnets at right. Extending radially from the center of the apparatus are ten pairs of incandescent heaters, each shielded from below with a stainless steel sheet. At center is the lower bearing seat which supports the outer sphere (not shown). Right: The exterior of the containment vessel. Both motors are visible at top, as are their stainless steel mounts. A drive belt couples to the outer shaft via a pulley, and our slip rings are mounted atop the pulley. The vertical bundle of black wires powers our magnets. The pink hoses supply kerosene for probe and magnet cooling. We cool the sodium with the black fans visible at left. All probes are powered by batteries (at bottom) to reduce noise and prevent ground loops.

44

Parameter	Earth	Experiment
$E = \frac{\nu}{\Omega_o b^2}$	10^{-14} [66]	$3.6 \times 10^{-8} \leq E \leq 8.4 \times 10^{-7}$
$Pm = \frac{\nu}{\eta}$	10^{-5} [66]	8.9×10^{-6}
$Re = \frac{\Omega_i ab}{\nu}$	$10^7 \leq Re \leq 10^8$ [66]	$|Re| \leq 1.2 \times 10^7$
$Rm = \frac{\Omega_i ab}{\eta}$	$300 \leq Rm \leq 600$ [66]	$|Rm| \leq 104$
$S = \frac{B_0 b}{\eta\sqrt{\rho\mu}}$	n/a	$0 \leq S \leq 4.3$
$\chi = \frac{\Omega_i}{\Omega_o}$	4×10^{-6} [67]	$0.1 \leq |\chi| \leq 30$
$\zeta = \frac{a}{b}$	0.35 [66]	0.328

Table 3.1: Relevant dimensionless parameters for Earth and for the experiment. Experimental parameters are calculated using the dimensions in Table 3.2 and the definitions given in Eqns. 2.36 and 2.41. Values for Earth are approximate. Rm and Re for Earth are calculated using estimated flow speeds, not boundary rotation rates. S is not applicable to Earth because external magnetic fields are not known to affect the dynamics of the core to first order.

3.2   Sodium as a test fluid

Using liquid sodium as a test fluid involves engineering challenges. First, the sodium is solid at room temperature and must be heated above its melting point (97.8°C) before each experiment. Second, because sodium is flammable, we must be careful to prevent direct contact with thermal or electrical ignition sources. Third, sodium reacts vigorously with water, yielding sodium hydroxide, hydrogen gas, and heat. The hydrogen is apt to detonate, so avoiding any mixing of sodium and water is a matter of paramount importance. Through more than a decade handling sodium experiments, our group has developed considerable expertise in meeting the engineering challenges, and we employ many safety procedures.

Those challenges are justified by the scientific advantages of sodium. The onset

of dynamo action (and other interesting hydromagnetic phenomena) is governed by the magnetic Reynolds number, Rm, defined in Eqn. 2.44. The power required to drive a test fluid scales with fluid density, fluid speed, and apparatus size: $\mathcal{P} \propto \rho U^3 L^2$, where U is the speed and L is the size. Substituting, we find

$$Rm = \frac{1}{\eta} \left(\frac{\mathcal{P}L}{\rho} \right)^{1/3}. \qquad (3.1)$$

Hence to improve the magnetic Reynolds number of an apparatus, we can input more power, build larger experiments, use fluid of lower density, or use fluid of lower magnetic diffusivity. Only changes in η give first-order increases in Rm; for example, doubling Rm requires an eightfold increase in $\mathcal{P}$, the difference between inputting a few kilowatts or a few tens of kilowatts! Choosing a test fluid with appropriate material properties is by far the easiest way for an experimentalist to increase Rm. Sodium has the lowest magnetic diffusivity of any liquid. Thus sodium is the fluid of choice for researchers interested in the dynamo problem (e.g., [6–8, 36–43, 53]).

3.3   Vessel

3.3.1   Outer sphere

The spherical shell that contains our test fluid has an inner radius $b = 30.48$ cm (see Table 3.2) and is composed of two hemispheres which screw together at the equator. Its design and construction were part of the dissertation work of W. L. Shew [37], who configured it as a rotating convection experiment. Machined from aircraft alloy titanium (Ti, 6% Al, 4% V), the shell is 2.54 cm thick and is engineered

for rotation rates up to 100 Hz, at which the centrifugal acceleration at the equator is about 12,000 times as large as gravity. We have rotated the sphere, filled with sodium, as fast as 37.5 Hz. The shell is integral with a hollow shaft, to which we attach ball bearings above (SKF 6016-2RSGA) and below (front-to-front pair of SKF 7216BECBY)to support the apparatus as it spins. These bearings are held in place by a cylindrical containment vessel, roughly 2 m in diameter and 1 m deep. The containment vessel also serves as protection for mechanical, thermal, and chemical safety hazards.

3.3.2   Inner sphere

The work described in this dissertation began when we removed the chilled inner sphere from the convection apparatus built for previous work [37] and replaced it with a solid inner sphere of radius 10 cm, which can rotate independent of the outer shell. At different times two inner spheres have been installed in the apparatus, one copper and one soft iron, both having identical geometry. (For mechanical drawings of the sphere, shaft, bearing seats, and other parts, see Appendix B.) The inner sphere rides on a 25 mm, stainless steel shaft which is supported by ball bearings at its base (back-to-back pair of SKF 7204BECBM) and a needle roller bearing above the sphere (SKF HK2520). The lower bearings are always submerged in liquid sodium — certainly not a situation anticipated by their designers, though the bearings seem able to survive for the 100 or so hours of run time typical between apparatus re-builds. We have seen them fail only once. The inner shaft exits the

Dimension	Value
a	0.1 m
b	0.3048 m
ρ	927 kg/m^3
ν	7.39×10^{-7} m^2/s
η	8.30×10^{-2} m^2/s
μ	$\mu_0 = 4\pi \times 10^{-7}$ m·kg/(A·s)^2
B_0	$0 \leq B_0 \leq 400$ G
$\Omega_o/2\pi$	1.5 Hz $\leq |\Omega_o/2\pi| \leq$ 35 Hz
$\Omega_i/2\pi$	4 Hz $\leq |\Omega_i/2\pi| \leq$ 45 Hz

Table 3.2: Dimensions of the experimental apparatus. Both spheres can rotate in either direction.

test volume through a lip seal which is intended to make sliding contact with the shaft in order to contain the sodium. The upper bearing is placed just above this lip seal, but because of chronic lip seal failures, the upper bearing often encounters solid sodium and/or sodium oxide (a ceramic), which shortens the life of the bearing. This problem deserves a bit more discussion.

3.3.3 Gas management

The biggest obstacle that prevents repeated and reliable performance of our apparatus is gas management. Sodium, like most materials, expands during melting (about 3%) and expands further as its temperature increases further ($2.13 \times 10^{-4}\, m/m°$C). In fact its expansion coefficient is greater than that of the titanium shell ($2.58 \times 10^{-5}\, m/m°$C), so that above some "full" temperature the volume of

sodium exceeds that of the vessel, and a leak is inevitable. The soft, rubber lip seal always leaks first. We avoid over-full leaks by filling the system at some relatively high temperature (say, 130°C) and making sure to stay well below that temperature during subsequent experiments.

Unfortunately, we find that the lip seal can leak even at lower temperatures, and the problem is gas. At room temperature, the volume of the sodium is a few percent (a few liters) smaller than that of the vessel. The remaining volume is vacuum — or gas, if the lip seal has allowed air in for any reason. Once gas leaks in through the lip seal, buoyancy causes it to rise to the top of the vessel, well above the height of the lip seal (Fig. 3.3), where it becomes trapped. When we heat the system again, both the gas and the sodium expand, pressuring the lip seal and potentially causing a sodium leak. If leaked sodium does not re-enter when the system cools, *more* gas can seep through the lip seal, leaving a bigger bubble and setting the stage for more expulsion the next time we heat. Hence the apparatus can act as a sodium pump. The leaked sodium is a safety hazard, impedes rotation of the inner shaft, and is difficult to remove even after draining and disassembling the apparatus. Also, if the bubble contains oxygen, it allows oxidation of the sodium.

We have attempted to address the problem by installing a vent near the top of the vessel, as shown in Fig. 3.3. During heating, we open the vent, allowing gas to escape by bubbling through a cup of oil (to prevent backflow). We close the valve before beginning experiments. During cooling, we connect low-pressure nitrogen gas and open the valve to prevent oxygen entry. The technique eases the gas management problem but does not solve it. Future rotating experiments should

be careful to address this problem in their designs. One solution is to locate the lip seal at the highest point in the system, so bubbles can always rise to escape. Another is to add an expansion tank in the rotating frame, so that it can remain connected to the experiment, as was done with DTS [39].

3.3.4 Copper and soft iron

As mentioned above, we have alternately experimented with two inner spheres of identical geometry but different composition, one copper and one soft iron. Copper more closely models the inner core of the Earth, composed of crystalline iron that likely has magnetic diffusivity smaller than the molten iron outer core. Copper has lower magnetic diffusivity (1.35×10^{-2} m^2/s) than sodium (8.3×10^{-2} m^2/s) and thus replicates the conductive boundary condition.

Soft iron is scientifically interesting because it is nearly pure iron and therefore ferromagnetic, with large permeability but small remembrance, particularly for applied magnetic fields well below its saturation point. Thus soft iron tends to amplify and concentrate magnetic fields while harboring little permanent magnetism. Perhaps more importantly, soft iron changes the magnetic boundary conditions — magnetic field lines must be normal to a ferromagnetic boundary. The particular alloy used in the construction of our soft iron inner sphere, ASTM A 848 Alloy 1, is detailed in Table 3.3.

Of the five previous, man-made, liquid metal dynamos (see Chapter 1), three employed ferromagnetic boundaries: both the Lowes and Wilkinson dynamos [4, 5]
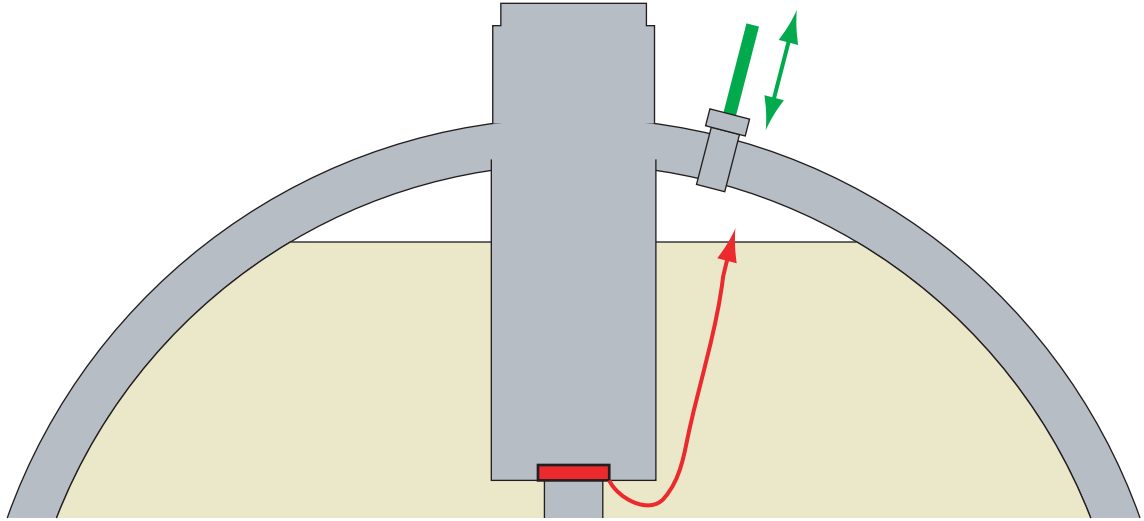
Figure 3.3: Scheme for management of gas flow. As the sodium contracts during cooling, a bubble can enter through the lip seal before becoming trapped at the top of the vessel, following a path like the one drawn in red. We have managed gas flow by installing a vent near the top of the vessel, so gas instead follows the path drawn in green.

Property	Value
Typical composition	99.634% Fe, 0.25% Mn, 0.04% Cu, 0.02% C, 0.02% Ni, 0.014% Si, 0.008% P, 0.007% S, 0.005% Ti, 0.002% Cr
Maximum permeability	$5000\mu_0$
Coercive force	64 A/m at 10 kG
Hysteresis loss	250 J/m^3/cycle at 10 kG
Saturation	17.5 kG
Electrical resistivity	1.07×10^{-7} Ω m
Linear expansion	1.36×10^{-5} 1/°C
Melting point	1532°C
Curie temperature	760°C
Density	7860 kg/m^3

Table 3.3: Properties of ASTM A 848 Alloy 1 soft iron, as given by supplier.

51

as well as VKS2 [8], which is also the only one not constructed to mimic a known, laminar, kinematic dynamo flow. Numerical simulations performed by the VKS2 team suggested that the critical magnetic Reynolds number (Rm_c) of their Von Kármán experiment would drop considerably if the stagnant sodium behind the rotating, stainless steel impeller at each end were eliminated. For engineering reasons it was not possible to remove the fluid, but the team instead replaced the stainless steel impellers with soft iron ones, reasoning that the ferromagnetic material would serve to magnetically isolate the stagnant sodium from the main test section. The new configuration did have lower Rm_c — low enough, in fact, that the apparatus became a quite interesting dynamo [8, 9]. Hence ferromagnetic boundaries have played a central role in historical dynamo studies. Unfortunately a detailed study of the effects of ferromagnetism was not undertaken for the Lowes dynamo, and for VKS2 such a study is beyond the capabilities of existing theory or numerics because of the complicated impeller shape.

An inner sphere has a shape that is much simpler and therefore much more amenable to theory and numerics. Hence a central goal of our experiments with soft iron is a better understanding of the effects of a ferromagnetic boundary conditions on hydromagnetic flows.[1] Some of the behaviors observed in our apparatus are present regardless of whether the inner sphere is copper or soft iron; others change dramatically when the inner boundary is ferromagnetic. Our results using a soft iron inner sphere are detailed in Chapter 5.

---

[1]The possibility of inducing dynamo action in our own apparatus, though not achieved, was also scientifically alluring.

3.4 Mechanical drive

The inner and outer spheres each rotate independently and are each driven by a separate motor. They are sketched, along with their mounts, in Fig. 3.1. We use AC induction motors of the sort common in industrial applications, typically General Electric 5KS215SAB105 (10 Hp 60 Hz), though we have sometimes coupled a General Electric 5KE184KC205C motor (5 Hp, 30 Hz) to the outer sphere to allow for smaller rotation rates. Each motor is controlled by a 10 Hp, variable frequency drive (ABB ACH-500) of the sort common in HVAC systems, which allows us to vary the rotation rate. The advantages of AC induction motors include their controllable speed, ease of use, low cost, and flexibility.

Despite all their abilities, variable frequency drives coupled to AC induction motors have one great disadvantage in scientific applications: radio frequency electrical noise. The drives synthesize AC control voltages of arbitrary frequency from square pulses modulated at a few kilohertz, with strong harmonics high up the spectrum that tend to introduce high-frequency noise to scientific instruments. To reduce this noise, we have installed filters between the drives and their power connections, and (for recent data sets) between the drives and the motors. Thorough electrical shielding and low-pass filtering of signal lines is also crucial.

Each motor drive detects the rotation rate and torque of its motor. The signals are available as analog voltages, and we acquire them using LabView code and a

National Instruments PCI-6024E acquisition card in our control PC.[2] (See Fig. 3.1.)
The rotation rate signals have been calibrated using optical sensors, but the torques
remain uncalibrated. A worthy future project would be the installation of a proper
torque sensor.

In addition to the information provided by the drives, we have during re-
cent experiments made independent measurements of the rotation rate of the outer
sphere (Ω_o) using an optical encoder (Accu-Coder 755A-07-S-1000-R-OC-1-S-S-N).
Connected to an idler pulley on the drive belt between motor and sphere, it produces
1000 open-collector pulses for each revolution of its shaft. The resulting signal could
be sampled directly with analog acquisition hardware, as are most of our probes,
but a prohibitively high sampling rate (e.g., 60 kHz sampling for 30 Hz rotation)
would be necessary. A digital counter circuit solves the problem by providing an
8-bit count of pulses, readable as parallel digital data. Thus much more reasonable
sampling rates are sufficient. We record this data using a National Instruments
PCI-6225 acquisition card and associated LabView code in our acquisition PC. To
extract a rotation rate from the pulse counts, some post-processing is necessary.
First the signal must be unwrapped (adding $2^8 - 1 = 255$ every time the counter
resets). Next we apply a least-squares linear fit to windows of data, and the fitted
slope is proportional to the rotation rate. Because of the large inertia of our rotating
system (the rotating parts are perhaps 250 kg), changes in the rotation rate are much
slower than the sampling rate, and we are able to perform the least-square fits over

---

[2]Making electrical connections between the acquisition PC and the motor drives causes ground
loop problems, so we acquire motor signals with the control PC.

large windows, yielding high precision. The error in our rotation rate measurements is about 1 mHz.

3.5 Magnets

In order to apply axial, DC magnetic fields to the test fluid, we constructed a Helmholtz pair of magnet coils. Each magnet has 210 turns of stranded aluminum wire, diameter 0.742 cm, and is cooled by kerosene circulating through seven turns of 0.625 inch copper tubing, all on one side of the magnet. Eight aluminum sheets lie between the wire wraps and give thermal paths to the cooling tubes.[3] The wires are insulated with fiberglass tape, applied as we hand-wound the coils. A cross-sectional diagram is shown in Appendix B. Each of the two magnets is separated into three electrical sections. We connect all six sections in parallel to a power supply, (EMHP-20-1000-D-1211) capable of providing 1000 A at 20 V. As assembled, including the wiring that connects the magnets to the supply, the load impedance is 32 mΩ at room temperature, so that the maximum available current is about 600 A. The resulting magnetic field is 400 G (0.04 T) at the location of the center of the sphere.

The magnet power supply is controlled by a National Instruments AT-A0-6 card in our control PC (see Fig. 3.1). Direct electrical connection between the PC and the supply is not possible because ground loop problems cause electrical shorts which can damage the card. To avoid the problem, we constructed an external

---

[3]This system for magnet cooling cannot remove enough heat to allow steady-state operation at full power (12 kW). Wire with a cooling channel at its center would work much better, but was unavailable at the time of construction.

digital-to-analog converter (D/A) with opto-isolated inputs. Connecting the digital outputs of the card to the inputs of the D/A, then connecting its analog output to the analog input of the magnet power supply, we can control the magnets without introducing a current path. Similarly, we wanted to measure the magnet current without connecting directly to the shunt provided with the supply, because doing so causes ground loops. By passing the magnet current through a long, cylindrical conductor and mounting a Hall probe (Honeywell SS94A1F; see below) near the conductor, we can measure the local magnetic field and thus the current without direct electrical connection. These measurements are recorded, along with rotation rates and torques, by our control PC.

3.6 Thermal control

Keeping the sodium warm enough to remain liquid is essential for the scientific validity of our experiments, while keeping it cool enough to avoid leaks is essential for safety. Thus we need good thermal control. A K-type thermocouple mounted on the shaft of the titanium shell, near the center of the apparatus, measures the temperature of the sodium directly (see Fig. 3.1). Its signal is amplified in the rotating frame, then passed to the laboratory frame through a pair of slip rings which we constructed. A second measurement of the sodium temperature comes from an infrared, E-type thermocouple mounted in the laboratory frame and aimed at the vessel (see Fig. 3.2). Both temperature signals are sampled and recorded by our acquisition PC, which saves the temperatures on a server. Our heaters

PC retrieves the temperatures and uses them in a PID algorithm for controlling the heaters power supply (Kinetics Industries SVR3-080PM43-TV/C), which can provide up to 300 A at 270 V. It powers a set of 20 incandescent heaters (Heraeus NobleLight 45132101) which altogether output 10 kW, mostly as infrared radiation. The heaters are mounted in a "burner" shape, different from the setup used in previous work [37] (see Fig. 3.1). When we need to cool the sodium, we use airflow by opening ports in the containment vessel and aiming fans, shown in Fig. 3.2 at the sphere.

Our magnets (see above) and some of our Hall probes (see below) also need thermal stabilization. They are cooled using a kerosene loop which is in turn cooled by chilled water via a heat exchanger in another room. We do not cool with water directly because of the safety hazard that a leak would pose; kerosene does not react with sodium. A K-type thermocouple inserted into one magnet gives us a laboratory readout of magnet temperature.

3.7 Magnetic measurements

3.7.1 Hall probes

The bulk of our experimental data comes from measuring magnetic fields. To make those measurements, we employ two types of Hall probe, the Ohio Semitronics HR72 and the Honeywell SS94A1F. Both are based on the Hall effect [69]: when a current runs through a magnetic field, a voltage difference appears between the two sides of the conductor, transverse to both the current and the field. This Hall

voltage is proportional to the magnetic field and is commonly used in many sensors, including ours. The HR72 probes are raw semiconductor, offering very good sensitivity and signal-to-noise ratio, but requiring an external current source and amplifier. With a 200 mA current and 10^3 amplifier gain, HR72 probes have 130 mV/G sensitivity. Unfortunately, the Hall voltage is also proportional to temperature, so signals from HR72 probes vary with temperature changes. We mount the probes on heatsinks cooled by our kerosene loop (see above) but observe significant slew nonetheless. Because of these temperature effects and because of the external electronics required, we use only four HR72 probes. The majority of our Hall probes are Honeywell SS94A1F, an inexpensive device with an on-board current source, amplifier, and temperature compensation circuit. Each requires nothing more than a 12 V supply and a signal line. Their sensitivity is 25 mV/G, inferior to the HR72 and the primary drawback to the design. These are our workhorse Hall probes.

Altogether the apparatus uses 37 Hall probes, a count determined by the number of analog channels our electronics can acquire (40 channels total, one defunct and two for thermocouples). Thirty of the probes comprise the Gauss array, detailed below. One probe is mounted just below the outer sphere and near its shaft, measuring magnetic field in the cylindrical radial direction $\hat{\mathbf{z}}$, in coordinates (s, ϕ, z). Six are spread around the equator ($\theta = \pi/2$) at locations $\phi \in \{0, \pi/2, \pi/3, \pi/4, \pi/5, \pi/7\} - 120°$, oriented to measure magnetic field in the $\hat{\mathbf{s}}$ direction. Some of these equatorial probes are constructed as an array (see Appendix B); the rest are mounted independently. The equatorial probes were placed to distinguish as many different single-mode azimuthal wavenumber induction patterns

as possible. In fact this particular arrangement (six probes alone) can distinguish single-mode azimuthal wavenumbers to $m = 40$ before degeneracy arises. Including probes at $\phi = \pi$ and $\phi = \pi/6$ gives the ability to distinguish wavenumbers to $m = 46$ without degeneracy, a slightly better result. When multiple wavenumbers are present simultaneously, however, the equatorial probes fail to identify them properly. An evenly-spaced array around the equator would allow for Fourier decomposition but would require many more probes. Our Gauss array allows for decomposition for $m \leq 4$ as long as the spherical harmonic degree also satisfies $l \leq 4$.

All analog inputs connected to our acquisition PC are equipped with signal conditioning. First, each passes through a solid-state 22 V surge suppressor which shorts the signal to ground if more than 22 V appears, intended to protect our expensive acquisition card from electrical damage. Second, each input is equipped with an RC, low-pass filter with roll-off frequency about 3 kHz, intended to remove high-frequency noise from the signals.

3.7.2 Projecting onto vector spherical harmonics: Gauss coefficients

Using 30 such probes, we have constructed an array, similar to the one devised by D. R. Sisan [70], which is well-suited for projection onto the vector spherical harmonics to yield Gauss coefficients (as defined by Eqn. 2.31) through degree and order four. Each probe is aligned to measure the component of the magnetic field in the cylindrical radial direction $\hat{\mathbf{s}}$. Aligning the probes perpendicular to $\mathbf{B}_0$ keeps

them from saturating. Probe locations are given in Table 3.4, and Fig. 3.4 shows a sketch. Obtaining Gauss coefficients makes our data set much richer because we can use single-component, local measurements to make reasonable assertions about all three components of the magnetic field throughout the volume of the experiment. Gauss coefficients are also useful in that they are the *lingua franca* of geophysics researchers. Of course, there is a trade-off — small-scale features are necessarily lost.
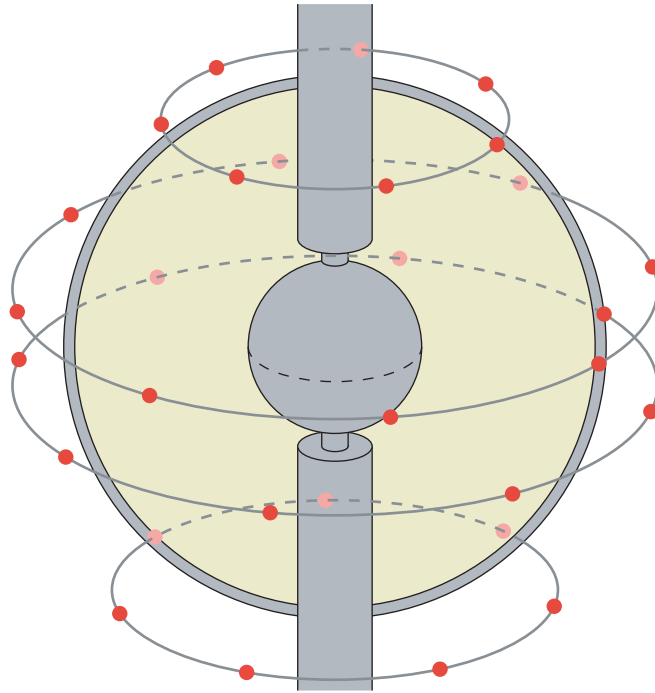
Figure 3.4: Gauss array design. Each dot represents a Hall probe, and each probe is oriented in the $\hat{\mathbf{s}}$ direction. Table 3.4 gives their locations. In this diagram, the axis of rotation is vertical.

We position and align the probes precisely by mounting them on four rigid, dielectric rings, each machined with 0.001 inch precision. (Mechanical drawings are given in Appendix B.) Each ring is itself aligned by carefully referencing to the bearings and bearing seats that support the outer sphere, limiting the error in this

r/b	θ	ϕ	r/b	θ	ϕ
1.16667	0.610865	0.365273	1.25	1.7017	0.18326
1.16667	0.610865	1.26287	1.25	1.7017	0.968658
1.16667	0.610865	2.16047	1.25	1.7017	1.75406
1.16667	0.610865	3.05807	1.25	1.7017	2.53945
1.16667	0.610865	3.95566	1.25	1.7017	3.32485
1.16667	0.610865	4.85326	1.25	1.7017	4.11025
1.16667	0.610865	5.75086	1.25	1.7017	4.89565
1.2625	1.37881	0.575959	1.25	1.7017	5.68105
1.2625	1.37881	1.36136	1.33333	2.44346	0.55676
1.2625	1.37881	2.14675	1.33333	2.44346	1.45436
1.2625	1.37881	2.93215	1.33333	2.44346	2.35196
1.2625	1.37881	3.71755	1.33333	2.44346	3.24955
1.2625	1.37881	4.50295	1.33333	2.44346	4.14715
1.2625	1.37881	5.28835	1.33333	2.44346	5.04475
1.2625	1.37881	6.07375	1.33333	2.44346	5.94235

Table 3.4: Locations of the Gauss array probes, in spherical coordinates (r, θ, ϕ). The experiment has radius $b = 0.3048$ m, with its center at the origin. Each probe is oriented to measure the $\hat{\mathbf{s}}$ component of the field (horizontal and toward the axis of rotation). Angles are in radians.

procedure to perhaps 5 mm. Past calculations show that the array design is fairly robust to errors in probe placement [70].

To extract the 24 Gauss coefficients having degree $l \leq 4$ from the 30 probe signals, we perform a calculation similar to the one that J. C. F. Gauss performed in the 1830s, a least-squares error minimization. Previous work [70] gives details of our procedure. First, the basis functions must be determined. In our case they are the poloidal vector spherical harmonics, projected onto the cylindrical radial direction: $\mathbf{S}_l^{mc} \cdot \hat{\mathbf{s}}$ and $\mathbf{S}_l^{ms} \cdot \hat{\mathbf{s}}$. Their explicit forms are listed in Table 3.5. The toroidal components of the magnetic field do not extend beyond the fluid itself and are thus inaccessible without probes that protrude into the test volume.[4] Next, a

---

[4]This fact follows from representing the magnetic field in scalar spherical harmonics outside the

matrix must be constructed from the values of the basis functions at each probe, and subsequently inverted (just once). The final step in calculating the Gauss coefficients, performed with each new set of measurements, is to multiply the inverted matrix onto a 24-element vector constructed from the measurements and the basis functions, summing over all probes. (Our C code that implements this algorithm is included in Appendix C.) The result is a 24-element vector of Gauss coefficients.

Since we seek 24 Gauss coefficients, the matrix that must be inverted is 24×24. Inverting a matrix can introduce large numerical errors if the matrix is nearly singular — that is, if its smallest eigenvalue is much smaller than its largest. The ratio of smallest to largest eigenvalue is known as the condition number of the matrix, and in our application the array probes must be placed to achieve a condition number as near unity as possible. After spending about a week exploring new designs that might improve on the previous arrangement [70] or that might achieve a similar condition number while being easier to build, we had no success whatsoever. In fact, a Monte Carlo analysis, randomly placing 30 probes around the surface of the sphere and determining the condition number of the resulting array design, found no improved design in more than 10^6 iterations! Hence our choice to use the Sisan design; imitation is the sincerest form of flattery. The condition number of our array, slightly modified from its predecessor for engineering reasons, is 0.0458.

fluid, representing it in vector spherical harmonics inside the fluid, and requiring that the field be continuous at the boundary. See, for example, [70].

Coefficient	Basis function
g_1^0	$\frac{1}{\rho^3}\sin 2\theta$
g_1^{1c}	$-\frac{2}{\rho^3}\sin\theta\sqrt{\sin^2\theta}\cos\phi$
g_1^{1s}	$-\frac{2}{\rho^3}\sin\theta\sqrt{\sin^2\theta}\sin\phi$
g_2^0	$\frac{3}{4\rho^4}(1+3\cos 2\theta)\sin\theta$
g_2^{1c}	$-\frac{3\sqrt{3}}{\rho^4}\cos\theta\sin\theta\sqrt{\sin^2\theta}\cos\phi$
g_2^{1s}	$-\frac{3\sqrt{3}}{\rho^4}\cos\theta\sin\theta\sqrt{\sin^2\theta}\sin\phi$
g_2^{2c}	$\frac{3\sqrt{3}}{2\rho^4}\sin^3\theta\cos 2\phi$
g_2^{2s}	$\frac{3\sqrt{3}}{2\rho^4}\sin^3\theta\sin 2\phi$
g_3^0	$\frac{2}{\rho^5}\sin\theta\cos\theta\left(5\cos^2\theta-3\right)$
g_3^{1c}	$-\frac{\sqrt{6}}{\rho^5}\sin\theta\sqrt{\sin^2\theta}\left(5\cos^2\theta-1\right)\cos\phi$
g_3^{1s}	$-\frac{\sqrt{6}}{\rho^5}\sin\theta\sqrt{\sin^2\theta}\left(5\cos^2\theta-1\right)\sin\phi$
g_3^{2c}	$\frac{2\sqrt{15}}{\rho^5}\sin^3\theta\cos\theta\cos 2\phi$
g_3^{2s}	$\frac{2\sqrt{15}}{\rho^5}\sin^3\theta\cos\theta\sin 2\phi$
g_3^{3c}	$-\frac{\sqrt{10}}{\rho^5}\sin\theta\left(\sin^2\theta\right)^{3/2}\cos 3\phi$
g_3^{3s}	$-\frac{\sqrt{10}}{\rho^5}\sin\theta\left(\sin^2\theta\right)^{3/2}\sin 3\phi$
g_4^0	$\frac{5}{64\rho^6}\sin\theta(9+20\cos 2\theta+35\cos 4\theta)$
g_4^{1c}	$-\sqrt{\frac{5}{2}}\frac{5}{8\rho^6}\sin\theta\sqrt{\sin^2\theta}(9\cos\theta+7\cos 3\theta)\cos\phi$
g_4^{1s}	$-\sqrt{\frac{5}{2}}\frac{5}{8\rho^6}\sin\theta\sqrt{\sin^2\theta}(9\cos\theta+7\cos 3\theta)\sin\phi$
g_4^{2c}	$\frac{5\sqrt{5}}{8\rho^6}\sin^3\theta(5+7\cos 2\theta)\cos 2\phi$
g_4^{2s}	$\frac{5\sqrt{5}}{8\rho^6}\sin^3\theta(5+7\cos 2\theta)\sin 2\phi$
g_4^{3c}	$-\sqrt{\frac{35}{2}}\frac{5}{4\rho^6}\sin 2\theta\left(\sin^2\theta\right)^{3/2}\cos 3\phi$
g_4^{3s}	$-\sqrt{\frac{35}{2}}\frac{5}{4\rho^6}\sin 2\theta\left(\sin^2\theta\right)^{3/2}\sin 3\phi$
g_4^{4c}	$\frac{5\sqrt{35}}{8\rho^6}\sin^5\theta\cos 4\phi$
g_4^{4s}	$\frac{5\sqrt{35}}{8\rho^6}\sin^5\theta\sin 4\phi$

Table 3.5: Basis functions for Hall probes measuring the $\hat{\mathbf{s}}$ component of the magnetic field, through degree and order four.

3.7.3 Biases in the Gauss coefficients

Empirically, the most delicate step in calculating Gauss coefficients is proper biasing. The voltage signal measured at each Hall probe in the Gauss array is composed of three parts,

$$V_t = V_e + V_{B_0} + V_s, \tag{3.2}$$

where V_t is the total voltage, V_e is an electronic offset, V_{B_0} is an offset due to the external magnets, and V_s is the desired signal. V_e depends on the details of the amplifier circuits and their power source; it is near 6 V, nearly constant in time, and varies from probe to probe. V_{B_0} is due only to the applied magnetic field $\mathbf{B}_0(\mathbf{r})$, which is intended to be uniform and orthogonal to the probes, but in actuality is somewhat nonuniform and nonorthogonal. V_{B_0} varies from probe to probe and varies linearly with B_0. V_s is the part of the signal that describes the magnetic fields induced by the flowing sodium, and in order to obtain it, we must accurately remove V_e and V_{B_0} from V_t. In order to do so, we record data with $B_0 = 0$ frequently during experiments, which gives V_e for each probe. Each time the apparatus is re-built, we also record data for at least one magnet ramp, varying B_0 through its full range, with the sodium solid. Hence $V_s=0$, and after subtracting V_e, we can plot V_{B_0} vs. B_0 for each probe, fitting a line and extracting its slope. With these calibrations in hand, we can remove V_e and V_{B_0} from experimental data as long as B_0 (or equivalently, the magnet current, which we measure) is known. With V_s in hand, we can calculate proper Gauss coefficients.

Without a doubt, these calibration steps introduce experimental error. In at

least one case, magnet ramps with the sodium solid have shown hysteresis measurable by our Gauss array, almost certainly due to material hysteresis in the soft iron sphere. The slope of each V_{B_0} as B_0 was increased closely matched the slope as B_0 was decreased, but the offsets differed. In many experiments we observe axisymmetric (DC) induction which is much larger than the oscillatory induction, so that errors of a few percent in removing biases can contribute more to the signal than its oscillatory components. One work-around is to subtract *all* DC signals, but by doing so we lose access to the very interesting axisymmetric flows which have been observed in many past experiments (e.g. [71–73]). An improved scheme for obtaining or verifying the DC components of the Gauss coefficients would be a great experimental contribution.

3.7.4   Aliasing

Limited by the number of available channels in our acquisition card, our array can resolve only the Gauss coefficients with $l \leq 4$, though certainly higher-degree, smaller-scale motions are present in the magnetic fields of interest. In other words, the field is under-sampled. When a signal is under-sampled in *time*, filters are commonly used to remove the higher frequencies which cannot be recorded properly. Sampling is mathematically similar to mixing, so that if those higher frequencies are not removed, they alias onto low frequencies, and the result is a noisier signal.[5] An analogous device for *spatial* sampling, which would remove high-degree modes while leaving modes with $l \leq 4$, does not exist. The radial dependence of the modes

---

[5]As mentioned above, all our analog inputs are low-pass filtered at 3 kHz.

helps somewhat — since each mode goes as $r^{-(l+1)}$, higher-degree modes become relatively weak far from the fluid (see Eqn. 2.31). The question remains, however: what effects does spatial aliasing have on our data?

Figure 3.5 gives a partial answer. To construct it, we began by calculating the analytic form of each basis function $\mathbf{S}_l^{mc} \cdot \hat{\mathbf{s}}$ and $\mathbf{S}_l^{ms} \cdot \hat{\mathbf{s}}$ for $l \leq 7$. The functions were evaluated at the coordinates of each probe, as if a measurement had been taken. Using the least-square algorithm outlined above, we projected back onto the vector spherical harmonics accessible to our array, yielding Gauss coefficients g_p^{qc} and g_p^{qs}. For inputs with $l \leq 4$, the outputs match the inputs ($p = l$ and $q = m$) as expected. For higher-degree inputs, aliasing is apparent. When $l > 4$ and $m < 4$, non-zero outputs occur only when $q = m$ and the azimuthal phase is preserved ($\cos(m\phi)$ aliasing to $\cos(q\phi)$ and $\sin(m\phi)$ aliasing to $\sin(q\phi)$). Inputs with $l > 4$ and $m \geq 4$ allow more complicated aliasing, strongest when $q = 8 - m$, and usually showing azimuthal phase inversion ($\cos(m\phi)$ aliasing to $\sin(q\phi)$ and vice-versa). The strongest aliasing of all shows up on $(p, q) = (4, 2)$, consistent with large noise observed on the g_4^2 signals in experimental data.

This aliasing calculation serves to characterize some of the strengths and weaknesses of our particular Gauss array design. It might be used to infer the presence in experimental data of particular modes with $l > 4$, though such an inference would be speculative because aliasing is non-unique. The figure might also prove useful for systematic design of higher-degree Gauss arrays. It seems likely that the condition number could be kept near unity by placing each new probe, one-by-one, at a location that reduces or eliminates the highest-amplitude aliasing at lowest degree.
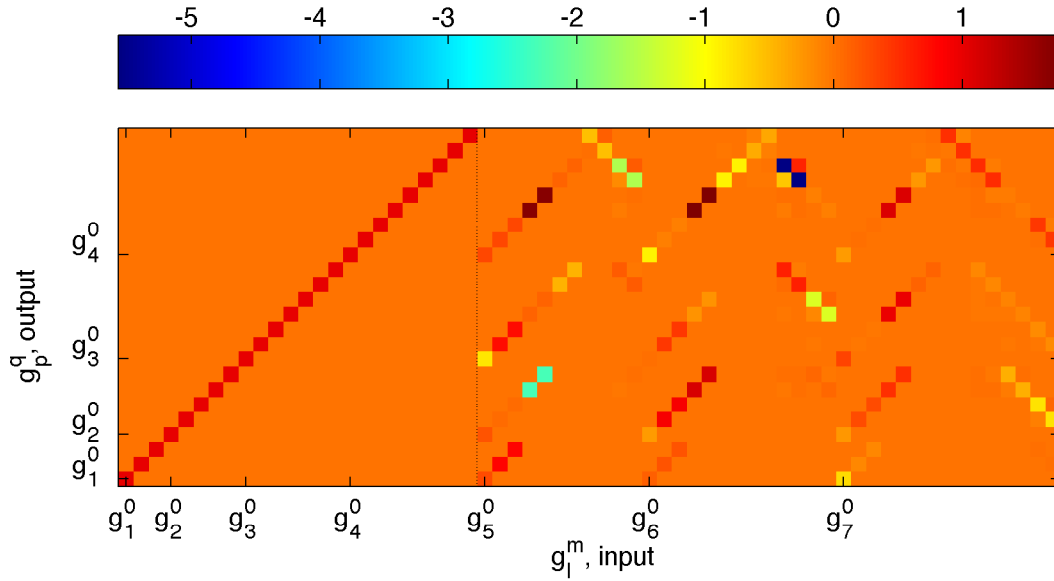
Figure 3.5: Aliasing properties of the Gauss array design. Single-mode input fields g_l^m with $l \leq 4$ produce output g_p^q with $(p, q) = (l, m)$, but aliasing occurs for $l > 4$. Here basis functions are ordered as in Table 3.5. The dotted line divides the low-degree modes, for which the array was designed, from the high-degree modes, which alias. A version of this figure better adapted for grayscale printing is included as Fig. D.2.

3.7.5 Meridional array

In addition to the probe array shown in Fig. 3.4, we should make brief mention of a previous probe array, which was used to acquire some of the data presented in Chapter 4. Constructed by D. S. Zimmerman, the previous array was composed of 21 Honeywell SS94A1F probes spaced at 7.5° increments along a meridian (from pole to pole), each measuring magnetic field in the cylindrical radial ($\hat{s}$) direction. Hence this meridional array could not provide Gauss coefficients at each sample, but offered high resolution for any induction pattern sweeping by, stationary in some rotating frame. Figure 3.6 gives a sketch.
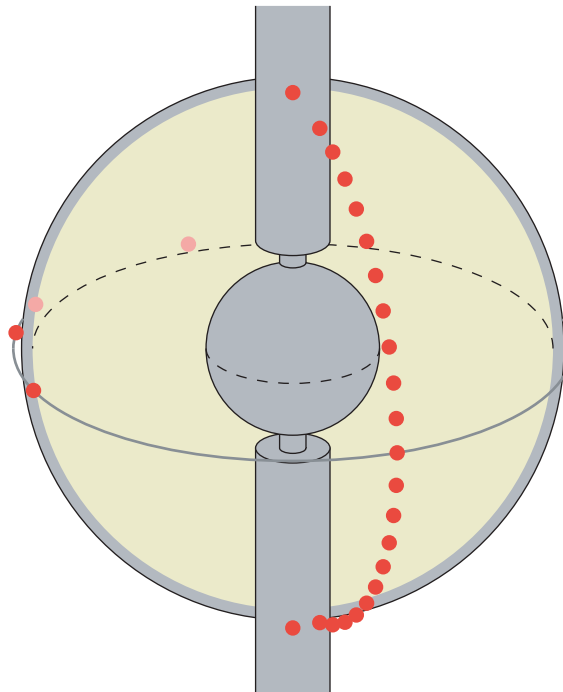
Figure 3.6: Meridional array design. Each dot represents a Hall probe, and each probe is oriented in the $\hat{s}$ direction. In this diagram, the axis of rotation is vertical.

3.7.6 Selection rules revisited

The selection rules listed in Table 2.2 are entirely general in that they apply to flows and background magnetic fields of arbitrary shape. In the special case where the total magnetic field is composed of a large, external component $\mathbf{B}_0$ and a small induction $\mathbf{B}_1$, as in Eqn. 2.20 and as is usually the case in our experiments, magnetic feedback can be neglected to first order. Moreover, since we know the geometry of the external field (it is $a_1\mathbf{S}_1^0 + a_3\mathbf{S}_3^0 + a_5\mathbf{S}_5^0 + \ldots$, or to first order just $\mathbf{S}_1^0$), we can write a much simpler set of selection rules, given in Table 3.6. Thus by projecting our magnetic measurements onto the vector spherical harmonics, we can say much about not only the magnetic field but also the underlying velocity field.

Observed induction	Flows of origin via S_1^0 field
S_1^0	S_2^0
S_1^{1c}	T_1^{1s}, S_2^{1c}
S_2^0	S_1^0, S_3^0
S_2^{1c}	T_2^{1s}, S_1^{1c}, S_3^{1c}
S_2^{2c}	T_2^{2s}, S_3^{2c}
S_3^0	S_2^0, S_4^0
S_3^{1c}	T_3^{1s}, S_2^{1c}, S_4^{1c}
S_3^{2c}	T_3^{2s}, S_2^{2c}, S_4^{2c}
S_3^{3c}	T_3^{3s}, S_4^{3c}
S_4^0	S_3^0, S_5^0
S_4^{1c}	T_4^{1s}, S_3^{1c}, S_5^{1c}
S_4^{2c}	T_4^{2s}, S_3^{2c}, S_5^{2c}
S_4^{3c}	T_4^{3s}, S_3^{3c}, S_5^{3c}
S_4^{4c}	T_4^{4s}, S_5^{4c}

Table 3.6: Mode selection rules for an applied S_1^0 magnetic field. Only cosine modes are listed in the "Observed induction" column; for sine modes, exchange all "c" labels with "s" and vice versa. More general selection rules are given in Table 2.2.

Chapter 4

Results with copper inner sphere

Having set the stage with historical background, theoretical underpinnings, and a description of our apparatus, we move now into the heart of the matter — our experimental results. In this chapter we describe behaviors observed with a copper inner sphere, providing conductive boundary conditions like those of the inner core of the Earth. First comes a description of the oscillatory magnetic behaviors that we have identified as inertial modes in the flow, along with some discussion of their dependence on parameters (E, χ, and S or, equivalently, Ω_o, Ω_i, and B_0) and their relation to previous studies. Next comes a review of the theory of over-reflection at a shear layer, which seems to be the energy source and selection mechanism for the inertial modes we have observed. The chapter concludes with a discussion of the axisymmetric zonal flows that co-exist with inertial modes. Results of a few of our other experiments, focused on parts of parameter space where inertial modes do not appear, are reserved for Chapter 5. There they are compared directly to similar experiments with a soft iron inner sphere.

4.1   Inertial modes

Consistent with the theory sketched in Chapter 2, in situations where the Ekman number E is small (or equivalently, the outer rotation rate Ω_o is large), we

observe that spherical Couette flow excites identifiable inertial modes. The details of our observations are presented below, beginning with raw data and building toward an agreement with theoretical predictions.

4.1.1 Oscillatory magnetic induction

Figure 4.1 shows raw data, a collection of time series recorded using an Ohio Semitronics HR72 probe mounted near the equator of our apparatus.[1] The signals are evidently oscillatory, suggesting wave motions, and each has a different fundamental frequency. Those frequencies are directly represented in Fig. 4.2, which shows power spectra calculated from the same data. Here it becomes evident that a narrow-band frequency peak rises orders of magnitude above all other signal components. These measurements were recorded at the same Ekman number $E = 4.4 \times 10^{-8}$ ($\Omega_o/2\pi = 29.9$ Hz), but with different inner sphere rotation rates, as listed in the caption. We find the main features of these spectra to be reproducible not only by returning to the same rotation rates Ω_o and Ω_i but simply by returning to the same rotation rate ratio χ, as long as E is sufficiently small (or, equivalently, Ω_o is sufficiently large).

Figure 4.3 further characterizes the parameter dependence. It shows a spectrogram, in which each column of pixels is a power spectrum, with normalized frequency on the vertical axis and power spectral density shown in color. The horizontal axis varies with χ. The high-power frequencies apparent as spikes in Fig. 4.2 are apparent as bright regions in the spectrogram. Below the spectrogram is a plot

---

[1]The mean has been removed from each signal, a fact which will become important below.
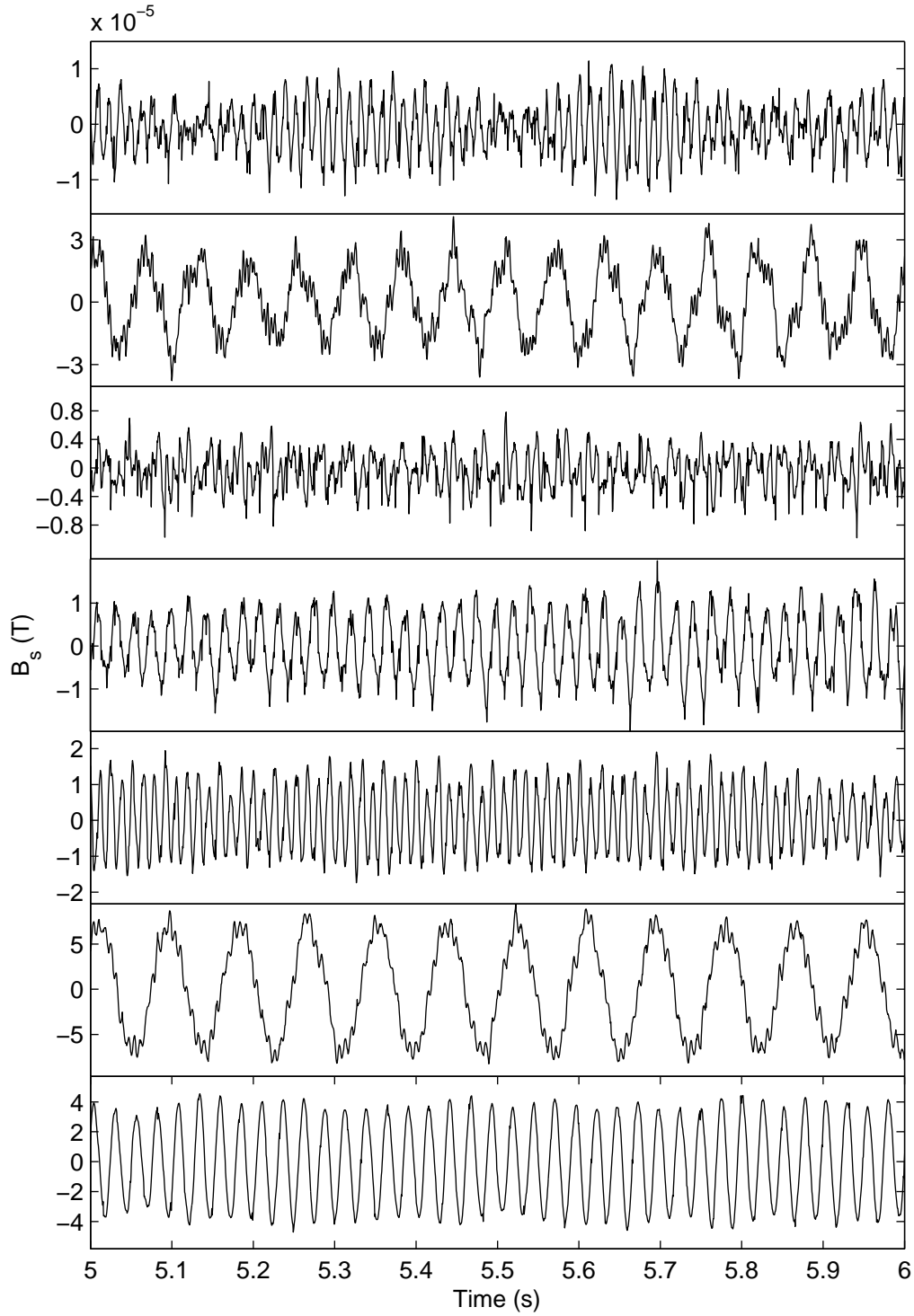
Figure 4.1: Typical B_s time traces at an equatorial probe when E is small. Only the oscillating component is shown, i.e., the means have been removed. For all data shown here, $E = 4.4 \times 10^{-8}$ and $S = 1.59$ ($\Omega_o/2\pi = 29.9$ Hz and $B_0 = 150$ G). From top to bottom, $\chi = 0.649$, -0.157, 0.692, 0.401, 0.562, 0.408, and 0.191 ($\Omega_i/2\pi = 19.4$, -4.7, 20.7, 12.0, 16.8, 12.2, 5.7 Hz).

73
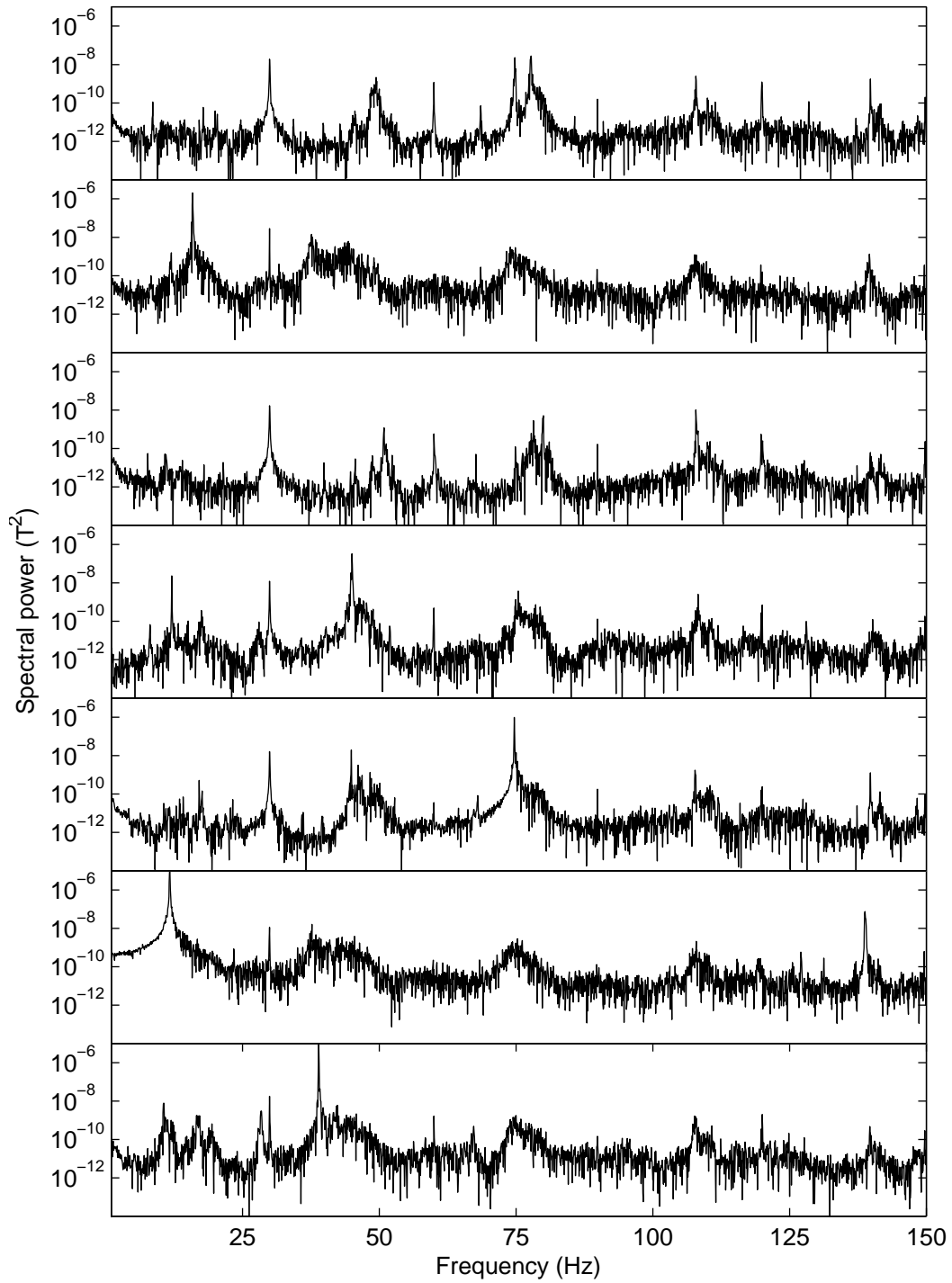
Figure 4.2: Power spectra of the data shown in Fig. 4.1.

of the standard deviation of the same data, showing that those bright regions are associated with the most intense oscillations observed.

4.1.2 Identifying inertial modes

Observing strongly oscillatory behavior in a rotating fluid, and being aware of the theory sketched in Chapter 2, it is natural to suspect that these oscillations are inertial modes. In order to identify them positively, we must extract the degree, order, and frequency of each. By calculating spectra, we have already obtained frequencies. With our more recent probe array (Fig. 3.4), the degree and order of the signal are immediately apparent as well (see, for example, Fig. 5.4). Our meridional array (Fig. 3.6) requires more laborious processing. By cross-correlating among the equatorial probes we obtain the order (azimuthal wavenumber) m of the mode. Knowing m, we choose a temporal window of data spanning exactly m oscillations in each probe signal — a single revolution of the presumed wave pattern. Then the data from our 21 meridional array probes, over the span of the window, gives a map of the induction B_s sampled over the surface,[2] which we project onto the (scalar) spherical harmonics up to degree and order 12 using a least-squares fit. The resulting pseudo-Gauss coefficients make it apparent which degree and order dominate, and we can approximate the induction B_s over the whole surface by summing appropriately. The images in the left column of Figs. 4.4 and 4.5 were produced this way. Each is a Mollweide projection, familiar to cartographers, in which features of equal area on the surface of the sphere are shown with equal area

---

[2]Here we are essentially employing Taylor's frozen turbulence hypothesis.

Experiment				Theory			
l_{mag}	l	m	ω/Ω_o	l	m	ω/Ω	θ_c
2	3	2	0.683 to 0.698	3	2	0.667	1.231
3	4	1	0.602 to 0.627	4	1	0.612	1.260
3	4	3	0.509 to 0.511	4	3	0.500	1.318
4	5	2	0.492 to 0.531	5	2	0.467	1.335
4	5	4	0.404 to 0.407	5	4	0.400	1.369
5	6	1	0.435 to 0.450	6	1	0.440	1.349
5	6	3	0.404 to 0.413	6	3	0.378	1.381

Table 4.1: Experimental and theoretical characteristics of inertial wave modes. By convention, waves with $\omega > 0$ are retrograde.

on paper as well. With each image is given the dominant degree l_{mag} and order m of the induction as well as its normalized frequency ω/Ω.

Each of these wave modes matches an analytically known, full-sphere inertial mode, identified according to the selection rules given in Table 3.6: the flow has the same normalized frequency ω/Ω, has the same order m, and has degree $l = l_{mag} \pm 1$. The set of matching modes are listed in Table 4.1.

Having identified the matching modes, we can calculate the flow field $\mathbf{u}$ of the analytical full-sphere mode. Our colleague A. Tilgner used the flow fields and our known background field B_0 as inputs to Eqn. 2.15, setting $\eta = 0$ and integrating numerically to solve for the induced magnetic field. The results are shown in the right column of Figs. 4.4 and 4.5. The agreement between measurement and theory supports the hypothesis that the oscillatory behaviors present in our experiment are inertial modes.
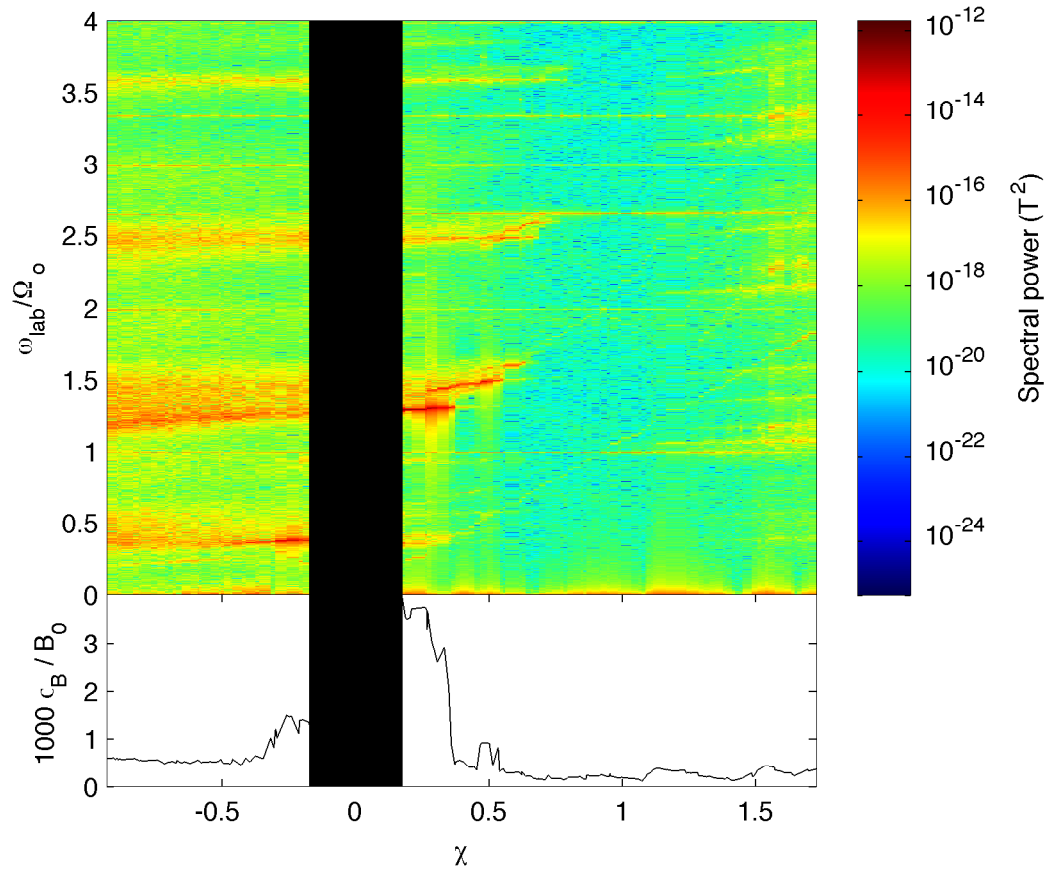
Figure 4.3: Magnetic field data taken from an equatorial Hall probe with $E = 7.26 \times 10^{-8}$ ($\Omega_o/2\pi = 18$ Hz). The upper plot is a spectrogram, with its vertical axis showing the normalized signal frequency $\omega_{\text{lab}}/\Omega_o$ as measured in the laboratory frame, and its horizontal axis showing the rotation rate ratio χ. Each column of pixels is a power spectrum of 32 s of data, with power indicated by the varying shades. The black central region lies at low speeds inaccessible with our AC motors. The lower plot shows the standard deviation of the same data, normalized by the applied magnetic field B_0. A version of this figure better adapted for grayscale printing is included as Fig. D.3.
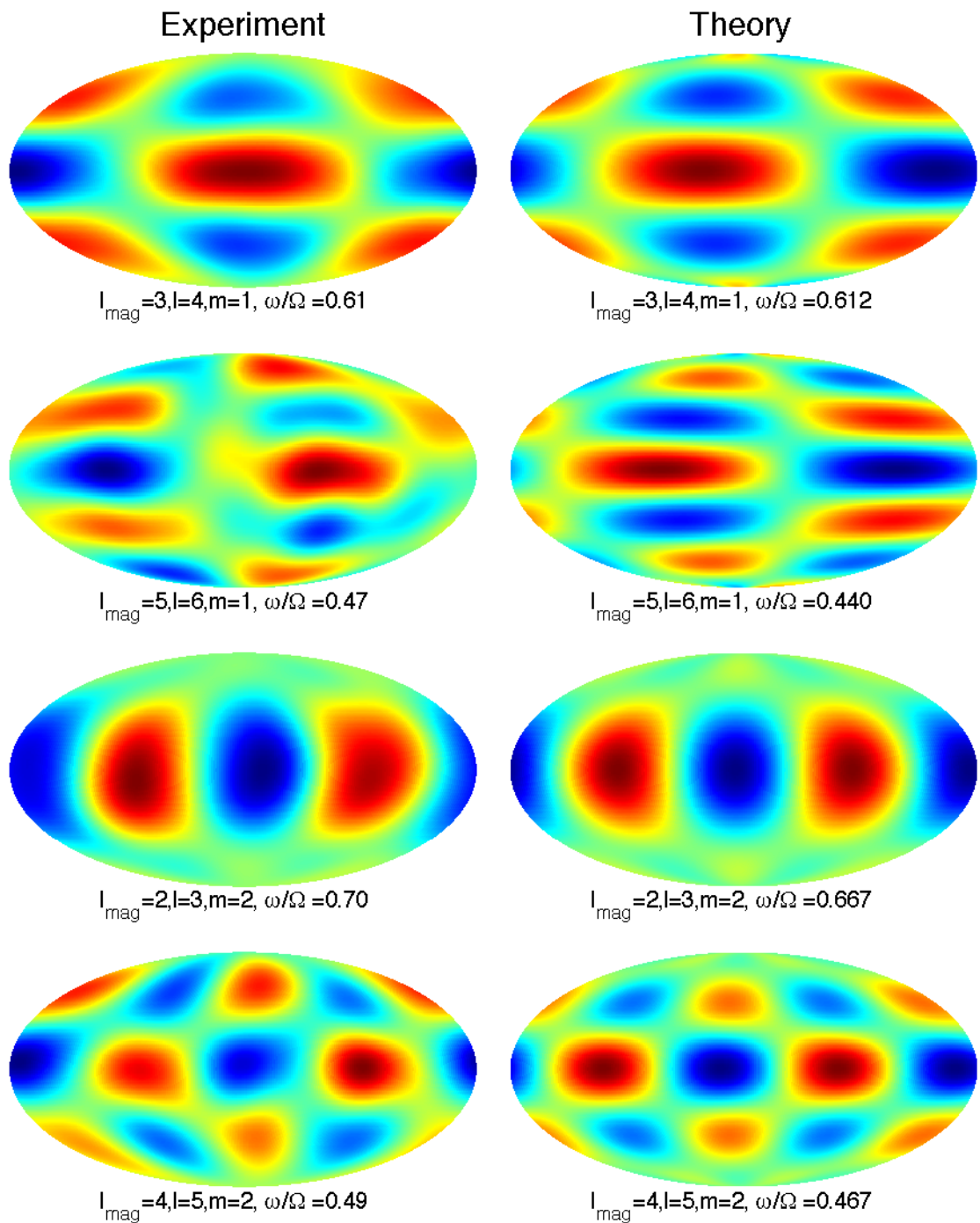
Figure 4.4: Induction B_s/B_0 at the surface of the fluid, shown as a Mollweide projection with the axis of rotation vertical. The left column shows data taken under the same experimental conditions as the first four traces shown in Fig. 4.1, respectively. Mean values have been removed. The right column shows numerical calculations of the induction produced by analytically-known inertial modes. A version of this figure better adapted for grayscale printing is included as Fig. D.4.

Figure 4.5: Induction B_s/B_0 at the surface of the fluid, shown as a Mollweide projection with the axis of rotation vertical. The left column shows data taken under the same experimental conditions as the last three traces shown in Fig. 4.1, respectively. Mean values have been removed. The right column shows numerical calculations of the induction produced by analytically-known inertial modes. A version of this figure better adapted for grayscale printing is included as Fig. D.5.

4.1.3 Parameter dependence

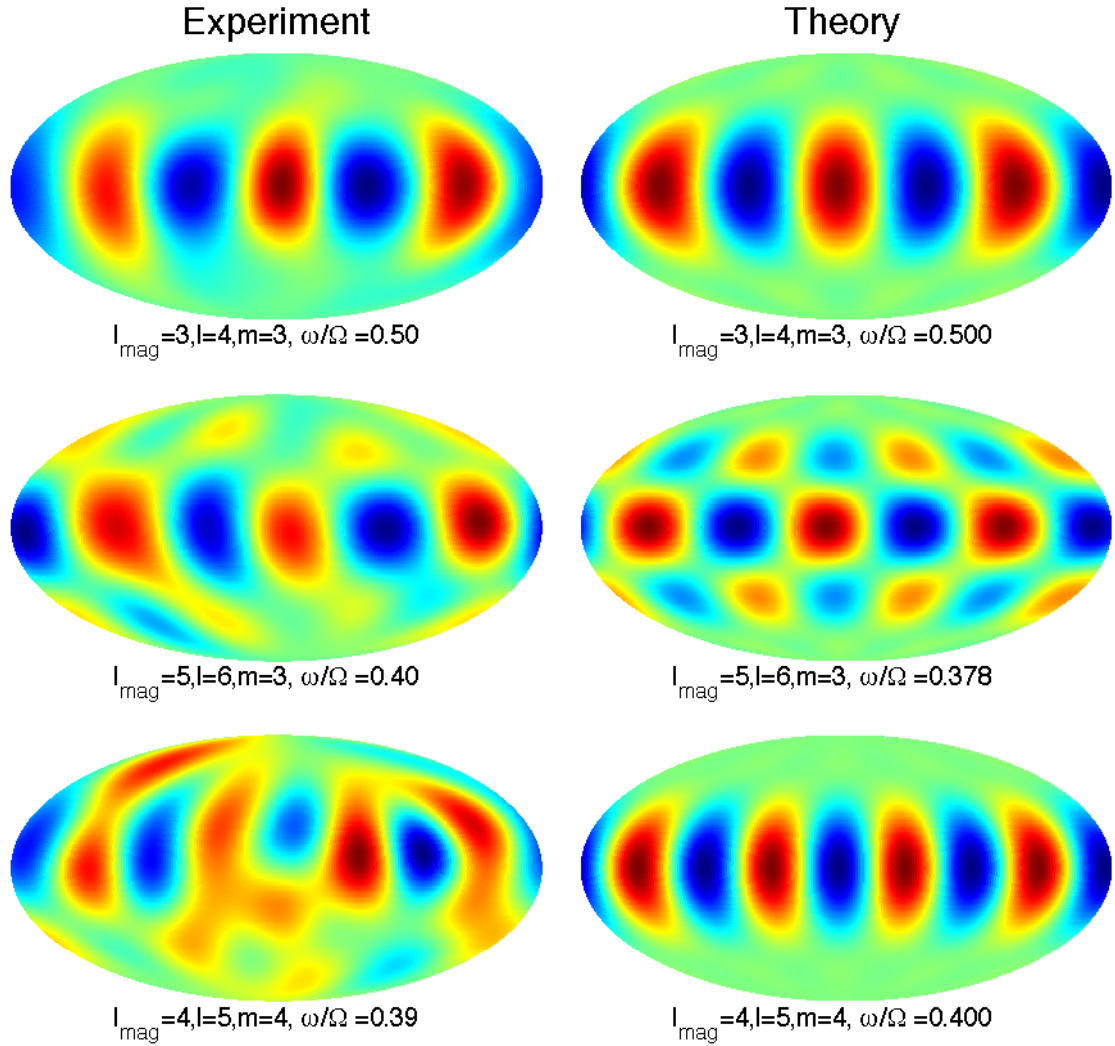Experimentally we observe that χ is the primary parameter relevant for inertial modes. The same modes evident in Fig. 4.3 are present in many different data sets with varying E (Ω_o), always at the same χ and always at the same normalized laboratory frequency $\omega_{\text{lab}}\Omega_o$. The frequency in the laboratory frame relates to the frequency in the rotating frame according to

$$\omega_{\text{lab}} = m\Omega_o - \omega. \tag{4.1}$$

Some hysteresis occurs, and typically we see more modes when gradually increasing χ during an experiment than when gradually decreasing χ, but the essential structure is the same. Nor does the exact Ekman number have primary importance; as long as $E \leq 10^{-7}$, we observe the same modes. Perhaps the waves are present at higher Ekman numbers (lower Ω_o) as well, but for a given χ, higher E implies lower Rm and therefore less induction. Eventually the modes become so weak that we can no longer detect them. We observe also that the modes depend only weakly on the applied magnetic field as represented by the Lundquist number S. Even for $S > 1$, inertial modes persist if E is small.

4.1.4 Comparison to past studies

Our findings are consistent with past studies. Most simply and most directly, because inertial modes are the linear eigenmodes of an inviscid ($\nu = 0$), rapidly rotating fluid, one should expect them to be common in experiments. More specifically, previous studies by Aldridge *et al.* have identified inertial modes (though not

the same ones we observe) in a sphere [74] and in a spherical shell [75]. Inertial waves have been identified experimentally in other geometries as well (e.g., [54, 76–78]). Asymptotic and numerical studies of inertial waves in spherical systems have also been published (e.g., [57, 58, 79, 80]).

Not seeking inertial waves per se, Hollerbach *et. al* [81] undertook numerical studies of spherical Couette flow with rapid overall rotation but small differential rotation ($E \ll 1$ and $\chi \approx 1$, or equivalently, $Re \approx 0$). Beginning with a steady, axisymmetric flow,[3] they increased Re until non-axisymmetric motions arose, seeking the azimuthal wavenumber m of the first such motion. For our radius ratio,[4] $m = 2$ motions arose first, at $Re \approx 500$, using their definition of Re. Using the same definition, however, $Re \geq 4 \times 10^5$ for all experimental conditions in our apparatus. Hence their interesting results may or may not be relevant to our work.

In a study that is perhaps more relevant, Rieutord [82] considered a spherical shell with radius ratio $\zeta = 0.35$, motivated as we are by the Earth's core. After linearizing the governing equations, the author calculated the linear eigenmodes numerically to predict which inertial modes are most likely to be present in Earth's core, and by extension, in an experimental apparatus with similar geometry, such as ours. The results are summarized in Table 4.2. Of the ten modes predicted, one is among the seven we have identified, and in fact it is the first to arise and the strongest for $\chi > 0$. That there is no further overlap may at first seem odd.

---

[3]The Stewartson layer, described below, is the dominant feature of this steady, axisymmetric flow.

[4]In our apparatus, $\zeta = 0.328$; see Table 3.1.

Rieutord, however, considered inertial modes in a spherical shell whose boundaries rotate rigidly ($\chi = 1$ always), whereas we have used differential rotation ($\chi \neq 1$) to excite inertial modes via shear. This particular forcing mechanism may not be a generic perturbation of the linear state, which was the particular sort of forcing studied by Rieutord. In fact, we will argue below that forcing by shear imposes mode selection, favoring some inertial modes over others, thereby choosing the particular modes we observe in an essentially non-generic way. The discrepancy in Ekman number between Rieutord's work and our own ($E = 10^{-5}$ vs. $E \leq 10^{-7}$) may also contribute to the mismatch between his predictions and our observations.

In a later study, Rieutord [83] took a more general focus and predicted that the dominant inertial modes in a real system are always low-frequency, low-wavenumber modes. Our observations are entirely consistent with this more general prediction, as discussed further below.

4.2   Over-reflection driving inertial modes

Having established the presence of inertial modes in our experiments, we come to a long list of follow-up questions, the first of which is this: what energy source drives inertial modes in our apparatus? From Fig. 4.3 and similar data, we know that inertial modes are present only with differential rotation ($\chi \neq 1$), so ultimately, differential rotation is the primary energy source. Still, what mechanism transfers energy from differential rotation to inertial modes? Our data suggest that over-reflection at a shear layer is the mechanism at work, but before asserting this claim,

l	m	ω/Ω	λ_{rr}	λ_{ff}
3	1	1.5099	$-5.977 \times 10^{-3} + 0.74383i$	$-1.621 \times 10^{-3} + 0.74354i$
5	0	1.5301	$-6.095 \times 10^{-3} + 0.75200i$	$-1.540 \times 10^{-3} + 0.75131i$
2	1	1	$-6.197 \times 10^{-3} + 0.50079i$	$0.50000i$
6	1	-1.4042	$-6.744 \times 10^{-3} - 0.69936i$	$-1.825 \times 10^{-3} - 0.69901i$
4	0	1.3093	$-7.190 \times 10^{-3} + 0.66216i$	$-2.484 \times 10^{-3} + 0.66109i$
5	2	1.4964	$-7.331 \times 10^{-3} + 0.74731i$	$-1.385 \times 10^{-3} + 0.74730i$
6	0	1.6604	$-7.463 \times 10^{-3} + 0.81736i$	$-3.117 \times 10^{-3} + 0.81736i$
6	2	1.6434	$-7.593 \times 10^{-3} + 0.81308i$	$-2.312 \times 10^{-3} + 0.81278i$
3	2	0.6667	$-8.224 \times 10^{-3} + 0.33355i$	$-0.058 \times 10^{-3} + 0.33333i$
8	0	1.3544	$-8.714 \times 10^{-3} + 0.68559i$	$-4.460 \times 10^{-3} + 0.68428i$

Table 4.2: The most unstable inertial modes in a spherical shell with $E = 10^{-5}$, as calculated in [82]. The eigenvalues λ_{rr} and λ_{ff} apply to non-slip and free-slip boundaries, respectively. We have identified one of these modes, $(l, m, \omega/\Omega) = (2, 3, 0.667)$, in our experiments. Table 1 of [82] identifies the modes with the notation of Greenspan [52]; here we use our notation, but the modes appear in the same order.

a bit of background is necessary.

4.2.1 Over-reflection theory

A shear layer, that is, a boundary between two regions of fluid at different speeds, can give rise to a variety of dynamical behaviors. Half a century ago, H. S. Ribner described a mechanism by which acoustic waves can be amplified by a shear layer [84]. The essence of his argument, sketched in Fig. 4.6, is that a pressure wave in region A impinging upon a shear layer causes a ripple to appear in that shear layer. The ripple moves in phase with the wave, which implies that the speed of the ripple along the boundary exceeds the transverse velocity of the incoming wave — the ripple is supersonic, in acoustic terms. Accordingly the ripple emits Mach waves, as would any supersonic object, back into region A. When the shear speed nearly matches the ripple speed, the ripple is subsonic with respect to the fluid on the other side of the shear layer (region B); hence Mach waves are not emitted into that layer, and effectively the incoming wave undergoes a total reflection. On the other hand, large shear speeds cause the ripple to emit Mach waves on both sides of the shear layer, allowing for both reflection and transmission. The coefficient of reflection is

$$R(\alpha, M) = \frac{1 - Z(\alpha, M)}{1 + Z(\alpha, M)}, \tag{4.2}$$

where

$$Z(\alpha, M) = -\frac{\sqrt{\csc^2 \alpha + M^2 - 2M \csc \alpha - 1}}{\sin 2\alpha (\csc^2 \alpha + M^2 - 2M \csc \alpha)} \tag{4.3}$$

is the acoustic impedance, α is the angle of incidence (which equals the angle of reflection), $M = u_{shear}/c_p$ is the ratio of shear speed to wave speed.[5] This expression is valid as long as transmission occurs.
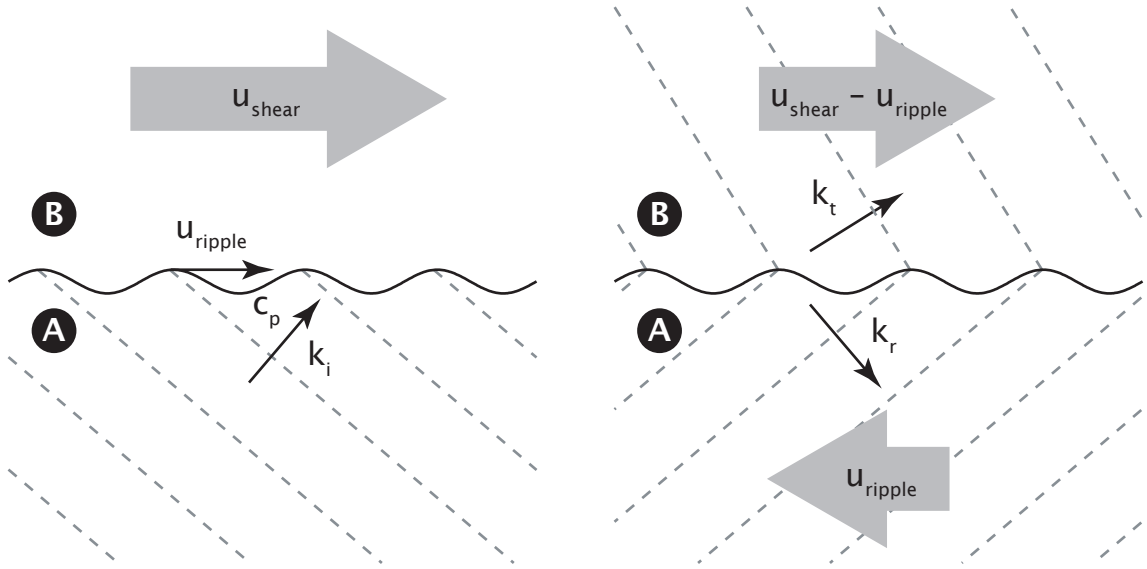

Figure 4.6: Over-reflection of a pressure wave at a shear layer. At left, the incoming wave approaches the shear layer with wave speed c_p and wave vector k_i. The pressure variations imposed by the wave (suggested by dashed lines) cause a propagating ripple on the boundary between the stationary fluid (region A) and the fluid shearing with speed u_{shear} (region B). Necessarily, the speed of the ripple $u_{ripple} > c_p$. At right, reflected and transmitted waves are shown in the frame of reference in which the ripple is stationary. In this frame, both regions A and B flow across the rippled boundary, at speeds $u_{shear} - u_{ripple}$ and $-u_{ripple}$, respectively. Mach waves can be emitted on both sides of the boundary, as sketched. Adapted from [84].

For certain angles α, we find $R > 1$, implying over-reflection, in which energy is transferred from the shear to the reflected wave. In fact, for $M \geq 2$, certain angles α yield $R = \infty$, such that waves incoming at these angles are greatly amplified until viscosity or nonlinear mechanisms necessarily cause saturation. The dependence of

[5]Following Ribner, we use the symbol M for this quantity, which in acoustics is a Mach number. In the interest of generality, we will refer to is as the normalized shear speed.

Range of shear speed	Count of critical angles
$0 \leq M \leq 2$	0
$2 < M \leq 2.36656$	1
$2.36656 < M \leq 5.22959$	3
$5.22959 < M$	5

Table 4.3: Count of critical angles. The first critical angle arises at $(\alpha, M) = (\pi/2, 2)$. Others arise in pairs at $(0.253869, 2.36656)$ and $(0.259104, 5.22959)$. No more than five critical angles are present for $M \leq 100$, and it seems unlikely that more arise at any M.

R^2 on M and α is plotted in Fig. 4.7, which partially reproduces Fig. 3 in [84], while making some features evident that did not appear in the original. A region of $R^2 = 0$ along the left side of the plot signifies angles at which the incoming wave is entirely transmitted. A region of total total reflection ($R^2 = 1$), noted in the original publication [84], is visible just right of center. And interestingly, while Ribner noted the three angles at which $R^2 = \infty$ for $M = 3$, in Fig. 4.7 it becomes clear that the number angles with $R^2 = \infty$ (we will call them "critical angles") varies with M from 0 to 5, as summarized in Table 4.3.

4.2.2 Over-reflection in our apparatus

Ribner wrote about over-reflection at a shear layer with acoustic waves in mind, but the hypotheses of his derivation are generic enough to apply to other pressure waves, including internal gravity waves and inertial waves, as well. Inertial
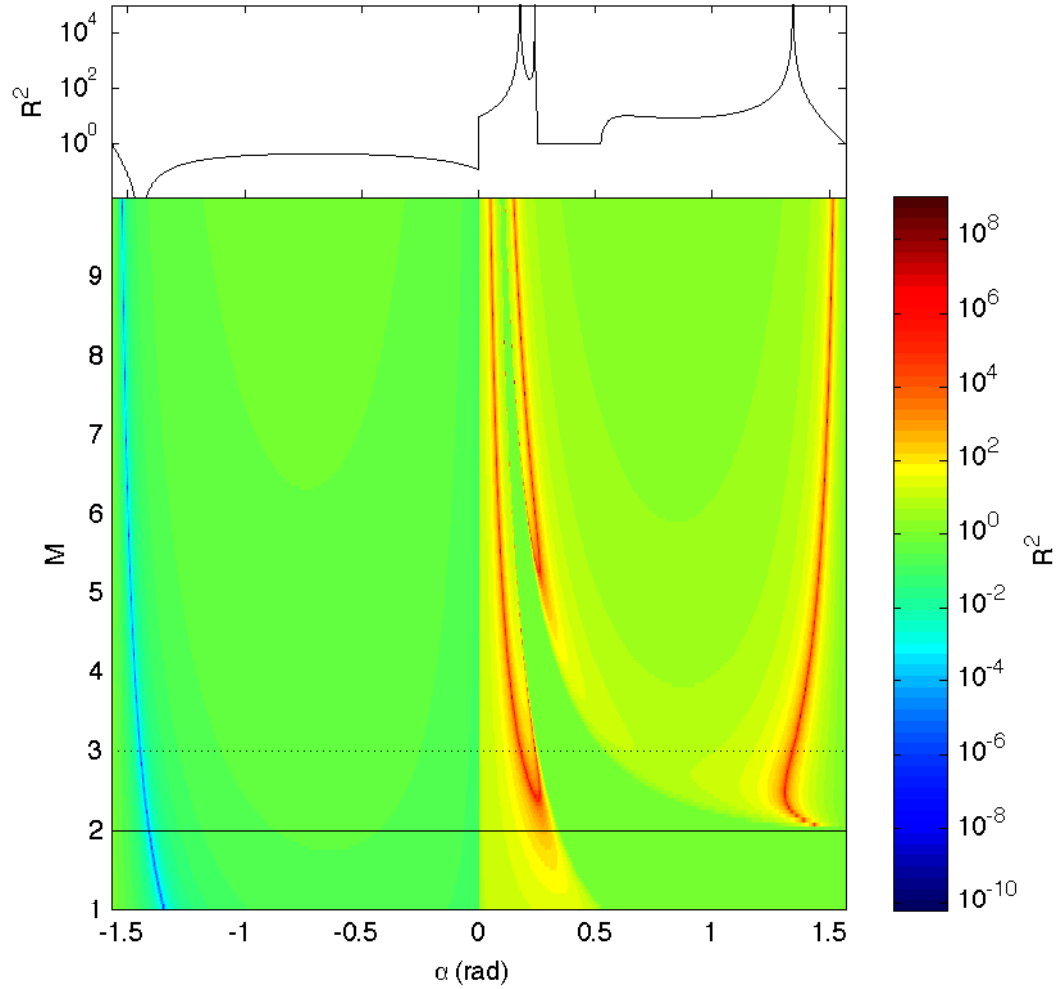
Figure 4.7: Intensity of waves reflected from a shear layer, normalized by intensity of the incoming wave. The lower plot shows intensity R^2 (in color) as a function of angle of incidence α and normalized shear speed M. Angles at which $R^2 = \infty$ first appear at $M = 2$, marked with a solid line. The upper plot reproduces Fig. 3 from [84], showing R^2 as a function of α at $M = 3$, which is marked with a dotted line in the lower plot.

modes in a sphere propagate azimuthally with angular velocity

$$c_p = \frac{\omega}{m},$$ (4.4)

where m is again the order of the mode, i.e., azimuthal wavenumber. Supposing that our apparatus exhibits a shear layer between a region of fluid rotating with the inner sphere and another rotating with the outer sphere, we can write the normalized shear speed as

$$M = m\frac{\Omega_o}{\omega}(\chi - 1)$$ (4.5)

in the rotating frame. Using Eqn. 4.1 and rearranging yields

$$\frac{\omega_{\text{lab}}}{\Omega_o} = \frac{m}{M}(\chi - 1 + M),$$ (4.6)

which, keeping the normalized shear speed M and order m fixed, specifies that the wave frequency goes linearly with χ.

Since Eqn. 4.2 and Fig. 4.7 show that regions of $R^2 = \infty$ first appear at $M = 2$, we use this value as an onset condition and plot a family of lines, one for each m, as shown in Fig. 4.8. The boundary lines correctly predict the onset of inertial modes as observed in our experiments. No induction is possible at $\chi = 1$, where neither shear nor relative motion are imposed on the fluid.[6] For $\chi < 1$, large amplification of inertial modes by over-reflection is possible only on the left side of the boundaries — that is, on the side opposite $\chi = 1$. Consistent with this condition, we observe strong inertial modes immediately left of the boundaries and broadband induction throughout the entire region left of the boundaries.

_____

[6]Unless some other forcing mechanism — such as precession — affects the flow.

The standard deviation of the magnetic field, whose square measures the energy contained in oscillatory flows, is near zero when the shear is zero ($\chi = 1$) and grows sharply when inertial modes arise, again left of the onset boundaries (Fig. 4.8). Plateaus in the deviation correlate with the presence of inertial modes in the spectrogram. Roughly speaking, the deviation grows as the shear increases (or equivalently, as χ differs more and more from unity) until narrowband modes can no longer be discerned ($\chi \approx -0.3$). There the deviation shrinks again, though it does not drop to the low values recorded with near-zero shear. We postulate that in this large-shear region, nonlinear interactions among a large group of inertial modes prevent any one mode from becoming dominant, thus reducing the deviation. The broadband nature of the spectrogram supports our assertion.

For $\chi > 1$, large amplification of inertial modes by over-reflection is possible on the right side of the boundaries. We observe magnetic induction, likely due to inertial modes pumped by over-reflection, in this region as well.

4.2.3   Mode selection by over-reflection

From Eqn. 4.2 and Fig. 4.7, we know that the coefficient of reflection $R(\alpha, M)$ depends not only on the normalized shear speed M but also on the angle of incidence α. When the incident wave is an infinite plane wave of the sort considered in [84] or in Eqn. 2.7, α is the angle between the normal to the shear layer and the constant wave vector $\hat{\mathbf{k}}$. When boundaries are relevant and our interest is in inertial modes, however, the meaning of α becomes less clear because $\hat{\mathbf{k}}$ is no longer a constant.

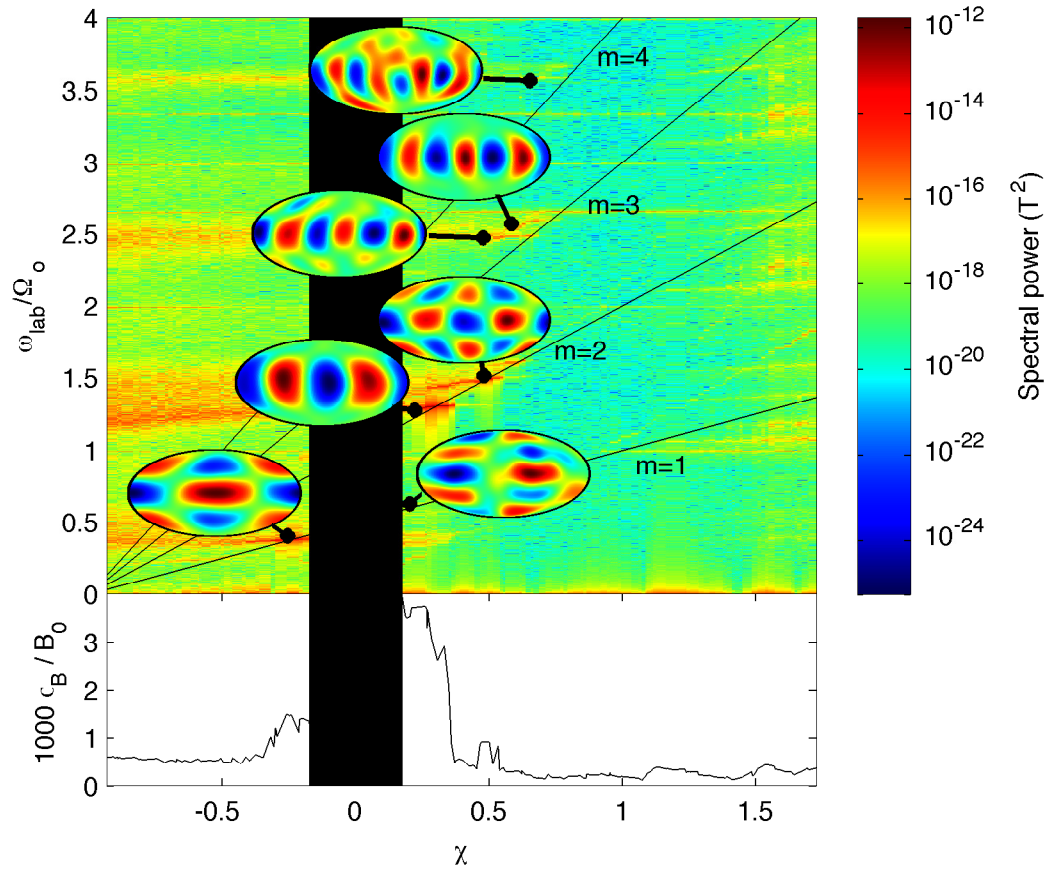Figure 4.8: The same plots shown in Fig. 4.3, with black lines indicating boundaries where the normalized shear speed $M = 2$ for various wavenumbers m. Overlaid are the induction patterns of inertial modes we have identified (Figs. 4.4 and 4.5), with a line connecting each to the region of the spectrogram where the mode appears. A version of this figure better adapted for grayscale printing is included as Fig. D.6.

What angle, if any, controls the reflected intensity of an inertial mode? We shall postulate that it is θ_c, the characteristic angle of the mode.

As described in Chapter 2, each inertial mode has a characteristic angle θ_c, the colatitude at which the Ekman boundary layer erupts and forms a conical shear layer in the bulk of the fluid. The first clue that leads us to associate θ_c with α is the fact that the characteristic angles of the seven inertial modes we have observed all fall within a small range around 1.3 (see Table 4.1), though they might take any angle $-\pi/2 \leq \theta_c \leq \pi/2$. Further, their values coincide with the region of the rightmost critical angle in Fig. 4.7, particularly at low M. It seems possible (though certainly not necessary) that $\theta_c = \alpha$.

Proceeding with this hypothesis, we can calculate the coefficient of reflection $R(\alpha, M)$ for any given inertial mode at any given normalized shear speed M. Constructing a list of all low-order ($l \leq 10$) inertial modes, we have calculated $R(\alpha, M)$ for each mode for $1 \leq M \leq 10$. At each M, some particular mode, which we will call the "strong mode," is reflected most strongly (that is, has the largest $R(\alpha, M)$). The characteristic angle θ_c of each strong mode is plotted as a function of M in Fig. 4.9. We would expect the strong modes to lie near critical angles shown in Fig. 4.7, where $R^2 = \infty$, and they do. What we would not have predicted, however, is the dominance of the rightmost critical angle. The strong modes are rarely in the region of any of the four critical angles in $0 \leq \alpha \leq 0.5$; instead they nearly always lie in the region of the rightmost critical angle —the same region where all seven identified modes (Table 4.1) lie. Thus the results of the calculation are consistent with our experimental observations.
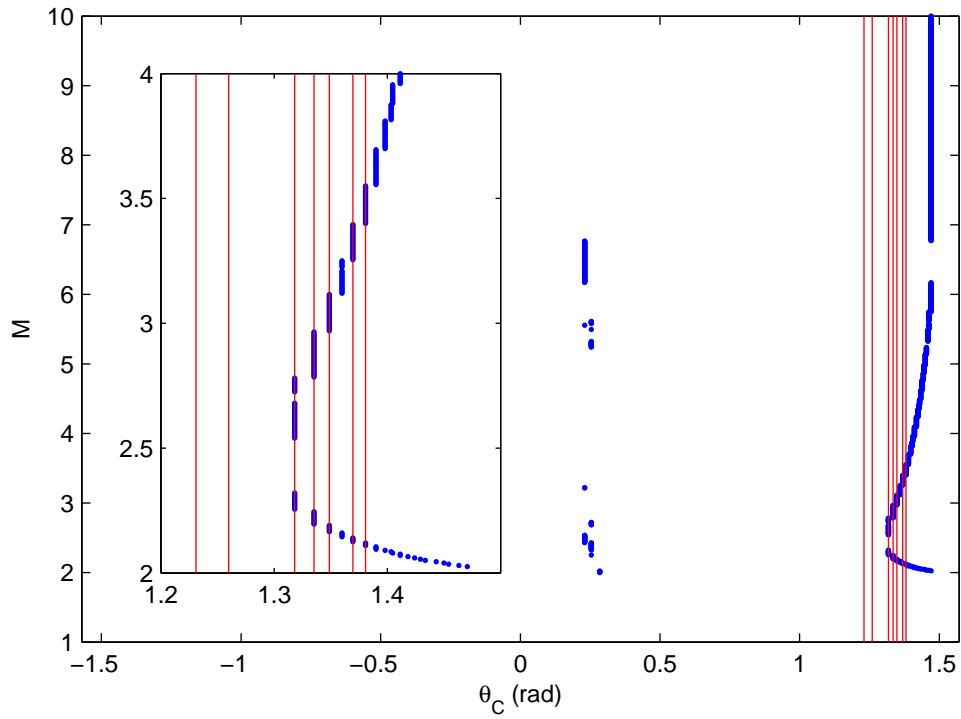
Figure 4.9: Characteristic angle of the most-amplified inertial mode, varying with normalized shear speed. The characteristic angles of the seven inertial modes listed in Table 4.1 are indicated with solid lines, and the inset magnifies the region of our interest. All modes up to $l = 10$ were considered in the calculation.

Figure 4.9 indicates the characteristic angles of the those seven modes with vertical lines.[7] Five of the seven are, for some values of M, the strong mode. In fact, those five are the lowest-order strong modes near $M = 2$. Of the strong modes that appear nearer to $M = 2$ (boxed in Fig. 4.9), one has $(l, m) = (6, 5)$, while all others have $l \geq 7$. The strong mode that appears among the five (circled in Fig. 4.9) has $(l, m) = (7, 0)$. All of these higher order modes are invisible to our Gauss array, which can detect only modes with $l_{mag} \leq 4$. Moreover measurements from any external array will always record weaker signals from higher-order modes, since the magnetic induction they produce goes as $r^{-(l+1)}$ (see Eqn. 2.31). It is not inconsistent, therefore, that we have observed only the lower-order modes; in fact, it agrees with the prediction of [83]. In light of these observations, we would hypothesize that the strong modes plotted in Fig. 4.9 are the first to arise for $M \geq 2$ in a spherical Couette apparatus at low Ekman number. Experiments with direct velocity measurements or a larger Gauss array could prove or disprove our prediction.

Associating θ_c with α can also explain another characteristic of our observations. The inertial modes we observe are segregated into frequency bands, with all modes having azimuthal wavenumber m falling into the particular band $m - 1 \leq \omega_{\text{lab}}/\Omega_o \leq m$. Figure 4.8 makes it most clear. Notice that the identified modes are grouped by m into bands, the over-reflection boundaries apply in bands, and that even the broadband induction at $\chi < 0$ is banded. It need not be so. In the rotating frame, $|\omega/\Omega_o| \leq 2$ for all inertial modes, as required by Eqn. 2.7. The

---

[7]The characteristic angles shown are theoretical, not calculated from experimental frequency observations.

m	Possible	Observed
1	$-1 \leq \omega_{\text{lab}}/\Omega \leq 3$	$0 \leq \omega_{\text{lab}}/\Omega \leq 1$
2	$0 \leq \omega_{\text{lab}}/\Omega \leq 4$	$1 \leq \omega_{\text{lab}}/\Omega \leq 2$
3	$1 \leq \omega_{\text{lab}}/\Omega \leq 5$	$2 \leq \omega_{\text{lab}}/\Omega \leq 3$
4	$2 \leq \omega_{\text{lab}}/\Omega \leq 6$	$3 \leq \omega_{\text{lab}}/\Omega \leq 4$

Table 4.4: Possible and observed inertial wave frequencies, as measured in the laboratory frame.

Galilean transform given by Eqn. 4.1 maps those frequencies to regions that differ according to the order m of the wave, but the regions overlap, as listed in Table 4.4: $m - 2 \leq \omega_{\text{lab}}/\Omega_o \leq m + 2$. The segregation occurs only because all the inertial modes we have identified conveniently have $0 \leq \omega/\Omega_o \leq 1$ in the rotating frame — they are retrograde[8] and slow.

The fact that the inertial modes we observe are retrograde and slow is not a coincidence. Rather, it is a direct consequence of the fact that all have characteristic angles in the region near the rightmost critical angle of Fig. 4.7. Having similar characteristic angles, they must also have similar frequencies, according to Eqns. 2.10 and 4.1. Over-reflection at a shear layer cannot excite inertial modes over the entire range of frequencies $-2 \leq \omega/\Omega_o \leq 2$; it will always give rise to modes that are banded in frequency according to m, as are those in Fig. 4.8. We predict that future spherical Couette experiments will observe inertial modes with characteristic angles (and therefore frequencies) in the same ranges.

---

[8]Again, our convention is $\omega > 0$ for retrograde waves.

4.2.4 Localizing the over-reflection

If the mechanism pumping inertial waves in our apparatus is over-reflection at a shear layer, perhaps next we should ask ourselves (as our collaborator A. Tilgner often asks us!) where, exactly, the responsible shear layer lies. In analytical studies of spherical Couette flow, Stewartson [85] established that small (but finite) differential rotation gives rise to a shear layer, now known as the Stewartson layer, on the cylindrical surface concentric with the axis of rotation and having the same radius as the inner sphere (the "tangent cylinder"), as sketched in Fig. 4.10. In other words, fluid above and below the inner sphere tends to rotate with the inner sphere, while fluid outside that region tends to rotate with the outer sphere, and a shear layer necessarily develops between the two regions of fluid. Stewartson layers are commonly observed in both laboratory and numerical experiments, and it seems natural to think first of the Stewartson layer when seeking a location for over-reflection.

The Stewartson layer is not the only possibility, however. Our hypothesis that over-reflection drives inertial modes requires nothing more than a shear layer between one region of fluid rotating at Ω_o and another at Ω_i. An Ekman boundary layer near the inner or outer sphere could suffice. And as we noted above, associated with each inertial mode is an eruption of the Ekman layer at colatitude θ_c, giving rise to a conical surface in the bulk of the fluid. That conical surface is in fact a shear layer [59]. In the inviscid limit, these free shear layers can become arbitrarily strong [83], and in a spherical shell their reflections can give rise to ray attractors [86, 87]. Similar free shear layers erupt at the inner sphere, as sketched in Fig. 4.10. It
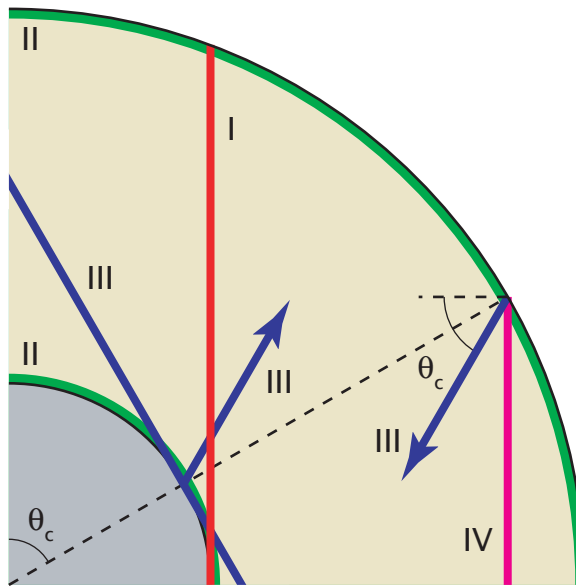
Figure 4.10: Shear layers where over-reflection might pump inertial modes. In this diagram, the axis of rotation is vertical, and only the top, right half of the vessel is shown. The Stewartson layer, at the tangent cylinder, is marked "I" and sketched in red. Ekman layers at the boundaries are marked "II" and sketched in green. Free shear layers erupting at colatitude θ_c from the inner and outer sphere are marked 'III" and sketched in blue. Busse's cylindrical shear layer, vertical at θ_c, is marked "IV" and sketched in magenta.

may be that a free shear layer associated with eruptions from an axisymmetric inertial mode is the location of over-reflection in our apparatus.

One more set of possible shear layers deserves mention. When the axis of rotation of a spinning body changes its direction periodically, the body is said to "precess." For example, Earth spins about its axis with a period of one day, but also the direction of its axis rotates with a period of 25,765 years. Hence Earth precesses, and Polaris is not always aligned with geographic north. In any oblate spheroid filled with inviscid fluid (of which a sphere is a special case), precession causes a motion known as the spin-over mode [88], which is in fact the inertial mode having $(l, m, \omega/\Omega) = (2, 1, 1)$. The spin-over mode has characteristic angle $\theta_c = \pi/3 = 60°$. Taking viscosity and first-order nonlinearity into account, Busse [89] performed an asymptotic analysis of a precessing, oblate spheroid to predict that an axial, cylindrical shear layer arises at colatitude θ_c, as sketched in Fig. 4.10. Extending Busse's work, Hollerbach and Kerswell [90] made a numerical study of nonlinear flows induced by the spin-over mode, finding not just Busse's shear layer, but a complicated, nested family of cylindrical shear layers. In at least one experimental study, researchers found Busse's shear layer, but not the nested layers of Hollerbach and Kerswell, in a laboratory experiment [80].

The 60 cm apparatus detailed in this dissertation was not designed to study precession, and has no mechanical device for changing the direction of the spin axis. The direction of its spin axis does rotate, however, because the apparatus is Earth-bound. Likewise the 3 m spherical Couette apparatus that is the work of our colleagues D. S. Zimmerman and S. A. Triana precesses only because of

Earth's rotation, not by design. Recent observations in that apparatus, however, show the clear presence of the spin-over mode. Moreover, its direction and strength are consistent with forcing by daily precession; these results will be published soon. Given the presence of spin-over, we immediately expect Busse's shear layer at θ_c. If diurnal spin-over also plays a role in the 60 cm apparatus, the same shear layer would arise, and would constitute another candidate for the location of pumping by over-reflection.

Hence there are at least four reasonable locations for pumping by over-reflection: the Stewartson layer at the tangent cylinder, an Ekman boundary layer, a free shear layer associated with an axisymmetric inertial mode, and Busse's shear layer arising from precession. Probably all are present in our apparatus, though with different strengths. Free shear layers and Busse's shear layer are driven by secondary, viscous effects in the fluid, and therefore we expect them to be relatively weak. The Stewartson and Ekman layers are both driven directly by mechanical forcing of the boundaries. Past numerical and experimental observations (e.g., [80, 81, 90]) have found the Stewartson layer to have considerable effect on spherical Couette flow, causing us to hypothesize that the Stewartson layer is the location of energy transfer from shear to inertial modes via over-reflection. We hope that future experiments in our 60 cm apparatus, in the 3 m apparatus, or in some other system will prove or disprove this claim by measuring velocities directly.

4.3   Zonal flows

Having made a case that we have observed and identified inertial modes, which are the linear eigenmodes of our inviscid, rotating fluid, we move on to consider behaviors that involve viscosity and nonlinearity in $\mathbf{u}$.[9] With a copper inner sphere, the most striking nonlinearity is the presence of strong zonal flows.

Even at low Ekman numbers, where inertial waves are prominent in our data, the modes do not explain all the induction we observe. Above we mentioned in passing that the means have been removed from the signals plotted in Figs. 4.1, 4.4, and 4.5. Removing the means is useful for emphasizing the oscillatory (wave) component of the signal, and it is easier to remove the means than to preserve them by carefully removing probe and magnetic biases as described in Chapter 3. Without the means, however, our story is incomplete. Figure 4.11 gives an example, showing the same data both with and without the mean induction. The means have significant amplitude, often larger than the waves themselves. In our measurements, non-oscillatory (steady) signals necessarily indicate axisymmetric ($m = 0$) induction because the vessel rotates while the probes do not, and from Table 3.6 we know that axisymmetric induction arises from axisymmetric flows, either toroidal ($\mathbf{T}_l^0$) or poloidal ($\mathbf{S}_l^0$). Toroidal flows of this sort, both non-oscillatory and axisymmetric, are often called "zonal" flows in the literature. They are a subset of the "geostrophic" flows, steady flows in which only pressure forces and Coriolis forces are appreciable.

---

[9]Effects of the Lorentz force do not yet become appreciable — we will re-visit this issue in Chapter 5.

Zonal flows are commonly observed to have large amplitude in rotating laboratory experiments and numerical simulations (e.g, [71, 72, 91, 92]), and so our observations of large, steady induction are consistent with much past work. The amplitude and structure of the zonal flows we observe is reproducible at various E (or various Ω_o), and like our inertial modes, is controlled primarily by the rotation rate ratio χ; see Fig. 4.12. One interesting feature of the data is that the zonal modes reach a local maximum at $\chi = 1$, where $\Omega_i = \Omega_o$ and no shear is imposed. We would expect little or no flow at $\chi = 1$; that the axisymmetric induction is actually at a maximum deserves further study.

The precise mechanism which gives rise to zonal flows, however, is a matter of some complexity. Though an infinite number of $m = 0$ inertial modes are possible in a sphere, Eqn. 4.4 asserts that they propagate at infinite speed, implying that a shear layer with $M > 2$ is impossible for $m = 0$ modes. Hence over-reflection cannot excite axisymmetric inertial waves. What then drives the axisymmetric flows we observe? Studying similar data, previous researchers have asked the same question. In the linear, inviscid problem we know that all flows can be represented as superpositions of inertial modes, and that those modes cannot interact linearly (see Chapter 2). Thus the axisymmetric flows in our experiments either are not inertial waves or are inertial waves that arise through viscosity and/or nonlinearity in $\mathbf{u}$. To understand them better, we consider the asymptotic case of weak nonlinearity.

For weakly nonlinear flows (small Re, or equivalently, small χ), it is possible
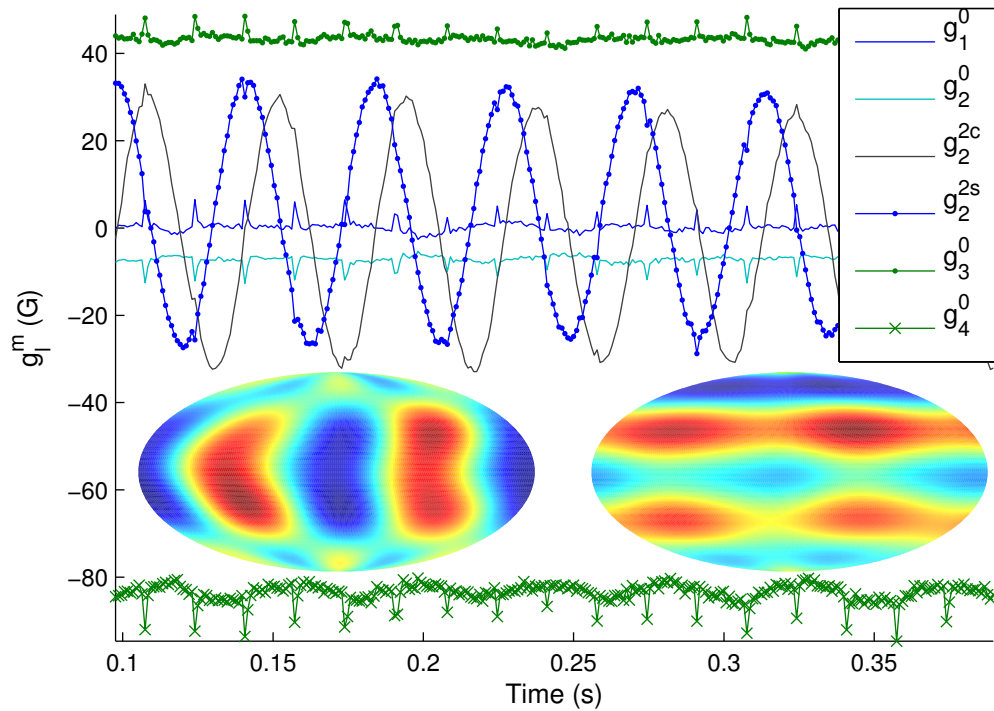
Figure 4.11: Signature of an inertial mode, with and without mean induction. A few Gauss coefficients g_l^m are plotted over time, showing oscillatory signals characteristic of a travelling wave in g_2^2 as well as large DC induction in the axisymmetric modes g_l^0. The left inset shows a snapshot of the induction at the surface, with means subtracted. The right inset shows the same snapshot, with mean induction retained. A version of this figure better adapted for grayscale printing is included as Fig. D.7.

Figure 4.12: Typical induction due to axisymmetric zonal flows. Each data point is the mean of 32 s of data, sampled at 1024 Hz. Here $E = 7.26 \times 10^{-8}$ ($\Omega_o / 2\pi = 18$ Hz).

to expand the velocity field in a perturbation analysis

$$\mathbf{u} = \mathbf{u}_0 + \epsilon \mathbf{u}_1 + \epsilon^2 \mathbf{u}_2 + \ldots, \tag{4.7}$$

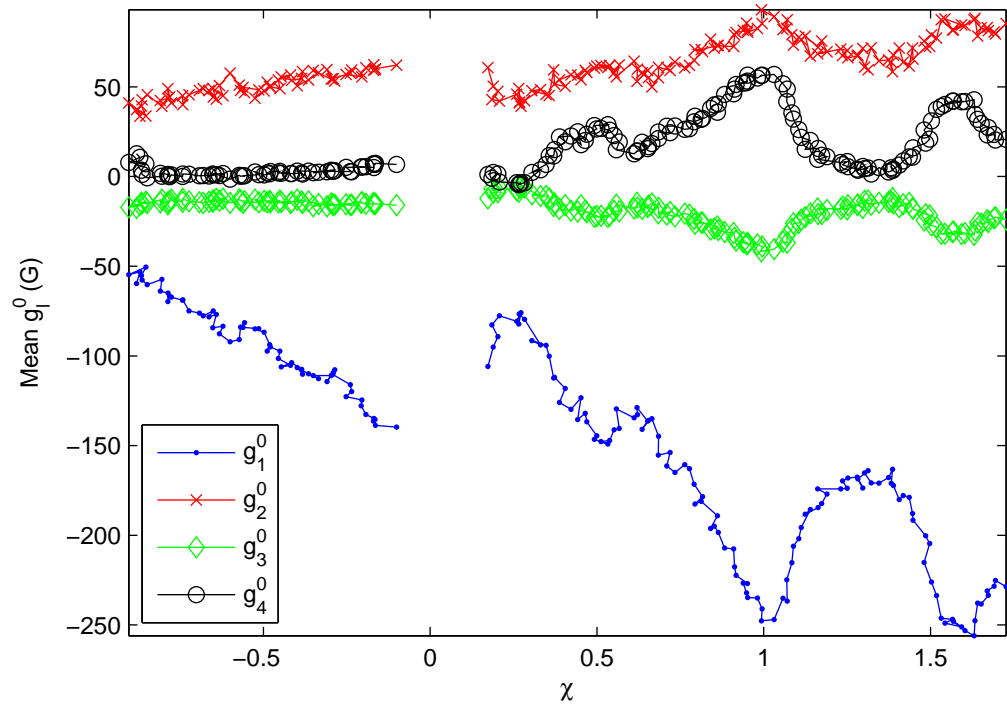in which ϵ measures the nonlinearity and is small. Proceeding with the analysis it is possible to show that first-order nonlinear interactions of inertial waves exchange energy among three waves and can occur if and only if

$$l_1 \pm l_2 \pm l_3 = 0, \tag{4.8}$$

$$m_1 \pm m_2 \pm m_3 = 0, \tag{4.9}$$

$$\omega_1 \pm \omega_2 \pm \omega_3 = 0, \tag{4.10}$$

where the three interacting waves are labelled 1, 2, and 3 [52, 93]. These behaviors are commonly called "triad interactions" in the literature. Triad interactions allow for a great many phenomena and have central importance in the inverse cascade often observed in rotating turbulence [94, 95]. Performing an expansion like the one above, Greenspan [96] has shown analytically that triad interactions in a full sphere of inviscid fluid cannot amplify axisymmetric inertial waves. However, no such mathematical assertion can be made in a spherical shell, nor when viscosity and/or higher-order nonlinear interactions are taken into account. In fact, the inclusion of viscosity and nonlinearities in numerical experiments seems to give rise to zonal flows in a wide variety of situations, suggesting that the phenomenon may be universal [92]. We would suppose, then, that the large zonal flows present in our apparatus arise through the same combination of viscosity and nonlinearity that seems so common in rotating fluids.

Chapter 5

Results with soft iron inner sphere

In this chapter we continue the description of our experimental results, focusing on behaviors observed with a soft iron inner sphere, which provides ferromagnetic boundary conditions like those of VKS2 [8] and the Lowes and Wilkinson dynamos [4, 5]. We begin with a brief discussion of the physics of ferromagnetic boundaries and, in simplest terms, how they affect a flowing, conductive fluid. Continuing, we discuss the issue of soft iron as it relates to the complicated flows present in an apparatus like our own or like VKS2, drawing from past numerical and experimental results. We detail our own results, first documenting observations of inertial modes, which closely resemble the observations described in Chapter 4. The modes co-exist with a more broadband background signal, however, which is consistent with the physics of ferromagnetic boundaries. We conclude the chapter with an overview of other experimental results in our apparatus and how they depend on the control parameters E, χ, and S (or, equivalently, Ω_o, Ω_i, and B_0), comparing to similar experiments with a copper inner sphere.

5.1   The physics of ferromagnetic boundaries

What can simple arguments from electomagnetic theory say about the effects of ferromagnetic boundaries on a hydromagnetic flow? First, from Ampere's law

(Eqn. 2.13) and Stokes's theorem (Eqn. A.6), we know that magnetic fields at a boundary are governed by

$$\left(\frac{\mathbf{B}_1}{\mu_1} - \frac{\mathbf{B}_2}{\mu_2}\right) \times \hat{\mathbf{n}} = \mathbf{K}_f \tag{5.1}$$

where $\hat{\mathbf{n}}$ is a unit vector normal to the boundary, $\mathbf{K}_f$ is the free surface current, and subscripts 1 and 2 label the two sides of the boundary. By definition, the free surface current $\mathbf{K}_f$ must have zero thickness. In a macroscopic, physical system, Ohmic diffusion always thickens currents, so for our purposes, $\mathbf{K}_f = 0$. Accordingly,

$$\mathbf{B}_1 \times \hat{\mathbf{n}} = \frac{\mu_1}{\mu_2}\mathbf{B}_2 \times \hat{\mathbf{n}}. \tag{5.2}$$

If $\mu_2 = \infty$, the right-hand side becomes zero and thus the tangential component of the magnetic field in region 1 must also be zero. To say it differently, with a perfect ferromagnet in region 2, the field in region 1 is always normal to the boundary. For soft iron, $\mu \sim 1000\mu_0$ (see Table 3.3), so that the field can be well approximated as normal to the boundary.

Second, we know that the energy stored per unit volume in a magnetic field is

$$\mathcal{E} = \frac{B^2}{2\mu}.$$

In order to minimize total energy, a physical system will tend to concentrate its magnetic fields in regions where μ is large. Since field lines neither begin nor end ($\nabla \cdot \mathbf{B} = 0$), regions adjacent to regions of large μ — for example, fluid near a soft iron boundary — also experience amplified fields.

Strong, local magnetic fields change the force balance that governs fluid flow, as specified by the Navier-Stokes equation. Its dimensionless form was first given in

Eqn. 2.40:

$$\frac{\partial \mathbf{u}'}{\partial t'} + \chi\zeta\left(\mathbf{u}' \cdot \nabla'\right)\mathbf{u}' = -\frac{1}{\chi\zeta}\nabla'P' + E\nabla'^2\mathbf{u}' + \frac{E^2 S^2}{\chi\zeta Pm^2}\left(\nabla' \times \mathbf{B}'\right) \times \mathbf{B}' - 2\left(\mathbf{\Omega} \times \mathbf{u}\right).$$

In Chapter 2 we showed that the inertial waves solve this equation in the special case where the nonlinear term, the viscous term, and the Lorentz force term can all be neglected. In Chapter 4 we took interest in zonal flows, which cannot gain energy in the linear and inviscid case but rather require viscosity and nonlinearity. Now, considering the effects of a soft iron inner sphere, we require the Lorentz force term as well. Using $E = 10^{-7}$, $S = 4$, $\chi = 1$, $\zeta = 0.328$, and $Pm = 8.9 \times 10^{-6}$ (see Table 3.1), we find that its prefactor is of order 1/100. The Lorentz force begins to rearrange the flow when $\mathbf{B}/\mathbf{B}_0 \sim 10$ locally, a situation unlikely to arise without dynamo action if the boundaries are insulating or conductive. With ferromagnetic boundaries concentrating the magnetic field, however, it may not be possible to neglect Lorentz forces.

5.2   Past observations and predictions

Our naïve arguments suggest that ferromagnetic boundaries will change the dynamics of a hydromagnetic system by causing the magnetic field to be normal to the boundary and by locally strengthening the field. A number of past studies have explored the effects of soft iron boundaries in more detail. Lowes and Wilkinson did not observe dynamo action with any apparatus having conductive boundaries, but did observe it after constructing an apparatus using Perminvar ($\mu \approx 250$) [4]. In a later apparatus, they observed oscillatory behaviors and field reversals as well, again

requiring a ferromagnetic boundary (annealed mild steel, $\mu \approx 150$) [5]. Noting that only the product $\mu\sigma$ enters the feedback equations, and never μ alone, the authors argued that using ferromagnetic boundaries was equivalent to using boundaries of increased conductivity, and therefore did not preclude direct comparisons between their laboratory model and the core of the Earth. They did not address the change in boundary conditions described above, however.[1]

A later experiment in our own lab also emphasized the importance of electromagnetic boundary conditions. In spherical Couette experiments, Sisan [70] found that the nature of the observed magnetic instabilities depended on boundary conditions. Driving those instabilities required twice as much torque with a solid copper inner sphere as with a copper spherical shell, and five times as much torque as with a stainless steel spherical shell. The study did not address ferromagnetism, however.

The success of the Riga and Karlsruhe devices in producing dynamo action motivated a numerical study of boundary conditions by Avalos-Zuniga *et al.* [97]. It disagreed with Lowes and Wilkinson, finding that changing the permeability of the boundaries had different effects than changing the conductivity of the boundaries. Adding a ferromagnetic layer outside the main flow always decreased the dynamo threshold Rm_c, thus encouraging dynamo action. Increasing boundary conductivity or increasing the thickness of a conductive boundary, however, did not affect the dynamo threshold of an oscillatory dynamo in a monotonic way. Rather, the authors found an optimal thickness for a given conductivity. Accordingly, the Karlsruhe

---

[1]When we solve differential equations, the boundary conditions can affect the character of the solution just as dramatically as the form of the equations themselves!

dynamo was constructed with rigid walls of optimal thickness. The researchers who built the Riga dynamo took a different approach, surrounding the main flow with a layer of stationary sodium. Since sodium is a good conductor, this technique encourages dynamo action via the same mechanism as thickening the rigid, conductive boundaries.

The first dynamo built in Cadarache, known in hindsight as VKS1, did not achieve either dynamo action or magnetic Reynolds numbers high enough to expect dynamo action, according to numerical modelling [98]. Given these findings, the VKS team engaged in further numerical study to optimize their apparatus. They made plans to surround their main test section with a stationary layer of sodium, as had been done in Riga. They also constructed improved impellers which were carefully tuned to produce the proper ratio of poloidal to toroidal flow [99].

The VKS2 apparatus implemented these improvements, but did not initially display dynamo action. A further study, making use of new numerical techniques that allowed for more realistic (not periodic) boundary conditions, led to an unpleasant surprise: the layers of sodium between the impellers and the ends of the test section *increased* the dynamo threshold, hindering dynamo action [100]. With stationary fluid, the increase was 12%. (This finding, based on calculations approximating the stationary, mean flow of VKS2, differed with the previous conclusions of Avalos-Zuniga *et al.* [97], who found that thicker conductive boundaries always lowered Rm_c in a stationary flow.) Worse still, the presence of flowing sodium behind the impellers was found to increase the dynamo threshold to 250% of its original value, eliminating any possibility of dynamo action in the VKS2 apparatus. Un-

able to remove the fluid behind the impellers, the VKS team found themselves at a quandary. After some deliberation, they decided to remove their stainless steel impellers and use ferromagnetic, soft iron impellers instead, hypothesizing that the ferromagnetic boundaries would provide magnetic shielding from the negative effects of the fluid behind the impellers. Dynamo action was observed soon thereafter [8].

Ongoing discussions of the precise effects of ferromagnetic boundary conditions on hydromagnetic flows ensued. Our experiments (suggested by J.-F. Pinton, a member of the VKS team) are directly motivated by the question of ferromagnetism. Experiments with the VKS2 apparatus continue as well. One recent numerical study [101] considered a variety of relevant boundary effects: insulating boundary conditions, stationary sodium on the side of the cylinder, stationary sodium behind the impellers, ferromagnetic impellers, and ferromagnetic walls. Consistent with previous work [99], it concludes that stationary sodium on the side of the cylinder lowers the dynamo threshold, while stationary sodium behind the impellers raises it. Ferromagnetic impellers lower the dynamo threshold, and ferromagnetic walls lower it further. Notably, the authors point out that ferromagnetic impellers lower the dynamo threshold more than simply removing any stationary sodium from behind the impellers. Soft iron impellers have physically different effects than the simple shielding hypothesized by the VKS2 team.

Another recent numerical study suggests that the ferromagnetic impellers may be responsible for the global structure of the magnetic field produced by VKS2. The mean flow induced in VKS2 is (nearly) axisymmetric, and by Cowling's theorem [27] (see Chapter 1), an axisymmetric flow cannot produce an axisymmetric magnetic

109

field. Nonetheless, a large axisymmetric component is observed in the real field, and its presence has previously been attributed to turbulent motions that are not part of the mean flow [102]. However, non-axisymmetric motions do occur in the mean flow in the small regions between the impeller blades. Laguerre *et al.* [103] found in their simulations that those small regions become important when the impellers are ferromagnetic. Thus the axisymmetry of the flow is effectively lost, and the ferromagnetic boundary condition is responsible for the global structure of the induced magnetic field.

Much remains to be understood about the effects of ferromagnetic boundaries on hydromagnetic flows. Soft iron consistently lowers the dynamo threshold of a system. It may also change the global structure of any resulting dynamo, and certainly changes the strength and shape of the magnetic field locally. Recent years have seen great progress in simulating hydromagnetic systems with cylindrical geometries, but real difficulties remain [100]. Simulating a spherical geometry is much more straightforward and provides motivation to undertake experiments with soft iron in our apparatus. At least one study of the effects of ferromagnetic boundaries on conductive fluid in a spherical shell is in progress (by C. Guervilly *et al.*), and we await its publication enthusiastically. In the mean time, we present our experimental observations here.

5.3 Inertial modes

First, an overview: We observe inertial modes in our apparatus with a soft iron inner sphere, just as we do with a copper inner sphere. Many of the same modes are present, but the modes can be more difficult to identify with certainty because their induction patterns are not as clean. The modes are somewhat weaker than they are with a copper inner sphere, and they coexist with broadband background induction that is much stronger than with copper. Onset boundaries inferred from the physics of over-reflection at a shear layer (see Chapter 4) still agree well with our data. Because the modes we observe are a subset of those observed with a copper inner sphere, the mode selection hypotheses developed in Chapter 4 are also still valid.

Now we present data to support our overview. A few typical time traces indicating inertial modes, taken from an equatorial probe during experiments at $E \ll 1$ (large Ω_o), are shown in Fig. 5.1. The signals are oscillatory and wave-like, though even a cursory glance shows that they contain a broader range of frequencies than the corresponding data recorded with a copper inner sphere (Fig. 4.1). Their frequencies are shown more clearly in Fig. 5.2, which gives spectra. A collection of frequency peaks, some narrow and others broader, rise out of the background spectra. The peaks do not rise as far, however, as the corresponding peaks shown in Fig. 4.2, recorded with a copper inner sphere. With a soft iron inner sphere, the dominant peak exceeds other peaks by perhaps an order of magnitude, but rarely more, and sometimes less. With a copper inner sphere, the dominant peak often

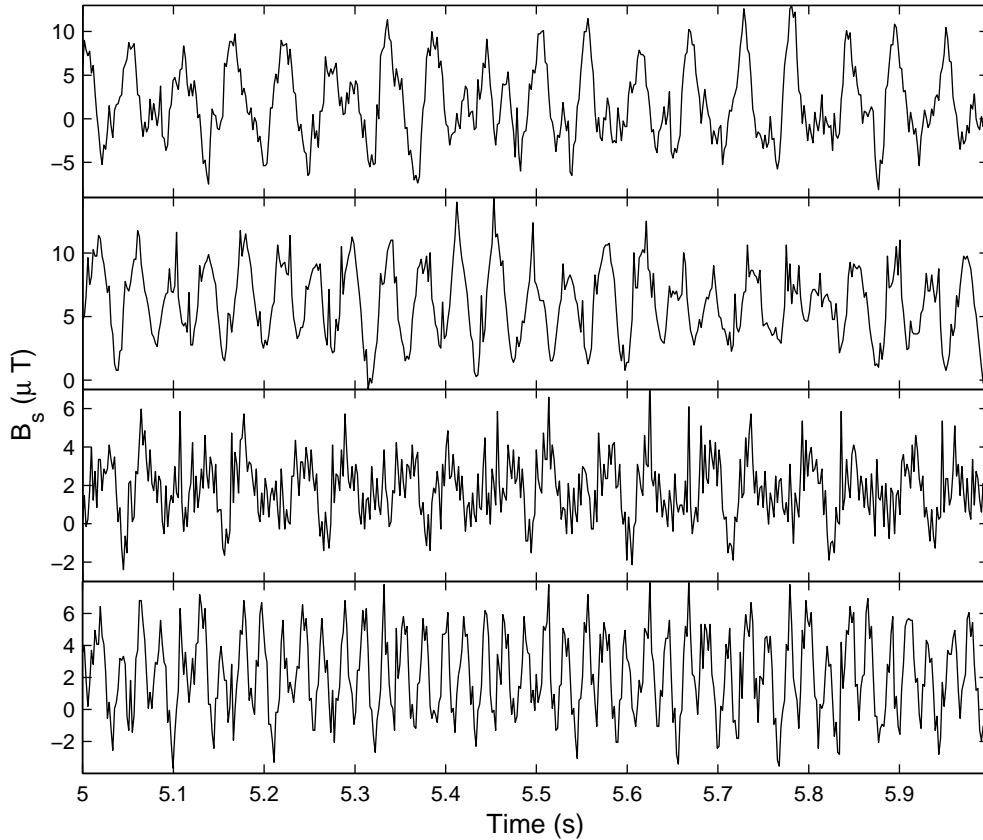exceeds all other peaks by three orders of magnitude.

Figure 5.1: Typical B_s time traces when E is small, with soft iron inner sphere. Only the oscillating component is shown, i.e., the means have been removed. For all data shown here, $E = 7.30 \times 10^{-8}$ and $S = 0.76$ ($\Omega_o/2\pi = 17.9$ Hz and $B_0 = 70.9$ G). From top to bottom, $\chi = -0.350$, 0.351, 0.593, and 0.669 ($\Omega_i/2\pi = $ -6.27, 6.28, 10.62, and 11.98 Hz). Compare to Fig. 4.1.

These spectral peaks, though weaker than the ones we observe with a copper inner sphere, can still be attributed to the presence of inertial modes. Clearly some sort of anisotropic behavior is manifesting itself; these are not the power-law spectra of isotropic, homogeneous turbulence. More to the point, Fig. 5.3 shows a spectrogram recorded in an experiment maintaining $E = 7.0 \times 10^{-8}$ ($\Omega_o/2\pi = 18$ Hz) and varying χ (Ω_i). As the rotation rate varies, spectral power shifts from
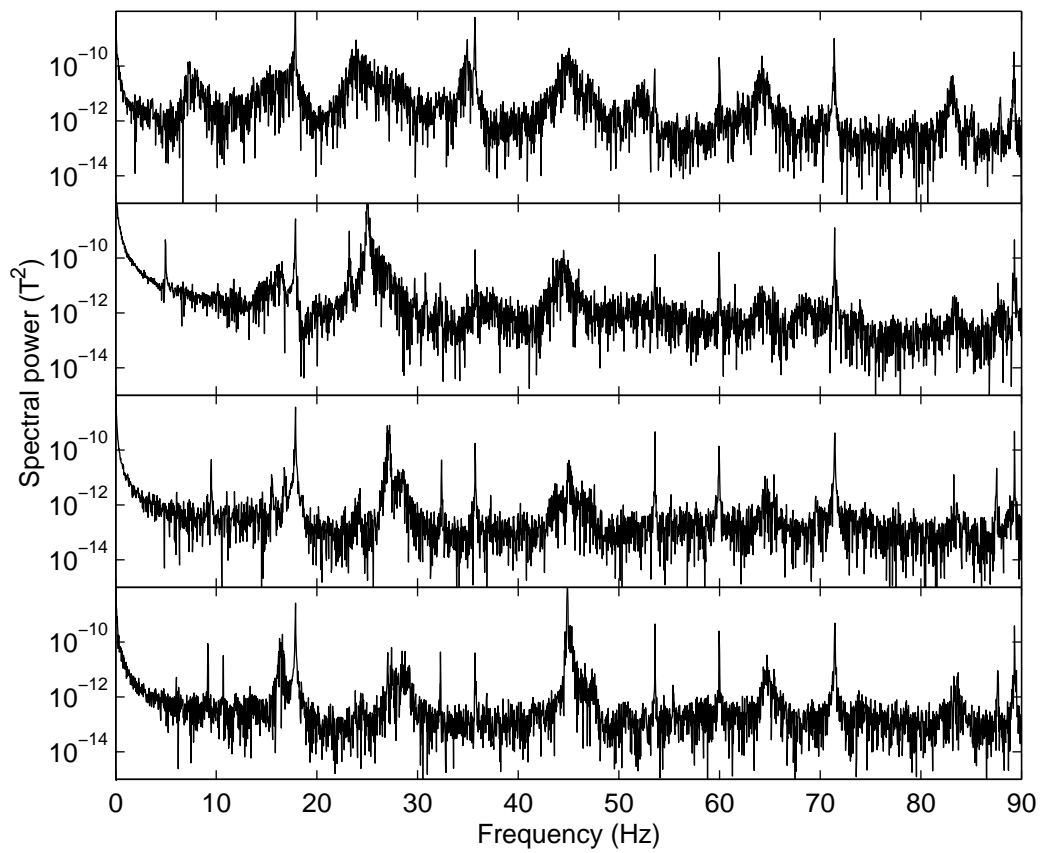
Figure 5.2: Power spectra of the data shown in Fig. 5.1. Compare to Fig. 4.2.

broadband induction to narrowband peaks, displayed in brighter shades. The peaks occur at the same rotation rate ratios χ and the same frequencies $\omega_{\text{lab}}/\Omega$ as the inertial modes identified previously (compare to Fig. 4.8). Furthermore the peaks again correspond to the strongest oscillations we have observed, as evidenced by the standard deviation, plotted below the spectrogram. Finally, the peaks align with the $M = 2$ onset boundaries predicted by over-reflection. We are thus led to believe that the spectral peaks again indicate the presence of inertial modes, and that those modes are again pumped by over-reflection (see Chapter 4). Also, since the same modes appear with a ferromagnetic boundary that appeared with a conductive boundary, the details of the electromagnetic boundary condition must not be important for mode selection. Our hypothesis that it is governed by the gain R^2 during amplification by over-reflection (as shown in Fig. 4.7) is consistent with our observation of the same modes, whether the inner boundary is copper or soft iron.

We can go a little further. To make a positive identification of an inertial mode, we need to know its degree l, order m, and frequency ω/Ω_o. Our Gauss array (see Chapter 3) makes the task almost trivial. Each Gauss coefficient $g^m_{l_{mag}}$ is a measure of the magnetic induction with degree $l_{mag}{}^2$ and order m. Calculating its spectrum, we can seek peaks and compare their frequencies to the frequencies of inertial modes with degree l and order m, which are analytically known. One result of this sort of analysis is Fig. 5.4, which shows spectra of Gauss coefficients taken from the same data first shown in Fig. 5.1. Notice that each spectral peak appearing

---

^{2}Recall $l_{mag} = l \pm 1$; see Table 3.6.
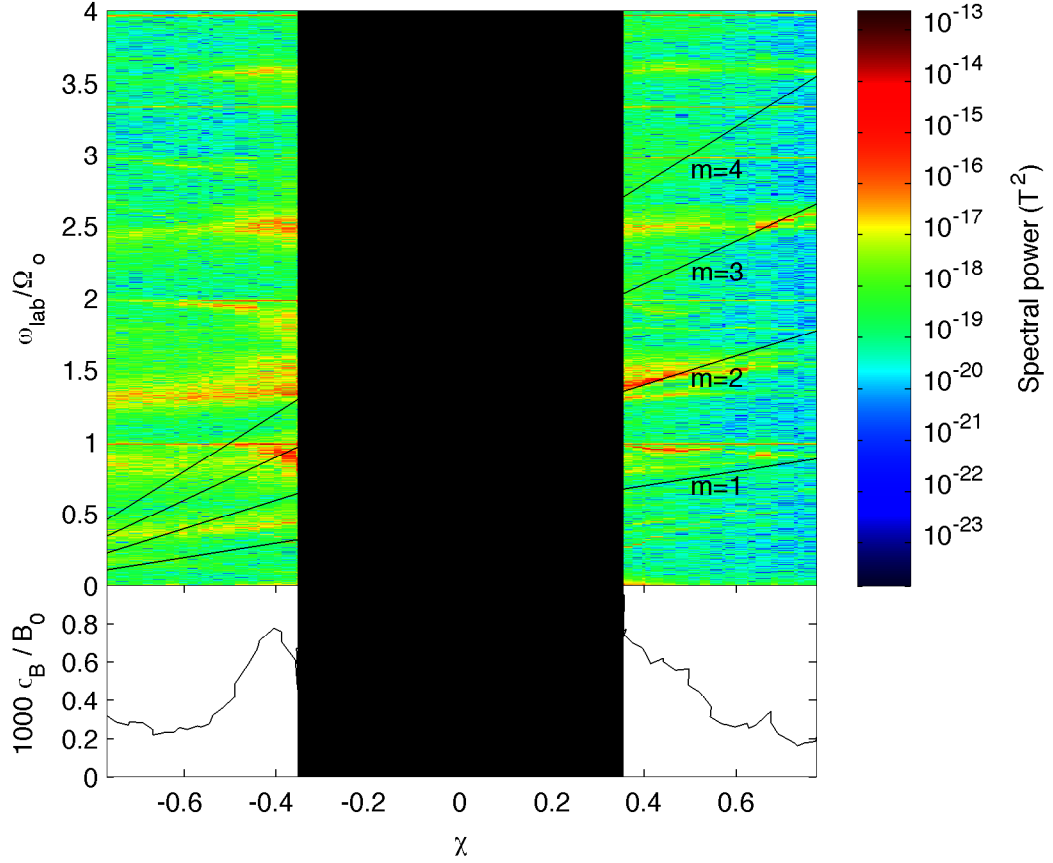
Figure 5.3: Spectrogram and standard deviation of magnetic induction, showing inertial modes, with soft iron inner sphere. The upper plot is a spectrogram, with its vertical axis showing the normalized signal frequency $\omega_{\text{lab}}/\Omega_o$ as measured in the laboratory frame, and its horizontal axis showing the rotation rate ratio χ. Here $E = 7.26 \times 10^{-8}$ ($\Omega_o/2\pi = 18$ Hz). Each column of pixels is a power spectrum of 32 s of data. The varying shades indicate spectral power, and black lines indicate boundaries where the normalized shear speed $M = 2$ for various wavenumbers m. The black central region lies at low speeds inaccessible with our AC motors. The lower plot shows the standard deviation of the same data, normalized by the applied magnetic field B_0. Compare to Fig. 4.3. A version of this figure better adapted for grayscale printing is included as Fig. D.8.

in Fig. 5.4 also occurs in the spectra calculated from a single probe (Fig. 5.2), but the converse is not true — by sorting the induction according to $g^m_{l_{mag}}$ we have separated its spatial components, disentangling our spectra and simplifying their interpretation. To state it mathematically, this is an orthogonal decomposition of the magnetic induction in three dimensions (l, m, and ω). The agreement between spectral peaks and inertial modes predicted by theory, as summarized in Table 5.1, further supports our assertion that inertial modes are again present with a soft iron inner sphere.
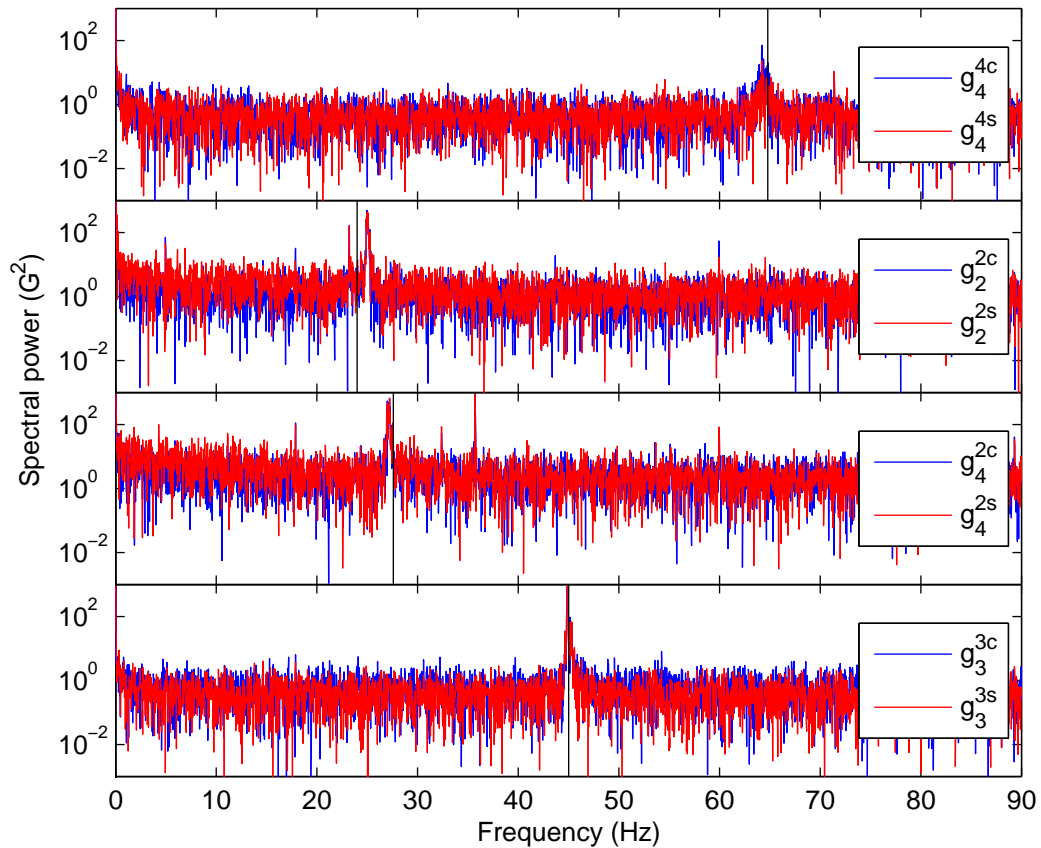

Figure 5.4: Spectra of selected Gauss coefficients, taken from same data as plotted in Figs. 5.1 and 5.2. Vertical lines indicate frequencies where inertial modes are predicted by theory; see Table 5.1.

116

	Experiment			Theory			
l_{mag}	l	m	ω/Ω_o	l	m	ω/Ω	θ_c
4	5	4	0.432	5	4	0.400	1.369
2	3	2	0.613	3	2	0.667	1.231
4	5	2	0.488	5	2	0.467	1.335
3	4	3	0.505	4	3	0.500	1.318

Table 5.1: Experimental and theoretical characteristics of inertial wave modes with a soft iron inner sphere. Experimental frequencies are taken from the same data shown in Figs. 5.1, 5.2, and 5.4. By convention, waves with $\omega > 0$ are retrograde.

This technique — comparing the spectra of Gauss coefficients to analytical predictions — also allows for automated identification of inertial modes in large data sets. Figure 5.5 plots the degree, order, and frequency of the strongest inertial mode present (if any mode is present) during each 32 s of data in two experiments, one with a copper inner sphere and one with a soft iron inner sphere, both at $E = 7.26 \times 10^{-8}$ ($\Omega_o/2\pi = 18$ Hz). The actual modal frequencies differ slightly from their theoretical values here as in Tables 5.1 and 4.1. At a given χ, the same mode is often present regardless of the boundary condition at the inner sphere. When they differ, modes with a soft iron inner sphere tend to favor lower frequencies, especially the $(l, m, \omega/\Omega_o) = (1, 1, 0)$ mode. Its characteristic angle $\theta_c = \pi/2$ is near the most-amplified mode for many values of χ (see Fig. 4.9); thus its presence seems reasonable.

The Gauss coefficients $g_{l_{mag}}^m$ also allow for easy calculation of the magnetic induction at the surface of the test fluid via Eqn. 2.33. Figure 5.6 shows the results of such calculations for the same data first shown in Fig. 5.1. In contrast to equivalent

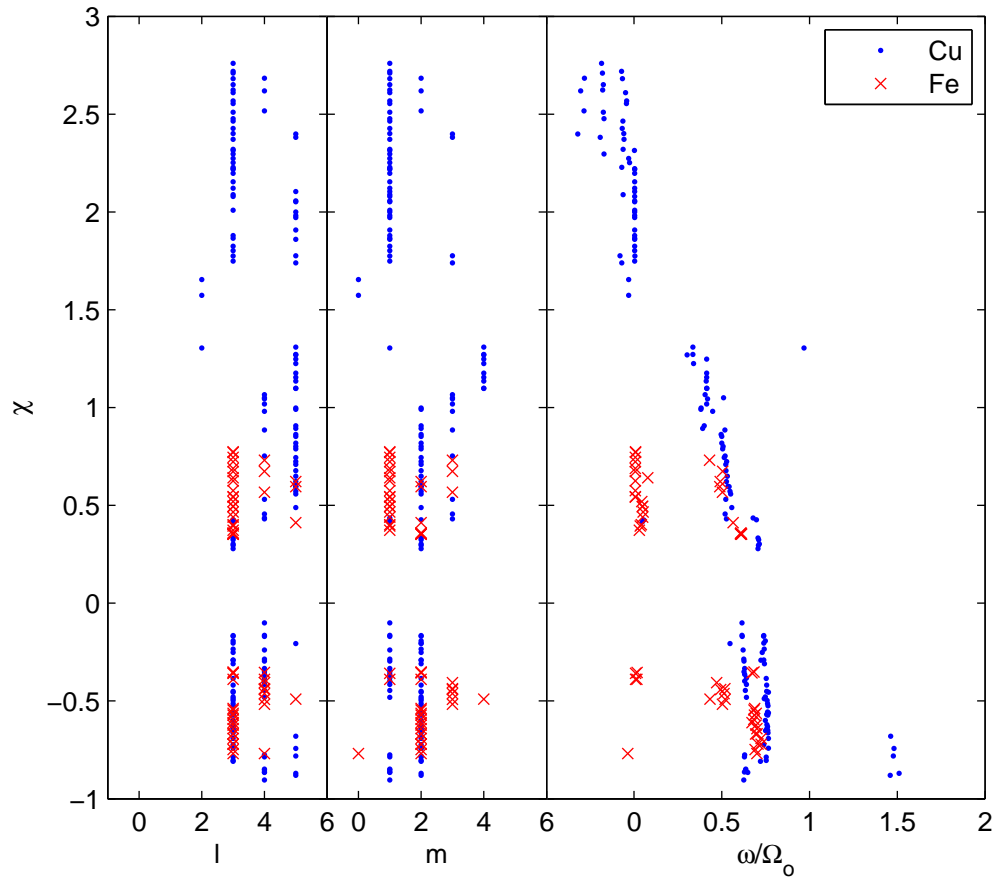Figure 5.5: Degree, order, and frequency of the strongest inertial mode, as a function of rotation rate χ. Data recorded with a copper inner sphere are marked with dots; data recorded with a soft iron inner sphere are marked "x". Here $B_0 = 123$ G for the copper inner sphere and $B_0 = 71$ G for the soft iron inner sphere. $E = 7.26 \times 10^{-8}$ ($\Omega_o/2\pi = 18$ Hz) for both experiments.

plots made from data recorded with a copper inner sphere (Figs. 4.4 and 4.5), these images do not make the degree and order of the primary wave mode immediately apparent. Their noisy composition again implies that the presence of a soft iron inner sphere prevents energy from being concentrated in a single wave mode.[3]

Perhaps we can explain these results as a consequence of local amplification of the magnetic field by the soft iron boundary. Larger fields causes larger Lorentz forces, which may in turn be balanced by the nonlinear term in the Navier-Stokes equation, leading to more mixing between inertial modes. However, if local amplification is causing the broadband character of our measurements with a soft iron sphere, reducing B_0 should yield measurements more like those with a copper inner sphere. What we observe, instead, is that at these rotation rates, changes in B_0 have little effect on the spectra. Thus we conclude that these nonlinear behaviors are caused not by local amplification of the magnetic field but by the requirement that the magnetic field be nearly perpendicular to its ferromagnetic boundary (Eqn. 5.2).

5.4   Zonal flows

With a soft iron inner sphere we observe large zonal flows, as with a copper inner sphere (see Chapter 4). They are are necessarily excited by mechanisms associated with viscosity and nonlinearity. Their relative strengths and dependence

---

[3]Incidentally, with narrowband temporal filtering around the frequency of the primary mode, it *is* possible to construct images nearly as clean as those with copper. But Fig. 5.4 already gives us strong evidence of the presence of the inertial modes; we need not press the issue here. Plots should tell stories about data, not about filters!

on the rotation rate ratio χ are different with a soft iron inner sphere than with copper, as shown in Fig. 5.7, a typical plot of the mean axisymmetric induction with varying χ. In fact, the axisymmetric induction changes little with χ, unlike in the case of a copper inner sphere. The magnitude of the axisymmetric induction is also much smaller with soft iron. We speculate that the ferromagnetic boundary condition undermines the viscous and nonlinear effects that typically give rise to zonal flows [92], perhaps by replacing the Ekman boundary layer at the inner sphere with a magnetic boundary layer (a Hartmann layer [104]), preventing viscosity from becoming relevant.

5.5   Overview of parameter dependence

Scientific questions about the effects of ferromagnetic boundaries on a hydromagnetic flow date back at least 45 years, to Lowes and Wilkinson [4]. But the questions have been explored by precious few theoretical studies (e.g., [97, 101, 103]) which made correspondingly few predictions about what would be observed in an apparatus like ours. For the most part they have focused on the dynamo threshold Rm_c, not the details of the flow. Toward this question our experiments can offer but one data point: the dynamo threshold of our apparatus exceeds the parameters available to us! Nor do other previous studies, using more conventional boundary conditions, make many predictions for our apparatus. The inertial wave modes predicted by Rieutord [82] relate tangentially to our study of inertial wave modes (as discussed in the previous section and in Chapter 4), but make no predictions

about behaviors when viscosity, nonlinearity, or the Lorentz force become appreciable. Hollerbach's study of the onset of non-axisymmetric hydrodynamic modes in spherical Couette flow [81] offers some guidance, but includes no Lorentz forces and considers Reynolds numbers orders of magnitude lower than ours (also discussed in Chapter 4).

Though theory makes few predictions and offers few constraints about the behavior of our apparatus or its dependence on parameters, below we offer a few figures summarizing our results with a soft iron inner sphere and, for comparison, a copper inner sphere. We hope that they will be valuable because of the unprecedented nature of the experiments and because of their power to raise new questions.

First, having spent considerable time observing, identifying, and analyzing inertial modes at $E \ll 1$ (large Ω_o) with varying χ, we take a moment now to consider behaviors at $E = \infty$ ($\Omega_o = 0$) with varying S. By removing overall rotation of our apparatus, we eliminate any global influence of the Coriolis force and would not expect inertial waves to arise. We also put ourselves on the same parameter plane available to previous experiments in which the Velikhov-Chandrasekhar instability was observed [26]. The magnetic induction we measure has different degree and order than the modes associated with the Velikhov-Chandrasekhar instability. We cannot reach Lundquist numbers S (or equivalently, applied fields B_0) as high as in the previous work, which may explain the discrepancy. At any rate it would not be easy to assert the presence of the Velikhov-Chandrasekhar instability in our apparatus without direct measurements of fluid velocity, since the instability is essentially rotational. What we can offer instead are spectrograms and signal

strengths at various S, given in Fig. 5.8 for a soft iron inner sphere and Fig. 5.9 for a copper inner sphere. In both cases we observe a comb of spectral peaks whose frequencies are on the order of $\Omega_i/4$ and increase linearly with S. The signal strength increases as these peaks become more distinct in the spectrum, an effect which is noticeably stronger with a soft iron inner sphere than with a copper inner sphere. Notice also that the signal strength is more than an order of magnitude larger with soft iron than with copper.

Oscillatory signals with frequencies that increase linearly with S are consistent with Alfvén waves, described in Chapter 2. Working from Eqn. 2.26 and supposing the waves travel along lines of $\mathbf{B}_0$, which are nearly vertical, we would expect wave frequencies

$$\omega_{\text{lab}} = \frac{\pi B_0}{\sqrt{\mu\rho}} \frac{n}{2b\cos(\theta)},\tag{5.3}$$

where n is the wavenumber. By varying n and θ we can fit this expression to nearly any oscillation that depends linearly on S. But varying θ changes the presumed location of the waves, bringing them closer or farther from the axis of rotation. If Alfvén waves are present in our apparatus and are localized in θ, we would expect probes at different locations to observe induction of significantly different strength. In fact, all our probes show induction of nearly the same strength, making the presence of Alfvén waves seem less likely. Scientific skepticism requires that we posit an alternate hypothesis as well: whenever the field induced by the flow is small ($|\mathbf{B}_1| \ll |\mathbf{B}_0|$, as in Eqn. 2.20), that field varies linearly with S (or equivalently, with B_0). It is possible that the frequency peaks shown in Figs. 5.8 and 5.9 arise from

strictly non-magnetic behaviors, though such a situation seems unlikely with a soft iron inner sphere present.

Another possible explanation comes from a previous numerical study [105]. Set in a spherical Couette geometry matching our own, with a stationary outer sphere and a rotating inner sphere, the study describes non-axisymmetric instabilities arising from magnetically-induced shear layers and jets. In particular, they find that larger magnetic fields (as mesaured by the Hartmann number) lead to instabilities with larger azimuthal wavenumbers. As with [81], however, the Reynolds number in this study is much smaller than ours, perhaps undermining direct comparison.

Another source of interesting — though so far unexplained — data has been the regime where shear is large ($|Re| \gg 1$). Anecdotally we have observed strong, broadband bursts of magnetic induction, both with a copper inner sphere and with a soft iron inner sphere. In one experiment with a soft iron inner sphere, we observed a sudden, large growth in axisymmetric induction (g_1^0 and g_3^0) coincident with a sudden growth in motor torque large enough to cause a 10 Hp motor drive to register an overload and de-energize the motor. With a larger data set, statistical analysis of these bursts themselves would be possible and might lead to interesting conclusions. Pending the future availability of that larger data set, we present a general characterization of behaviors with large shear in Figs. 5.10 (soft iron inner sphere) and 5.11 (copper inner sphere). With a soft iron inner sphere, we see a comb of spectral peaks whose frequencies increase with $|\chi|$ but whose power is maximum near $\chi = -8$, while their frequencies are still near zero. With a copper inner sphere but otherwise identical experimental conditions we see much weaker signals with

no sign of a comb of spectral peaks. Interestingly, what looks like an instability occurs at $\chi = -12$, where both the primary frequency and the signal power change abruptly.
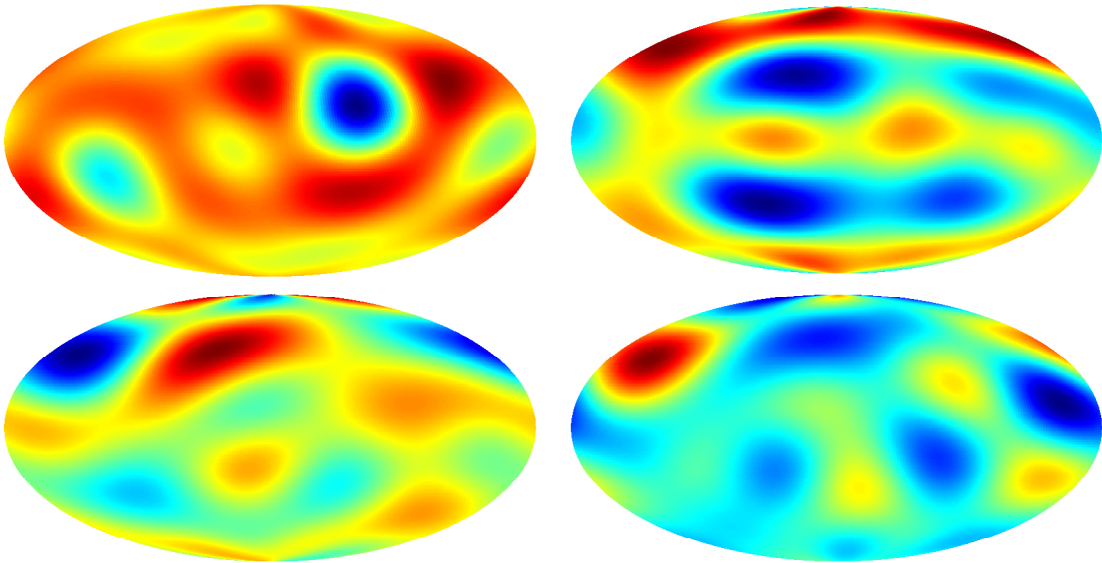
Figure 5.6: Induction B_s/B_0 at the surface of the fluid, shown as a Mollweide projection with the axis of rotation vertical, with soft iron inner sphere. These images, from top left to bottom right, show data recorded under the same experimental conditions as the data shown in Fig. 5.1, from top to bottom, respectively. Mean values have been removed. A version of this figure better adapted for grayscale printing is included as Fig. D.9.
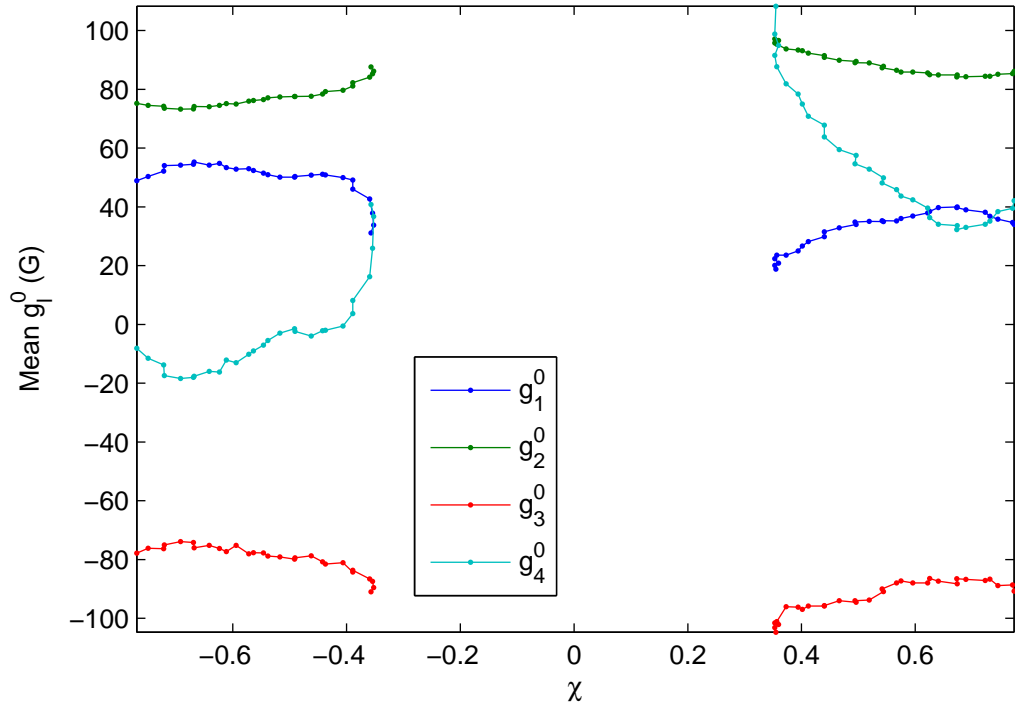
Figure 5.7: Typical induction due to axisymmetric zonal flows, with soft iron inner sphere. Each data point is the mean of 32 s of data, sampled at 512 Hz. Here $E = 7.26 \times 10^{-8}$ ($\Omega_o/2\pi = 18$ Hz). We observe similar relative amplitudes, as well as peaks at the same values of χ, for other values of E (Ω_o). Compare to Fig. 4.12.
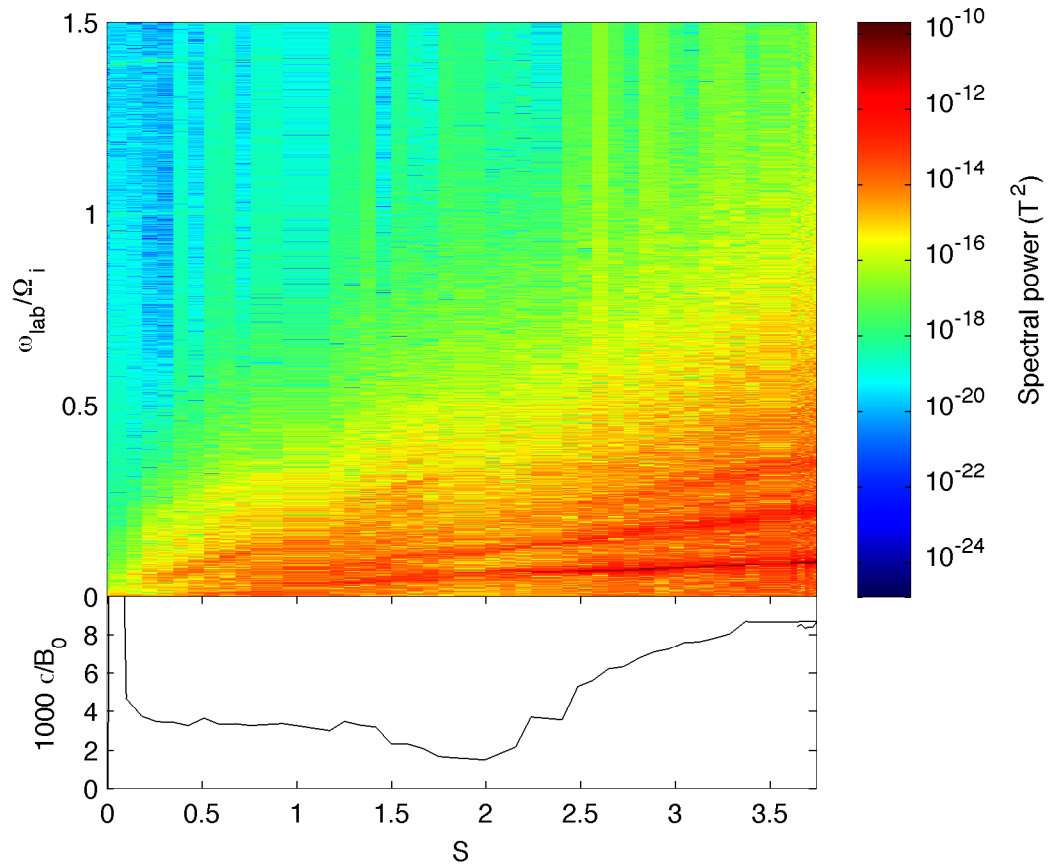
Figure 5.8: Behavior at $E = \infty$ ($\Omega_o = 0$) and varying S (B_0), with soft iron inner sphere. The upper axes show a spectrogram, while the lower axes show the standard deviation of a probe at the equator. Here $\Omega_i/2\pi = 20$ Hz. A version of this figure better adapted for grayscale printing is included as Fig. D.10.
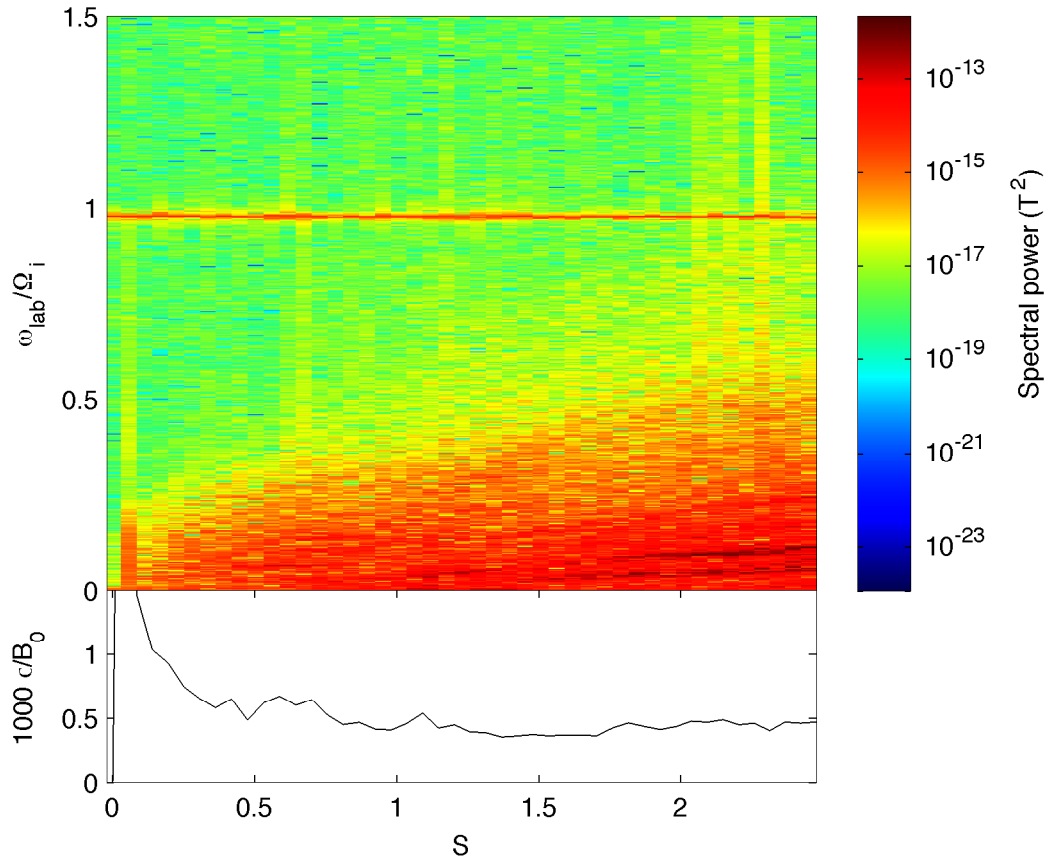
Figure 5.9: Behavior at $E = \infty$ ($\Omega_o = 0$) and varying S (B_0), with copper inner sphere. The upper axes show a spectrogram, while the lower axes show the standard deviation of a probe at the equator. Here $\Omega_i/2\pi = 5.25$ Hz. A version of this figure better adapted for grayscale printing is included as Fig. D.11.
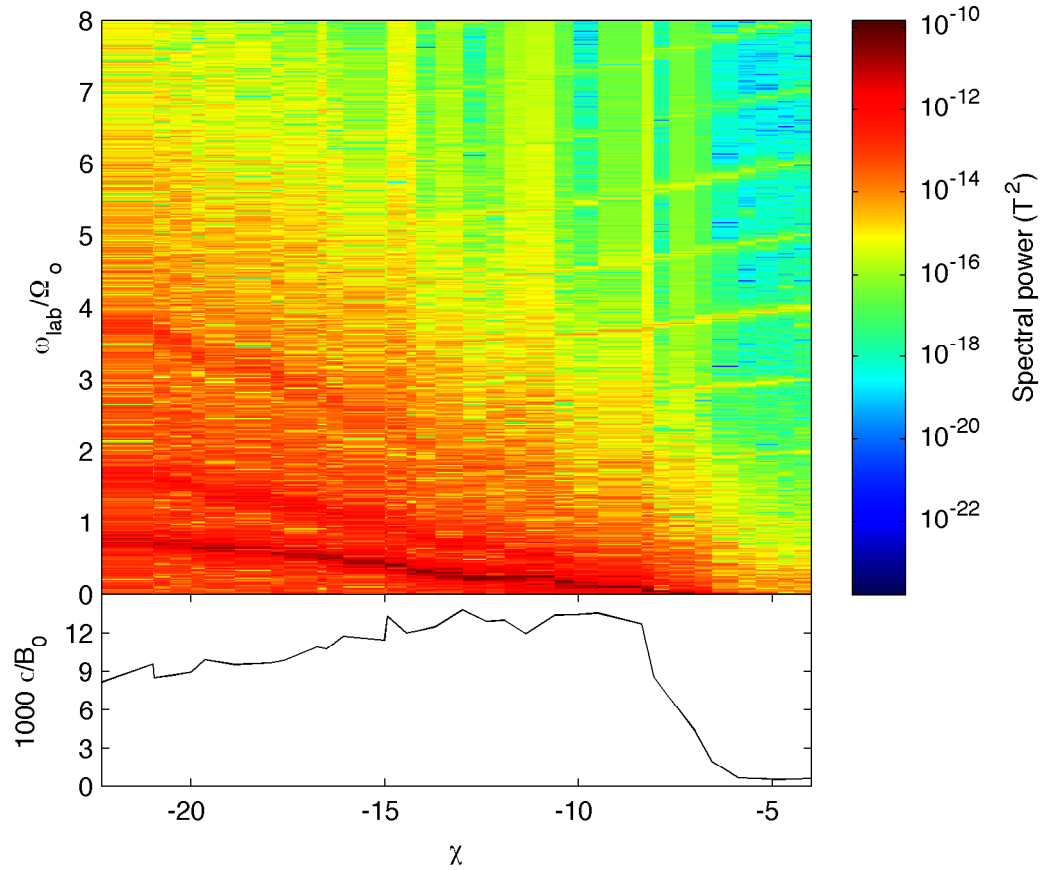
Figure 5.10: Behavior at $|Re| \gg 1$ (large shear) and varying χ (Ω_i), with soft iron inner sphere. The upper axes show a spectrogram, while the lower axes show the standard ca of a probe at the equator. Here $E = 6.3 \times 10^{-7}$ and $S = 2.1$, or equivalently, $\Omega_o/2\pi = 2$ Hz and $B_0 = 195$ G. A version of this figure better adapted for grayscale printing is included as Fig. D.12.

Figure 5.11: Behavior at $|Re| \gg 1$ (large shear) and varying χ (Ω_i), with copper inner sphere. The upper axes show a spectrogram, while the lower axes show the standard deviation of a probe at the equator. Here $E = 6.3 \times 10^{-7}$ and $S = 2.1$, or equivalently, $\Omega_o/2\pi = 2$ Hz and $B_0 = 195$ G. A version of this figure better adapted for grayscale printing is included as Fig. D.13.
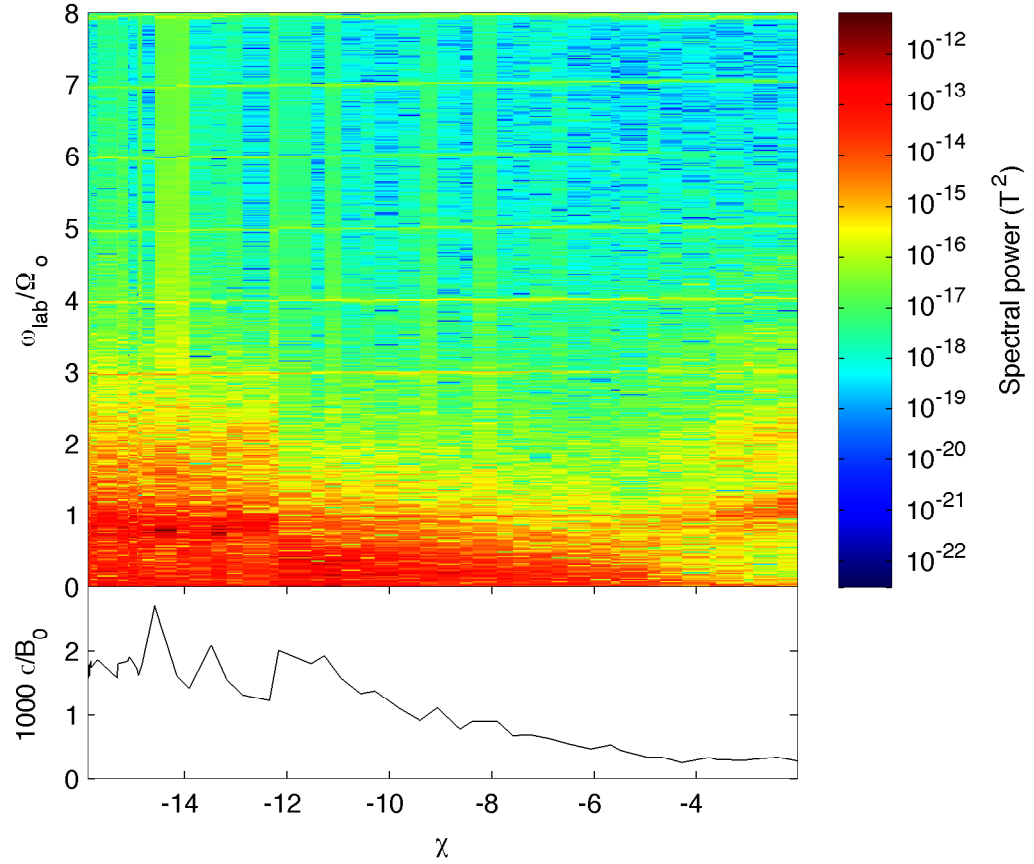
Chapter 6

On rotating turbulence

In this chapter we offer a few thoughts on the nature of turbulence in a rapidly rotating fluid. In brief, rotating turbulence is neither isotropic nor homogeneous and therefore not well modelled by power law energy spectra or by other approaches, common in the turbulence literature, that are based on assumptions of isotropy and homogeneity. As an alternative, we suggest a paradigm more like the eigenmode decompositions common in quantum mechanics, akin to recent advances in understanding turbulent flow using the tools of dynamical systems theory, in which inertial modes should be the first behavior expected to arise.

6.1   K41 in rotation

The most famous theory of turbulence, long the paradigm around which the majority of turbulence studies are constructed, is the theory developed by A. N. Kolmogorov in 1941 and abbreviated in perpetuity as "K41" [106, 107]. A mathematician, Kolmogorov built on the earlier ideas of Richardson [108], hypothesizing that at high Reynolds number, turbulence should be independent of details like the shape of its vessel or the mechanism that excites it. Rather, he asserted that $Re \gg 1$ turbulence must be isotropic and homogeneous, with characteristics depending only on the viscosity ν and the energy dissipation rate ϵ. With these hypotheses he was

able to show that the energy spectrum of such a flow behaves according to

$$\mathcal{E} = C\epsilon^{2/3}k^{-5/3}, \tag{6.1}$$

where C is a universal constant. Thus a long lineage of turbulence researchers have fit power law curves to their energy spectra, using either Kolmogorov's 5/3 slope or some different value derived according to the particular dimensionality or forcing of the system of their interest. In many cases, power law curves fit turbulent spectra remarkably well, but in other situations the statistics break down and K41 no longer models the right physics. Rare, high-intensity events may be important in explaining many of the discrepancies that arise [109].

Rotating turbulence is a different case. Over the years a number of experimental teams have set out to characterize rotating turbulence according to smooth, power-law spectra of the sort envisioned in K41. Few were successful in their stated goal, however, finding instead spectral peaks that did not at all align with a power law. Those peaks, as past researchers realized and as readers of this dissertation have likely guessed, arise from inertial modes. Great efforts were undertaken to eliminate inertial modes from many previous studies, replacing them with a supposed underlying turbulence more closely resembling K41.

By definition, however, a rotating fluid is not isotropic; the presence of an axis of rotation breaks its symmetry and provides a preferred direction. This symmetry breaking occurs at all scales and for all motions, because both the centrifugal force[1] and the Coriolis force are local forces present everywhere in the fluid. Thus one

---

[1]Call it "centripetal" if you prefer, but we write our equations in the rotating frame!

of the mathematical hypotheses necessary to construct the K41 theory is false in a rotating system.

Given the past successes of the analysis techniques established with K41, it is natural to hope that they might find success again in rotating turbulence, despite the lack of isotropy. That has not been the case. One explanation comes from a recent experimental study that finds power law fits agree well with observational data only during a transitory state [110]. The lifetime of this transitory state is the Ekman time,

$$\tau = \frac{2\pi}{\Omega\sqrt{E}} = \frac{2\pi L}{\sqrt{\nu\Omega}},$$ (6.2)

the timescale required for the effects of rotation to propagate from a rotating boundary through the bulk of the fluid it contains. In other words, power law models succeed only in the transitory state occurring before the fluid is actually rotating!

A number of other researchers have sought a sort of rotating turbulence that, though it may not be isotropic, nonetheless maintains homogeneity. Their experimental devices usually rotate a tank of fluid or pass fluid through rotating boundaries. In one well-known study, Jacquin *et al.* performed experiments in a wind tunnel, imposing axial speed as usual with a blower, then imposing azimuthal speed with a rotating section of the tunnel's boundary [111]. Discounting previous studies that observed the strong effects of inertial modes, the researchers found that the average velocities of their fluid were largely independent of radial location. Thus they claimed to have achieved rotating, homogeneous turbulence and went on to analyze its spectra and energy decay.

However, the rotating section of their wind tunnel was not simply a hollow cylinder but rather a cylindrical section of hexagonal "honeycomb," 10 cm long, 30 cm in diameter (to match the wind tunnel), having a 1.5 mm mesh size. Its role in fluid forcing is an important issue. By breaking up the 30 cm flow into a collection 1.5 mm flows, it dramatically changed the boundary conditions. In particular, no wave modes larger than the 1.5 mm mesh size could exist in the honeycomb. The experimental device was specifically designed to exclude the low-frequency, large-scale inertial modes that naturally dominate rotating flows [83]. Small-scale inertial modes likely remained in the flow, but by averaging over many such modes, the researchers found their mean velocity profiles to be smooth. Thus in a sense, they did achieve their goal of rotating, homogeneous turbulence. Such a state may be vanishingly rare in nature, however.

6.2   Inertial modes and an alternate view

We propose an alternate paradigm for rotating turbulence, one in which homogeneity and universal power-law spectra are neither the goals nor the expectations, and in which inertial modes are no mere nuisance to be eliminated but rather are the likely behavior of all rotating fluids. Central to this paradigm are our observations that rotating turbulence is anisotropic and inhomogeneous, oscillatory, and always affected by its boundaries. Our point of view is supported by all the data presented in this dissertation, by other recent [54] and current [112] experiments in our laboratory, and by a large body of previous work in fluids taking place outside

the K41 paradigm, mostly in geophysics.

6.2.1 Mathematical underpinnings

As we have noted above, the K41 theory of turbulence cannot rigorously apply to rotating fluids because imposing an axis of rotation immediately breaks the symmetry and makes the system anisotropic. In practice, all rotating fluids are not only anisotropic, but also inhomogeneous. In theory, we can envision an infinite rotating fluid, as we did initially in Chapter 2 (see Eqns. 2.6 and 2.7, for example). Lacking boundaries, such a fluid allows inertial waves at all wavenumbers and frequencies, each existing as an infinite plane wave in space. Such a theoretical system is therefore homogeneous. Any physical system, however, must have boundaries, and when boundaries are present, inertial modes[2] are allowed only at specific wavenumbers and frequencies. Accordingly, some locations in the fluid happen to be near nodes for many of the modes, while other locations in the fluid happen to be near anti-nodes for many of the modes. Nodes and anti-nodes experience different velocity fluctuations as the inertial modes propagate, and so homogeneity is lost.

It is correct to point out that homogeneity can be preserved for a transient time, but the transient endures only until the presence of the boundaries has been communicated throughout the fluid [54, 110]. The time required for that communication, τ, is exactly the same time required for the fluid to come into rotation. Thus from our point of view, for $t \ll \tau$, homogeneous turbulence is present, and for $t \gg \tau$, rotating turbulence is present, but rotating, homogeneous turbulence never

---

[2]With boundaries, it would be improper to call them waves.

occurs. The approximate homogeneity observed in [111] is also a direct consequence of the boundary conditions. By setting up rotation within small boundaries (the 1.5 mm honeycomb mesh), then flowing the fluid into much larger boundaries (the 30 cm test section), Jacquin *et al.* approximated the theoretical situation of infinite boundaries by making the characteristic size of allowed wave modes much smaller than the vessel size. Small-scale inertial modes did persist, however, as demonstrated in power spectra (Fig. 5 in [111]). The spectra recorded without rotation closely match those recorded with rotation whenever the signal frequency is greater than twice the rotation rate, where inertial modes cannot exist (see Eqn. 2.7). At frequencies less than twice the rotation rate, rotation increases the spectral power in all cases, indicating the presence of inertial waves. Thus we predict that if velocities were measured at various locations *inside a single honeycomb cell*, they would not be homogeneous. The velocity field would instead be governed by cell-sized inertial modes.

While the basic physics of rotating flows rules out both isotropy and homogeneity, it puts primary importance on inertial modes. In dimensionless form, the equation that governs the flow of a rotating, turbulent fluid is (compare to Eqn. 2.43)

$$\frac{\partial \mathbf{u}'}{\partial t'} + ERe\left(\mathbf{u}' \cdot \nabla'\right)\mathbf{u}' = -\frac{1}{ERe}\nabla' P' + E\nabla'^2 \mathbf{u}' - 2\left(\mathbf{\Omega} \times \mathbf{u}\right). \qquad (6.3)$$

Here we see clearly that inertial waves are exact solutions of the equation of motion when the fluid rotates rapidly ($E \ll 1$, allowing us to neglect the viscous term) and when its motions have small amplitude ($ERe \ll 1$, allowing us to neglect the nonlinear term). When $E = 0$, no motions are possible other than inertial waves.

To say it differently, inertial waves are the linear eigenmodes of a rapidly rotating fluid, and all linear motions are necessarily superpositions of inertial waves [49]. When $0 < E \ll 1$, nonlinear motions become possible, so that viscous boundaries and motions with $\omega > 2\Omega$ do arise, but they are confined to boundary layers whose thickness is roughly Re^{-1}, so that inertial waves dominate nonlinear mechanisms as long as $ERe \ll 1$. Thinking in terms of force balances, we can assert that the Coriolis force is balanced primarily by pressure when $ERe \ll 1$.[3] When $ERe \sim 1$, a three-way balance between the Coriolis force, pressure, and nonlinear effects governs the flow. Viscous forces are appreciable in the bulk only when rotation effectively ceases ($E \sim 1$).[4] In all cases, the decay rate of inertial modes scales as $E^{1/2}$ [83]; at $E \ll 1$, they decay correspondingly slowly.

Note that we establish no requirement for low-Reynolds-number flow; inertial waves are still dominant in highly turbulent flows. Our apparatus, for example, produces highly turbulent flows ($Re \geq 10^6$) at all parameters discussed in this dissertation (see Table 3.2). Nonetheless, inertial modes often dominate the observed induction because $E < 10^{-7}$. This is a generic quality of rotating turbulence, and one way in which it differs starkly from K41 turbulence: linear motions can dominate nonlinear ones, even at large Reynolds number.

---

[3]The special case of *stationary* flows with $ERe \ll 1$ is the geostrophic limit.

[4]Viscous forces also affect the fluid outside its thin Ekman layers via boundary layer eruptions; see Chapters 2 and 4.

6.2.2 Experimental support

The experimental data collected through the course of this dissertation consistently supports the mathematical arguments we have just outlined. At Ekman numbers below 1.3×10^{-7} (rotation rates above 10 Hz), inertial waves are the most striking feature of our spectra. When the inner sphere is copper and magnetic effects are consequently weak, inertial modes are often stronger than any other frequency in the data by 10^3, as shown in Figs. 4.2 and 4.8. The orderly nature of the surface induction shown in Figs. 4.4 and 4.5 also attests to the dominance of inertial modes in the data. When the inner sphere is soft iron, magnetic effects can impose large Lorentz forces locally, and the nonlinear term must grow to balance those forces. Accordingly we observe more broadband induction and less distinct inertial modes. Even in this weakened, hydromagnetic state, the inertial modes are still the strongest frequencies in our data, exceeding all others by about an order of magnitude, as shown in Figs. 5.2 and 5.3. At larger Ekman numbers $E \sim 10^{-6}$, individual inertial modes do not dominate to the point that they are easily identifiable, but fluid behaviors are still essentially oscillatory, whether the inner sphere is copper (Fig. 5.11) or soft iron (Fig. 5.10).

In all these cases, our three assertions about the nature of rotating turbulence hold true: it is evidently oscillatory (Figs. 4.2, 4.8, 5.2, and 5.3), it is anisotropic and inhomogeneous (Figs. 4.4, 4.5, and 5.6), and the boundaries play a key role, as evidenced by the dominance of global inertial modes over local phenomena.

Ours is but one of many experimental devices to underscore these facts about

rotating turbulence. They are clear in the data presented in a wide variety of rotating, fluid experiments (e.g., [38, 41, 54]). Recent observations in the 3 m apparatus in our own laboratory also support our assertions. A larger, improved version of the apparatus detailed in this dissertation, it has an inner sphere 1 m in diameter and an outer sphere 3 m in diameter, both of which rotate independently, driven by motors. It is currently filled with water, and our colleagues D. S. Zimmerman and S. A. Triana are studying its hyrodynamic behaviors using pressure and wall shear stress probes. A typical power spectrum from the wall shear stress probe is given in Fig. 6.1. For $\omega/\Omega_o < 2$, we see a forest of spectral peaks, often orders of magnitude stronger than the surrounding frequencies, consistent with the presence and prominence of inertial modes. A "knee" appears at $\omega/\Omega_o = 2$, above which the spectral power drops rapidly, following a power law to good approximation, but never showing any behaviors whose strength competes with the inertial modes.

A third line of experiments by our colleagues has also demonstrated the dominance of inertial modes in rotating flows. G. P. Bewley used novel optical techniques [113] to observe the flow of liquid helium (which has an unusually low viscosity) in a rotating, rectangular channel 5 cm x 5 cm x 25 cm. Turbulence was produced by dragging a grid, and the dominance of identifiable inertial modes is clear, as described in [54] and as shown in Fig. 6.2.
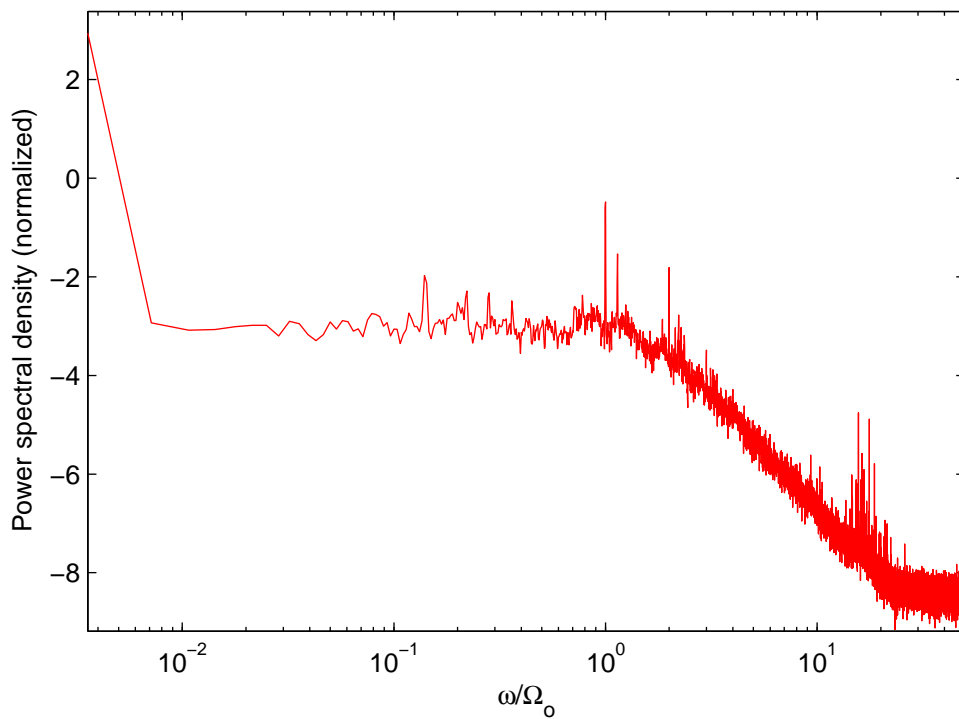
Figure 6.1: Power spectrum showing inertial modes in the 3 m apparatus. Here $E = 1.01 \times 10^{-7}$ and $\chi = 0.857$ (or equivalently, $\Omega_o/2\pi = 0.7$ Hz and $\Omega_i/2\pi = 0.6$ Hz, with $\nu = 1.00 \times 10^{-6}$ m²/s and $b = 1.5$ m) [112].
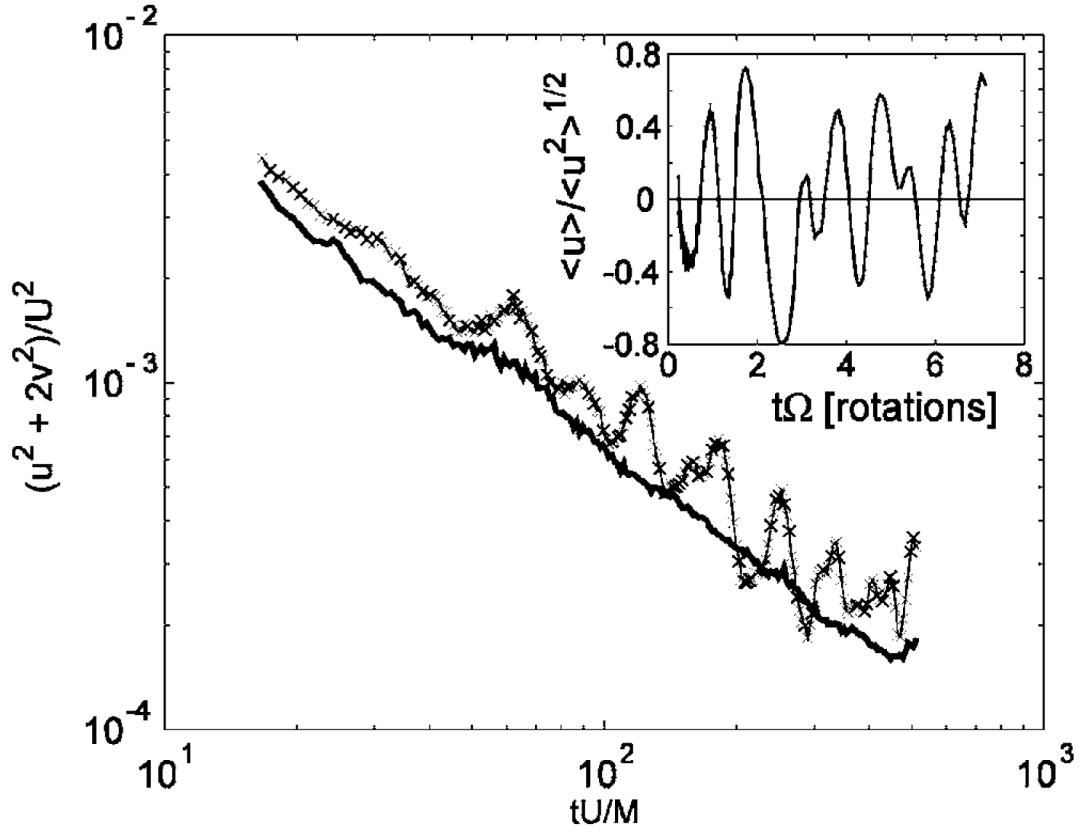
Figure 6.2: Power spectrum showing inertial modes in rotating, liquid helium. Here $E = 2 \times 10^{-5}$ ($\Omega = 2$ Hz). The symbols u, v, U, t, M, and Ω represent the velocity along the rotation axis, the velocity perpendicular to the rotation axis, the root-mean-square velocity, time, the mesh spacing of the grid, and the rotation rate, respectively. Reproduced with permission from [54].

6.2.3 Putting it in context

Though our views on the nature of turbulence contradict past researchers who have insisted on homogeneity in rotation, they are consistent with many other previous studies. The geophysical community, interested more in modelling fluids in planetary geometries than in studying turbulence *per se*, have long been aware of inertial modes (e.g., [52, 58, 74, 80, 83, 89, 90, 114]). By extension, they know that rotating flows are oscillatory, anisotropic, inhomogeneous, and affected by their boundaries. A. Tilgner is particularly fond of reiterating that inertial modes are the linear eigenmodes of a rapidly rotating fluid [49, 92] and well knows the physical consequences of that mathematical statement.

Nor will researchers who study the well-known inverse cascade find our conception of rotating turbulence to be surprising. Rapidly rotating fluid systems are known to transfer energy in both directions from the length scale at which the flow is forced. A "forward cascade," like the one understood by Richardson and Kolmogorov in non-rotating turbulence, carries energy to the small lengthscales (large wavenumbers), where that energy is *dissipated* by viscosity. Simultaneously, an "inverse cascade" carries energy to the large lengthscales, amplifying the lowest-wavenumber modes [94], which consequently *contain* the majority of the energy. The mechanisms responsible for the inverse cascade are thought to rely on near-resonant triad interactions,[5] which are first-order nonlinear interactions among inertial modes, also requiring viscosity. Though its mechanism may be complicated,

---

[5] We have previously mentioned triad interactions with regard to zonal flows in Chapter 4.

the inverse cascade begins with inertial modes.

Since experimental techniques have made flow visualization possible, turbulence researchers have also pointed out the presence of "coherent structures" (as they are often called in the literature), thereby noting inhomogeneity in turbulent flows [115–119]. Over time the coherent structures that began as observational phenomenology have acquired a mathematical basis in the equations of motion [120, 121]. Now, a number of particularly promising studies are moving closer to fulfilling the long-standing hope that turbulence will be concisely understood as a dynamical system, or better still, a dynamical system of low dimension. Travelling waves that are particular solutions of the Navier-Stokes equation in pipe flow have been found numerically [122] and subsequently observed experimentally [123]. These travelling waves, which might be called coherent structures and which are analogous to inertial modes in a rotating fluid, play a key role in transitions to and from turbulence in pipe flow [124, 125]. The streaks commonly observed in shear flows have also been associated with an exact numerical solution of the Navier-Stokes equation [121] and have likewise been found to play important roles in system dynamics [126, 127].

Thus our conception of rotating turbulence — anisotropic and inhomogeneous, oscillatory, and always affected by its boundaries — is consonant with a number of related findings and consistent with published literature. We would even conjecture that when dynamically important exact solutions to the equations of motion of rotating turbulence, similar to those known for pipe flow and shear flow, are found, they will differ only slightly from familiar inertial modes.

Chapter 7

Conclusions and implications

In this chapter we wrap things up with a summary of the work described in previous chapters, a discussion of the implications of that work for geophysics, and a few musings about possible future studies.

7.1   Summary of our work

The work described in this dissertation began when the 60 cm apparatus was modified to allow for spherical Couette flow instead of convection. In the time since then, most of the experimental systems have been rebuilt or substantially modified. The larger, more powerful magnets constructed for our work allow for experiments in parameter regimes where Lorentz forces become substantial, up to $S = 4$. Perhaps more interesting than the magnets is the Gauss array of Hall probes, based on a predecessor's design [70], allowing for global characterization of the magnetic induction via vector spherical harmonics up to degree and order four. The data sets produced by our Gauss array are far richer than our previous data, even data recorded using a meridional array that had nearly as many probes. Projecting onto the Gauss coefficients $g_{l_{mag}}^m$ allows for easy identification of inertial modes (see Chapter 5), separates other sorts of induction based on their symmetries, and in general does much to disentangle the sometimes-overwhelming zoo of behaviors active in a

rotating, turbulent, hydromagnetic experiment. We emphatically recommend Gauss arrays to future experimentalists!

The scientific accomplishments described in this dissertation begin with the discovery and identification of inertial modes in spherical Couette flow. We have matched the oscillatory behaviors measured in our experiment to analytically-known inertial modes [53]. Drawing from a long-standing theory in acoustics [84], we have shown that inertial mode amplification by over-reflection at a shear layer makes predictions consistent with our observations. We have also shown that geometrical arguments about over-reflection lead to predictions about mode selection. Of the infinite number of inertial modes possible in a full sphere, not all appear with equal strength in our experiments, and the strong modes we observe are consistent with selection by over-reflection.

Motivated by experimental devices that display dynamo action, we have also characterized the effects of a ferromagnetic, soft iron boundary on hydromagnetic flows. We find that inertial modes remain prominent at low Ekman number, and that the same modes are present with a soft iron inner sphere as with a copper inner sphere. Soft iron tends to broaden the modes and encourage nonlinear effects, however, and changes the associated zonal flows significantly. We have also given some initial results with a soft iron sphere at experimental parameters outside the regimes that produce prominent, narrowband inertial modes, comparing to similar measurements with a copper inner sphere. More scientific insights will come when these results are compared to the forthcoming numerical study of C. Guervilly.

Our work also gives insights into the physics of rotating, hydrodynamic turbu-

lence, without magnetic fields. All our observations suggest that in strongly rotating ($E \ll 1$), turbulent flows, inertial modes are typically more prominent than viscous, small-scale effects. Our data support a paradigm of rotating turbulence that has little relation to the statistical K41 theory, building instead on pioneering work in geophysics [49, 52, 83]. Such a paradigm is analogous to conceptions of turbulence as a dynamical system — perhaps one of low dimension — in which a finite number of attractors and repellers largely govern the behavior [126–128].

7.2   Implications for geophysics

By all accounts, the Earth's core is a rapidly rotating fluid object. Given that its Ekman number is estimated as 10^{-14} and that the damping rate of inertial modes goes as $E^{1/2}$ [83], their presence in the core is hardly debatable. Detecting them is not so easy, however, because of the remoteness of the core. The problem is compounded by the fact that inertial waves are dense in frequency — no distinct modes need necessarily rise out of the forest of other modes. Rotating convection in the core is predicted by theory to pump only a small number of wave modes [129], which might be quite string, but their high degree and order would make them nearly impossible to detect at Earth's surface. At least one group [130] has reported identifying inertial waves in the core by studying gravimetric data, but the signal quality of that data later came into question [131]. Thus observational identification of inertial modes in Earth's core remains a topic for further work.

Strong zonal flows of the sort observed in our experiments are also likely to be

present in the core of the Earth [92]. They will not likely be identified by selection rules similar to the ones we used to infer zonal flows in our apparatus (Table 3.6) because the complex structure of Earth's magnetic field, especially on small scales, prevents the construction of any simple selection rules. Estimating a dynamo flow from its external field is no easy thing.[1] Ironically, the same small-scale magnetic features that prevent simple selection rules may also help us to infer flow patterns. Such features can act as tracers of the fluid, drifting along with the molten iron as it flows. Thus the westward drift of Earth's magnetic field provides good evidence for zonal flows in the core [114, 132].

VKS2 is a profoundly interesting scientific apparatus, the first laboratory device to show dynamo action in a relatively unconstrained fluid where turbulence is important. Accordingly, questions about its soft iron impellers and about ferromagnetic boundaries in general will receive much attention in coming years. Our work may be the first to study the details of hydromagnetic induction with a ferromagnetic boundary, asking about more than just the changes to the dynamo threshold. Extrapolating from our results, we predict that future experiments with soft iron boundaries will observe induction and flows that are more broadband and more nonlinear than their counterparts with conductive boundaries. We also predict that the importance of the Lorentz force will increase the prevalence of intermittent, bursty behaviors in both the induced field and the flow.

---

[1]Of course, if the full magnetic field $\mathbf{B}$ were known everywhere, the corresponding flow $\mathbf{u}$ could be calculated by inverting Eqn. 2.15. But we have no knowledge of $\mathbf{B}$ within the Earth, and therefore no knowledge of its toroidal components at all.

7.3 Some ideas for future work

Perhaps a dissertation always ends on a bittersweet note. Naturally a student is excited to continue his career, undertaking new projects in new surroundings with new insights to gain. But his experimental apparatus has come through a host of engineering challenges and is finally running well, producing interesting data and raising new scientific questions. Leaving it behind seems almost a shame. At least he can placate himself by passing a long list of ideas for future work to his successors!

First, there is hydromagnetic spin-down. Long-standing questions about the dynamics of the core of Mercury are being laid to rest by data acquired in recent years, just as new questions are being raised. We now know that Mercury librates, its angle oscillating with an amplitude of 2.11 ± 0.1 arc minutes as it spins, clearly indicating the presence of a liquid core [133]. Moreover we know that Mercury's core supports dynamo action, producing a magnetic field which is weak (230 to 290 nT R_M^3) but nonetheless was measured conclusively by the MESSENGER probe on its recent approach [21]. Little is known about the dynamics of flows in librating, hydromagnetic, spherical shells — like Mercury's core — and no experimental studies of these flows have been previously attempted. J. Noir and J. M. Aurnou are engaged in water experiments studying libration of a spherical shell, intended to model Mercury's core. Their initial results show that libration can cause zonal flows and broadband turbulence.

At their suggestion, we have been working toward hydromagnetic experiments to complement their hydrodynamic work. After some attempts, we found that

our current mechanical drive system cannot impose libration reliably. However, the spin-up phase of libration is stable; instabilities occur only during spin-down. Hence we have collected preliminary data in hydromagnetic spin-down experiments using our existing apparatus. So far, all observations are with a soft iron inner sphere. Spin-down experiments with a copper inner sphere are our next goal, and will take place in the coming weeks. From them we hope to make predictions about the character and amplitude of Mercury's magnetic field. When MESSENGER begins orbiting Mercury in 2011, it will thoroughly map the planet's magnetic field, perhaps confirming our predictions

Second, being able to measure velocity could dramatically improve the scientific impact of the experiment. Data from an ultrasound probe could make a strong case for the presence or absence of the Velikhov-Chandrasekhar instability in our apparatus, as it did in [26]. Velocity data would also allow for more detailed comparison to numerical simulations, and would be useful in constructing sub-grid models for numerics [134]. An ultrasound probe could offer another confirmation of inertial modes in our apparatus, and would likely be able to locate the particular shear layer where over-reflection is pumping those modes.

The engineering challenges of installing ultrasound are significant, however. Having the probe in contact with the test fluid means drilling a large hole (more than an inch in diameter) through the vessel. For safety reasons it is absolutely crucial to ensure that such a hole does not leak — a back-of-the-envelope calculation predicts that at $\Omega_o/2\pi = 30$ Hz, a 1 inch hole at the equator can empty the entire vessel in less than a second! Transmitting a low-noise, 4 MHz signal wirelessly from the

149

rotating probe might also pose a challenge (though our colleague D. S. Zimmerman has solved it elegantly in the 3 m apparatus). The wall velocity probe developed in the group of J.-F. Pinton [135] could address many of the same scientific questions. It requires a smaller hole, and its signal could be digitized in the rotating frame for easy transmission. Or instead of installing direct velocimetry, perhaps we could draw conclusions about zonal flows by applying a transverse magnetic field and studying its advection by the flowing sodium.

Third, adding more Hall probes could improve experimental data. With a larger ($l > 4$) Gauss array, it would be possible to identify higher-order inertial modes and to better resolve the magnetic induction in all cases. Having at least one Hall probe in the rotating frame, attached to the vessel, would also be interesting, and could directly address the question of whether the spin-over mode (see Chapter 4) is present in our 60 cm apparatus, as it is in the 3 m one. A wireless, digital transmission system and a battery power system for such a probe are already under construction.[2] We plan to mount our first rotating probe at a colatitude $\theta = 65°$. Mounting a probe inside the outer shaft would also be very interesting, giving a window into the toroidal induction.

Finally, a big engineering project that might yield correspondingly big scientific payoffs would be to add a mechanism for precessing the experiment. We discussed precession a bit in Chapter 4; an object precesses when its spin axis changes direction (usually periodically). Precession is common among astrophysical objects, and

---

[2]The Xbee 2.5 and Arduino Diecimilla are a great combination for anybody who works on rotating equipment!

past researchers have proposed Earth's precession as an energy source for the dynamo [71]. Even without the effects of magnetic fields, precession causes interesting fluid behaviors, including the spin-over mode. Spin-over has been observed in the 3 m apparatus in our lab [112], but its precession rate is the rotation of the Earth and is therefore fixed. A mechanism for precessing the 60 cm apparatus at variable rates would allow for a wide array of new experiments. Only one hydromagnetic precession device, which was cylindrical, has been constructed previously [136]. Because of its spherical geometry, our 60 cm apparatus would make a far more faithful laboratory model of precessing planetary cores.

Appendix A

Vector identities

Here we include a list of helpful vector identities.

$$\nabla \times \nabla a = 0 \tag{A.1}$$

$$\nabla \times (\mathbf{A} \times \mathbf{B}) = (\nabla \cdot \mathbf{B})\mathbf{A} - (\nabla \cdot \mathbf{A})\mathbf{B} + (\mathbf{B} \cdot \nabla)\mathbf{A} - (\mathbf{A} \cdot \nabla)\mathbf{B} \tag{A.2}$$

$$\nabla \times (\nabla \times \mathbf{A}) = \nabla(\nabla \cdot \mathbf{A}) - \nabla^2\mathbf{A} \tag{A.3}$$

$$\nabla(\mathbf{A}^2) = 2\mathbf{A} \times (\nabla \times \mathbf{A}) + 2\mathbf{A} \cdot \nabla\mathbf{A} \tag{A.4}$$

$$\nabla \cdot a\mathbf{A} = \mathbf{A} \cdot \nabla a + a(\nabla \cdot \mathbf{A}) \tag{A.5}$$

$$\int \nabla \times \mathbf{A} \cdot \mathbf{da} = \oint \mathbf{A} \cdot \mathbf{dl} \tag{A.6}$$

Appendix B

Mechanical drawings

We include on the following pages a collection of mechanical drawings detailing the major parts constructed during the course of our work.

Inner Shaft

Top Inner Bearing: SKF 61805

Lip Seal: Chicago Rawhide 9805 CRWA5

Top Inner Bearing Seat

Inner Sphere

Bottom Inner Bearings: SKF 7204 BECBM, back-to-back

Large Spacer

Bottom Bearing Retainer Ring

Small Spacer

Nut N-040

Bottom Inner Bearing Seat

Bottom Bearing Seat Washer

Inner Assembly	
	12 May 2005
Kelley	
Scale 1:5.48	
All units in inches unless otherwise noted.	

End View

ø 7.874

ø 0.25 ±0.01

A

A

ø 0.787 ±0.01
thru bore

View AA

1.0 ±0.1

keyways

1.0 ±0.1

Chamfer @ 45° x 0.25 deep
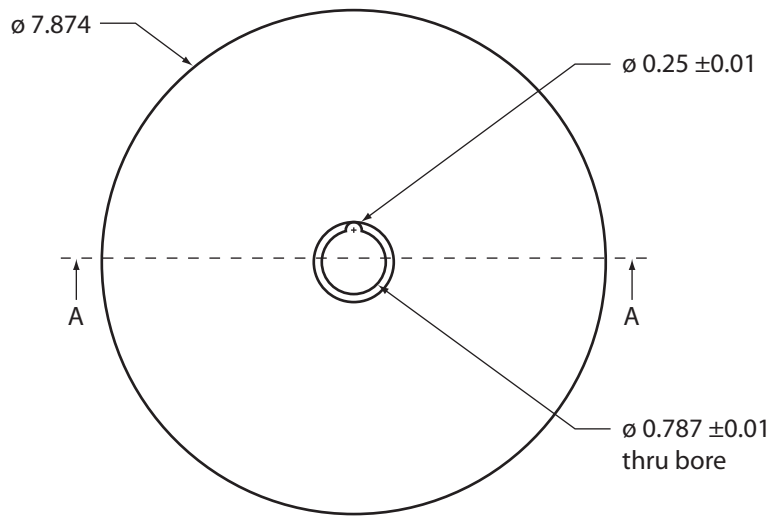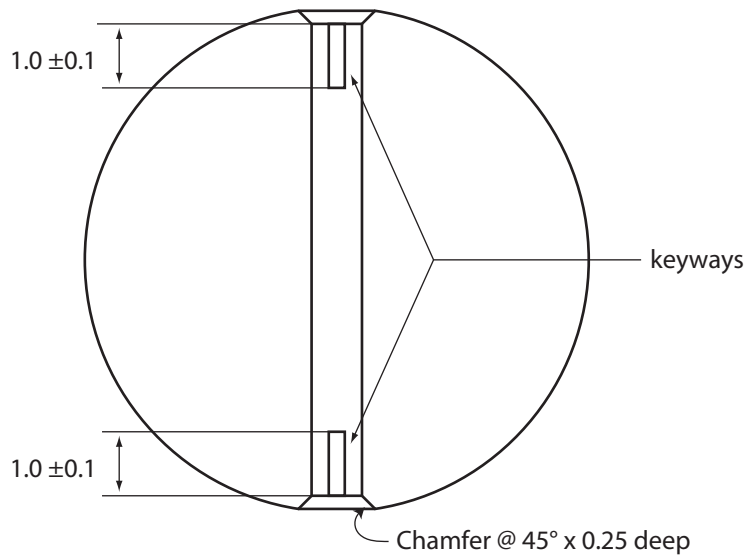
Inner Sphere	
Kelley	12 May 2005
Scale 1:3 All units in inches unless otherwise noted.	

32 threads/inch
0.7756 < D < 0.7810
0.7573 < d < 0.7607

0.095

0.375

ø 0.787 +000 / -0.002

9.760 ±0.01

2 keyways for 0.25 key stock,
snug, 180° apart

Chamfer @ 45°

1.0

0.20

ø 25 mm

29.873

keyway for 0.25 key stock, clearance

Chamfer @ 45°

ø 0.28 thru hole

ø 0.9375

1.0

2.00

2.25
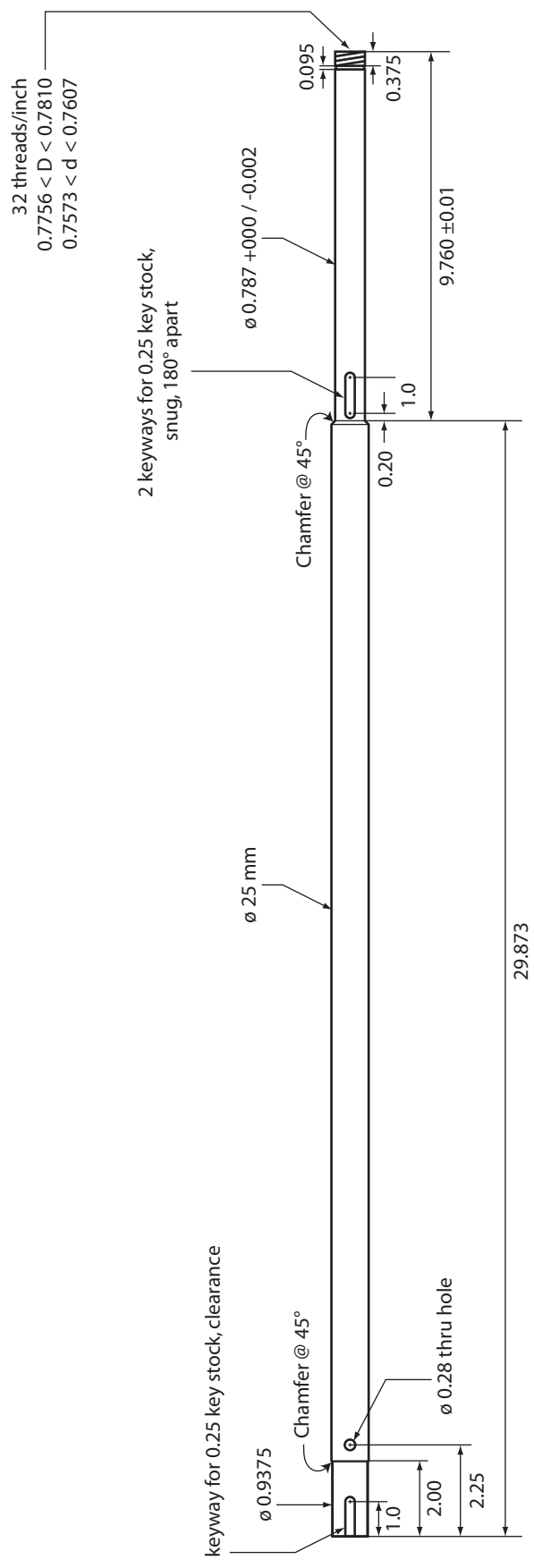
Inner Shaft, v.4

Kelley	shaft4.pdf	23 January 2006

Scale 1:4.54

All units in inches unless otherwise noted.
Tolerances unless otherwise noted:
X.XX $^{+0.01}_{-0.01}$ X.XXX $^{+0.005}_{-0.005}$

Drill & tap for #8
6 pl eq sp
0.375 deep
on a 2.368 BCD.

A

A

ø 1.653 ±0.001
1.759 ±0.05 deep

ø 3.50

ø 1.852 ±0.002
1.09 ±0.004 deep

View AA

0.25 ±0.05

2.00 ±0.05

2.8758 Acme 2G
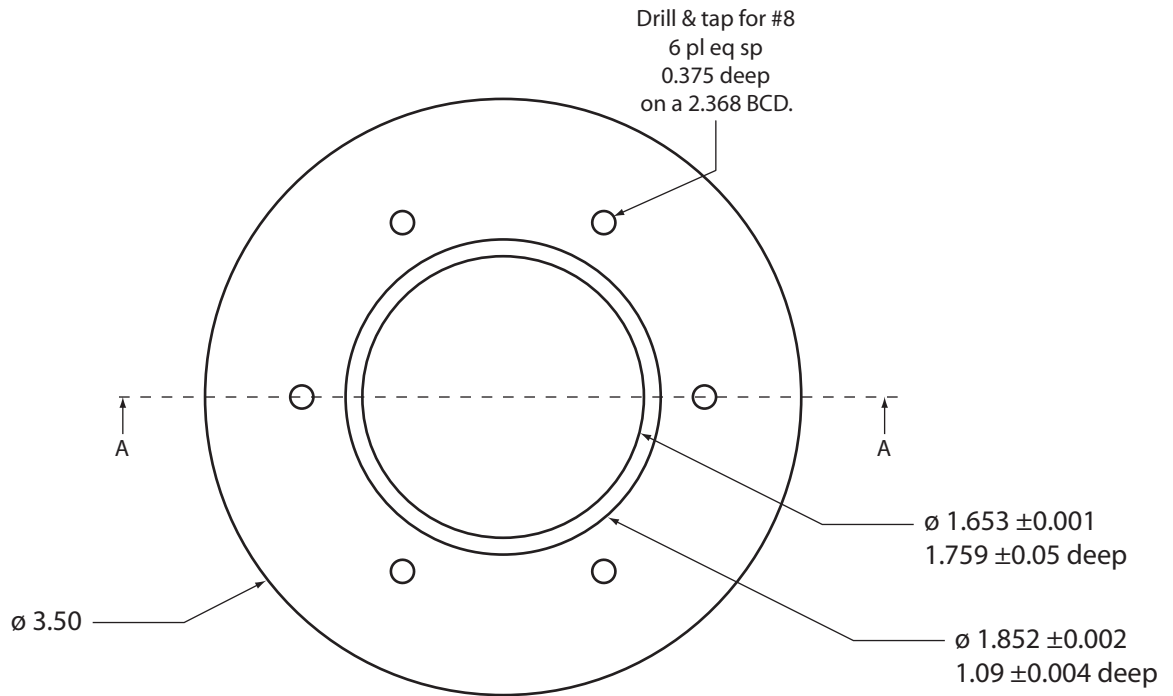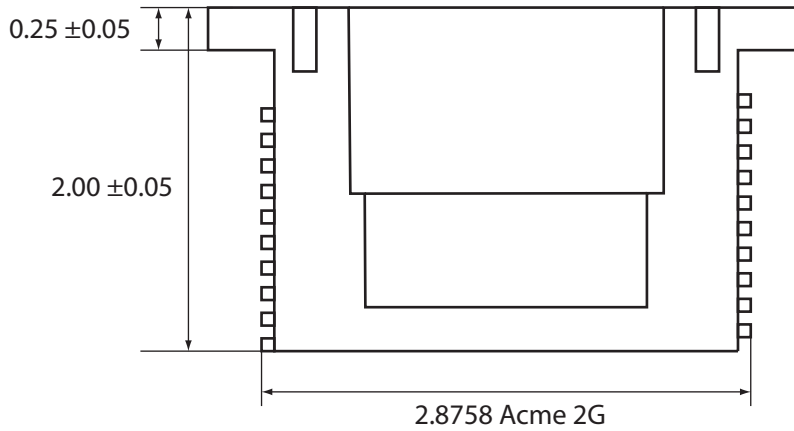
Bottom inner bearing seat		
Kelley	BIBS.pdf	12 Nov 2008
Scale 1:1.13 All units in inches unless otherwise noted. Tolerances unless otherwise noted: X.XX $^{+0.01}_{-0.01}$ X.XXX $^{+0.005}_{-0.005}$		

Drill thru for #8 clearance
6 pl eq sp
on a 2.368 BCD.

ø 1.653 +0.006
        -0.003

ø 3.5

0.20

Bottom bearing retainer ring		
Kelley	BIRR.pdf	12 Nov 2008
Scale 1:1 All units in inches unless otherwise noted. Tolerances unless otherwise noted: X.XX $^{+0.01}_{-0.01}$ X.XXX $^{+0.005}_{-0.005}$		

ø 2.9

ø 3.5

0.0765
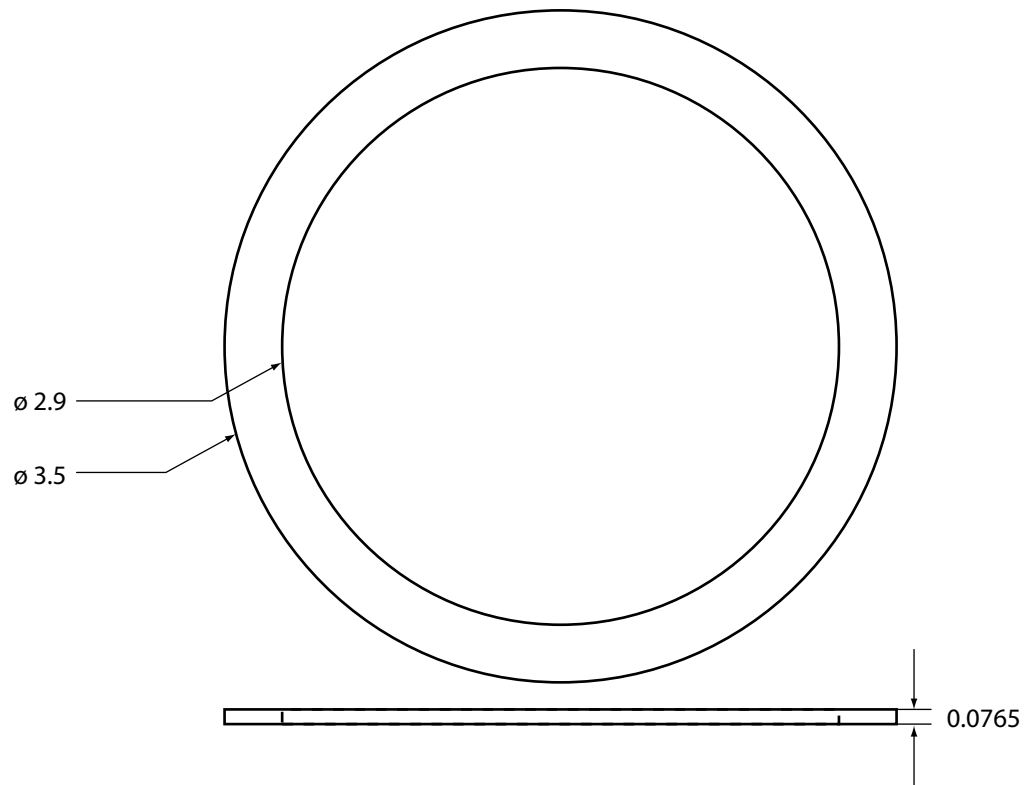
Bottom Bearing Seat Washer	
Kelley	10 May 2005
Scale 1:1 All units in inches unless otherwise noted.	

Top View

ø 1.720 $^{+0.001}_{-0.001}$

ø 3.482

ø 1.063

ø 1.260 $^{+0.001}_{-0.001}$

ø 2.753 $^{+0.005}_{-0.000}$

View AA

60°

0.430

0.690

1.217

1.70

This surface does
not contact,
can be rough.

0.350

Bottom View

ø 1.752 $^{+0.001}_{-0.001}$

A

A

Drill thru & counter
bore for socket-cap
#8 clearance
6 pl eq sp
on a 3.125 BCD.
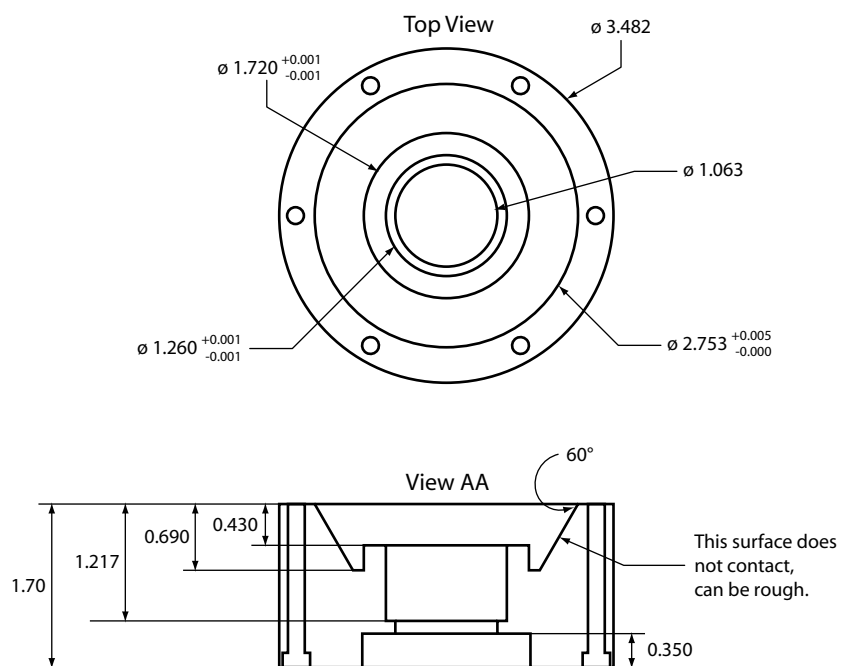
Fits SKF HK2520 bearing and
Chicago Rawhide 9805 CRWA5 lip seal.

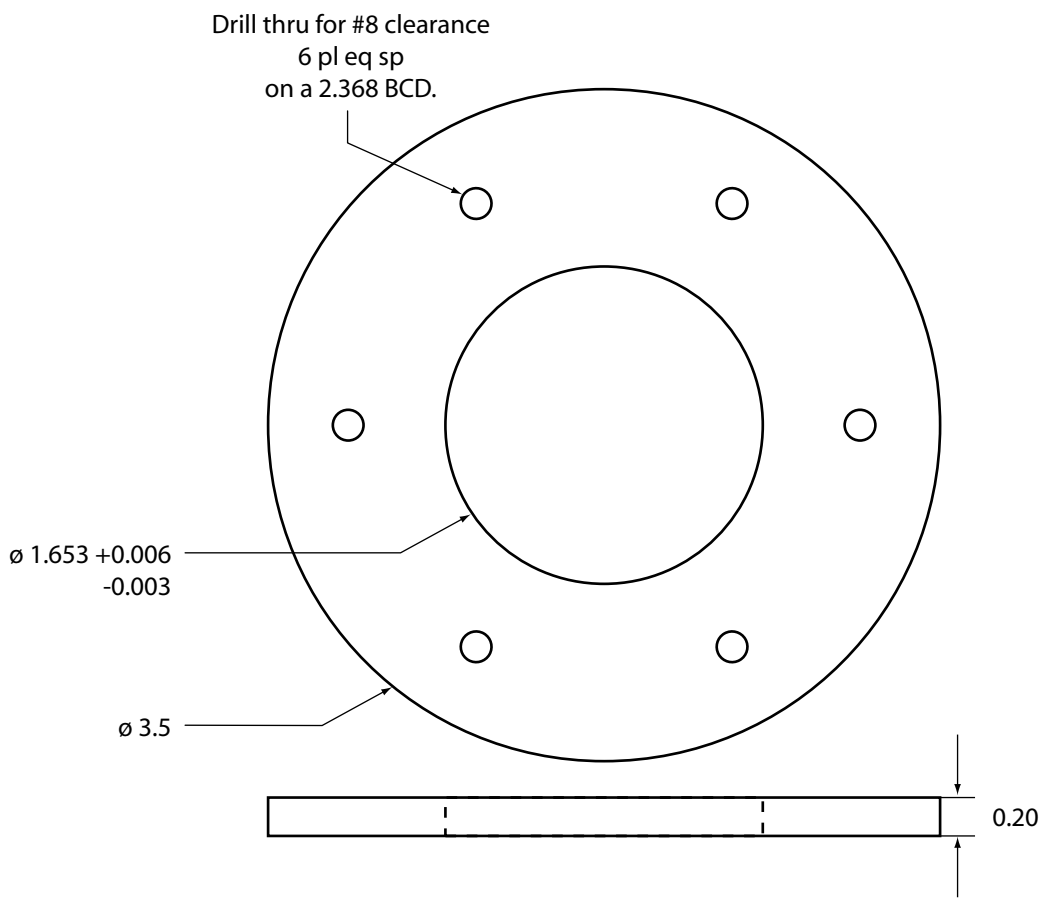| Top Inner Bearing Seat, v.4	
Kelley	19 December 2005
Scale 1:2 All units in inches unless otherwise noted. Tolerances unless otherwise noted: X.XX $^{+0.01}_{-0.01}$ X.XXX $^{+0.005}_{-0.005}$	

ø 0.777

ø 1.25

45°

0.84 ±.01

0.043

Large Spacer	
Kelley	9 May 2005
Scale 1:1 All units in inches unless otherwise noted.	

0.125

Chamfer @ 45°

1.25

2.713

0.50

ø 4.50

ø 4.935

ø 6.00

ø 10.00
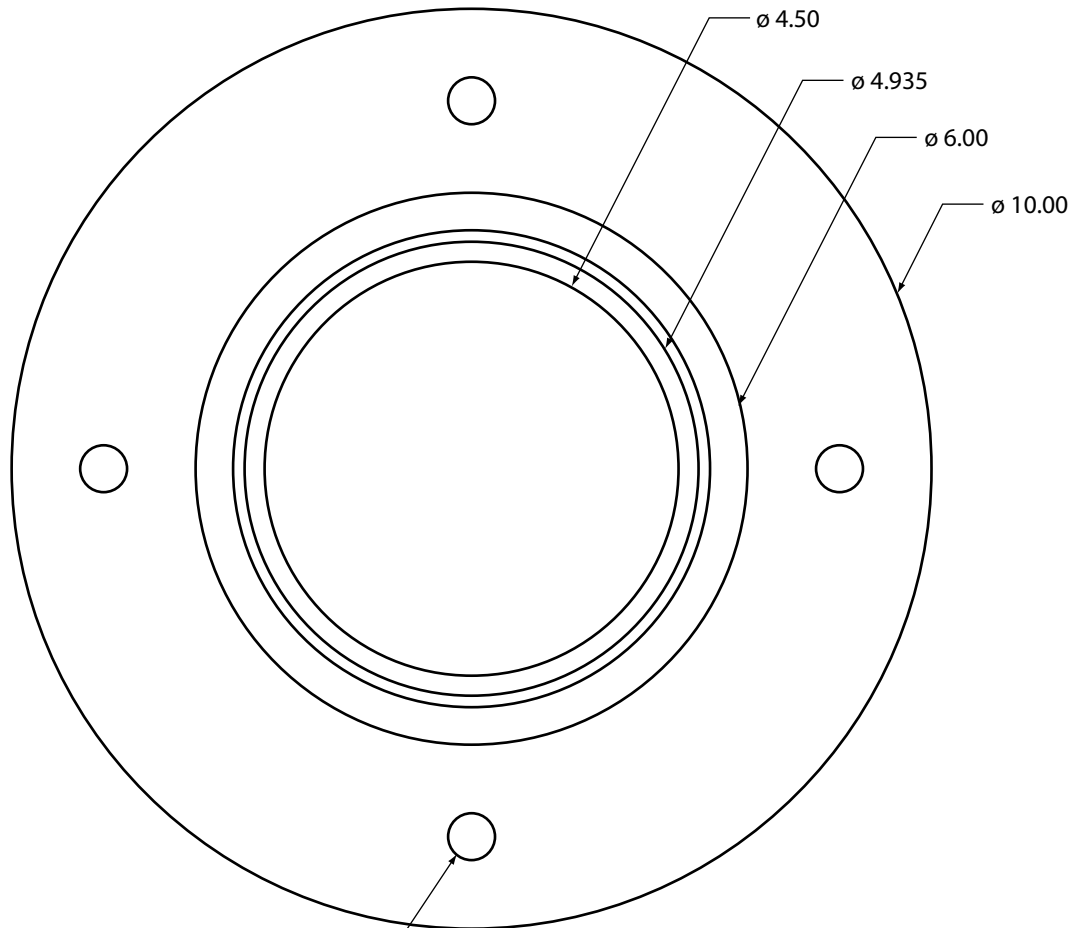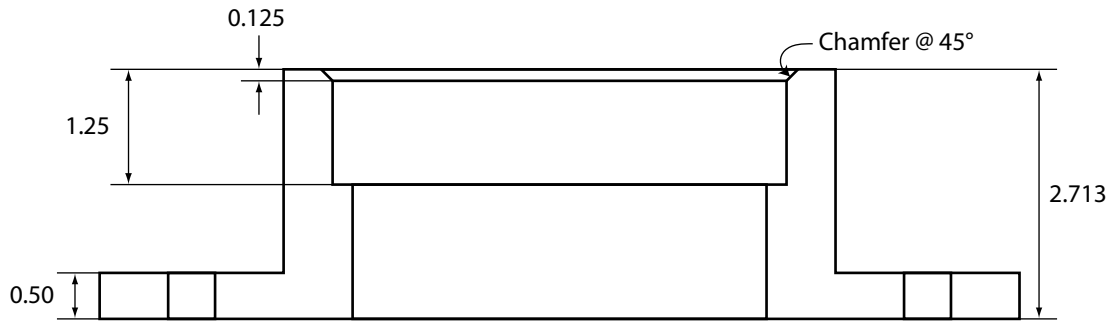
Drill thru for 1/2″ clearance
4 pl eq sp
on an 8″ BCD.

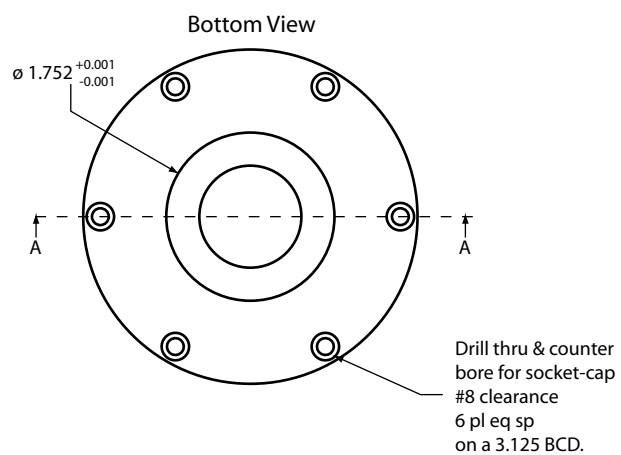| Lid bearing seat		
Kelley	lidseat3.pdf	6 May 2008
Scale 1:2.09 All units in inches unless otherwise noted. Tolerances unless otherwise noted: X.XX $^{+0.01}_{-0.01}$ X.XXX $^{+0.005}_{-0.005}$		

5/8 Cu tubing, flattened

14 AWG Al sheet

1/8" G-10 sheet

80/20, 1"

Ø 0.292 - Iris
Al stranded wire

Fiberglass tape
0.007 thick x 2 layers

OUTSIDE

INSIDE

5.6

8.35

4.75

80/20, 1.5"

Magnet Cross Section, v.2	
Kelley	30 November 2005
Scale 1.5:1 All units in inches unless otherwise noted.	

2A
2B
2C
2D
4A
4B
1A

(10.870,-4.649)
(10.516,-5.002)

(10.870,-6.149)
(10.516,-6.502)

(10.870,-7.649)
(10.516,-8.002)

(10.870,-9.149)
(10.516,-9.502)

x
y
O

r=15.872, c_y=15.872
r=14.872, c_y=15.872

r=15.872, c_y=17.372
r=14.872, c_y=17.372

r=15.872, c_y=18.872
r=14.872, c_y=18.872

r=15.872, c_y=20.372
r=14.872, c_y=20.372

r=11.285, c_y=17.035
r=12.285, c_y=17.035

r=11.285, c_y=18.535
r=12.285, c_y=18.535

r=9.030, c_y=17.530
r=8.030, c_y=17.530

(2.847,-0.512)
(2.756,-1.003)

(2.847,-2.012)
(2.756,-2.503)

(2.847,-3.512)
(2.756,-4.003)

(2.847,-5.012)
(2.756,-5.503)

(2.501,-6.287)
(2.388,-6.774)

(0.940,-7.791)
1/4-20 thru

(3.581,-9.514)
(3.377,-9.970)

(1.340,-0.558)
1/4-20 thru

(1.340,-2.058)
1/4-20 thru

(1.340,-3.558)
1/4-20 thru

(1.340,-5.058)
1/4-20 thru

(0.940,-6.291)
1/4-20 thru

(0.047,-7.500)
(0.045,-8.000)

(0.743,-9.032)
1/4-20 thru

(-4.036,-9.730)
(-3.805,-10.176)

(-8.848,-2.998)
(-8.565,-3.470)

(-8.848,-4.498)
(-8.565,-4.970)

(-8.848,-5.998)
(-8.565,-6.470)

(-8.848,-7.498)
(-8.565,-7.970)

(-6.844,-8.378)
(-6.533,-8.774)

(-7.626,-9.055)
(-7.273,-9.409)

(-7.626,-10.555)
(-7.273,-10.909)

(6.032,-11.145)
(5.678,-11.498)

(-6.032,-11.145)
(-5.678,-11.498)

(-10.870,-4.649)
(-10.516,-5.002)

(-10.870,-6.149)
(-10.516,-6.502)

(-10.870,-7.649)
(-10.516,-8.002)

(-10.870,-9.149)
(-10.516,-9.502)

(-7.626,-9.055)
(-7.273,-9.409)

(-7.626,-10.555)
(-7.273,-10.909)

Coordinates noted in (x,y) format.
All holes #8-32 thru except where otherwise noted.
See also GaussringsII.pdf.

Gauss plate 1, design II

| Kelley | Gaussplate1II.pdf | 25 October 2007 |

Scale 1:4
All units in inches unless otherwise noted.
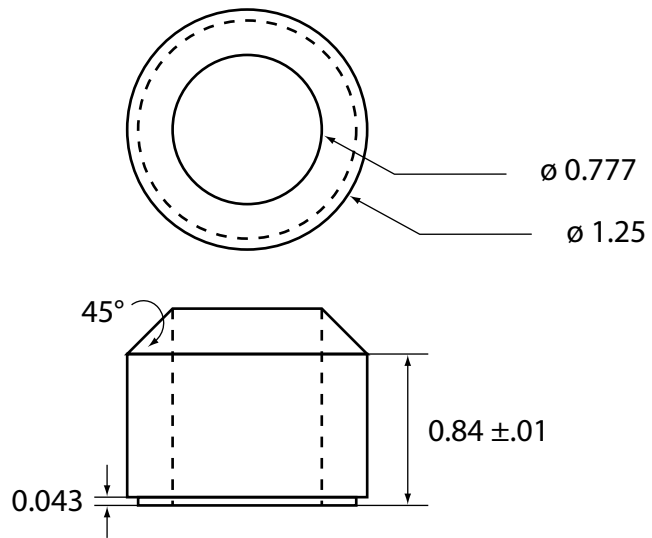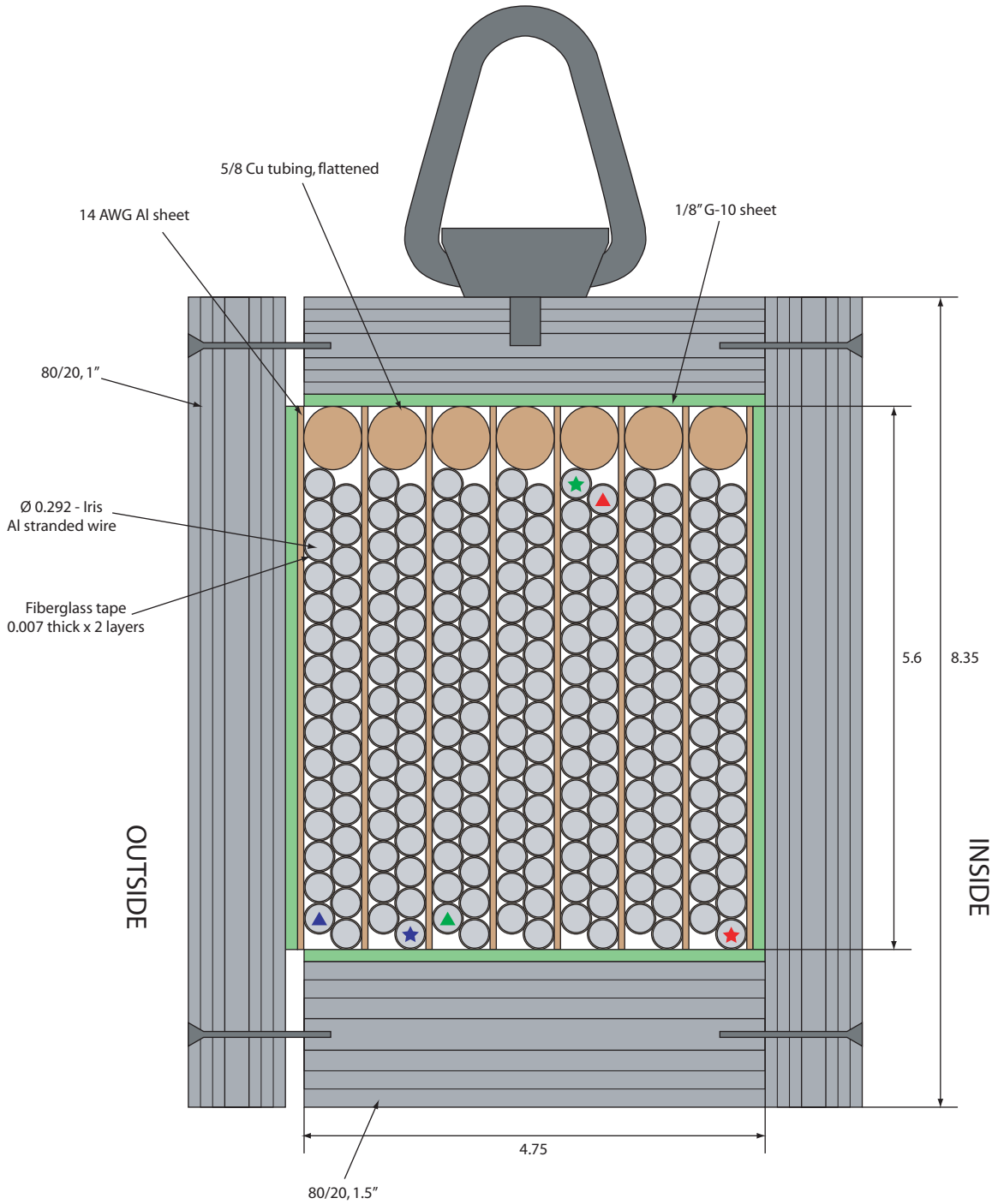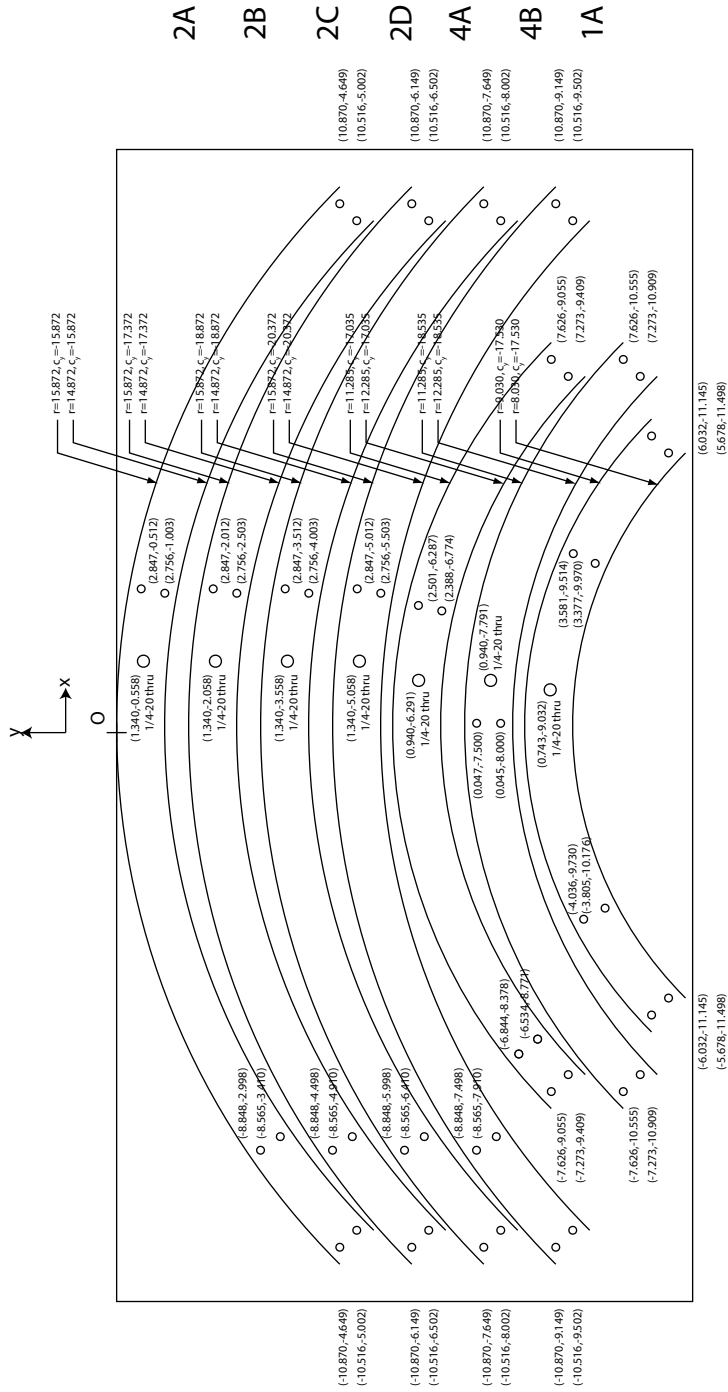Tolerances unless otherwise noted:
X.XX +0.01 -0.01   X.XXX +0.005 -0.005

x

y

O

3A
3B
3C
3D
4C
4D
1B

(10.870,-4.649)
(10.516,-5.002)

(10.870,-6.149)
(10.516,-6.502)

(10.870,-7.649)
(10.516,-8.002)

(10.870,-9.149)
(10.516,-9.502)

(8.508,-2.770)
(8.236,-3.190)

(8.508,-4.270)
(8.236,-4.690)

(8.508,-5.770)
(8.236,-6.190)

(8.508,-7.270)
(8.236,-7.690)

(7.626,-9.055)
(7.273,-9.409)

(7.626,-10.555)
(7.273,-10.909)

(6.032,-11.145)
(5.678,-11.498)

(6.917,-8.437)
(6.503,-8.826)

(4.830,-8.613)
(4.611,-9.063)

(4.746,-8.573)
(4.531,-9.024)

(0.940,-7.791)
1/4-20 thru

(1.708,-8.918)
(1.610,-9.408)

(0.743,-9.032)
1/4-20 thru

r=9.030, c_x=-17.530
r=8.030, c_y=-17.530

(1.340,-0.558)
1/4-20 thru

(1.340,-2.058)
1/4-20 thru

(1.340,-3.558)
1/4-20 thru

(1.340,-5.058)
1/4-20 thru

(0.940,-6.291)
1/4-20 thru

(-3.248,-0.591)
(-3.144,-1.081)

(-3.248,-2.091)
(-3.144,-2.581)

(-3.248,-3.591)
(-3.144,-4.081)

(-3.248,-5.091)
(-3.144,-5.581)

(-2.410,-6.266)
(-2.301,-6.754)

(-5.669,-10.024)
(-5.346,-11.207)

r=15.872, c_x=15.872
r=14.872, c_y=15.872

r=15.872, c_x=17.372
r=14.872, c_y=17.372

r=15.872, c_x=18.872
r=14.872, c_y=18.872

r=15.872, c_x=20.372
r=14.872, c_y=20.372

r=11.285, c_x=17.035
r=12.285, c_y=17.035

r=11.285, c_x=18.535
r=12.285, c_y=18.535

(-6.032,-11.145)
(-5.678,-11.498)

(-7.626,-9.055)
(-7.273,-9.409)

(-7.626,-10.555)
(-7.273,-10.909)

(-10.870,-4.649)
(-10.516,-5.002)

(-10.870,-6.149)
(-10.516,-6.502)

(-10.870,-7.649)
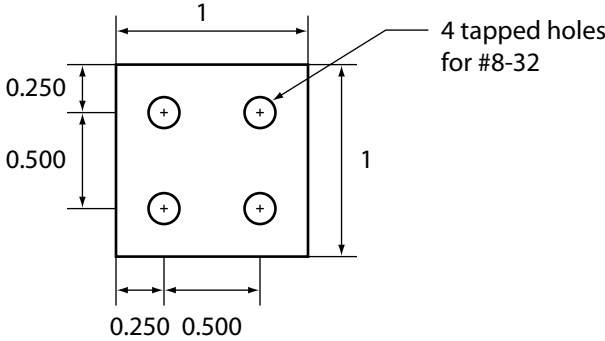(-10.516,-8.002)

(-10.870,-9.149)
(-10.516,-9.502)

Coordinates noted in (x,y) format.
All holes #8-32 thru except where otherwise noted.
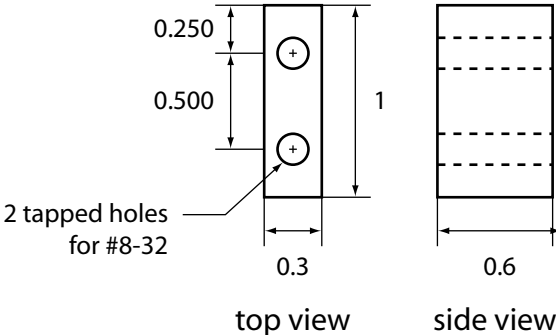See also Gaussrings II.pdf.

Gauss plate 2, design II
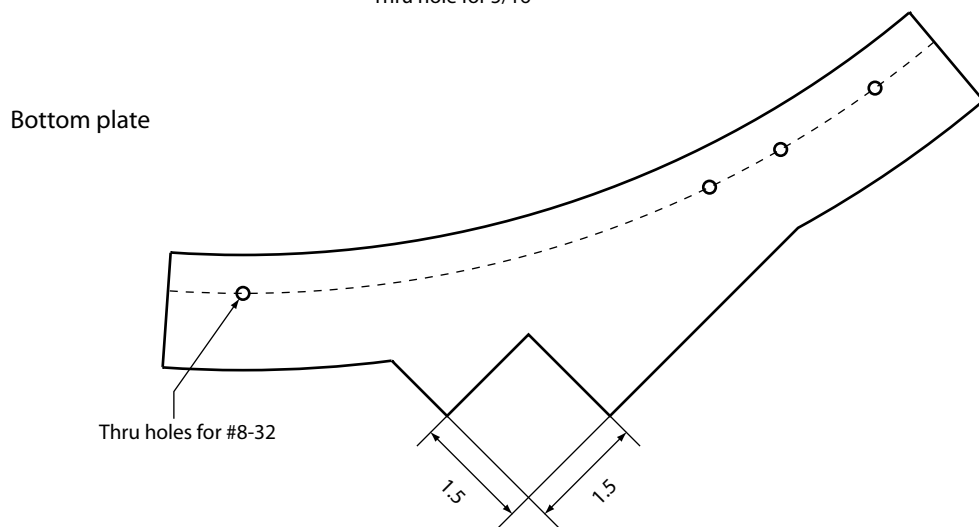
Kelley | Gaussplate2II.pdf | 25 October 2007

Scale 1:3
All units in inches unless otherwise noted.
Tolerances unless otherwise noted:
X.XX +0.01 -0.01   X.XXX +0.005 -0.005

1C

1D

y

x

O

(6.032,-2.645)
(5.678,-3.000)

(6.032,-4.145)
(5.678,-4.499)

(5.275,-3.511)
(4.975,-3.911)

(0.744,-0.532)
1/4-20 thru

(0.744,-2.032)
1/4-20 thru

(-0.252,-0.254)
(-0.237,-0.753)

(-2.198,-2.030)
(-2.073,-2.514)

$r=9.030, c_x=-9.030$
$r=8.030, c_y=-9.030$

$r=9.030, c_x=-10.530$
$r=8.030, c_y=-10.530$

(-6.032,-2.645)
(-5.678,-3.000)

(-6.032,-4.145)
(-5.678,-4.499)

Coordinates noted in (x,y) format.
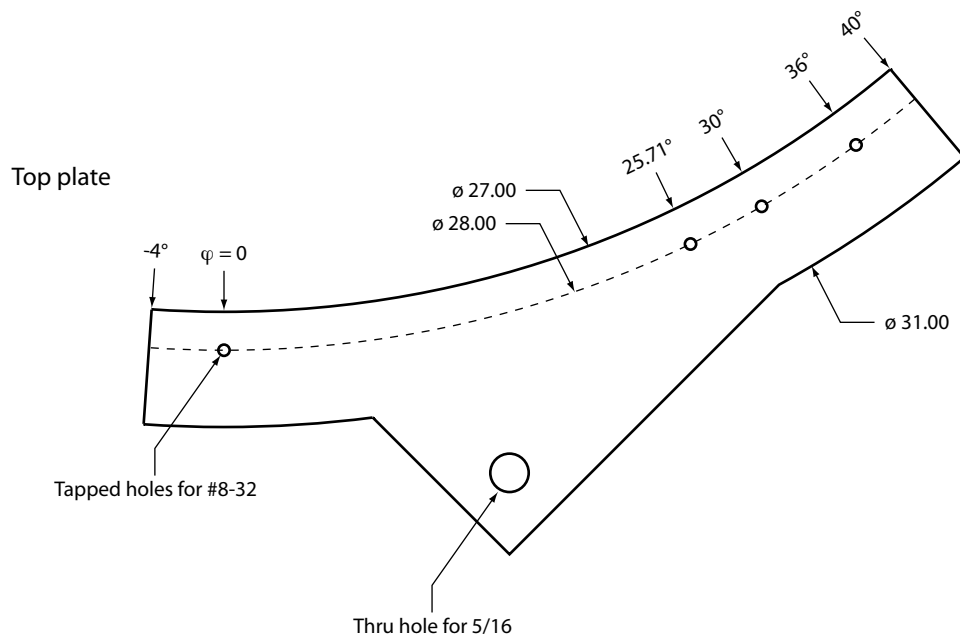All holes #8-32 thru except where otherwise noted.
See also GaussringsII.pdf.
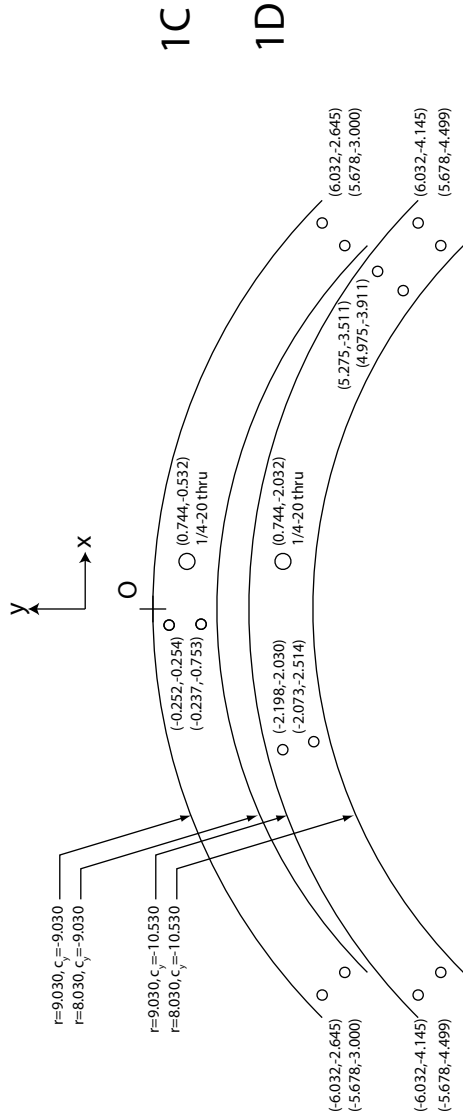
Gauss plate 3, design II		
Kelley	Gaussplate3II.pdf	11 October 2007
	Scale 1:3	
	All units in inches unless otherwise noted.	
	Tolerances unless otherwise noted:	
	X.XX $^{+0.01}_{-0.01}$ X.XXX $^{+0.005}_{-0.005}$	

Joining block
qty 16

1

4 tapped holes
for #8-32

0.250

0.500

1

0.250 0.500

Probe mount
qty 30

0.250

0.500

1

2 tapped holes
for #8-32

0.3

0.6

top view

side view

Gauss ring hardware, design II		
Kelley	GausshardwareII.pdf	25 October 2007
Scale 1:1 All units in inches unless otherwise noted. Tolerances unless otherwise noted: X.XX $^{+0.01}_{-0.01}$ X.XXX $^{+0.005}_{-0.005}$		

Top plate

40°

36°

30°

25.71°

ø 27.00

ø 28.00

-4°   φ = 0

ø 31.00

Tapped holes for #8-32

Thru hole for 5/16

Bottom plate

Thru holes for #8-32

1.5

1.5

For full-size template, see electronic file.

Equatorial array		
Kelley	equatorialarray.pdf	31 August 2007
Scale 1:2.5 All units in inches unless otherwise noted. Tolerances unless otherwise noted: $X.XX\,^{+0.01}_{-0.01}$ $X.XXX\,^{+0.005}_{-0.005}$		

Appendix C

Code for calculating Gauss coefficients

On the following pages we include the C code used to project onto the vector spherical harmonics, yielding Gauss coefficients. It has been slightly censored for your emotional safety.

```c
/* Usage: getcoeff2008 [-lims tstart tmax] [-bias biasfile] [-current I] [-off toffstart
toffmax] hallfile Nsamples

This C program reads data from hallfile (containing Nsamples samples), calculates Gauss
coefficients through l=4 and writes them to stdout. Use the -lims option to calculate
coefficients only for data between times tstart and tmax. Use the -bias option to
subtract DC offsets, as listed in biasfile, from the probes before calculating
coefficients. Use the -current option to subtract DC offsets, according to the magnet
current I, from the probes before calculating coefficients. Use the -off option to
subtract the mean value of each probe, between times toffstart and toffmax, from the
probes before calculating coefficients. If none of the options -bias, -current, and -off
are used, only the fluctuating components of the signals are used (no DC).

Requires auxiliary files containing probe positions, the inverted matrix that depends on
probe positions and Gauss basis functions, and the effect of magnet current on each
probe. File locations are set in the code below. The column layout of hallfile is also
set in the code below. To undersample, set tstep > 1 below.

To compile: cc -o getcoeff2008 getcoeff2008.c -lm

This code updated for dynamo3.5 by Doug Kelley, 30 January 2008. Original version by Dan
Sisan. Last modified 1 August 2008.
*/

#include <stdlib.h>
#include <stdio.h>
#include <math.h>
#include <ctype.h>
#include <string.h>

#define Ncoeff 24 /* Number of Gauss coefficients */
#define PROBES 30 /* Number of hall probes */
/*#define Ncols 40 /* Hallfile column layout as per /zero/probeinfo on 29 Jan 2008. */
#define Ncols 41 /* Hallfile column layout as per /zero/probeinfo on 28 July 2008. */
#define firstcol 7 /* Hallfile column layout as per /zero/probeinfo on 29 Jan 2008.
Includes G probes only. */
#define timecol 0 /* time column */
#define probeposfile "/zero/probepos2008_allprobes.dat" /* Path to probe positions file */
#define matrixfile "/zero/invLS2008_allprobes.dat" /* Path to inverted matrix file */
#define gshiftfile "/zero/gshift.dat" /* from 032408 calibration */

/* -=- Variables -=------------------------------------------------------- */
float sum[PROBES], bias[PROBES], gshift[Ncoeff];
double **data2, wvec[Ncoeff], sum2[PROBES], prod, Floor[PROBES];
int i, j, t, p, c, tnum2, Nsamples, argpos, offflag, biasflag, currentflag, limsflag;
float **data, probepos[PROBES][3], minv[Ncoeff][Ncoeff], pscale[PROBES]; /* arrays */
float tstart, tmax, tstart2, tmax2, tstep=1., tfactor, current; /* scalars */
FILE *datpt, *probePospt, *minvpt, *biaspt, *gshiftpt;
double getF (int fnum, int probe); /* a subroutine defined below */
char biasfile[256]; /* string */


/* -=- Function Definitions for subroutine getF -=----------------------------------------
------------- */
double f1 (float r,float th, float ph) { return 3.*cosf(th)*sinf(th)/powf(r,3.);}
double f2 (float r,float th, float ph) { return (-2.+3.*powf(cosf(th),
2.))*fabs(sinf(th))/sinf(th)*cosf(ph)/powf(r,3.);}
double f3 (float r,float th, float ph) { return (-2.+3.*powf(cosf(th),
2.))*fabs(sinf(th))/sinf(th)*sinf(ph)/powf(r,3.);}
```

```c
double f4 (float r,float th, float ph) { return .75*(3.+5.*cosf(2.*th))*sinf(th)/powf(r,
4.); }
double f5 (float r,float th, float ph) { return sqrt(3.)*(-4.+5.*powf(cosf(th),
2.))*cosf(th)*fabs(sinf(th))/sinf(th)*cosf(ph)/powf(r,4.);}
double f6 (float r,float th, float ph) { return sqrt(3.)*(-4.+5.*powf(cosf(th),
2.))*cosf(th)*fabs(sinf(th))/sinf(th)*sinf(ph)/powf(r,4.);}
double f7 (float r,float th, float ph) { return .5*sqrt(3.)*(3.-5.*powf(cosf(th),
2.))*sinf(th)*cosf(2.*ph)/powf(r,4.);}
double f8 (float r,float th, float ph) { return .5*sqrt(3.)*(3.-5.*powf(cosf(th),
2.))*sinf(th)*sinf(2.*ph)/powf(r,4.); }
double f9 (float r,float th, float ph) { return
5./16.*(2.*sinf(2.*th)+7.*sinf(4.*th))/powf(r,5.);}
/* double f10 (float r,float th, float ph) { return sqrt(3/2.)*(-
3+35*cosf(4.*th))*cosf(th)*cosf(ph)*fabs(sinf(th))/sinf(th)/16./powf(r,5.);} */
/* double f11(float r,float th, float ph) {return sqrt(3./2)*(-
3+35*cosf(4.*th))*cosf(th)*sinf(ph)*fabs(sinf(th))/sinf(th)/16./powf(r,5.); } */
double f10 (float r,float th, float ph) { return
1./16.*sqrt(3./2.)*(sinf(th)/fabs(sinf(th)))*(35.*cosf(4.*th)-3.)*cosf(ph)/powf(r,5.);}
double f11 (float r,float th, float ph) { return
1./16.*sqrt(3./2.)*(sinf(th)/fabs(sinf(th)))*(35.*cosf(4.*th)-3.)*sinf(ph)/powf(r,5.);}
double f12 (float r,float th, float ph) { return .5*sqrt(15.)*cosf(th)*(5.-
7.*powf(cosf(th),2.))*sinf(th)*cosf(2.*ph)/powf(r,5.);}
double f13 (float r,float th, float ph) { return .5*sqrt(15.)*cosf(th)*(5.-
7.*powf(cosf(th),2.))*sinf(th)*sinf(2.*ph)/powf(r,5.); }
double f14 (float r,float th, float ph) { return sqrt(5./2.)*(-
1.+7.*cosf(2.*th))*cosf(3.*ph)*sinf(th)*fabs(sinf(th))/4./powf(r,5.);}
double f15 (float r,float th, float ph) { return sqrt(5./2.)*(-
1.+7.*cosf(2.*th))*sinf(3.*ph)*sinf(th)*fabs(sinf(th))/4./powf(r,5.);}
double f16 (float r,float th, float ph) { return 15.*(2.*sinf(th) + 7.*(sinf(3.*th) +
3.*sinf(5.*th)))/128./powf(r,6.);}
/* double f17 (float r,float th, float ph) { return sqrt(5./2.)*(-
6*cosf(th)+7*cosf(3*th)+63*cosf(5*th))*cosf(ph)*fabs(sinf(th))/sinf(th)/32./powf(r,6);} */
/* double f18 (float r,float th, float ph) { return sqrt(5./2.)*(-
6*cosf(th)+7*cosf(3*th)+63*cosf(5*th))*sinf(ph)*fabs(sinf(th))/sinf(th)/32./powf(r,6);} */
double f17 (float r,float th, float ph) { return .5*sqrt(5./2.)*cosf(th)*(18.-
77.*powf(cosf(th),2.)+63.*powf(cosf(th),4.))*cosf(ph)*sinf(th)/fabs(sinf(th))/powf(r,6.);}
double f18 (float r,float th, float ph) { return .5*sqrt(5./2.)*cosf(th)*(18.-
77.*powf(cosf(th),2.)+63.*powf(cosf(th),4.))*sinf(ph)*sinf(th)/fabs(sinf(th))/powf(r,6.);}
double f19 (float r,float th, float ph) { return -
sqrt(5.)*(5.+28.*cosf(2.*th)+63.*cosf(4.*th))*cosf(2.*ph)*sinf(th)/32./powf(r,6.);}
double f20 (float r,float th, float ph) { return -
sqrt(5.)*(5.+28.*cosf(2.*th)+63.*cosf(4.*th))*sinf(2.*ph)*sinf(th)/32./powf(r,6.);}
double f21 (float r,float th, float ph) { return 1.5*sqrt(35./2.)*cosf(th)*(-
2.+3.*powf(cosf(th),2.))*cosf(3.*ph)*fabs(sinf(th))*sinf(th)/powf(r,6.);}
double f22 (float r,float th, float ph) { return 1.5*sqrt(35./2.)*cosf(th)*(-
2.+3.*powf(cosf(th),2.))*sinf(3.*ph)*fabs(sinf(th))*sinf(th)/powf(r,6.);}
double f23 (float r,float th, float ph) { return -sqrt(35.)*(-
1.+9.*cosf(2.*th))*cosf(4.*ph)*powf(sinf(th),3.)/16./powf(r,6.);}
double f24 (float r,float th, float ph) { return -sqrt(35.)*(-
1.+9.*cosf(2.*th))*sinf(4.*ph)*powf(sinf(th),3.)/16./powf(r,6.);}


/* -=- Main Program Start -=--------------------------------------------------- */
main(int argc, char *argv[])
{

/* -=- Parse Inputs -=--------------------------------------------------- */
if (argc<3) {
```

```c
  fprintf(stderr,"Usage: %s [-lims tstart tmax] [-bias biasfile] [-current I] [-off
toffstart toffmax] hallfile Nsamples\n",argv[0]);
  exit(1);
}


limsflag=0;
biasflag=0;
currentflag=0;
offflag=0;

if (argc>3) {
  argpos = 1;
  while (argpos<argc && argv[argpos][0]=='-') {
    if (!strcmp(argv[argpos],"-lims")) {
      tstart=atof(argv[argpos+1]);
      tmax=atof(argv[argpos+2]);
      /* fprintf(stderr,"Using data between %f s and %f s.\n",tstart,tmax); */
      argpos+=3;
      limsflag=1;
    }
    else if (!strcmp(argv[argpos],"-off")) {
      if ((biasflag)||(currentflag)) {
        fprintf(stderr,"Cannot use -off option with -bias or -current option.\n");
        exit(1);
      }
      tstart2=atof(argv[argpos+1]);
      tmax2=atof(argv[argpos+2]);
      /*fprintf(stderr,"Using toffstart=%f s, toffmax=%f s.\n",tstart2,tmax2);*/
      argpos+=2;
      offflag=1;
    }
    else if (!strcmp(argv[argpos],"-bias")) {
      if (offflag) {
        fprintf(stderr,"Cannot use -off option with -bias or -current option.\n");
        exit(1);
      }
      strcpy(biasfile,argv[argpos+1]);
      /*fprintf(stderr,"Using %s for biases.\n",biasfile);*/
      argpos+=2;
      biasflag=1;
    }
    else if (!strcmp(argv[argpos],"-current")) {
      if (offflag) {
        fprintf(stderr,"Cannot use -off option with -bias or -current option.\n");
        exit(1);
      }
      current=atof(argv[argpos+1]);
      /*fprintf(stderr,"Using current = %f amps.\n",current);*/
      argpos+=2;
      currentflag=1;
    }
    else {
      fprintf(stderr,"Usage: %s [-lims tstart tmax] [-bias biasfile] [-current I] [-off
tstart2 tmax2] hallfile Nsamples\n",argv[0]);
      exit(1);
    }
  }
  if ((argc-argpos)!=2) {
```

```c
      fprintf(stderr,"Usage: %s [-lims tstart tmax] [-bias biasfile] [-current I] [-off
tstart2 tmax2] hallfile Nsamples\n",argv[0]);
      exit(1);
    }
    else {
      datpt = fopen(argv[argpos],"r");
      Nsamples=atoi(argv[argpos+1]);
    }
  }
  else {
    datpt = fopen(argv[1],"r");
    Nsamples=atoi(argv[2]);
  }

  /* -=- Read Data -=------------------------------------------------------ */

  /* -=- hall* file -=- */
  data=(float **) malloc(Nsamples*sizeof(float *));
  for (i=0;i<Nsamples;i++) {
    data[i]=(float *) malloc(Ncols*sizeof(float));
  }
  for (i=0;i<Nsamples;i++) {
    for (j=0;j<Ncols;j++) {
      fscanf(datpt,"%f",&data[i][j]);
    }
  }
  fclose(datpt);

  /* -=- probepos file -=- */
  probePospt=fopen(probeposfile,"r");
  if (probePospt == NULL) {
    fprintf(stderr,"probePos f***ed up, yo.\n"); /* Sisan-style interface! */
    exit(1);
  }
  i=0;
  while(!feof(probePospt)) {
    for (j=0; j<3; j++) fscanf(probePospt,"%f",&probepos[i][j]);
    i++;
  }
  fclose(probePospt);

  /* -=- Inverted Matrix -=- */
  minvpt=fopen(matrixfile,"r");
  if (minvpt == NULL) {
    fprintf(stderr,"minvpt f***ed up, yo.\n"); /* Sisan-style interface! */
    exit(1);
  }
  i=0;
  while(!feof(minvpt)) {
    for (j=0; j<24; j++) fscanf(minvpt,"%f",&minv[i][j]);
    i++;
  }
  fclose(minvpt);

  /* -=- Biases file -=- */
  if (biasflag) {
    biaspt=fopen(biasfile,"r");
    if (biaspt == NULL) {
```

```c
      fprintf(stderr,"Biases file f***ed up, yo.\n");
      exit(1);
    }
    else {
      i=0;
      while(!feof(biaspt)) {
        fscanf(biaspt,"%f",&bias[i]);
        i++;
      }
    fclose(biaspt);
    }
}

/* -=- gshift file -=- */
if (currentflag) {
  gshiftpt=fopen(gshiftfile,"r");
  if (gshiftpt == NULL) {
    fprintf(stderr,"gshift file f***ed up, yo.\n");
    exit(1);
  }
  else {
    i=0;
    while(!feof(gshiftpt)) {
      fscanf(gshiftpt,"%f",&gshift[i]);
      i++;
    }
    fclose(gshiftpt);
  }
}

/* -=- Initialize a few things... -=---------------------------------------------------
*/

tfactor=data[Nsamples-1][timecol]/(Nsamples-1);

/* Time limits of data to be calc'd -=- */
if (limsflag) {
  tstart/=tfactor;
  if (tmax/tfactor>(Nsamples-1)) {
    tmax=Nsamples-1;
  }
  else {
    tmax/=tfactor;
  }
}
else {
  tstart=0;
  tmax=Nsamples-1;
}

/* Time limits for offset -=- */
if (offflag) {
  tstart2/=tfactor;
  if (tmax2/tfactor>(Nsamples-1)) {
    tmax2=Nsamples-1;
  }
  else {
    tmax2/=tfactor;
```

```c
    }
}
else if (!biasflag) {
  /*fprintf(stderr,"Calculating fluctuating components only.\n");*/
  tstart2=tstart;
  tmax2=tmax;
}
else {
  tstart2=0;
  tmax2=0;
}

for (j=0;j<PROBES;j++) {
  sum[j]=0.;
  sum2[j]=0.;
  wvec[j]=0;
  pscale[j]=839.5; /* From array calibration; see dhk notes 29 Feb 2008. */
  Floor[j]=0.;
}

/* -=- Allocate for data2, exclude extra columns and get offset -=----------------------
--------------------------- */
data2=(double **) malloc((tmax-tstart)*sizeof(double *));
for (i=0;i<Nsamples;i++) {
  data2[i]=(double *) malloc((PROBES)*sizeof(double));
}

tnum2=0;

for(i=0;i<=(tmax-tstart);i+=tstep){
  for (j=firstcol;j<(firstcol+PROBES);j++) {
    data2[i][j-firstcol]=data[i+(int)tstart][j];
    if ((i+tstart>tstart2)&&(i+tstart<tmax2)) {
      sum2[j-firstcol]+=data2[i][j-firstcol];
      if(j==firstcol){tnum2++;}
    }
  }
}

if (biasflag) {
  for (i=0;i<PROBES;i++) {
    Floor[i]+=bias[i];
  }
}

if ((!biasflag)&&(!currentflag)) {
  for (i=0;i<PROBES;i++) {
    Floor[i]=sum2[i]/tnum2;
  }
}

/* -=- Compute wvec -=-------------------------------------------------- */

for(t=0;t<=(tmax-tstart);t+=tstep) {
  for(c=0;c<Ncoeff;c++) {
    wvec[c]=0;
    for( p=0;p<PROBES;p++) {
      wvec[c]+=(data2[t][p]-Floor[p])*getF(c+1,p)*pscale[p];
```

```c
    }
  }

  /* -=- matrix multiply -=- */
  printf("%f ",t*tfactor);
  if (currentflag) {
    for (i=0;i<Ncoeff;i++) {
      prod=0.;
      for (j=0;j<Ncoeff;j++) {
        prod+=minv[i][j]*wvec[j];
      }
      prod-=current*gshift[i];
      printf("%.10f ",prod);
    }
  }
  else {
    for (i=0;i<Ncoeff;i++) {
      prod=0.;
      for (j=0;j<Ncoeff;j++) {
        prod+=minv[i][j]*wvec[j];
      }
      printf("%.10f ",prod);
    }
  }
  printf("\n");
}
return(0);
} /* end of main */


/* -=- subroutine getF -=------------------------------------------------- */
double getF (int fnum, int probe) {
if (fnum==1){return f1(probepos[probe][0],probepos[probe][1],probepos[probe][2]);}
if (fnum==2){return f2(probepos[probe][0],probepos[probe][1],probepos[probe][2]);}
if (fnum==3){return f3(probepos[probe][0],probepos[probe][1],probepos[probe][2]);}
if (fnum==4){return f4(probepos[probe][0],probepos[probe][1],probepos[probe][2]);}
if (fnum==5){return f5(probepos[probe][0],probepos[probe][1],probepos[probe][2]);}
if (fnum==6){return f6(probepos[probe][0],probepos[probe][1],probepos[probe][2]);}
if (fnum==7){return f7(probepos[probe][0],probepos[probe][1],probepos[probe][2]);}
if (fnum==8){return f8(probepos[probe][0],probepos[probe][1],probepos[probe][2]);}
if (fnum==9){return f9(probepos[probe][0],probepos[probe][1],probepos[probe][2]);}
if (fnum==10){return f10(probepos[probe][0],probepos[probe][1],probepos[probe][2]);}
if (fnum==11){return f11(probepos[probe][0],probepos[probe][1],probepos[probe][2]);}
if (fnum==12){return f12(probepos[probe][0],probepos[probe][1],probepos[probe][2]);}
if (fnum==13){return f13(probepos[probe][0],probepos[probe][1],probepos[probe][2]);}
if (fnum==14){return f14(probepos[probe][0],probepos[probe][1],probepos[probe][2]);}
if (fnum==15){return f15(probepos[probe][0],probepos[probe][1],probepos[probe][2]);}
if (fnum==16){return f16(probepos[probe][0],probepos[probe][1],probepos[probe][2]);}
if (fnum==17){return f17(probepos[probe][0],probepos[probe][1],probepos[probe][2]);}
if (fnum==18){return f18(probepos[probe][0],probepos[probe][1],probepos[probe][2]);}
if (fnum==19){return f19(probepos[probe][0],probepos[probe][1],probepos[probe][2]);}
if (fnum==20){return f20(probepos[probe][0],probepos[probe][1],probepos[probe][2]);}
if (fnum==21){return f21(probepos[probe][0],probepos[probe][1],probepos[probe][2]);}
if (fnum==22){return f22(probepos[probe][0],probepos[probe][1],probepos[probe][2]);}
if (fnum==23){return f23(probepos[probe][0],probepos[probe][1],probepos[probe][2]);}
if (fnum==24){return f24(probepos[probe][0],probepos[probe][1],probepos[probe][2]);}
return(0);
} /* end of getF */
```

Appendix D

Grayscale figures

Some of our figures, originally shown in color, are reproduced poorly by grayscale printers — deep red and deep blue, usually representing opposite ends of the colormap, both print as dark gray. Here we reproduce those figures using a colormap better adapted for grayscale printing.
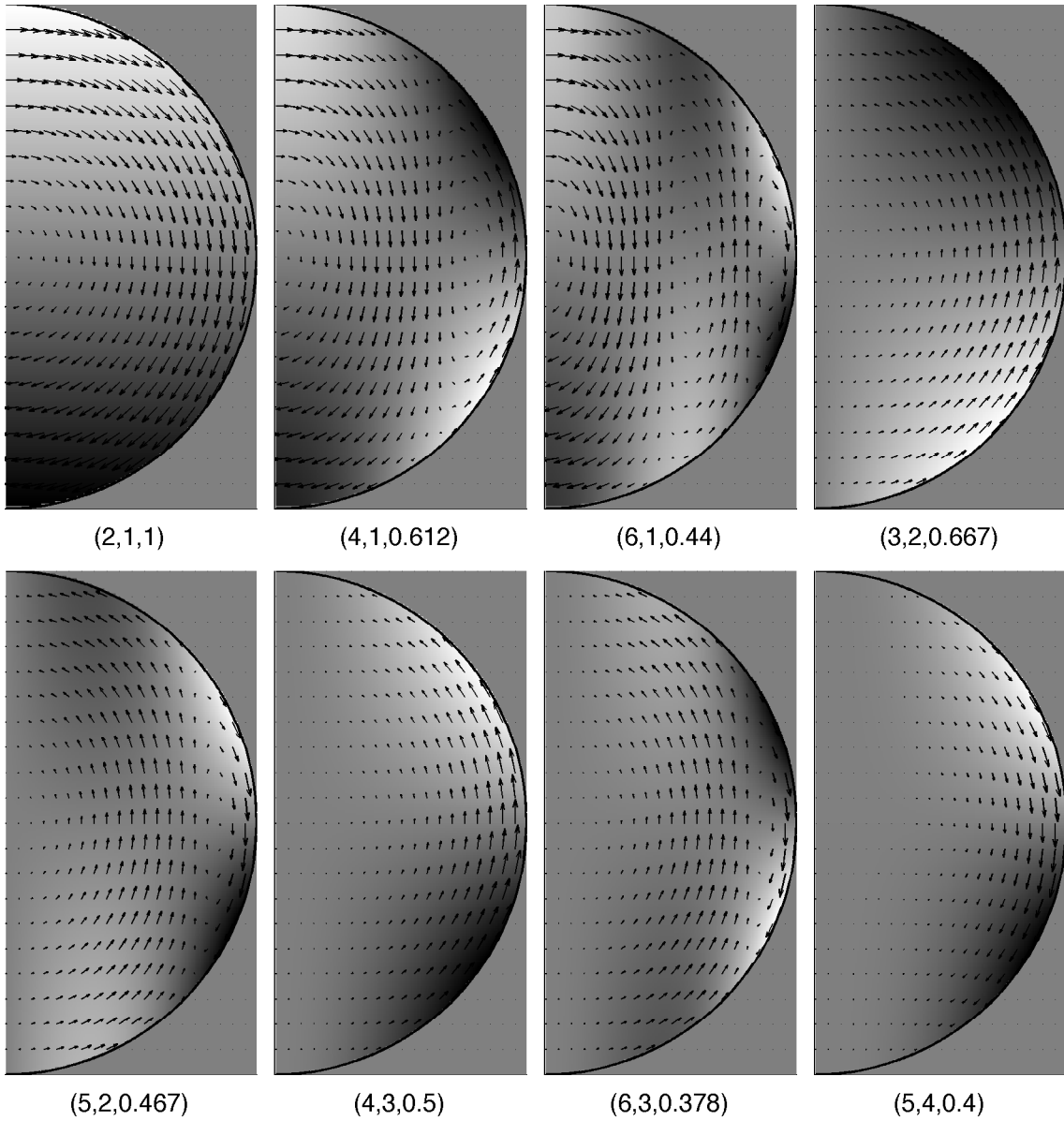
Figure D.1: Examples of inertial modes in a full sphere. Each image shows a meridional cross-section of the sphere, with the axis of rotation at left. The polar and radial components of the velocity are indicated with arrows, while the azimuthal component is indicated with color (light colors indicate flow out of the page; dark colors, into the page). The amplitudes are arbitrary. The corresponding degree l, order m, and normalized frequency ω/Ω are listed below each image. See also Fig. 2.1.

179
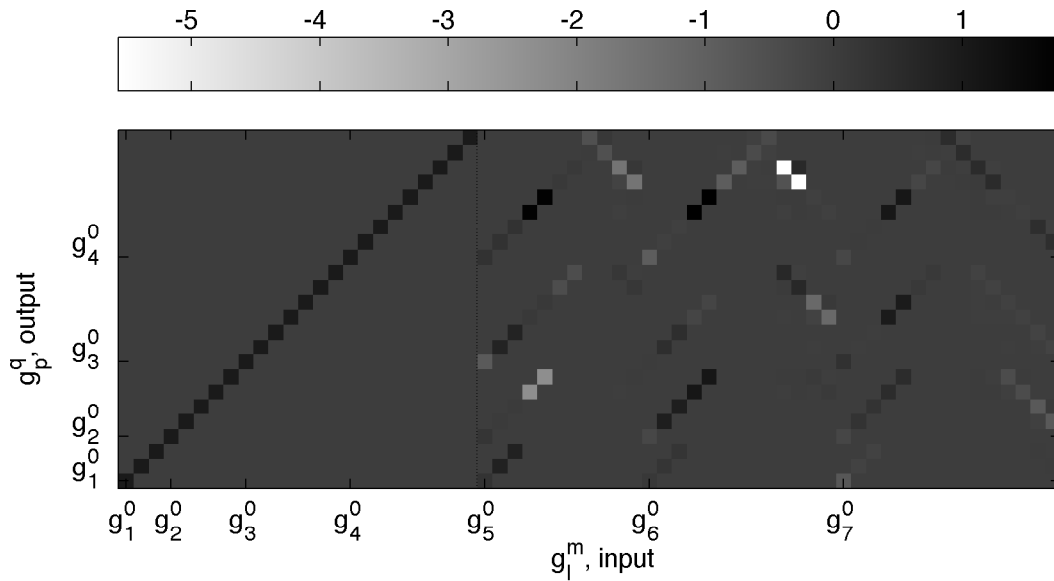
Figure D.2: Aliasing properties of the Gauss array design. Single-mode input fields g_l^m with $l \leq 4$ produce output g_p^q with $(p,q) = (l,m)$, but aliasing occurs for $l > 4$. Here basis functions are ordered as in Table 3.5. The dotted line divides the low-degree modes, for which the array was designed, from the high-degree modes, which alias. See also Fig. 3.5.

180
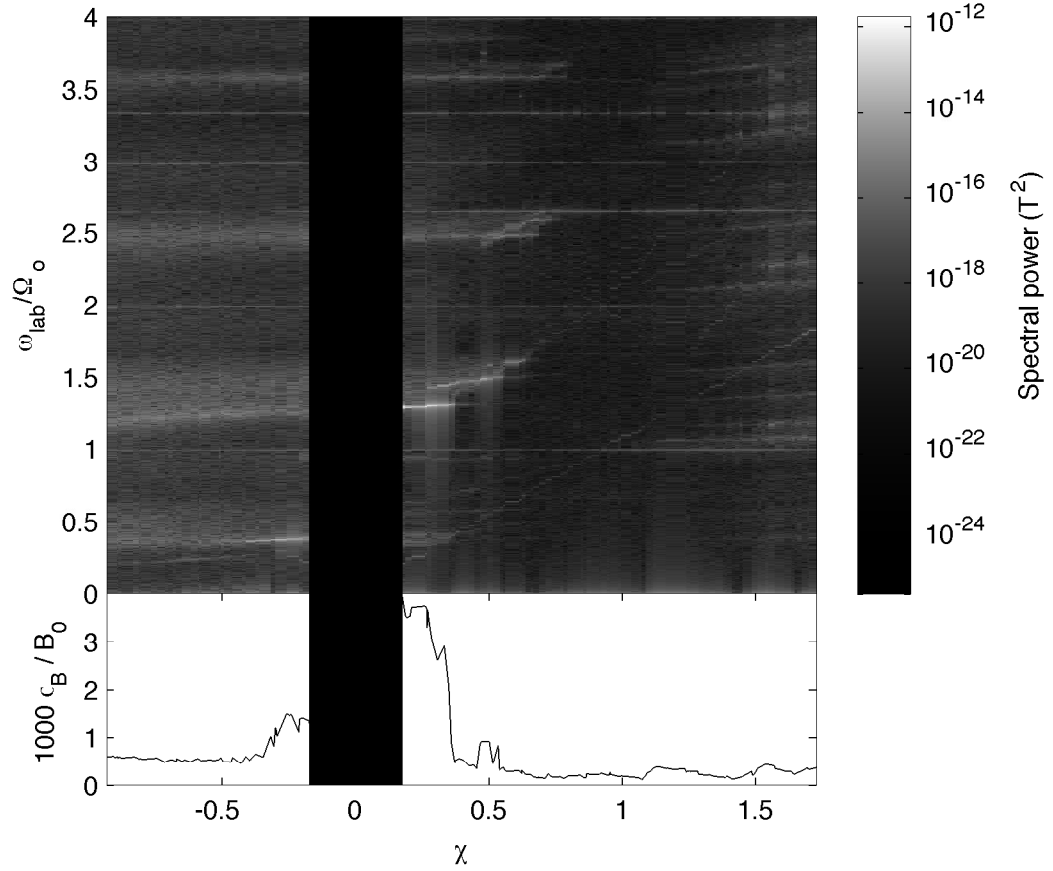
Figure D.3: Magnetic field data taken from an equatorial Hall probe with $E = 7.26 \times 10^{-8}$ ($\Omega_o/2\pi = 18$ Hz). The upper plot is a spectrogram, with its vertical axis showing the normalized signal frequency $\omega_{\text{lab}}/\Omega_o$ as measured in the laboratory frame, and its horizontal axis showing the rotation rate ratio χ. Each column of pixels is a power spectrum of 32 s of data, with power indicated by the varying shades. The white central region lies at low speeds inaccessible with our AC motors. The lower plot shows the standard deviation of the same data, normalized by the applied magnetic field B_0. See also Fig. 4.3.
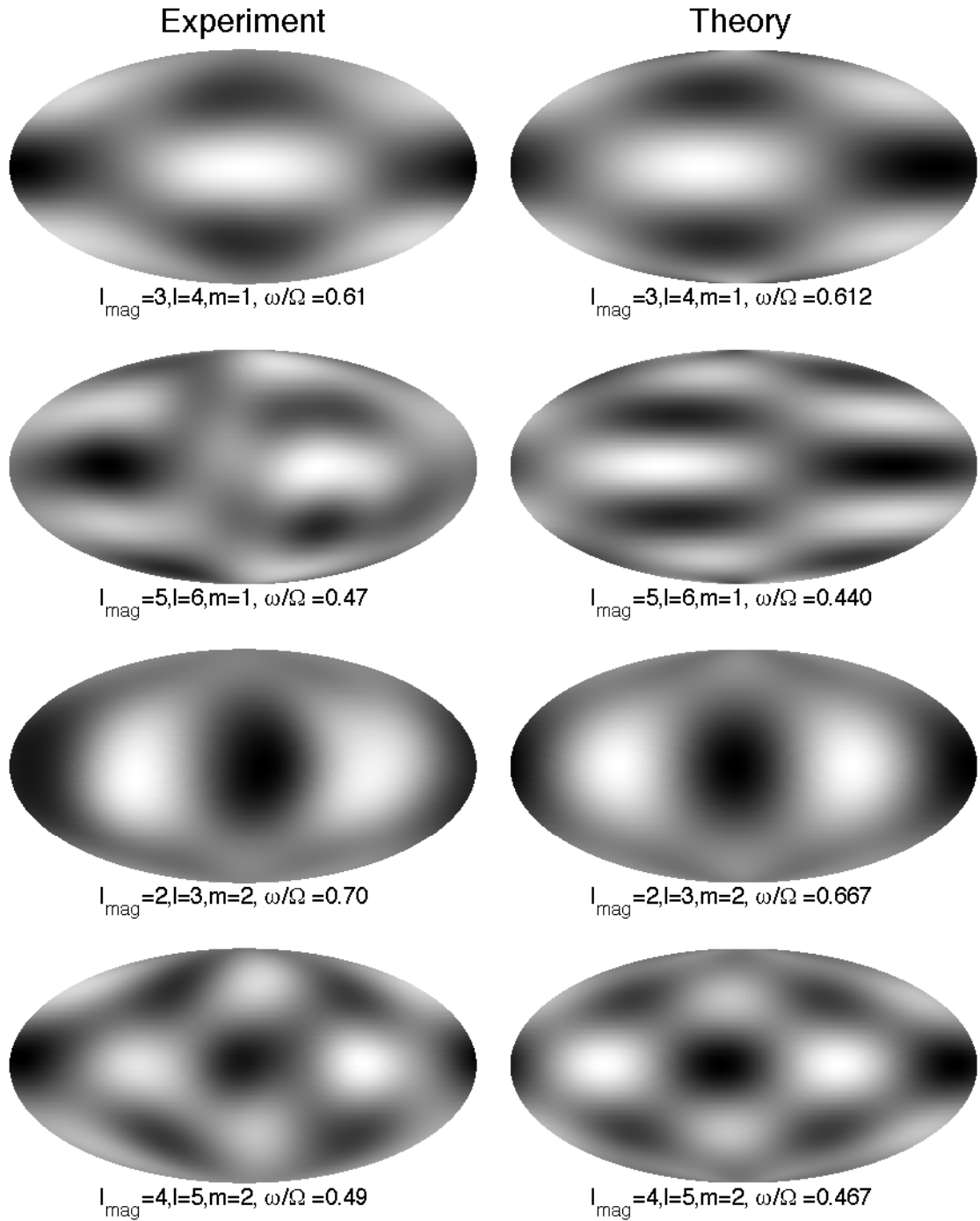
Figure D.4: Induction B_s/B_0 at the surface of the fluid, shown as a Mollweide projection with the axis of rotation vertical. The left column shows data taken under the same experimental conditions as the first four traces shown in Fig. 4.1, respectively. Mean values have been removed. The right column shows numerical calculations of the induction produced by analytically-known inertial modes. See also Fig. 4.4.
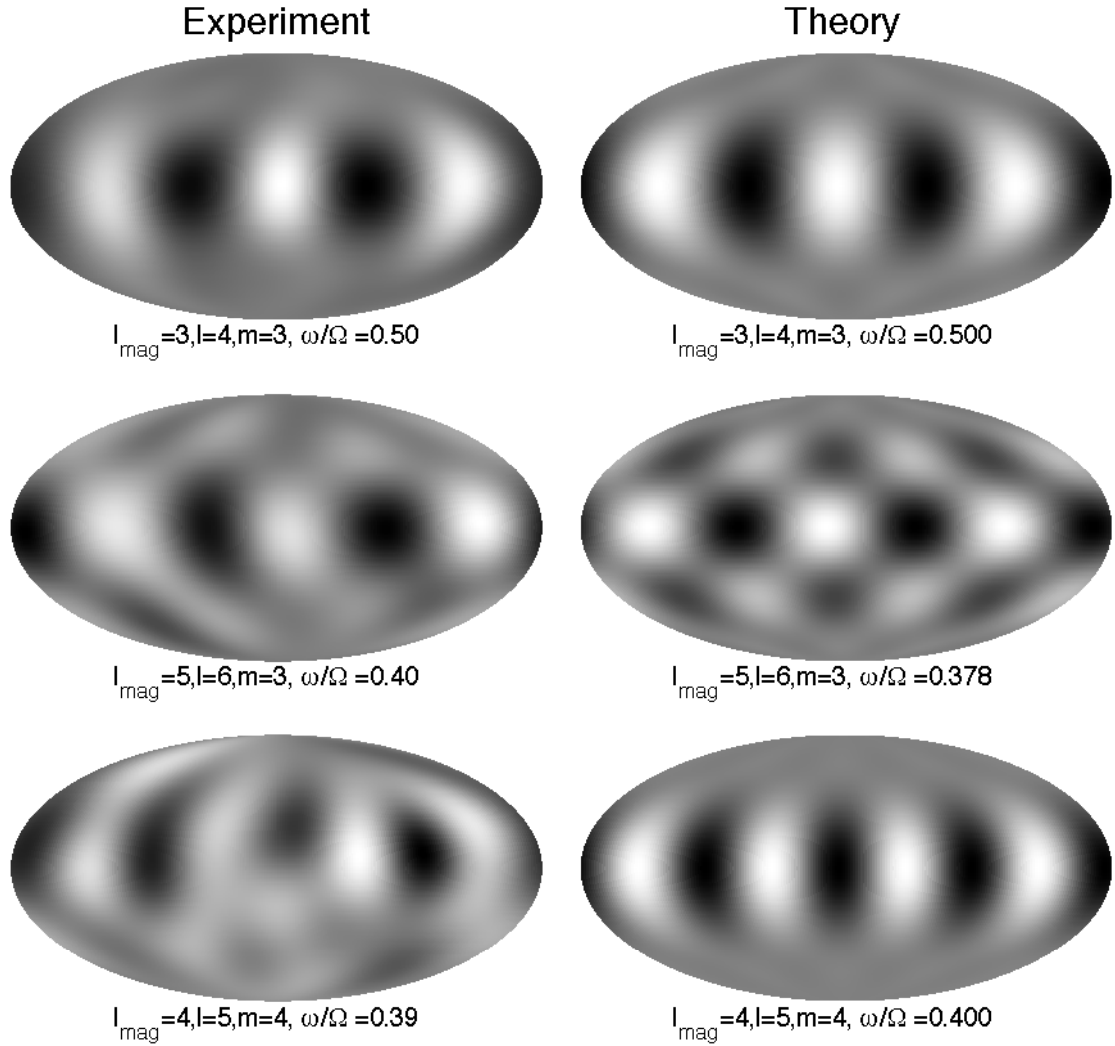
Experiment	Theory
I_{mag}=3,l=4,m=3, ω/Ω =0.50	I_{mag}=3,l=4,m=3, ω/Ω =0.500
I_{mag}=5,l=6,m=3, ω/Ω =0.40	I_{mag}=5,l=6,m=3, ω/Ω =0.378
I_{mag}=4,l=5,m=4, ω/Ω =0.39	I_{mag}=4,l=5,m=4, ω/Ω =0.400

Figure D.5: Induction B_s/B_0 at the surface of the fluid, shown as a Mollweide projection with the axis of rotation vertical. The left column shows data taken under the same experimental conditions as the last three traces shown in Fig. 4.1, respectively. Mean values have been removed. The right column shows numerical calculations of the induction produced by analytically-known inertial modes. See also Fig. 4.5.
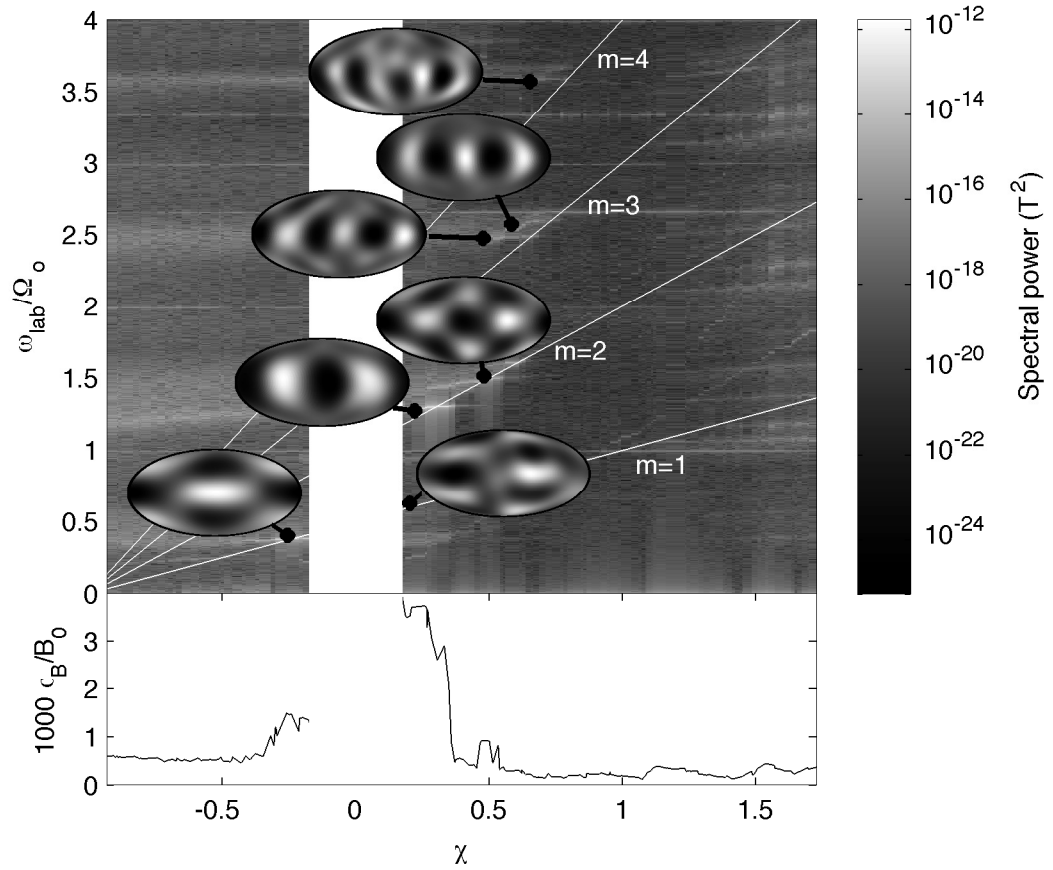
Figure D.6: The same plots shown in Fig. D.3, with white lines indicating boundaries where the normalized shear speed $M = 2$ for various wavenumbers m. Overlaid are the induction patterns of inertial modes we have identified (Figs. D.4 and D.5), with a line connecting each to the region of the spectrogram where the mode appears. See also Fig. 4.8.
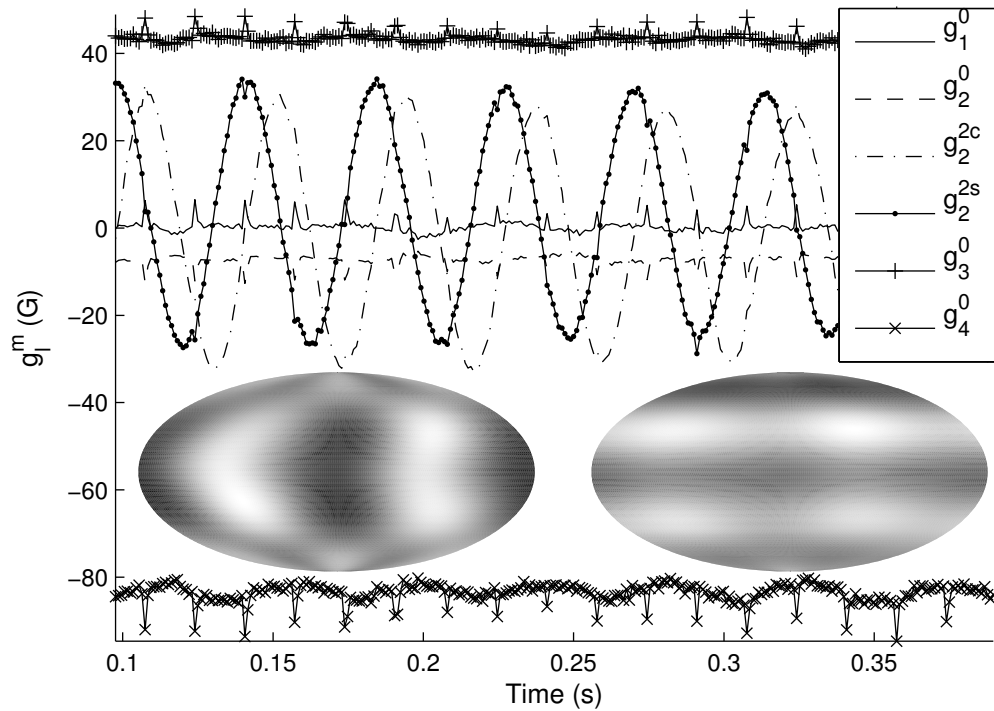
Figure D.7: Signature of an inertial mode, with and without mean induction. A few Gauss coefficients g_l^m are plotted over time, showing oscillatory signals characteristic of a travelling wave in g_2^2 as well as large DC induction in the axisymmetric modes g_l^0. The left inset shows a snapshot of the induction at the surface, with means subtracted. The right inset shows the same snapshot, with mean induction retained. See also Fig. 4.11.
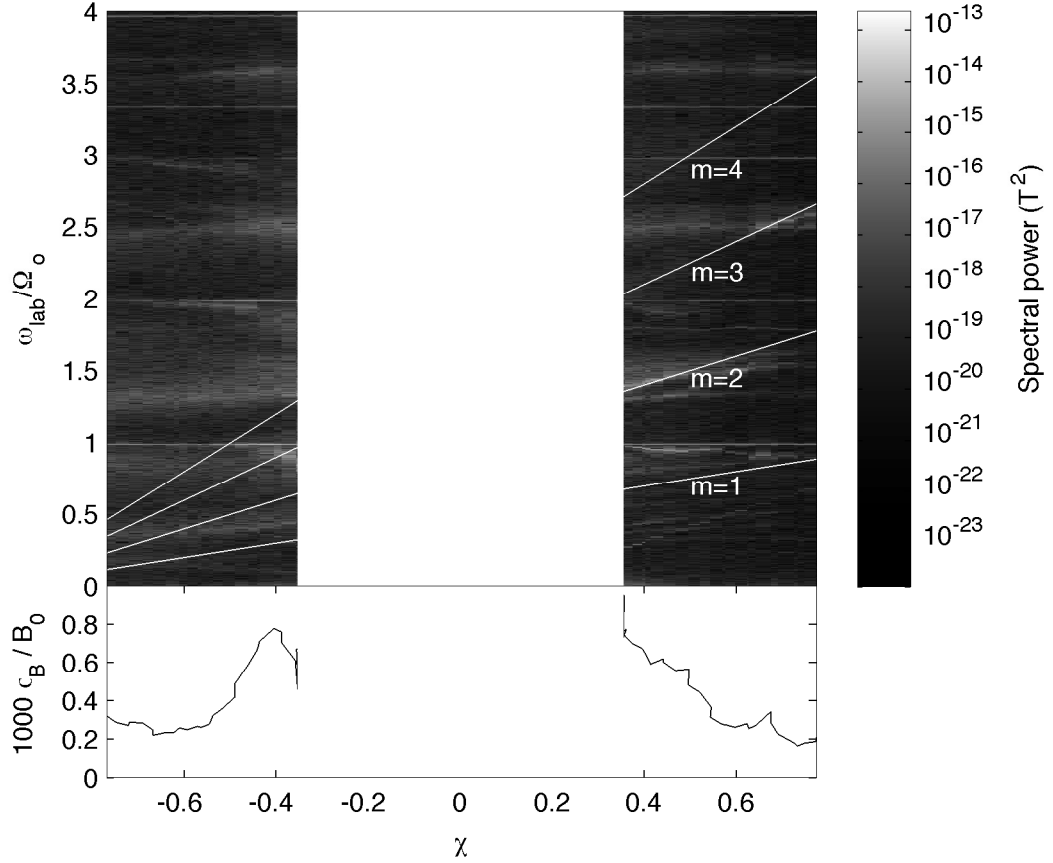
Figure D.8: Spectrogram and standard deviation of magnetic induction, showing inertial modes, with soft iron inner sphere. The upper plot is a spectrogram, with its vertical axis showing the normalized signal frequency $\omega_{\mathrm{lab}}/\Omega_o$ as measured in the laboratory frame, and its horizontal axis showing the rotation rate ratio χ. Here $E = 7.26 \times 10^{-8}$ ($\Omega_o/2\pi = 18$ Hz). Each column of pixels is a power spectrum of 32 s of data. The varying shades indicate spectral power, and white lines indicate boundaries where the normalized shear speed $M = 2$ for various wavenumbers m. The white central region lies at low speeds inaccessible with our AC motors. The lower plot shows the standard deviation of the same data, normalized by the applied magnetic field B_0. Compare to Fig. 4.3. See also Fig. 5.3.
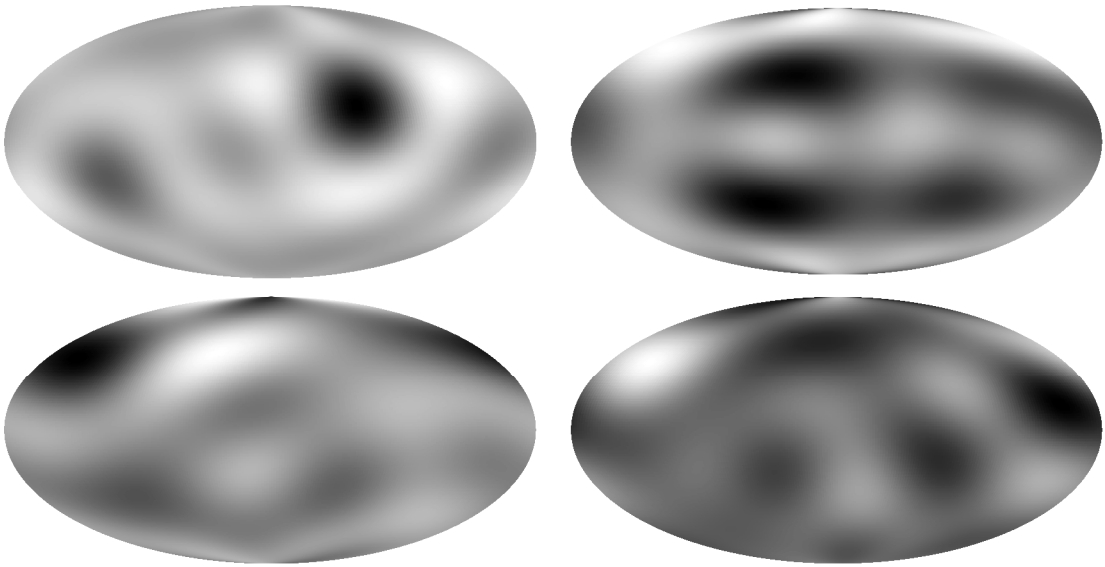
Figure D.9: Induction B_s/B_0 at the surface of the fluid, shown as a Mollweide projection with the axis of rotation vertical, with soft iron inner sphere. These images, from top left to bottom right, show data recorded under the same experimental conditions as the data shown in Fig. 5.1, from top to bottom, respectively. Mean values have been removed. See also Fig. 5.6.
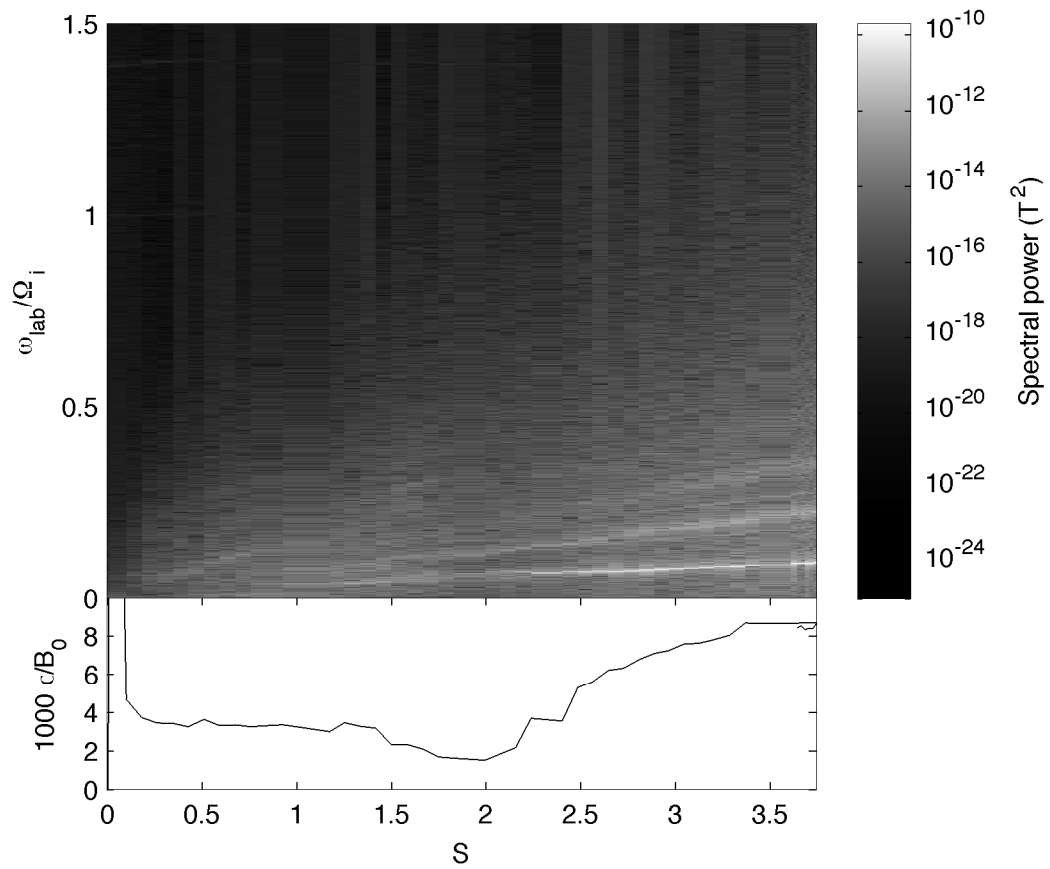
Figure D.10: Behavior at $E = \infty$ ($\Omega_o = 0$) and varying S (B_0), with soft iron inner sphere. The upper axes show a spectrogram, while the lower axes show the standard deviation of a probe at the equator. Here $\Omega_i/2\pi = 20$ Hz. See also Fig. 5.8.

Figure D.11: Behavior at $E = \infty$ ($\Omega_o = 0$) and varying S (B_0), with copper inner sphere. The upper axes show a spectrogram, while the lower axes show the standard deviation of a probe at the equator. Here $\Omega_i/2\pi = 5.25$ Hz. See also Fig. 5.9.
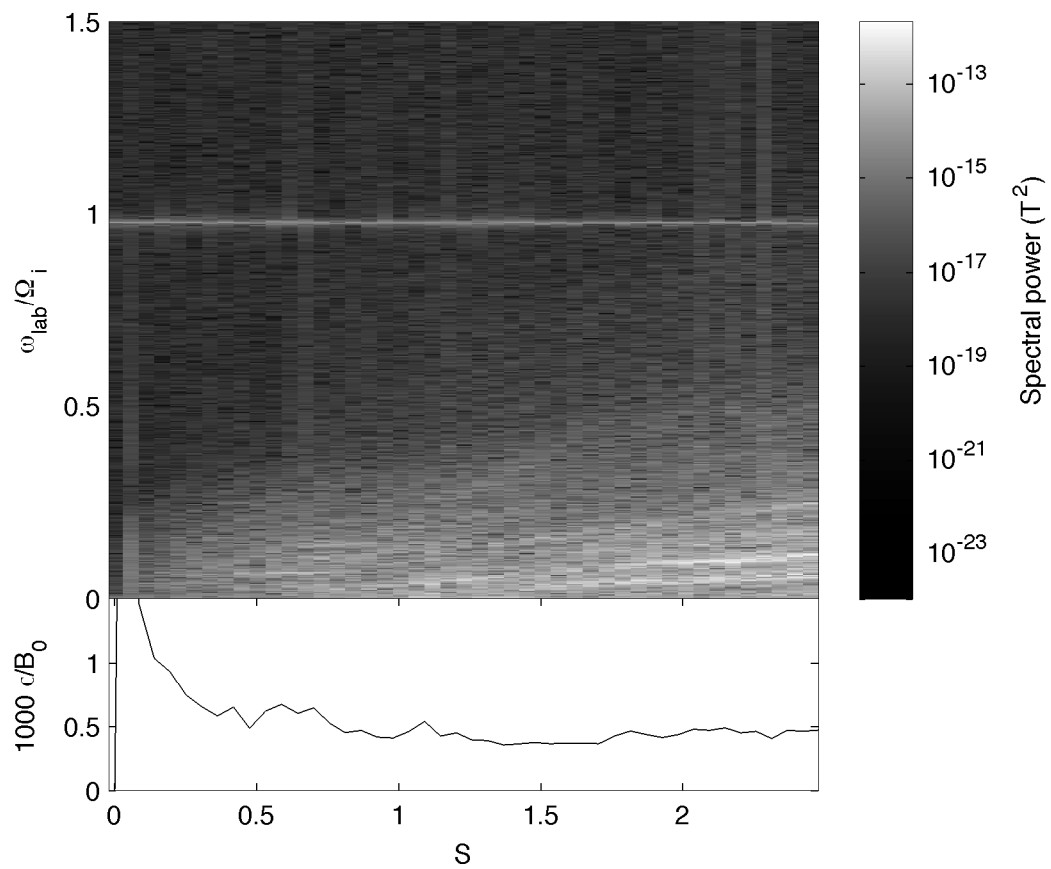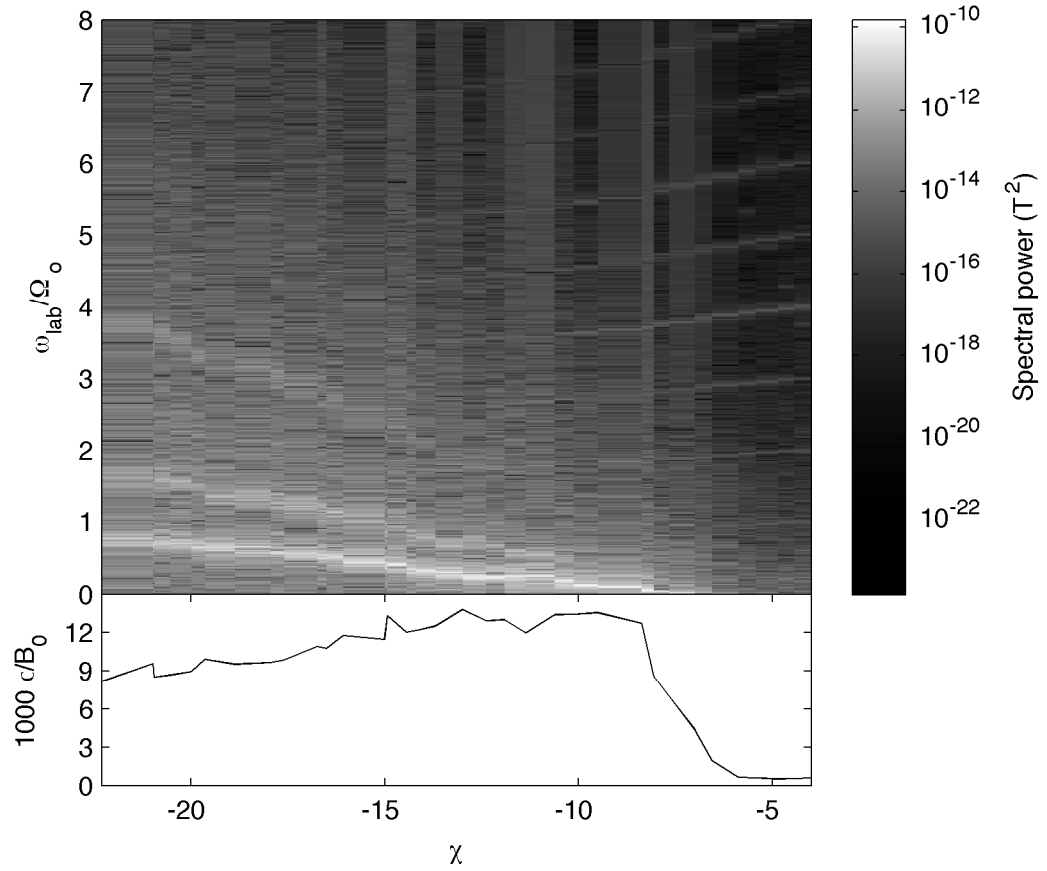
Figure D.12: Behavior at $|Re| \gg 1$ (large shear) and varying χ (Ω_i), with soft iron inner sphere. The upper axes show a spectrogram, while the lower axes show the standard deviation of a probe at the equator. Here $E = 6.3 \times 10^{-7}$ and $S = 2.1$, or equivalently, $\Omega_o/2\pi = 2$ Hz and $B_0 = 195$ G. See also Fig. 5.10.

Figure D.13: Behavior at $|Re| \gg 1$ (large shear) and varying χ (Ω_i), with copper inner sphere. The upper axes show a spectrogram, while the lower axes show the standard deviation of a probe at the equator. Here $E = 6.3 \times 10^{-7}$ and $S = 2.1$, or equivalently, $\Omega_o/2\pi = 2$ Hz and $B_0 = 195$ G. See also Fig. 5.11.
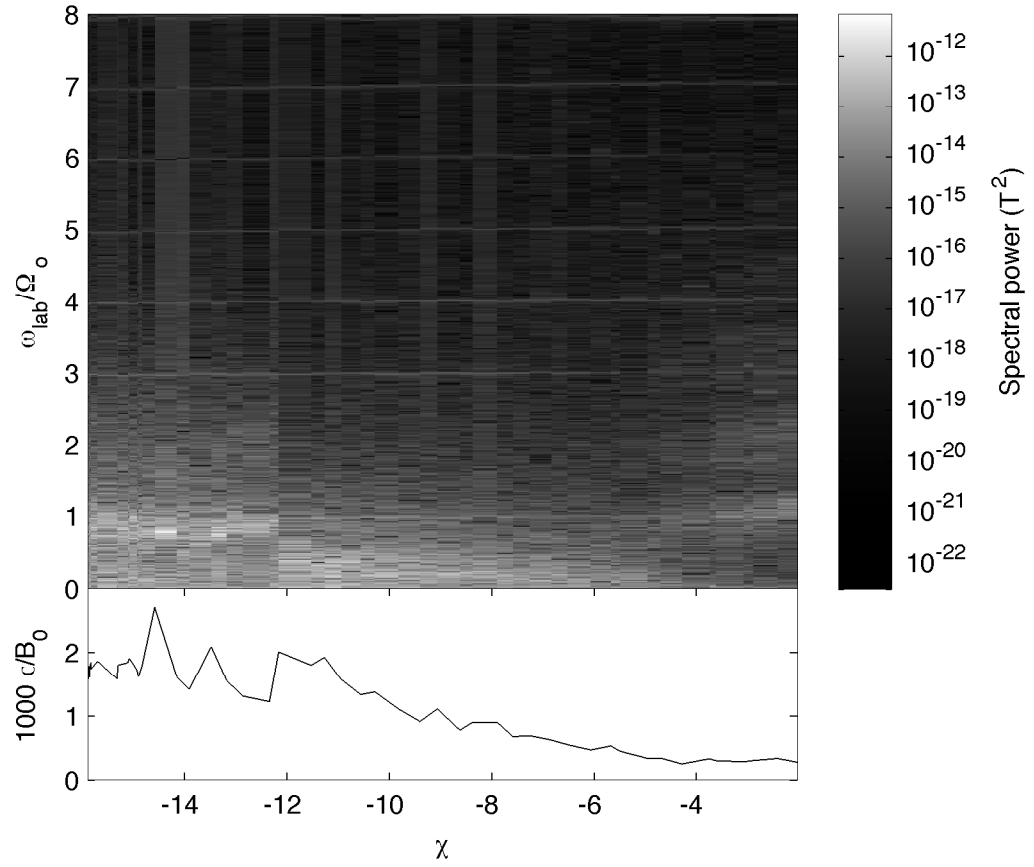
Bibliography

[1] J. Larmor. How the sun might have become a magnet. *Elec. Rev.*, 85(2183): 412, September 1919.

[2] G. A. Glatzmaier and P. H. Roberts. A three-dimensional convective dynamo solution with rotating and finitely conducting inner core and mantle. *Phys. Earth Plan. Int.*, 91(1):63–75, September 1995.

[3] W. Kuang and J. Bloxham. An Earth-like numerical dyamo model. *Nature*, 389:371–374, September 1997.

[4] F. J. Lowes and I. Wilkinson. Geomagnetic dynamo: A laboratory model. *Nature*, 198:1158–1160, 1963.

[5] F. J. Lowes and I. Wilkinson. Geomagnetic dynamo: An Improved laboratory model. *Nature*, 219:717–718, 1968.

[6] A. Gailitis, O. Lielausis, S. Dement'ev, E. Platacis, A. Cifersons, G. Gerbeth, T. Gundrum, F. Stefani, M. Christen, H. Hanel, and G. Will. Detection of a flow induced magnetic field eigenmode in the Riga dynamo facility. *Phys. Rev. Lett.*, 84(19):4365–4368, May 2000.

[7] R. Stieglitz and U. Muller. Experimental demonstration of a homogeneous two-scale dynamo. *Phys. Fluids*, 13(3):561–564, March 2001.

[8] R. Monchaux, M. Berhanu, M. Bourgoin, M. Moulin, Ph. Odier, J.-F. Pinton, R. Volk, S. Fauve, N. Mordant, F. Petrelis, A. Chiffaudel, F. Daviaud, B. Dubrulle, C. Gasquet, L. Marie, and F. Ravelet. Generation of a Magnetic Field by Dynamo Action in a Turbulent Flow of Liquid Sodium. *Phys. Rev. Lett.*, 98(4):044502–4, 2007.

[9] M. Berhanu, R. Monchaux, S. Fauve, N. Mordant, F. Pétrélis, A. Chiffaudel, F. Daviaud, B. Dubrulle, L. Marié, F. Ravelet, M. Bourgoin, P. Odier, J-F. Pinton, and R. Volk. Magnetic field reversals in an experimental turbulent dynamo. *Europhys. Lett.*, 77(5):59001 (5pp), 2007.

[10] W. Gilbert. *De Magnete, Magneticisque Corporibus, et de Magno Magnete Tellure (On the Magnet and Magnetic Bodies, and on the Great Magnet the Earth)*. 1600.

[11] E. Halley. An account of the cause of the change of the variation of the magnetical needle; with an hypothesis of the structure of the internal parts of the Earth: As it was proposed to the Royal Society in one of their late meetings. *Phil. Trans. R. Soc. London*, 16:563–578, 1692. ISSN 02607085.

[12] J. C. F. Gauss. Allgemeine Theorie des Erdmagnetismus. *Resultate aus den Beobachtungen magnetischen Vereins im Jahre 1838*, pages 1–57, 1839.

[13] A. M. Dziewonski and D. L. Anderson. Preliminary reference Earth model. *Phys. Earth Plan. Int.*, 25:297–356, June 1981.

[14] J. J. Love. Magnetic monitoring of Earth and space. *Physics Today*, 61(2): 31–37, Feb 2008.

[15] A. Jackson, A. R. T. Jonkers, and M. R. Walker. Four centuries of geomagnetic secular variation from historical records. *Phil. Trans. R. Soc. London A*, 358: 957–990, 2000.

[16] X. Quidelleur, J.-P. Valet, V. Courtillot, and G. Hulot. Long-term geometry of the geomagnetic field for the last five million years: An updated secular variation database. *Geophys. Res. Lett.*, 21:1639–1642, July 1994.

[17] J.-P. Valet, L. Meynadier, and Y. Guyodo. Geomagnetic dipole strength and reversal rate over the past two million years. *Nature*, 435:802–805, June 2005.

[18] V. Courtillot and P. Olson. Mantle plumes link magnetic superchrons to phanerozoic mass depletion events. *Earth Plan. Sci. Lett.*, 260:495–504, August 2007.

[19] D. J. Stevenson. Mission to Earth's core — a modest proposal. *Nature*, 423: 239–240, May 2003.

[20] A. Brandenburg and K. Subramanian. Astrophysical magnetic fields and non-linear dynamo theory. *Phys. Reports*, 417:1–4, October 2005.

[21] B. J. Anderson, M. H. Acuña, H. Korth, M. E. Purucker, C. L. Johnson, J. A. Slavin, S. C. Solomon, and R. L. McNutt. The Structure of Mercury's Magnetic Field from MESSENGER's First Flyby. *Science*, 321:82–85, July 2008.

[22] D. Lynden-Bell and J. E. Pringle. The evolution of viscous discs and the origin of the nebular variables. *Mon. Not. R. Astron. Soc.*, 168:603–637, September 1974.

[23] S. A. Balbus and J. F. Hawley. A Powerful Local Shear Instability in Weakly Magnetized Disks: I. Linear Analysis. *Bull. Am. Astron. Soc.*, 22:1209, September 1990.

[24] E. P. Velikhov. Stability of an ideally conducting liquid flowing between cylinders rotating in a magnetic field. *Sov. Phys. JETP*, 1959.

[25] S. Chandrasekhar. *Hydrodynamic and Hydromagnetic Stability.* Dover, New York, 1961.

[26] D. R. Sisan, N. Mujica, W. A. Tillotson, Y.-M. Huang, W. Dorland, A. B. Hassam, T. M. Antonsen, and D. P. Lathrop. Experimental observation and characterization of the magnetorotational instability. *Phys. Rev. Lett.*, 93(11): 114502, September 2004.

[27] T. G. Cowling. The stability of gaseous stars. *Mon. Not. R. Astron. Soc.*, 94: 768–782, June 1934.

[28] S. I. Braginsky. Structure of the F layer and reasons for convection in the core. *Dokl. Akad. Nauk SSSR English Trans.*, 149:1311–1314, 1963.

[29] Ya. B. Zeldovich. The magnetic field in the two-dimensional motion of a conducting turbulent fluid. *Sov Phys JETP*, 4:460–462, 1957.

[30] Yu. B. Ponomarenko. On the theory of hydromagnetic dynamo. *J. Appl. Mech. Tech. Phys.*, 775:775, 1973.

[31] G. O. Roberts. Dynamo action of fluid motions with two-dimensional periodicity. *R. Soc. London Phil. Trans. A*, 271:411–454, 1972.

[32] S. Kumar and P. H. Roberts. A three-dimensional kinematic dynamo. *Proc. R. Soc. London A*, 344(1637):235–258, June 1975.

[33] M. L. Dudley and R. W. James. Time-dependent kinematic dynamos with stationary flows. *Proc. R. Soc. A*, 425(1869):407–429, October 1989.

[34] M. Ossendrijver. The solar dynamo. *Astron. Astrophys. Rev.*, 11:287–367, 2003.

[35] A. Herzenberg. Geomagnetic dynamos. *Phil. Trans. R. Soc. London A*, 250 (986):543–583, August 1958.

[36] N. L. Peffley, A. B. Cawthorne, and D. P. Lathrop. Toward a self-generating magnetic dynamo: The role of turbulence. *Phys. Rev. E*, 61(5):5287–5294, May 2000.

[37] W. L. Shew. *Liquid sodium model of earth's outer core.* PhD thesis, University of Maryland, 2004.

[38] W. L. Shew and D. P. Lathrop. Liquid sodium model of geophysical core convection. *Phys. Earth Plan. Int.*, 153:136–149, 2005.

[39] P. Cardin, D. Brito, D. Jault, H-C. Nataf, and J-P. Masson. Towards a rapidly rotating liquid sodium dynamo experiment. *Magnetohydrodynamics*, 38(1): 177–189, 2002.

[40] H.-C. Nataf, T. Alboussière, D. Brito, P. Cardin, N. Gagnière, D. Jault, and D. Schmitt. Rapidly rotating spherical Couette flow in a dipolar magnetic field: An experimental study of the mean axisymmetric flow. *Phys. Earth Plan. Int.*, 170:60–72, 2008.

[41] D. Schmitt, T. Alboussière, D. Brito, P. Cardin, N. Gagnière, D. Jault, and H. C. Nataf. Rotating spherical Couette flow in a dipolar magnetic field: Experimental study of magneto-inertial waves. *J. Fluid Mech.*, 604:175–197, 2008.

[42] E. J. Spence, M. D. Nornberg, C. M. Jacobson, R. D. Kendrick, and C. B. Forest. Observation of a turbulence-induced large scale magnetic field. *Phys. Rev. Lett.*, 96(5):055002, 2006.

[43] M. D. Nornberg, E. J. Spence, R. D. Kendrick, C. M. Jacobson, and C. B. Forest. Intermittent magnetic field excitation by a turbulent flow of liquid sodium. *Phys. Rev. Lett.*, 97(4):044503, July 2006.

[44] J. M. Aurnou and P. L. Olson. Experiments on Rayleigh-Bénard convection, magnetoconvection and rotating magnetoconvection in liquid gallium. *J. Fluid Mech.*, 430:283–307, 2001.

[45] W. Liu, J. Goodman, I. Herron, and H. Ji. Helical magnetorotational instability in magnetized Taylor-Couette flow. *Phys. Rev. E*, 74(5):056302, 2006.

[46] E. Bullard and H. Gellman. Homogeneous dynamos and terrestrial magnetism. *Phil. Trans. R. Soc. London A*, 247(928):213–278, November 1954.

[47] L. D. Landau and E. M. Lifshitz. *Fluid Mechanics*. Theoretical Physics. Elsevier, Oxford, England, second edition, 2004.

[48] Lord Kelvin. Vibrations of a Columnar Vortex. *Phil. Mag.*, 10(155), 1880.

[49] A. Tilgner. *Core dynamics*, volume 8 of *Treatise on geophysics*, chapter Rotational dynamics of the core, pages 208–243. Elsevier, 2007.

[50] C.-G. Rossby. Relation between variations in the intensity of the zonal circulation of the atmosphere and the displacements of the semi-permanent centers of action. *J. Marine Res.*, pages 38–55, 1939.

[51] Joseph Pedlovsky. *Geophysical fluid dynamics*. Springer-Verlag, 2nd edition, 1987.

[52] H. P. Greenspan. *The theory of rotating fluids*. Cambridge monographs on mechanics and applied mathematics. Cambridge University Press, London, 1968.

[53] D. H. Kelley, S. A. Triana, D. S. Zimmerman, A. Tilgner, and D. P. Lathrop. Inertial waves driven by differential rotation in a planetary geometry. *Geophys. Astrophys. Fluid*, 101(5/6), 2007.

[54] G. P. Bewley, D. P. Lathrop, L. R. M. Maas, and K. R. Sreenivasan. Inertial waves in rotating grid turbulence. *Phys. Fluids*, 19(7):071701, 2007.

[55] Gregory Bewley. *Using frozen hydrogen particles to observe rotating and quantized flows in liquid helium*. PhD thesis, Yale University, 2006.

[56] G. H. Bryan. The waves on a rotating liquid spheroid of finite ellipticity. *Phil. Trans. R. Soc. London A*, 180:187–219, 1889.

[57] M. D. Kudlick. *On transient motions in a contained, rotating fluid.* PhD thesis, Massachusetts Institute of Technology, February 1966.

[58] K. Zhang, P. Earnshaw, X. Liao, and F. H. Busse. On inertial waves in a rotating fluid sphere. *J. Fluid Mech.*, 437:103–119, 2001.

[59] R. R. Kerswell. On the internal shear layers spawned by the critical regions in oscillatory Ekman boundary layers. *J. Fluid Mech.*, 298:311–325, 1995.

[60] H. Alfvén. Existence of electromagnetic-hydrodynamic waves. *Nature*, 150: 405–406, October 1942.

[61] J. D. Jackson. *Classical electrodynamics.* John Wiley & Sons, Inc., third edition, 1999.

[62] C. C. Finlay. *Encyclopedia of Geomagnetism and Paleomagnetism*, chapter Magnetohydrodynamic Waves, pages 1–34. 2005.

[63] R. A. Langel. *Geomagnetism*, volume 1, chapter 4, pages 249–512. Academic Press, London, 1987.

[64] E. Buckingham. On physically similar systems; Illustrations of the use of dimensional equations. *Phys. Rev.*, 4:345–376, October 1914.

[65] O. Reynolds. An experimental investigation of the circumstances which determine whether the motion of water shall be direct or sinuous, and the law of resistance in parallel channels. *Phil. Trans. R. Soc. London*, 174:935–982, 1883.

[66] P. Olson. Composition and physical properties of the core. Lecture given at Les Houches Dynamo School, August 2007.

[67] J. Zhang, X. Song, Y. Li, P. G. Richards, X. Sun, and F. Waldhauser. Inner core differential motion confirmed by earthquake waveform doublets. *Science*, 309(5739):1357–1360, 2005.

[68] X. Song and P. G. Richards. Seismological evidence for differential rotation of the Earth's inner core. *Nature*, 382:221–224, July 1996.

[69] E. H. Hall. On a new action of the magnet on electric currents. *Am. J. Math.*, 2(3):287–292, 1879.

[70] D. R. Sisan. *Hydromagnetic turbulent instability in liquid sodium experiments.* PhD thesis, University of Maryland, 2004.

[71] W. V. R. Malkus. Precession of the Earth as the cause of geomagnetism. *Science*, 160(3825):259–264, April 1968.

[72] J. Vanyo, P. Wilde, P. Cardin, and P. Olson. Experiments on precessing flows in the Earth's liquid core. *Geophys. J. Int.*, 121(1):136–142, 1995.

[73] J. Noir, P. Cardin, D. Jault, and J.-P. Masson. Experimental evidence of non-linear resonance effects between retrograde precession and the tilt-over mode within a spheroid. *Geophys. J. Int.*, 154(2):407–416, 2003.

[74] K. D. Aldridge and A. Toomre. Axisymmetric inertial oscillations of a fluid in a rotating spherical container. *J. Fluid Mech.*, 37:307–323, 1969.

[75] K. D. Aldridge. Axisymmetric inertial oscillations of a fluid in a rotating spherical shell. *Mathematika*, 19:163–168, 1972.

[76] A. M. M. Manders and L. R. M. Maas. Observations of inertial waves in a rectangular basin with one sloping boundary. *J. Fluid Mech.*, 493:59–88, 2003.

[77] J. Noir, D. Brito, K. Aldridge, and P. Cardin. Experimental evidence of inertial waves in a precessing spheroidal cavity. *Geophys. Res. Lett.*, 28(19): 3785–3788, October 2001.

[78] D. Fultz. A note on overstability and the elastoid-inertia oscillations of Kelvin, Solberg, and Bjerknes. *J. Atmos. Sci.*, 16:199–208, April 1959.

[79] R. R. Kerswell. Secondary instabilities in rapidly rotating fluids: Inertial wave breakdown. *J. Fluid Mech.*, 382:283–306, 1999.

[80] J. Noir, D. Jault, and P. Cardin. Numerical study of the motions within a slowly precessing sphere at low Ekman number. *J. Fluid Mech.*, 437:283–299, June 2001.

[81] R. Hollerbach, M. Junk, and C. Egbers. Non-axisymmetric instabilities in basic state spherical Couette flow. *Fluid Dyn. Res.*, 38:257–273, April 2006.

[82] M. Rieutord. Inertial modes in the liquid core of the Earth. *Phys. Earth Plan. Int.*, 91:41–46, 1995.

[83] M. Rieutord, B. Georgeot, and L. Valdettaro. Wave Attractors in Rotating Fluids: A Paradigm for Ill-Posed Cauchy Problems. *Phys. Rev. Lett.*, 85(20): 4277–4280, Nov 2000.

[84] H. S. Ribner. Reflection, transmission, and amplification of sound by a moving medium. *J. Acoust. Soc. Am.*, 29(4):435–441, April 1957.

[85] K. Stewartson. On almost rigid rotations, Part 2. *J. Fluid Mech.*, 26:131–144, 1966.

[86] M. Rieutord and L. Valdettaro. Inertial waves in a rotating spherical shell. *J. Fluid Mech.*, 341:77–99, 1997.

[87] M. Rieutord, B. Georgeot, and L. Valdettaro. Inertial waves in a rotating spherical shell: Attractors and asymptotic spectrum. *J. Fluid Mech.*, 435: 103–144, 2001.

[88] H. Poincaré. Sur la précession des corps déformables. *Bull. Astron. I*, 27: 321–356, 1910.

[89] F. H. Busse. Steady fluid flow in a precessing spheroidal shell. *J. Fluid Mech.*, 33:739–751, 1968.

[90] R. Hollerbach and R. R. Kerswell. Oscillatory internal shear layers in rotating and precessing flows. *J. Fluid Mech.*, 298:327–339, 1995.

[91] J. M. Aurnou and P. L. Olson. Strong zonal winds from thermal convection in a rotating spherical shell. *Geophys. Res. Lett.*, 28(13):2557–2560, July 2001.

[92] A. Tilgner. Zonal wind driven by inertial modes. *Phys. Rev. Lett.*, 99(19): 194501, 2007.

[93] M. S. Longuet-Higgins and A. E. Gill. Resonant interactions between planetary waves. *Proc. R. Soc. London A*, 299:120–140, June 1967.

[94] L. M. Smith, J. R. Chasnov, and F. Waleffe. Crossover from two- to three-dimensional turbulence. *Phys. Rev. Lett.*, 77:2467–2470, September 1996.

[95] L. M. Smith and F. Waleffe. Transfer of energy to two-dimensional large scales in forced, rotating three-dimensional turbulence. *Phys. Fluids*, 11:1608–1622, June 1999.

[96] H. P. Greenspan. On the non-linear interaction of inertial modes. *J. Fluid Mech.*, 36:257–264, 1969.

[97] R. Avalos-Zuniga, F. Plunian, and A. Gailitis. Influence of electromagnetic boundary conditions onto the onset of dynamo action in laboratory experiments. *Phys. Rev. E*, 68(6):066307, Dec 2003.

[98] L. Marié, J. Burguete, F. Daviaud, and J. Léorat. Numerical study of homogeneous dynamo based on experimental von Kármán type flows. *Eur. Phys. J. B*, 33:469–485, June 2003.

[99] F. Ravelet, A. Chiffaudel, F. Daviaud, and J. Léorat. Toward an experimental von Kármán dynamo: Numerical studies for an optimized design. *Phys. Fluids*, 17(11):117104, 2005.

[100] F. Stefani, M. Xu, G. Gerbeth, F. Ravelet, A. Chiffaudel, F. Daviaud, and J. Léorat. Ambivalent effects of added layers on steady kinematic dynamos in cylindrical geometry: application to the VKS experiment. *Eur. J. of Mech. B*, 25(6):894 – 908, 2006. ISSN 0997-7546.

[101] C. Gissinger, A. Iskakov, S. Fauve, and E. Dormy. Effect of magnetic boundary conditions on the dynamo threshold of von Kármán swirling flows. *Europhys. Lett.*, 82(29001), April 2008.

[102] F. Pétrélis, N. Mordant, and S. Fauve. On the magnetic fields generated by experimental dynamos. *Geophys. Astrophys. Fluid*, 101:289–323, June 2007.

[103] R. Laguerre, C. Nore, A. Ribeiro, J. Léorat, J.-L. Guermond, and F. Plunian. Impact of impellers on the axisymmetric magnetic mode in the VKS2 dynamo experiment. *Phys. Rev. Lett.*, 101(10):104501, 2008.

[104] J. Hartmann and F. Lazarus. *Hg-dynamics II: Experimental investigations on the flow of mercury in a homogeneous magnetic field.* Levin and Munksgaard, 1937.

[105] R. Hollerbach and S. Skinner. Instabilities of magnetically induced shear layers and jets. *Proc. R. Soc. A*, 457:785, April 2001.

[106] A. N. Kolmogorov. The local structure of turbulence in incompressible viscous fluid for very large Reynolds numbers. *Proc. USSR Acad. Sci.*, 20:299–303, 1941.

[107] A. N. Kolmogorov. Dissipation of energy in locally isotropic turbulence. *Proc. USSR Acad. Sci.*, 32:16–18, 1941.

[108] L. F. Richardson. *Weather prediction by numerical processes.* Dover, New York, 1965.

[109] A. Arnèodo, R. Benzi, J. Berg, L. Biferale, E. Bodenschatz, A. Busse, E. Calzavarini, B. Castaing, M. Cencini, L. Chevillard, R. T. Fisher, R. Grauer, H. Homann, D. Lamb, A. S. Lanotte, E. Lévèque, B. Lüthi, J. Mann, N. Mordant, W.-C. Müller, S. Ott, N. T. Ouellette, J-F. Pinton, S. B. Pope, S. G. Roux, F. Toschi, H. Xu, and P. K. Yeung International Collaboration for Turbulence Research. Universal intermittent properties of particle trajectories in highly turbulent flows. *Phys. Rev. Lett.*, 100(25):254504, 2008.

[110] C. Morize and F. Moisy. Energy decay of rotating turbulence with confinement effects. *Phys. Fluids*, 18(6):065107, 2006.

[111] L. Jacquin, O. Leuchter, C. Cambon, and J. Mathieu. Homogeneous turbulence in the presence of rotation. *J. Fluid Mech.*, 220:1–52, 1990.

[112] D. S. Zimmerman and S. A Triana. Personal communication., 2009.

[113] G. P. Bewley, D. P. Lathrop, and K. R. Sreenivasan. Superfluid helium: Visualization of quantized vortices. *Nature*, 441:588, June 2006.

[114] C. C. Finlay and A. Jackson. Equatorially dominated magnetic field change at the surface of Earth's core. *Science*, 300(5628):2084–2086, 2003.

[115] A. K. M. F. Hussain and K. B. M. Q. Zaman. An experimental study of organized motions in the turbulent plane mixing layer. *J. Fluid Mech.*, 159: 85–104, October 1985.

[116] L. P. Bernal and A. Roshko. Streamwise vortex structure in plane mixing layers. *J. Fluid Mech.*, 170:499–525, September 1986.

[117] S. K. Robinson. Coherent motions in the turbulent boundary layer. *Ann. Rev. Fluid Mech.*, 23:601–639, January 1991.

[118] L. Ong and J. M. Wallace. Joint probability density analysis of the structure and dynamics of the vorticity field of a turbulent boundary layer. *J. Fluid Mech.*, 367:291–328, July 1998.

[119] J. D. Diorio, D. H. Kelley, and J. M. Wallace. The spatial relationships between dissipation and production rates and vortical structures in turbulent boundary and mixing layers. *Phys. Fluids*, 19(3):035101, March 2007.

[120] J. M. Hamilton, J. Kim, and F. Waleffe. Regeneration mechanisms of near-wall turbulence structures. *J. Fluid Mech.*, 287:317–348, 1995.

[121] F. Waleffe. Exact coherent structures in channel flow. *J. Fluid Mech.*, 435: 93–102, May 2001.

[122] H. Faisst and B. Eckhardt. Traveling waves in pipe flow. *Phys. Rev. Lett.*, 91 (224502), November 2003.

[123] B. Hof, C. W. H. van Doorne, J. Westerweel, F. T. M. Nieuwstadt, H. Faisst, B. Eckhardt, H. Wedin, R. R. Kerswell, and F. Waleffe. Experimental observation of nonlinear traveling waves in turbulent pipe flow. *Science*, 305(5690): 1594–1598, September 2004.

[124] B. Eckhardt, T. M. Schneider, B. Hof, and J. Westerweel. Turbulence transition in pipe flow. *Ann. Rev. Fluid Mech.*, 39(1):447–468, 2007.

[125] B. Hof, J. Westerweel, T. M. Schneider, and B. Eckhardt. Finite lifetime of turbulence in shear flows. *Nature*, 443:59–62, September 2006.

[126] J. Wang, J. Gibson, and F. Waleffe. Lower branch coherent states in shear flows: Transition and control. *Phys. Rev. Lett.*, 98(20):204501, 2007.

[127] J. F. Gibson, J. Halcrow, and P. Cvitanović. Visualizing the geometry of state space in plane Couette flow. *J. Fluid Mech.*, 611:107–130, 2008.

[128] E. N. Lorenz. Deterministic nonperiodic flow. *J. Atmos. Sci.*, 20(2):130–141, 1963.

[129] K. Zhang and X. Liao. A new asymptotic method for the analysis of convection in a rapidly rotating sphere. *J. Fluid Mech.*, 518:319–346, November 2004.

[130] K. D. Aldridge and I. Lumb. Inertial waves identified in the Earth's fluid outer core. *Nature*, 325:421–423, January 1987.

[131] J. Hinderer, D. Crossley, and H. Xu. A 2-year comparison between the French and Canadian superconducting gravimeter data. *Geophys. J. Int.*, 116(2): 252–266, Feb 1994. ISSN 0956-540X.

[132] D. Jault, C. Gire, and J. L. Le Mouel. Westward drift, core motions and exchanges of angular momentum between core and mantle. *Nature*, 333:353–356, May 1988.

[133] J. L. Margot, S. J. Peale, R. F. Jurgens, M. A. Slade, and I. V. Holin. Large longitude libration of Mercury reveals a molten core. *Science*, 316(5825):710–714, 2007.

[134] H. Matsui and B. A. Buffett. Sub-grid scale model for convection-driven dynamos in a rotating plane layer. *Phys. Earth Plan. Int.*, 153:108–123, November 2005.

[135] V. Noskov, R. Stepanov, S. Denisov, P. Frick, G. Verhille, N. Plihon, and J-F. Pinton. Dynamics of a turbulent spin-down flow inside a torus. Submitted to Phys. Fluids, 2009.

[136] R. F. Gans. On hydromagnetic precession in a cylinder. *J. Fluid Mech.*, 45: 111–130, 1971.